FINAL REPORT

Electrolytic Plasma Processing for Sequential Cleaning and Coating Deposition for Cadmium Plating Replacement

SERDP Project WP-1406

AUGUST 2008

Keith Legg
Rowan Technology Group

This document has been approved for public release.

Strategic Environmental Research and Development Program

Report Documentation Page

Form Approved
OMB No. 0704-0188

Public reporting burden for the collection of information is estimated to average 1 hour per response, including the time for reviewing instructions, searching existing data sources, gathering and maintaining the data needed, and completing and reviewing the collection of information. Send comments regarding this burden estimate or any other aspect of this collection of information, including suggestions for reducing this burden, to Washington Headquarters Services, Directorate for Information Operations and Reports, 1215 Jefferson Davis Highway, Suite 1204, Arlington VA 22202-4302. Respondents should be aware that notwithstanding any other provision of law, no person shall be subject to a penalty for failing to comply with a collection of information if it does not display a currently valid OMB control number.

1. REPORT DATE	2. REPORT TYPE	3. DATES COVERED
AUG 2008	**N/A**	**-**

4. TITLE AND SUBTITLE	5a. CONTRACT NUMBER
Electrolytic Plasma Processing for Sequential Cleaning and Coating Deposition for Cadmium Plating Replacement	5b. GRANT NUMBER
	5c. PROGRAM ELEMENT NUMBER
6. AUTHOR(S)	5d. PROJECT NUMBER
	5e. TASK NUMBER
	5f. WORK UNIT NUMBER
7. PERFORMING ORGANIZATION NAME(S) AND ADDRESS(ES) **Rowan Technology Group**	8. PERFORMING ORGANIZATION REPORT NUMBER
9. SPONSORING/MONITORING AGENCY NAME(S) AND ADDRESS(ES)	10. SPONSOR/MONITOR'S ACRONYM(S)
	11. SPONSOR/MONITOR'S REPORT NUMBER(S)

12. DISTRIBUTION/AVAILABILITY STATEMENT
Approved for public release, distribution unlimited

13. SUPPLEMENTARY NOTES
The original document contains color images.

14. ABSTRACT

15. SUBJECT TERMS

16. SECURITY CLASSIFICATION OF:			17. LIMITATION OF ABSTRACT	18. NUMBER OF PAGES	19a. NAME OF RESPONSIBLE PERSON
a. REPORT	b. ABSTRACT	c. THIS PAGE			
unclassified	**unclassified**	**unclassified**	**SAR**	**219**	

Standard Form 298 (Rev. 8-98)
Prescribed by ANSI Std Z39-18

This report was prepared under contract to the Department of Defense Strategic Environmental Research and Development Program (SERDP). The publication of this report does not indicate endorsement by the Department of Defense, nor should the contents be construed as reflecting the official policy or position of the Department of Defense. Reference herein to any specific commercial product, process, or service by trade name, trademark, manufacturer, or otherwise, does not necessarily constitute or imply its endorsement, recommendation, or favoring by the Department of Defense.

EXECUTIVE SUMMARY

The technique of Electro-Plasma Processing (EPP) was developed and evaluated for DoD use. The EPP process is a high voltage aqueous process (150-200V) that takes place in an electrolyte jet or foam. It can be used to clean metal surfaces or to deposit alloy coatings, the easiest and most common of which are Zn-based. The process operates in the continuous discharge region of the electrolytic current-voltage curve, where the cathodic workpiece is covered with a plasma envelope from a layer of hydrogen electrolyzed at its surface. Material from the solution is deposited by a combination of electrolytic deposition and evaporation across the hydrogen layer.

When used as a cleaning method, the technique produces a very clean, roughened, practically amorphous surface comprising a thin heat-treated outmost layer (0.5-2m or 0.00002-0.0001" thick). Nevertheless, there was no measurable fatigue debit for EPP-cleaned surfaces. Nor was there any hydrogen embrittlement, even though copious quantities of hydrogen are evolved in the process.

When used as a coating method, the technique produced nodular coatings with very high porosity. A number of different coating chemistries were evaluated, culminating in corrosion, embrittlement and fatigue testing of ZnNi with chromate (Dipsol IZ-258S) and trivalent chrome (Metalast TCP-HF) sealers, and ZnMg with a phosphate/silicate sealer. Again there was no hydrogen embrittlement, but there was a fatigue debit of perhaps a factor of two, with a larger debit for ZnNi at high stress (above 130ksi). This debit is similar to that caused by standard electroplated alkaline ZnNi.

EPP ZnNi coatings performed well in environmental embrittlement (re-embrittlement) testing, with performance second only to AlumiPlate among the Cd alternative coatings tested by the Army Research Laboratory (ARL) for the DoD Joint Cadmium Alternatives Team (JCAT).
The ZnMg coatings performed poorly in B117 corrosion testing, showing white corrosion almost immediately and red rust by 696 hours. The corrosion performance of the Metalast-sealed ZnNi specimens was quite good, and significantly better than the chromate converted specimens. One trivalent-sealed specimen performed particularly well, maintaining a corrosion ranking of 7 out to 16 weeks, when the test was terminated. This particular specimen was more carefully sealed than the others, and emphasizes the importance of care in applying non-chromate sealers.
It had been hoped that this process would make it possible to deposit Al coatings or ZnAl alloys from aqueous solution. Unfortunately this proved impossible, producing only Al hydroxides and oxides, which are not sacrificial coatings.

The disadvantages of the process are that the coatings are very porous while the technique is more complicated and expensive than standard ZnNi electroplating. We conclude that the EPP process has several disadvantages compared with standard cleaning and electroplating processes for the types of complex components that make up the typical depot workload. It does not have sufficient advantages over standard ZnNi and similar electroplates to make it worthwhile developing for general DoD operations. However, it may have some niche applications in cleaning and paint adhesion. There may also be some potential uses for the technology for niche OEM coatings.

Note: This project was principally executed by two separate groups, the first a collaboration between the University of Texas at Arlington (UTA) and CAP Technologies LLC in Baton Rouge, LA, and the second by the University of Sheffield in the UK. These groups essentially operated separately and therefore they each submitted a final report. The main body of this report summarizes the results obtained by UTA/CAP and by Sheffield, with the actual reports submitted by the groups provided as appendices.

TABLE OF CONTENTS

1. Introduction ..... - 5 -
2. Electrolytic Plasma Processing ..... - 5 -
   2.1. EPP Process ..... - 6 -
      2.1.1. DC vs pulsed current ..... - 6 -
      2.1.2. EPP cleaning ..... - 7 -
      2.1.3. EPP coating deposition ..... - 8 -
   2.2. Equipment ..... - 8 -
3. Results ..... - 9 -
   3.1. Equipment design ..... - 9 -
      3.1.1. Anode design ..... - 10 -
   3.2. EPP cleaning ..... - 10 -
      3.2.1. Metallurgical effects of EPP cleaning ..... - 10 -
      3.2.2. Effect of cleaning on hydrogen embrittlement ..... - 13 -
      3.2.3. Effect of cleaning on fatigue ..... - 14 -
   3.3. Coating deposition ..... - 15 -
      3.3.1. Zn coating ..... - 15 -
      3.3.2. Zn-Al coating ..... - 16 -
      3.3.3. Zn-Ni coating (CAP) ..... - 16 -
      3.3.4. Zn-Mg coating (Sheffield) ..... - 19 -
   3.4. Coating performance ..... - 21 -
      3.4.1. Hydrogen embrittlement ..... - 21 -
      3.4.2. Fatigue ..... - 23 -
      3.4.3. Corrosion ..... - 24 -
         3.4.3.1. Zn-Mg coatings ..... - 24 -
         3.4.3.2. Zn-Ni coatings ..... - 28 -
4. Evaluation of Suitability for DoD Use ..... - 30 -
5. References ..... -31-
6. Appendix A – Final Report from University of Texas and CAP Technologies
7. Appendix B – Final Report from University of Sheffield

LIST OF TABLES

Table 1. EPP cleaning conditions (CAP). ..... - 13 -

Table 2. ZnNi Deposition conditions for test specimens (CAP). ..... - 17 -

Table 3. Chemistry and corrosion properties of specimens of Table 2. ..... - 17 -

Table 4. Deposition conditions for Zn-Ni B117 corrosion test specimens (CAP) ..... - 18 -

Table 5. Deposition conditions for Zn-Mg specimens (Sheffield). ..... - 19 -

Table 6. Hydrogen embrittlement, ASTM F519, 75% NTS, extended time. ..... - 21 -

Table 7 GM 9540 re-embrittlement test of EPP Zn-Ni compared with JCAT coatings 65% NTS load.. ..... - 22 -

LIST OF FIGURES

Figure 1. Schematic of the various regions of the current-voltage curve under an electrolyte. ..... - 6 -

Figure 2. Typical current and voltage waveforms at different stages of EPP cleaning in DC (a, b, c and d) and pulsed unipolar current mode (e and f). Ub and Uc are voltages shown in Figure 1. (Sheffield)..... - 7 -

Figure 3. CAP reactor V-8 built to deposit Zn-Ni coatings..... - 8 -

Figure 4. University of Sheffield EPP reactor showing vertical spray system..... - 9 -

Figure 5. (a) and (b) SEM and (c) EDS analysis of 4340 steel treated by EPP, Condition 1; (d), (e), (f) Condition 2. ..... - 11 -

Figure 6. SEM cross section of 4340 steel treated by EPP for 30 s in NaHCO3 solution; magnification increases from (a) to (d). ..... - 12 -

Figure 7. Hardness of 4340 steel as function of depth after EPP cleaning, measured at CAP. Left hardness vs depth, right indentations on cross-section. ..... - 12 -

Figure 8. Depth profile of hydrogen content in 4340 steel treated in NaHCO3 under Condition 1 and Condition 2. ..... - 13 -

Figure 9. Hydrogen depth profile in 4340 steel treated in NH4Cl under Condition 3. ..... - 14 -

Figure 10. Fatigue of unpeened 4340 steel, cleaned at CAP and Sheffield by EPP (260-280ksi heat treat). Smooth bar, R=-1. ..... - 15 -

Figure 11. SEM of EPP Zn coating (CAP). ..... - 16 -

Figure 12. Cross section of EPP Zn coating (CAP). ..... - 16 -

Figure 13. Morphologies of CAP ZnNi specimens. ..... - 18 -

Figure 14. SEM images of surface (left) and cross-sectional view of EPP coatings produced from binary Zn-Mg sulfate electrolyte systems with various concentrations of Mg sulfate: (a) 0.1 M; (b) 0.2 M; (c) 0.3 M, followed by the phosphate-silicate passivation treatment. ..... - 20 -

Figure 15. C-ring embrittlement specimen (F-519 Type 1d) with tensioning bolt. ..... - 21 -

Figure 16. Fatigue of EPP-coated 4340 R=-1. Zn-Ni (CAP), Zn-Mg (Sheffield). ..... - 24 -

Figure 17. Potentiodynamic polarization curves in 3.5% NaCl solution of EPP Zn-Mg coatings phosphated and silicate sealed. (a) the passivation post-treatment (Batch 1) and (b) Mg salt content in the bath per Table 6 (Sheffield). ..... - 25 -

Figure 18. B117 Corrosion Ranking vs exposure time for Zn-Mg coatings on 4340, (Sheffield). Measured at PAX. ..... - 26 -

Figure 19. Typical Zn-Mg corrosion specimens during B117 testing. ..... - 27 -

Figure 20. B117 Corrosion Ranking vs exposure time for Zn-Ni coatings on 4340 steel (CAP). Deposition conditions Table 4. Testing at NAVAIR PAX. Specimens 34-43 chromated, 44-50 TCP-sealed. ..... - 28 -

Figure 21. Zn-Ni specimens during B117 corrosion test. Specimen number at left, hours at top (CAP). Testing at NAVAIR PAX..... - 29 -

1. Introduction

Cd plate is an excellent sacrificial corrosion coating that continues to provide corrosion resistance even when damaged. It works well in air and marine environments, has low volume corrosion products, fungus resistance, lubricity, solderability, good adhesion, consistent torque-tension, good ductility, conductivity, and uniform thickness within standard thread tolerances. Because Cd is a heavy metal poison, it has been eliminated from almost all industrial products, except aircraft by the European ELV, WEEE and RoHS rules. The Department of Defense and the aircraft industry are the sole remaining large scale Cd users. The military is by far the largest user of Cd-plated parts, with landing gear, fasteners, actuator rods, lock washers, thrust pins and springs dominating the HS steel applications. These components are diversely located in military air, land and marine vehicles.

DoD has been investigating alternatives to cadmium plating for more than 40 years, with laboratory studies and field trials conducted on coatings such as Zn-Ni, Sn-Zn, IVD Al, electroplated Al, molten salt bath Al-Mn, and SerMetel. Many of these are being used in practice, but there is still a significant problem with finding a replacement for Cd plating on high-strength steel (HSS). In general, HS steels are those with an ultimate tensile strength (UTS) in the range of 180-280 ksi (hardness values ranging from about 40-52 HRC). Those onto which Cd is currently being applied include AISI 4340, Hy-Tuf, Aermet 100, M50, 300M, PH13-8Mo stainless steel and maraging grades 200-250. The commercial specification for the application of electrodeposited Cd, AMS SAE QQ-P-416, requires that steel parts having a UTS greater than 150 ksi must be stress relieved prior to cleaning and plating to remove residual stresses and that steel parts having a hardness of 40 HRC or greater must be baked subsequent to plating (at various time and temperature schedules based on the final hardness of the component) to provide hydrogen embrittlement relief. During plating, molecular hydrogen is evolved which can migrate to traps within the steel part (such as dislocations, carbides and grain boundaries) and, if baking is not done or is done incorrectly, can result in a delayed hydrogen embrittlement failure of the part in service.

Although QQ-P-416 does not specify which method to use, currently the most common method of electroplating Cd onto HS steel is the alkaline cyanide bath to produce low hydrogen embrittlement Cd (LHE Cd). Cyanide is also toxic and is on the list of EPA-17 hazardous chemicals. There are other plating solutions that do not use cyanide, including Cd acid and Cd alkaline plating solutions. However, these baths purportedly do not have the throwing power of the cyanide solutions. Additional corrosion resistance is often gained by applying a chromate conversion coating to the Cd-plated components. This supplementary chromate treatment (Type II of QQ-P-416) can be applied using either an aqueous solution of salts or acids or both. This treatment contains hexavalent chromium, a known carcinogen that is also severely restricted by the EU rules and by its OSHA PEL. Thus, the most widely used method of Cd plating and post-treatment contain three hazardous materials, which provide a very high incentive to finding a suitable alternative.

At this point the best Cd alternatives for general use appear to be LHE ZnNi, developed by Dipsol of America and Boeing, and AlumiPlate electroplated Al. AlumiPlate has performed best in Joint Cd Alternative Team (JCAT) testing, while ZnNi has also performed very well. AlumiPlate is used in some locations on the landing gear of the F-35 and on the F-22, but it requires an enclosed plating line with an inert atmosphere, giving it a high capital cost. LHE ZnNi is a standard bath process, but it still requires validation (an ESTCP process is just beginning to validate pulse plated ZnNi). Without a paint system ZnNi performs worse than unpainted AlumiPlate in the Navy's G85 SO_2 salt fog corrosion test, but both coatings perform well when painted.

There is one other aspect related to the entire Cd plating process which is also an issue with all other proposed alternatives listed or discussed above, and that is the cleaning that must be done prior to application of the coating. Components made from steel all have iron oxides on the surface and normally also have grease, dirt and oil from handling. Removal of these is normally done in one of two ways. The component may be grit blasted with something like aluminum oxide, or it may go through a sequence of vapor degrease, electrolytic cleaning, hot water rinse, acid dip, and finally water rinse. Both of these processes generate waste that must be disposed of in an acceptable manner. The second process especially generates large volumes of waste water because of the two-step rinse. Determining an alternative cleaning process that is more environmentally acceptable would be a further benefit related to replacing Cd plating.

2. Electrolytic Plasma Processing

There are various types of high voltage electrolytic processes on the commercial market today. These are processes that take place in solution, but involve generating a plasma at the substrate surface. They are most closely related to anodizing, but take place at a voltage high enough to create a plasma. Unlike anodizing they often incorporate additional compounds into the solution, which then deposit onto the surface, usually as an oxide. The most widely used of these processes are Keronite™, which is used for protection of Al, and Tagnite™, which is used for Mg. The process evaluated in this project is a Russian-developed technology known as the Electro Plasma Process (EPP), also known as Electrolytic Plasma Technology (EPT), which was

provided by CAP Technologies in Louisiana and by the University of Sheffield in Britain. The CAP process is patented under US Pat # 6,585,875.

2.1. EPP Process

Figure 1 shows the current-voltage curve for a substrate in an electrolyte. Common processes such as anodizing and electroplating take place at the low voltage left hand side of the curve. As the voltage is increased, gas evolution becomes very rapid and above U_b on the curve microarc discharges begin to take place at the substrate surface. Above U_c the surface becomes enveloped in a plasma envelope.

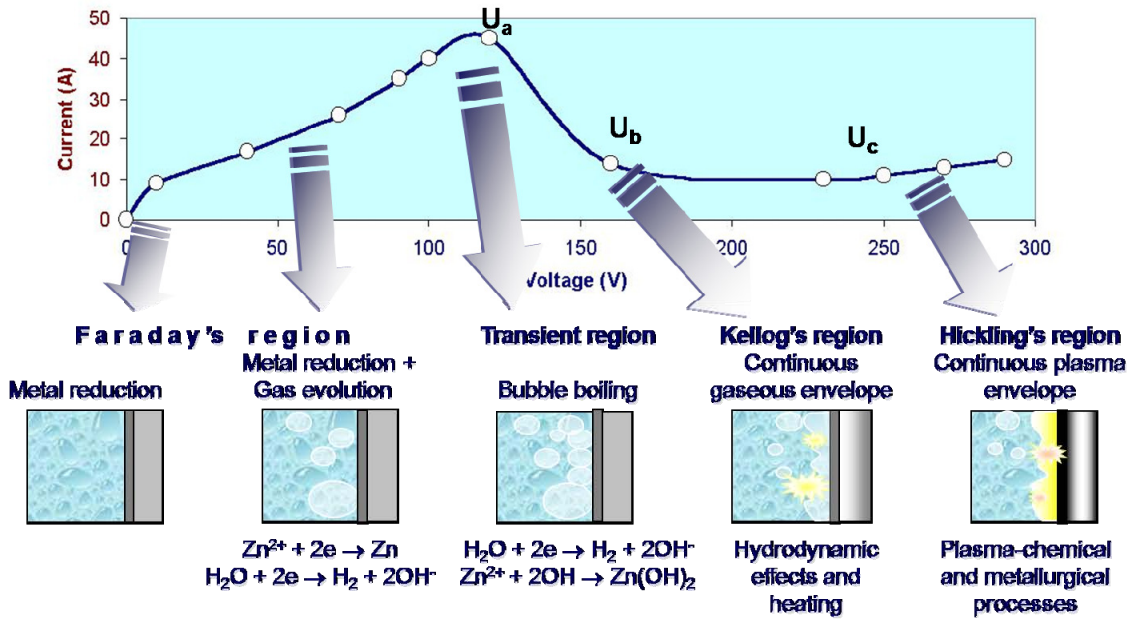

Figure 1. Schematic of the various regions of the current-voltage curve under an electrolyte.

EPP usually takes place in the stable region between U_b and U_c, with the substrate cathodic with respect to a perforated anode. In this region there are two primary effects

1. Electrolysis of the solution, releasing hydrogen bubbles at the surface of the substrate
2. Microarcs, which take place from the electrolyte, across the bubble and onto the substrate surface.

Because a strong electrical potential is established on the bubble adjacent to the workpiece surface, a hydrogen plasma is generated in a thin layer. The lifespan of an average hydrogen bubble is less than 1 ms and the plasma exists for 1-10 μs [1]. The plasma is continuously forming at this high rate over the entire steel surface. Metal cations present in the electrolyte film begin to migrate toward the steel surface, but the large majority of these ions are attached to the bubbles. These ions are either original additions to the electrolyte or are generated from the anode metal by electrolytic decomposition, and they can form a coating on the surface. In this way EPP can be used either for cleaning a surface or for depositing a coating.

2.1.1. DC vs pulsed current

Figure 2 shows how DC EPP current and voltage compares with pulsed EPP. At low voltage the DC current and voltage are stable, but near the transient region of Figure 1 both become very unstable, and then stabilize again in the EPP working region between Ub and Uc. The pulsed system is more stable, which is quite common for many electrochemical and plasma processes. However, pulse power supplies are more complex and expensive and care must be taken when installing them in a plating shop, because power line lengths are limited by capacitance and inductance, which change the pulse shapes and power transmission.

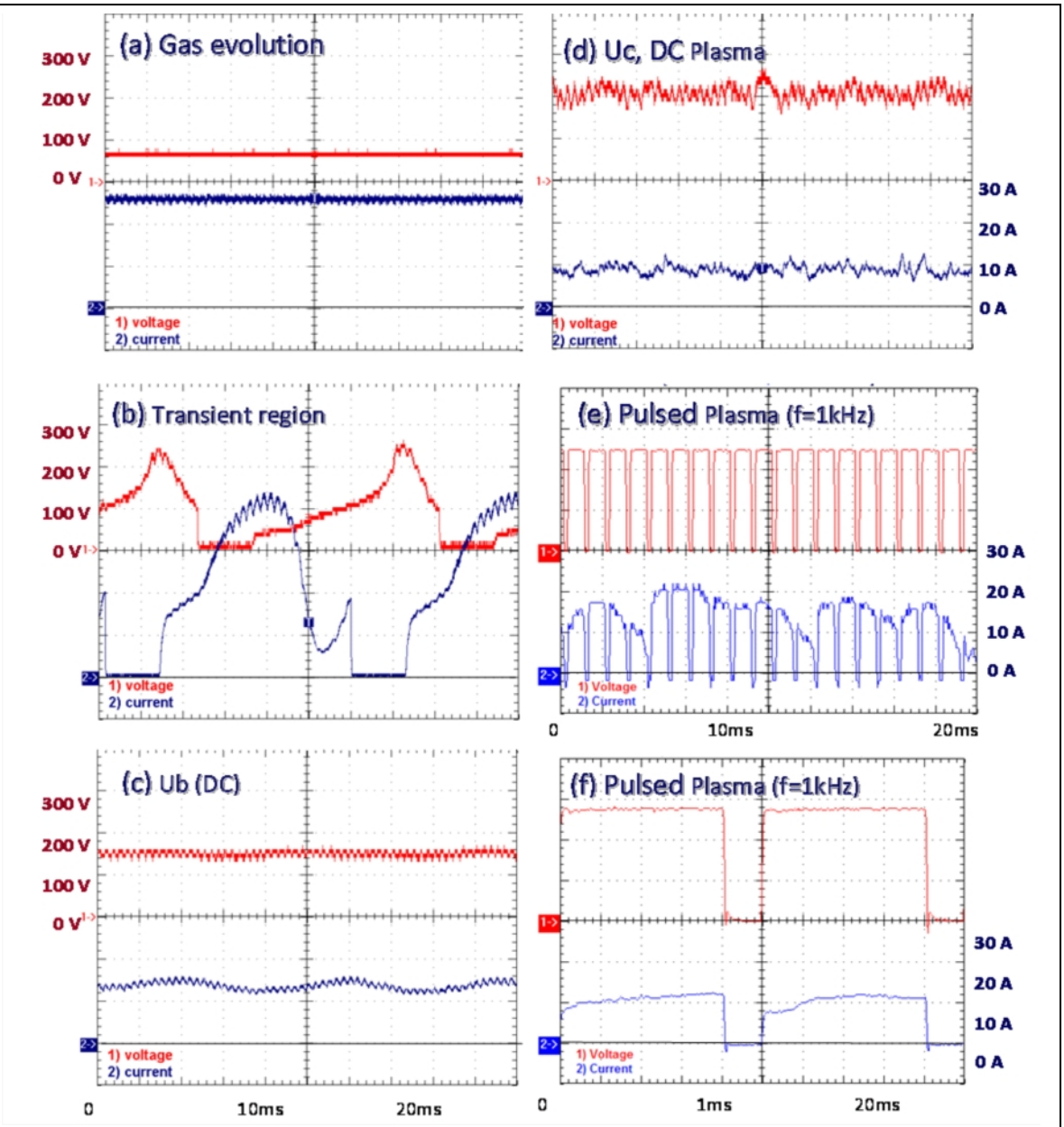

Figure 2. Typical current and voltage waveforms at different stages of EPP cleaning in DC (a, b, c and d) and pulsed unipolar current mode (e and f). Ub and Uc are voltages shown in Figure 1. (Sheffield)

2.1.2. EPP cleaning

For cleaning a steel surface, the cations may be sodium from a sodium carbonate solution which will participate in the process but ultimately remain in solution. The nature of the plasma bubble generation and extinction results in local surface melting and also creates high pressure disruption at the surface associated with bubble collapse and shock wave production. The net effect of these processes is to reduce the surface oxide and remove organic contaminants. It also results in surface micro-roughening that is beneficial for the adhesion of a coating that might subsequently be applied (such as a paint). The rapid cooling following localized melting of the surface causes a quenching effect that can result in ultra-fine-grained structures. It has been found that EPP-cleaned steel has significantly improved corrosion resistance over non-cleaned steel in both tap water and a 3.5% NaCl solution. EPP is used commercially as a cleaning process for wire and rod prior to coating.

2.1.3. EPP coating deposition

Metal coatings are deposited by adding compounds such as zinc sulfate or a combination of zinc sulfate and aluminum sulfate to the electrolyte. Some of the metal ions are deposited onto the substrate surface by diffusion through the electrolyte, but the predominant modes of transport are ion acceleration through the plasma and ion bubble adsorption transport where ions are carried to the steel surface by riding the surface of the H bubble as it collapses. Both of the latter processes eliminate the boundary layer diffusion and result in exceptionally high deposition rates. The rough surface of the coating is caused by force impact craters generated by the collapse of the hydrogen bubbles, producing a rough profile that would enhance adhesion of subsequent coating or paint. Anodic polarization studies of EPP-deposited Zn and Zn-Al coatings had previously shown equivalent corrosion resistance to standard galvanized steel.

A particularly important possibility that the project sought to examine was that it might be possible to deposit metallic aluminum coatings in this manner. The only other techniques for Al deposition are vacuum deposition (CVD and PVD) and non-aqueous electroplating (molten salt bath and organic electrolyte processes).

2.2. Equipment

Although the process takes place in an electrolyte, the electrolyte does not have to be in a tank, as is done with the Keronite and Tagnite processes. In fact, the CAP process takes place in a foam, while the Sheffield process takes place in a spray.

Figure 3 shows the CAP reactor, with the plasma visible in blue. Figure 4 shows the Sheffield reactor set up in the vertical position (electrodes can spray vertically or horizontally).

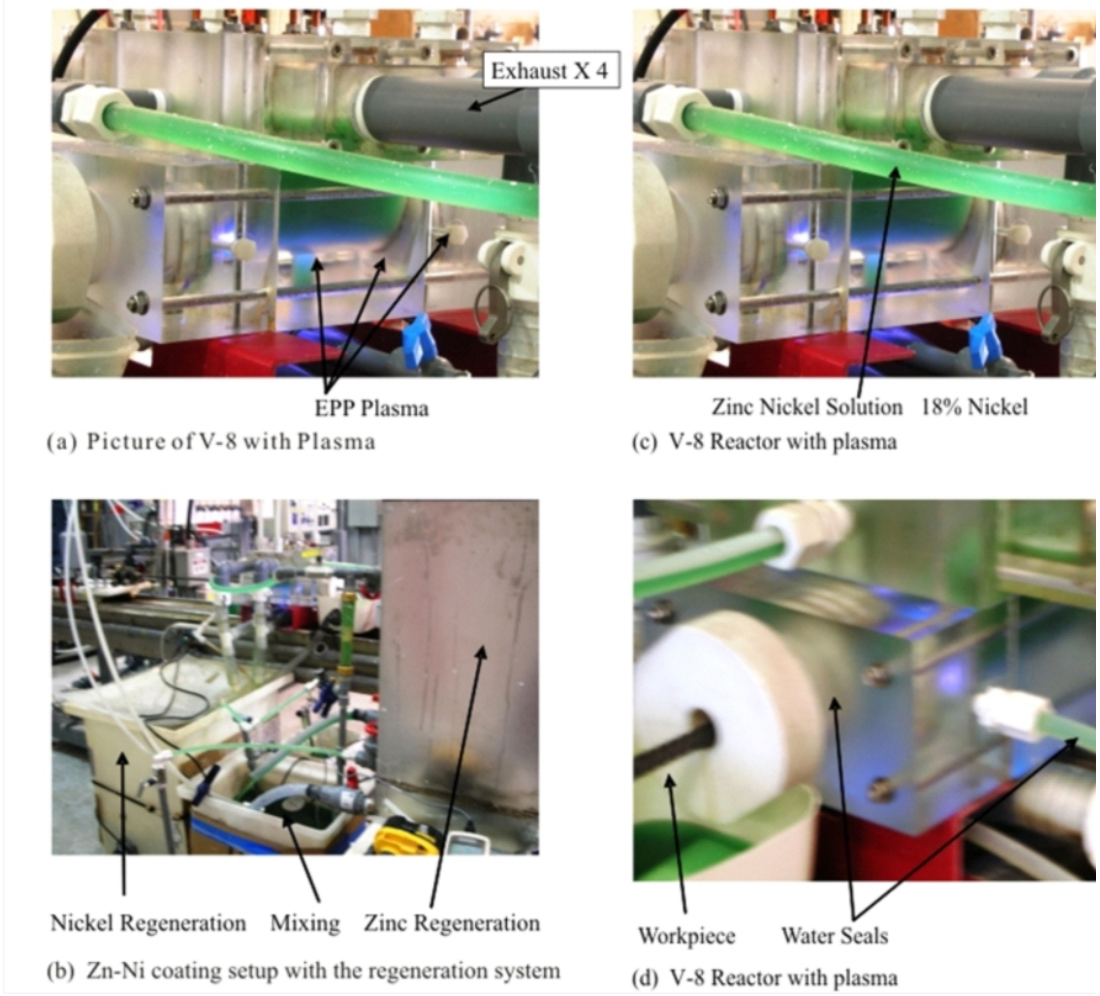

Figure 3. CAP reactor V-8 built to deposit Zn-Ni coatings

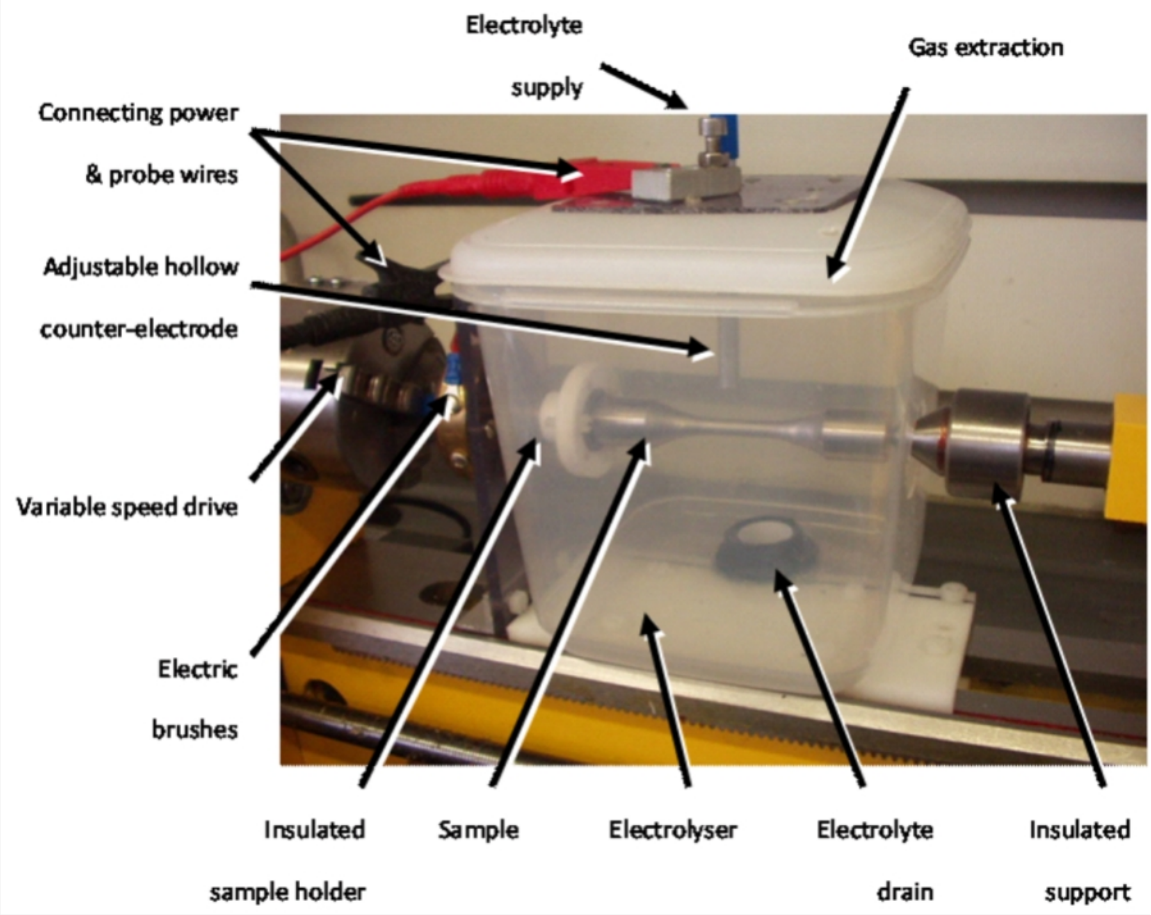

Figure 4. University of Sheffield EPP reactor showing vertical spray system.

3. Results

3.1. Equipment design

In the CAP method the process was operated in the DC mode. The equipment (Figure 3) was designed around the use of a foam blanket between the anode and the cathodic specimen. This meant that the configuration of the cathode had to be matched to the substrate geometry to ensure process uniformity, although it did not need to follow the exact geometrical profile. Thus a flat substrate required a flat anode and a wire or rod substrate a cylindrical anode. The anode was perforated to allow the electrolyte foam into the anode/substrate region. Uniformity over a large area or length was achieved by scanning the substrate beneath the anode. Electrolyte was flowed through the anode and regenerated as needed outside the deposition system.

In the Sheffield system the equipment could be operated either in DC or in unipolar pulsed mode, but most of the work was done in the pulsed mode. Electrolyte was sprayed from the anode onto the cathodic substrate (Figure 4), with the spray either vertically downwards or horizontal. Larger specimens were scanned back and forth in front of the anode. Sheffield experimented with both DC and unipolar pulsed power, settling on the pulsed power as the most stable arrangement.

Both types of equipment functioned well, and acceptable results were achieved in both DC and pulsed modes.

3.1.1. Anode design

Proper design of the anode proved to be critical, and erosion of the anode was a significant problem that limited anode life. CAP expended significant effort to design anodes and reduce their dissolution. This is detailed in the Appendix to their report. The more serious anode issues were encountered in the CAP design since this technique requires the formation of a foam layer at the substrate surface.

- For the CAP method to work the anode-surface distance must be within a range capable of sustaining the foam blanket (typically a few millimeters to two or three centimeters). This requires that for a complex part the anode must be shaped to roughly conform to the shape of the component to ensure uniformity. Alternatively, an anode might be scanned over the surface.
- Anodes must be made with an array of holes to supply the foam to the substrate surface, but the holes erode electrochemically.
- Anode erosion occurs in both types of system.

CAP tested various substrate materials and coatings for use as anodes, including graphite, nickel and gold- and platinum-coated stainless steel, but all were subject to erosion.

3.2. EPP cleaning

EPP has been shown to be an effective method for cleaning a surface. For cleaning, the electrolyte can be a simple sodium bicarbonate solution (typically 10%) or ammonium chloride. As measured by SEM and EDX, the plasma is an effective cleaning method, removing oxides and scale from the surface, while creating localized melt and recrystallization zones. The depth of the heat-affected zone and the roughening of the surface caused by the plasma both increase with exposure time.

3.2.1. Metallurgical effects of EPP cleaning

Figure 5 shows the development of the surface morphology as cleaning takes place. Melt zones first develop along the machining marks and then spread across the surface.

A typical cleaning cycle was a 30s plasma cleaning step, which removed most of the surface oxide and carbon. At the end of this process the surface was modified into two layers (Figure 6):

- The top layer was a 200-500nm (0.2-0.5μm) thick layer that was essentially featureless and characteristic of an amorphous or nanocrystalline structure.
- A subsurface layer 0.5-2μm thick consisted of a fine-grained (about 10-40 nm grain size) structure, with the size of the grains increasing gradually with depth.

The heat treating of the surface layer causes some softening of the surface (by about 50 HV points in this case of a 260ksi 4340 steel measured at CAP), see Figure 7.

Using X-ray diffraction, the internal stress in the surface region was measured as -1.8 GPa (compressive).

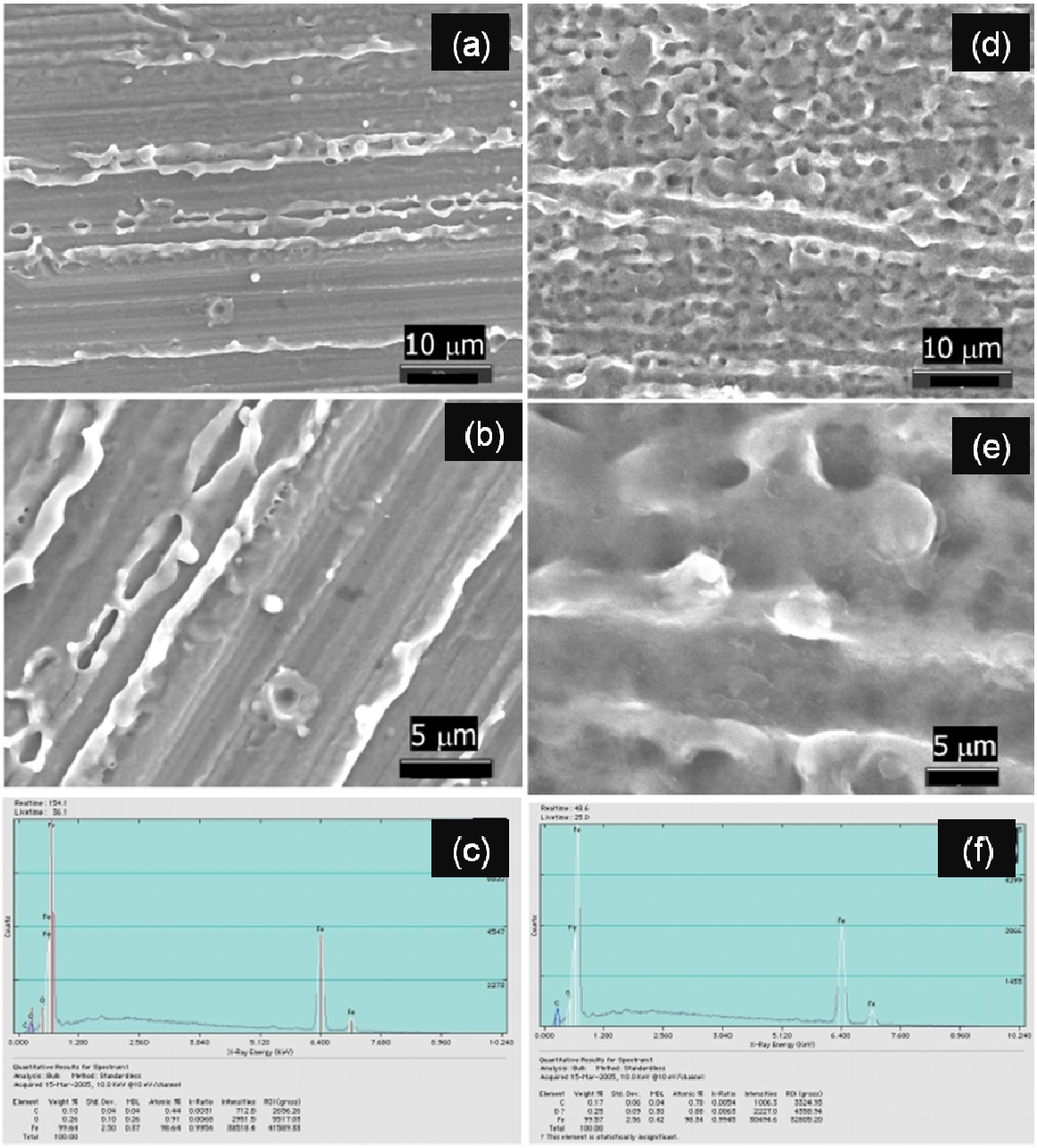

Figure 5. (a) and (b) SEM and (c) EDS analysis of 4340 steel treated by EPP, Condition 1; (d), (e), (f) Condition 2.

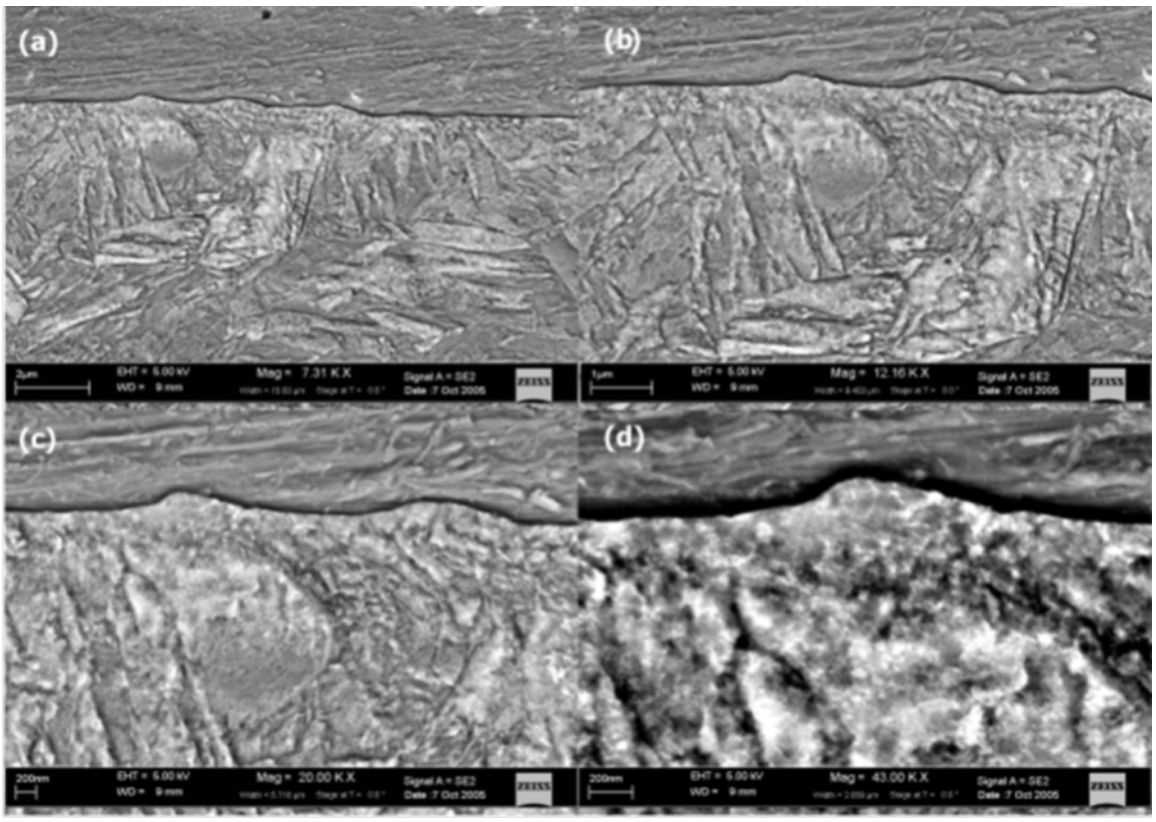

Figure 6. SEM cross section of 4340 steel treated by EPP for 30 s in NaHCO3 solution; magnification increases from (a) to (d).

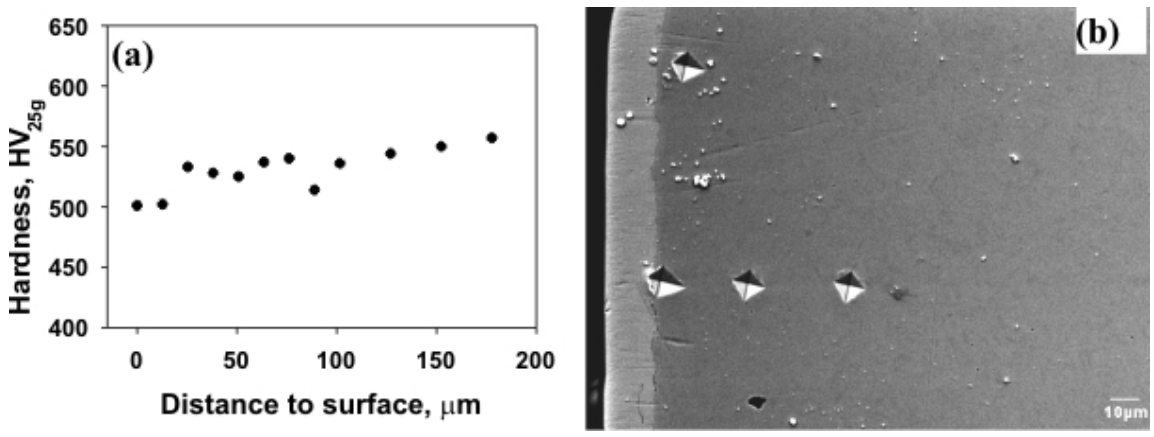

Figure 7. Hardness of 4340 steel as function of depth after EPP cleaning, measured at CAP. Left hardness vs depth, right indentations on cross-section.

3.2.2. Effect of cleaning on hydrogen embrittlement

SEM and EDX analysis were used to evaluate the extent of cleaning in the notch of type 1a.1 or 1a.2 F-519 embrittlement specimens. Care was taken to ensure that the plasma penetrated properly to the bottom of the notch. Cleaning conditions were tested using the EPP parameters shown in Table 1. Hydrogen in cleaned surfaces was measured by nuclear reaction analysis (NRA). This is a technique in which 6.385 MeV N^{15} isotope ions are fired into the surface. These ions have a high nuclear reaction cross section when they encounter H atoms, releasing characteristic gamma rays that can be used to measure hydrogen concentration as a function of depth.

Table 1. EPP cleaning conditions (CAP).

Processing Parameters	*Condition 1*	*Condition 2*	*Condition 3*
Voltage, V	140	180	140
Current, A	6-7	6-7	5
Treatment Time, sec	10	30	15
Electrolyte	$NaHCO_3$	$NaHCO_3$	NH_4Cl
Temperature, °C	65	60	70

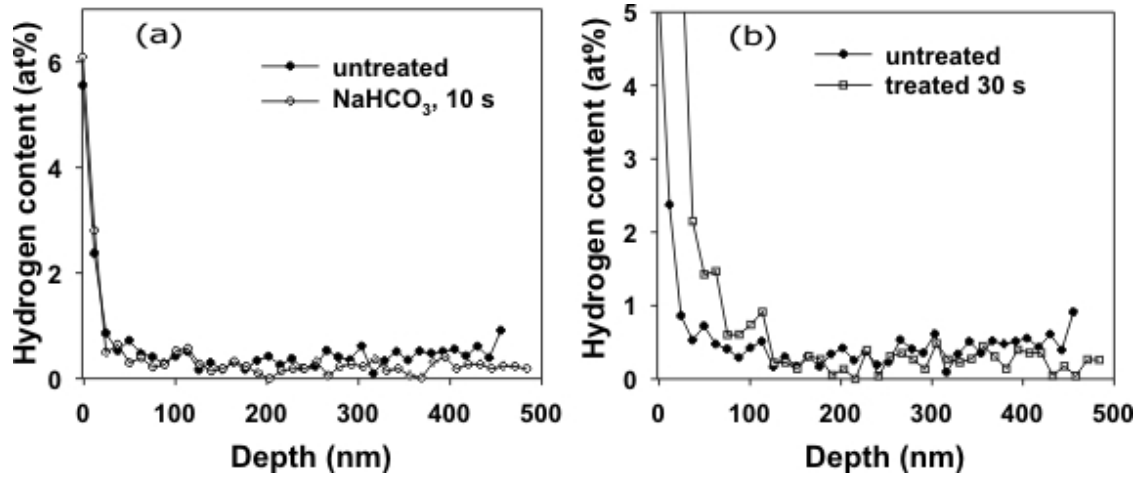

Figure 8. Depth profile of hydrogen content in 4340 steel treated in NaHCO3 under Condition 1 and Condition 2.

The analysis showed that for Condition 1 there was no measurable increase in H content (Figure 8, left). But for Condition 2 (the condition most commonly used for cleaning) there was an additional H content in the outermost 150nm (0.15μm) of the surface. Condition 3 introduced significantly more H (approximately 0.5 a/o) into the top 200nm (0.2μm) (see Figure 9).

After it was established that cleaning was effective into the bottom of the notch (using a notch opened up to 90° from the normal 60°), specimens were cleaned using conditions close to Conditions 1 and 2, and embrittlement tested per ASTM F-519. No embrittlement was found. **Thus, the process does introduce hydrogen into the outermost few tenths of a micron of the surface region, but it does not cause embrittlement.** Presumably this is either because the amount of H is too low or because it does not become trapped at stress raisers where it will lead to embrittlement.

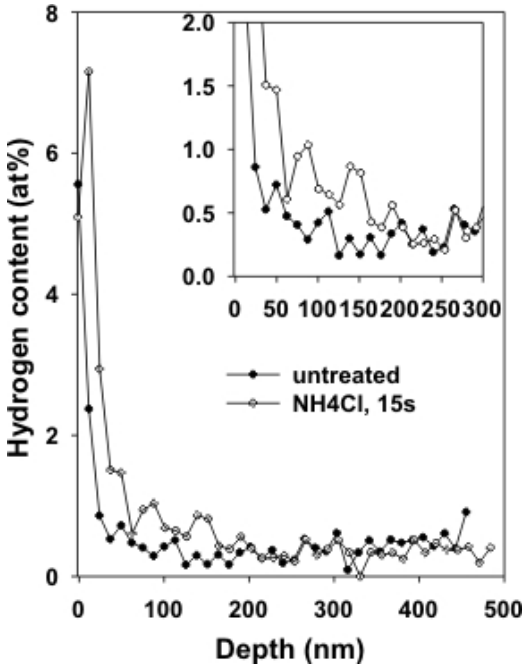

Figure 9. Hydrogen depth profile in 4340 steel treated in NH4Cl under Condition 3.

3.2.3. Effect of cleaning on fatigue

One would expect that any surface heating and softening of the surface, such as that seen in Section 3.2.1, would lead to a fatigue debit, while roughening of the surface as shown in Figure 5e would create stress raisers that would also initiate fatigue. Figure 10 shows the fatigue of EPP-cleaned unpeened 4340. There is no significant difference between the baseline peened and EPP-cleaned material, showing that neither the surface heating nor the roughening causes any significant debit. The spread in the unpeened data is too large to make any definitive comparison for the unpeened condition.

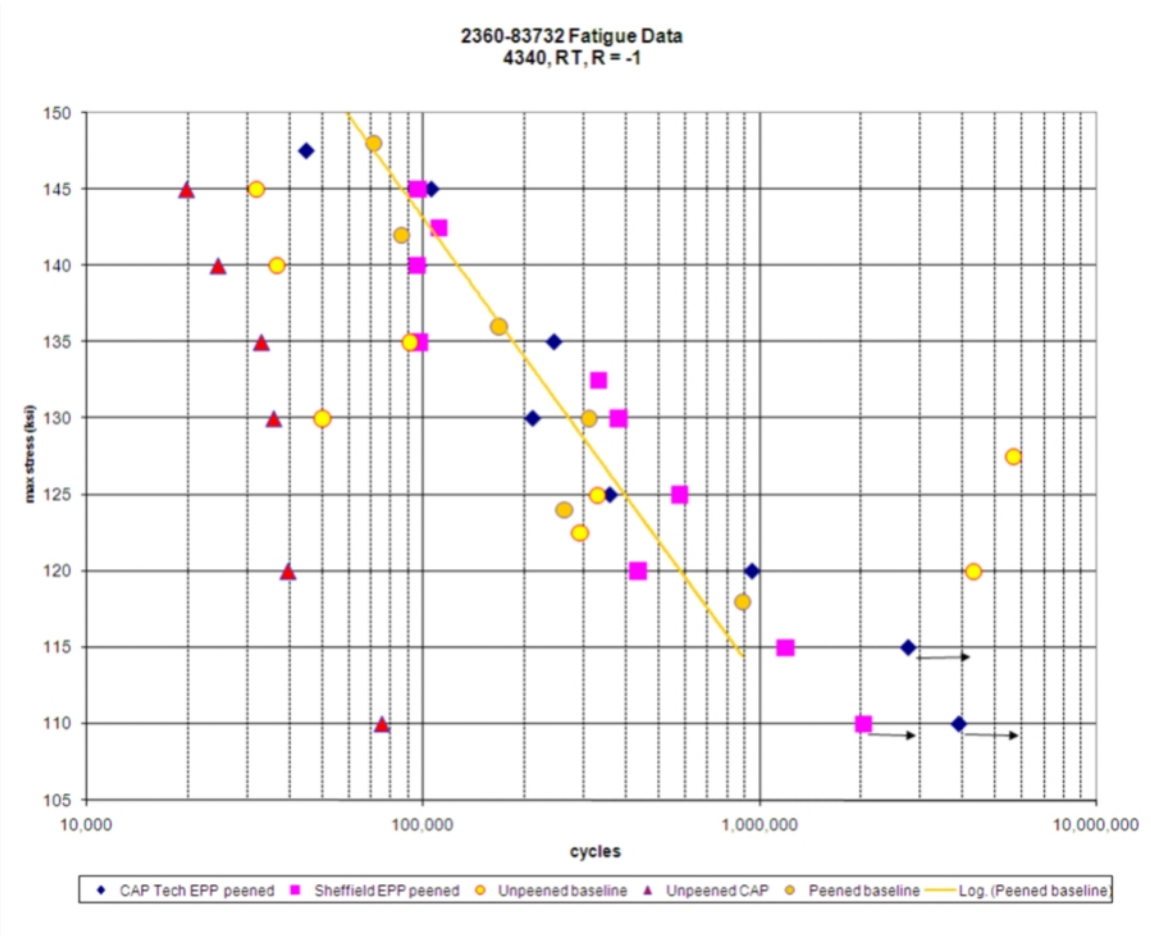

Figure 10. Fatigue of unpeened 4340 steel, cleaned at CAP and Sheffield by EPP (260-280ksi heat treat). Smooth bar, R=-1.

3.3. Coating deposition

Various approaches were tried to create sacrificial coatings. It was hoped that it would be possible to use EPP to deposit Al or at least Al-rich coatings, which cannot be deposited by normal aqueous electroplating methods. A great deal of effort was expended on attempts to produce metallic Al alloys, but no satisfactory way of doing so was found, although Zn-rich coatings were produced quite easily. To demonstrate the technology CAP coated fatigue and corrosion test specimens with ZnNi, while Sheffield produced ZnMg specimens.

3.3.1. Zn coating

CAP Technologies deposited Zn coatings using a 23% $ZnSO_4.7H_2O$ solution. Processing voltage, current, flow rate, and temperature were 150-180 V, 25-30 A, 3.2 l/min, and 75-80°C, respectively. Coatings were porous and nodular rather than flat (see Figure 11 and Figure 12).

Pulsed deposition at Sheffield also formed coatings with nodules, which clustered along machining marks on the surface.

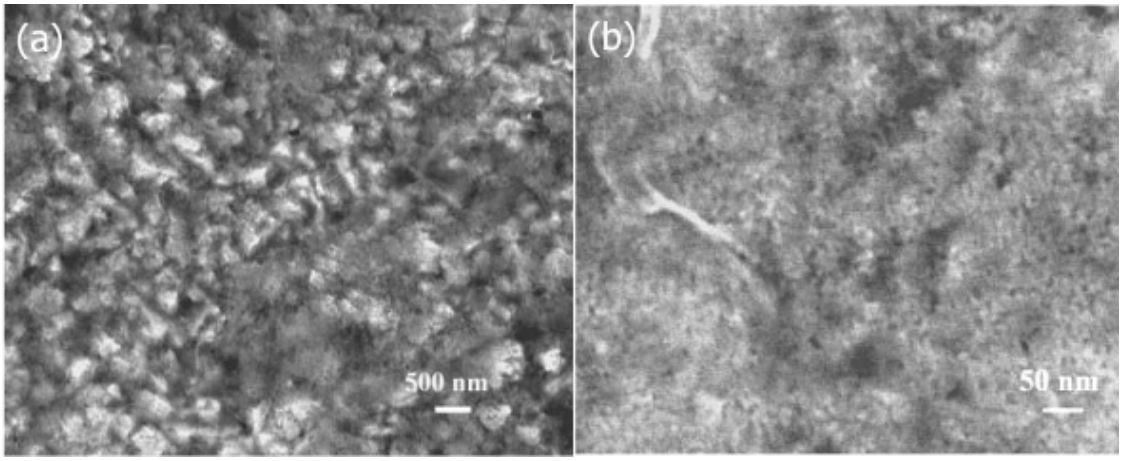

Figure 11. SEM of EPP Zn coating (CAP).

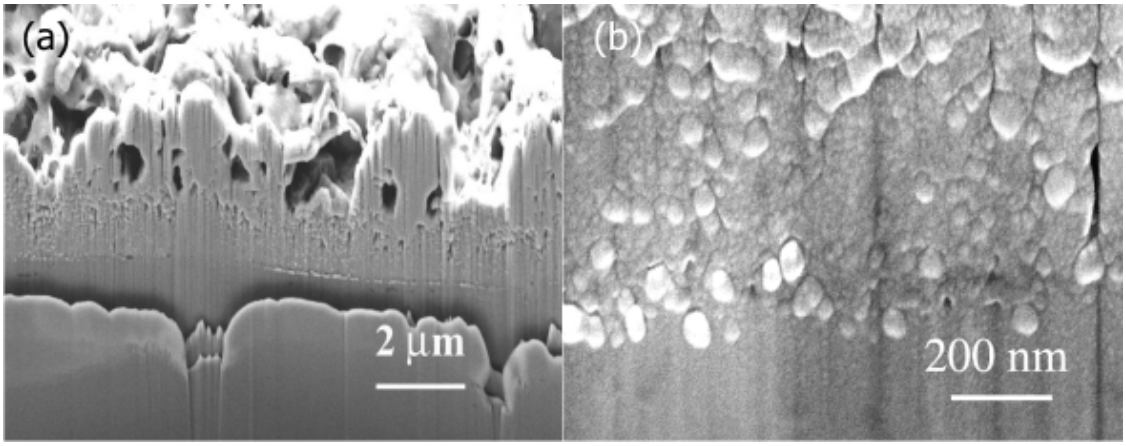

Figure 12. Cross section of EPP Zn coating (CAP).

3.3.2. Zn-Al coating

Attempts were made to create Zn-Al alloys by adding $Al_2(SO_4)_3.14H_2O$ to the $ZnSO_4.7H_2O$ solution. At CAP the total $Al_2(SO_4)_3.14H_2O$ + $ZnSO_4.7H_2O$ concentration was held at 23% with the ratio of Al:Zn salt was varied from 0 to 40:1. While this did produce Zn and Al in the coatings, the Al was always in oxide or hydroxide form, and therefore not sacrificial. Using argon instead of air to create the foam did not prevent compound formation.

Sheffield attempted to solve this problem by introducing a third element to reduce the Al. However, attempts to do this using V, Mn and Mg were not successful. The coatings containing V and Mn were of poor quality and the Al remained in compound form. The quality and uniformity of the Zn-Al-Mg coatings were better but the Al was still in compound form.

3.3.3. Zn-Ni coating (CAP)

A common Cd alternative used in the automotive industry is ZnNi, which is now being introduced into the aerospace industry. According to data from Boeing, who have developed a low hydrogen embrittlement ZnNi with Dipsol of America [2], the optimum Ni percentage is 13-17%. Above this the coating is no longer sacrificial. This can be seen in Table 3, for coatings deposited under the conditions of Table 2. Only specimen numbers 333 and 336 are more electronegative than 4340, and thus sacrificial. For this reason CAP concentrated their further efforts on the production of ZnNi coatings in this chemistry range.

For ZnNi deposition the electrolyte was $ZnSO_4.7H_2O$ and $NiSO_4.6H_2O$ for a total of 17% metal salt. About 3% Na_2SO_4 was added to increase the conductivity of the electrolyte solution. Deposition conditions are given in Table 2 for a set of hydrogen embrittlement specimens. Table 4 gives the deposition conditions for the specimens used for B117 salt fog corrosion testing. These coatings were approximately 12µm (0.0005") thick. The morphology of the coatings varied widely from place to place on each specimen, as well as between specimens deposited with different conditions (see Figure 13). Clearly the coatings were not flat as would be expected for an electroplate, but were primarily nodular, with some acicular regions and platelets.

Table 2. ZnNi Deposition conditions for test specimens (CAP).

Sample	Conversion coating	pH	Conductivity (mS @ °C)	Electrolyte temp (°C)	Voltage (V)	Current (Amps)	Rotation (RPM)	Dwell time (sec)
333	None	3.9	36 @ 85	85	195	20	N/A	60
336	Dipsol IZ-258	3.8	36 @ 85	85	195	20	N/A	60
349	Metalast TCP-HF	3.7	40 @ 85	85	195	20	N/A	60
334	None	3.9	39 @ 85	85	195	20	N/A	60
335	None	3.9	39 @ 85	85	195	20	N/A	60
351	None	3.6	42 @ 85	85	195	20	N/A	60

Table 3. Chemistry and corrosion properties of specimens of Table 2.

	Atomic %				Ratio		Corr potential (mV)		Corr rate (mA/cm^2)	
Sample	C	O	Ni	Zn	Ni	Zn	3.5% NaCl lab	3.5% NaCl deaerated	3.5% NaCl lab	3.5% NaCl deaerated
4340 Steel							-728	-760	320.88	0.92
333	47.48	22.07	6.67	23.77	14.8%	85.2%	-759	-833	4.18	2
336	48.08	23.99	5.34	22.59	16.8%	83.2%	-879	-862	5.88	3.56
349	37.64	28.01	6.76	27.59	18.1%	81.9%	-715	-757	3.01	2.53
334	47.48	22.07	6.67	23.77	18.9%	79.7%	-731	-747	5.5	1.9
335	43.56	26.3	7.15	22.99	20.7%	79.3%	-712	-741	6.52	1.89
351	37.39	31.01	8.71	22.9	25.8%	74.2%	-698	-765	?	0.87

Table 4. Deposition conditions for Zn-Ni B117 corrosion test specimens (CAP).

Sample	pH	Conductivity (mS@°C)	Electrolyte temp (°C)	Voltage (V)	Current (Amps)	Dwell time(sec)
337 (marked 39)	3.8	40@85	85	195	20	60
338 (marked 41)	3.7	40@85	85	195	20	60
339 (marked 42)	3.6	41@85	85	195	20	60
340 (marked 34)	3.6	41@85	85	195	20	60
341 (marked 40)	3.6	41@86	86	195	20	60
342 (marked 43)	3.5	42@85	85	195	20	60
343 (marked 44)	4.1	38@85	85	195	20	60
344 (marked 45)	4.0	38@85	85	195	20	60
345 (marked 46)	3.9	38@85	85	195	20	60
346 (marked 47)	3.9	39@85	85	195	20	60
347 (marked 48)	3.8	39@85	85	195	20	60
348 (marked 48)	3.8	39@85	85	195	20	60

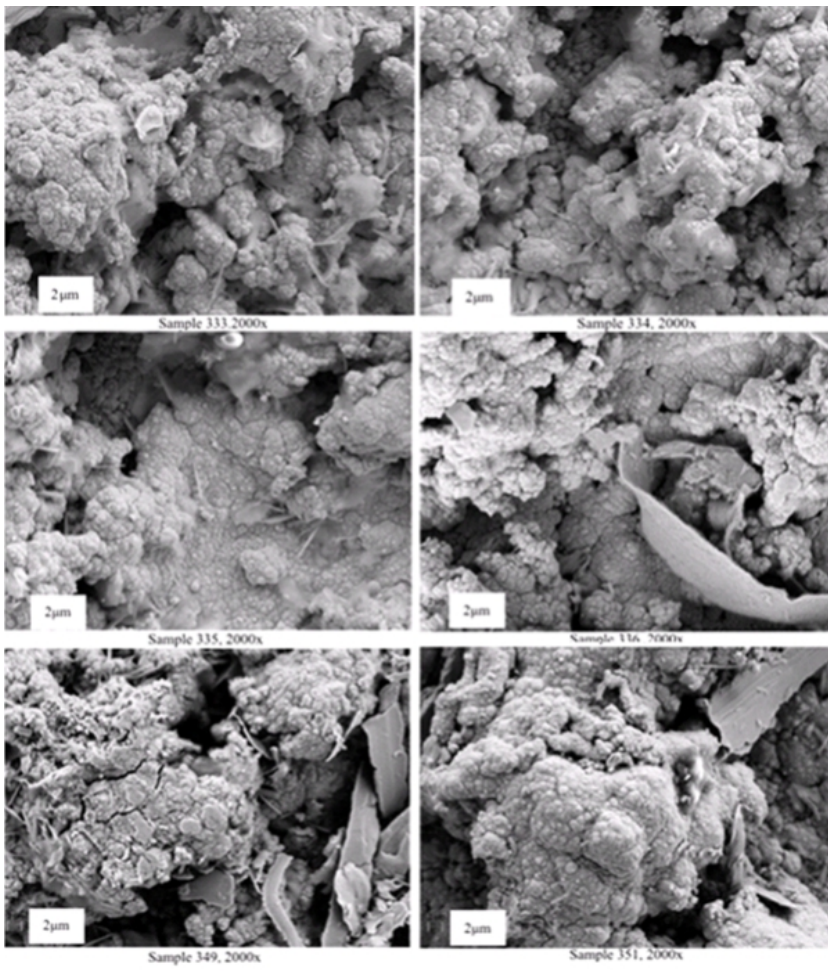

Figure 13. Morphologies of CAP ZnNi specimens.

3.3.4. Zn-Mg coating (Sheffield)

Sheffield made various attempts to produce Zn-Al, including ternary alloys Zn-Al-V, Zn-Al-Mn and Zn-Al-Mg. Of these the most promising was Zn-Al-Mg. Sheffield concentrated their efforts on Zn-Mg coatings, having concluded that Zn-Al-Mg appeared to work best and that the Al provided no benefit.

The deposition conditions for test specimens of Zn-Mg are shown in Table 5. Micrographs of the coatings are shown in Figure 14. Like the CAP coatings, the Sheffield coatings were very porous, but they were not nodular.

Table 5. Deposition conditions for Zn-Mg specimens (Sheffield).

I	**Coating deposition:**		
	Batch 1	Batch 2	Batch 3
Electrolyte:			
(0.2 M $ZnSO_4$) + x M MgSO4; x =	0.1	0.15	0.2
Temperature (^oC)	90	90	90
Flow rate (l min^{-1})	1	1	1
Current mode:			
Frequency (kHz)	10	10	15
Duty cycle	0.6	0.6	0.7
Voltage amplitude (V)	250	250	270
Average Current (A)	6-8	6-9	5-10
Reactor:			
Interelectrode gap (mm)	8	8	8
Linear speed (mm min^{-1})	15	15	15
Rotation rate (rpm)	120	120	120
No of Fatigue samples	**10**	10	10
II	**Post-treatment:**		
Step 1:			
Electrolyte: 1.2g l-1 ZnO + 15 g l-1 NaNO3 + 11 ml l-1 85%H3PO4			
Temperature (^oC)	45	45	45
Time (min)	5	5	5
Step 2:			
Electrolyte: 5 g l-1 Na2SiO3			
Temperature (^oC)	85	85	85
Time (min)	5	5	5
No of Corrosion plates	**6**	6	6

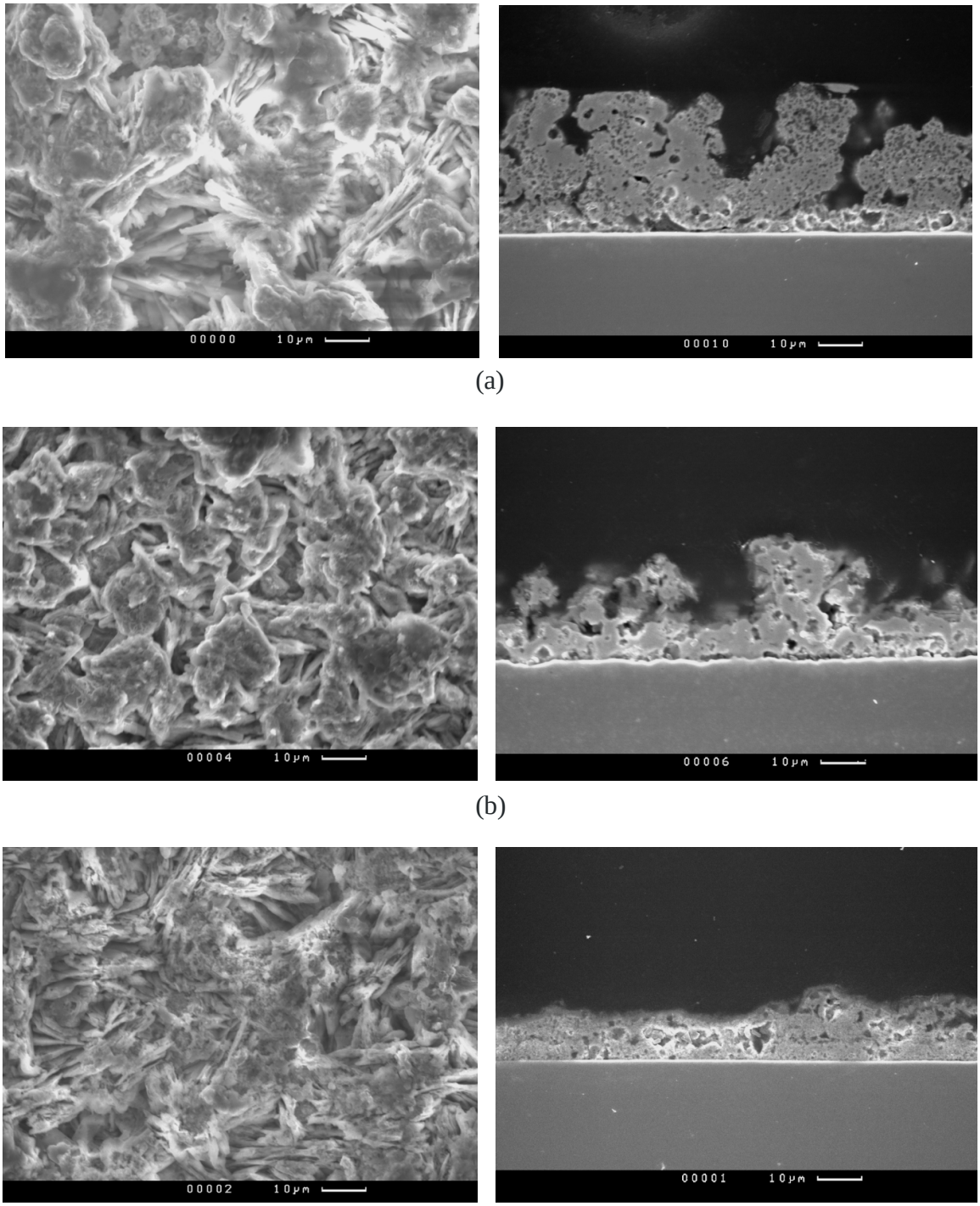

Figure 14. SEM images of surface (left) and cross-sectional view of EPP coatings produced from binary Zn-Mg sulfate electrolyte systems with various concentrations of Mg sulfate: (a) 0.1 M; (b) 0.2 M; (c) 0.3 M, followed by the phosphate-silicate passivation treatment.

3.4. Coating performance

3.4.1. Hydrogen embrittlement and re-embrittlement

ASTM F519 Type 1d specimens (C-rings) were EPP cleaned and Zn-Ni coated by CAP, then treated either with Dipsol IZ-258S chromate conversion coating or with Metalast TCP-HF trivalent chrome sealer. They were not hydrogen baked. They were tested IAW ASTM F519 at a static load of 75% notch tensile strength. No failures occurred up to 1,680hr, well beyond the normal 200hr limit (see Table 6). This constitutes a pass of ASTM F519.

To test for environmental embrittlement (re-embrittlement) similar specimens were subjected to the same testing as C-ring specimens from the JCAT testing program, for which there is a large volume of embrittlement data. Note that C-rings are stressed using a bolt (Figure 15), and can be placed in a salt fog chamber for extended testing. The data are shown in Table 7, together with the data for the various JCAT coatings tested in the same manner, all at a 65% NTS load.

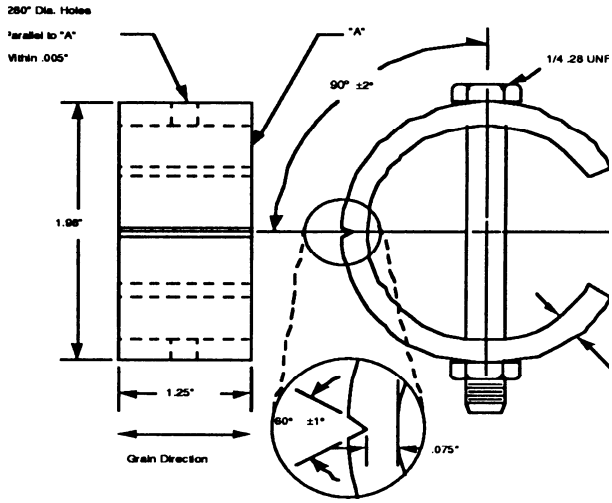

Figure 15. C-ring embrittlement specimen (F-519 Type 1d) with tensioning bolt.

Table 6. Hydrogen embrittlement, ASTM F519, 75% NTS, extended time.

Specimen Identification	Beginning Width	Final Width at Fracture	Hours Until Failure
EPP Zn-Ni (Dipsol IZ-258S - 204)	1.962	1.863	1680 - not failed
EPP Zn-Ni (Dipsol IZ-258S - 205)	1.962	1.863	1680 - not failed
EPP Zn-Ni (Dipsol IZ-258S - 206)	1.962	1.863	1680 - not failed
EPP Zn-Ni (Metalast TCP-HF- 210)	1.962	1.863	1680 - not failed
EPP Zn-Ni (Metalast TCP-HF - 211)	1.962	1.863	1680 - not failed
EPP Zn-Ni (Metalast TCP-HF - 212)	1.961	1.862	1680 - not failed

Table 7 GM 9540 re-embrittlement test of EPP Zn-Ni compared with JCAT coatings 65% NTS load..

Specimen Identification	Beginning Width	Final Width at Fracture	Hours Until Failure	Raw GM 9540P Minutes	GM 9540P Cycles
LHE Cd	1.958	1.874	N/A	163	0.1272
LHE Cd	1.957	1.873	N/A	480	0.3747
LHE Cd	1.960	1.876	N/A	129	0.1007
LHE Cd	1.956	1.872	N/A	123	0.0960
LHE Cd	1.959	1.875	N/A	176	0.1374
LHE Cd	1.952	1.868	N/A	138	0.1077
LHE Cd	1.958	1.874	N/A	480	0.3747
LHE Cd	1.957	1.873	N/A	480	0.3747
LHE Cd	1.953	1.869	N/A	85	0.0664
IVD Al	1.962	1.878	N/A	38	0.0297
IVD Al	1.960	1.876	N/A	22	0.0172
IVD Al	1.960	1.876	N/A	33	0.0258
IVD Al	1.960	1.876	N/A	19	0.0148
IVD Al	1.959	1.875	N/A	31	0.0242
IVD Al	1.959	1.875	N/A	24	0.0187
IVD Al	1.956	1.872	N/A	480	0.3747
IVD Al	1.958	1.874	N/A	29	0.0226
IVD Al	1.958	1.874	N/A	30	0.0234
Al Sputter	1.958	1.874	N/A	135	0.1054
Al Sputter	1.955	1.871	N/A	480	0.3747
Al Sputter	1.960	1.876	N/A	480	0.3747
Al Sputter	1.957	1.873	N/A	480	0.3747
Al Sputter	1.959	1.875	N/A	480	0.3747
Al Sputter	1.956	1.872	N/A	36	0.0281
Al Sputter	1.956	1.872	N/A	480	0.3747
Al Sputter	1.958	1.874	N/A	480	0.3747
Al Sputter	1.952	1.868	N/A	511	0.3989
Alumiplate	1.964	1.880	N/A	42273	33
Alumiplate	1.956	1.872	N/A	7686	6
Alumiplate	1.959	1.875	N/A	38430	30
Alumiplate	1.958	1.874	N/A	20	0.0156
Alumiplate	1.956	1.872	N/A	46116	36
Alumiplate	1.956	1.872	N/A	37149	29
Alumiplate	1.957	1.873	N/A	47397	37
Alumiplate	1.959	1.875	N/A	28	0.0219
Alumiplate	1.953	1.869	N/A	56364	44
ZnNi Acid Boeing	1.958	1.874	N/A	25	0.0195
ZnNi Acid Boeing	1.957	1.873	N/A	38	0.0297
ZnNi Acid Boeing	1.958	1.874	N/A	110	0.0859
ZnNi Acid Boeing	1.953	1.869	N/A	50	0.0390
ZnNi Acid Boeing	1.958	1.874	N/A	44	0.0343
ZnNi Acid Boeing	1.958	1.874	N/A	35	0.0273
ZnNi Acid Boeing	1.952	1.868	N/A	29	0.0226
ZnNi Acid Boeing	1.959	1.875	N/A	190	0.1483
ZnNi Acid Boeing	1.961	1.877	N/A	37	0.0289

Table 8 continued

ZnNi Alk LHE D.G.	1.960	1.876	N/A	124	0.0968
ZnNi Alk LHE D.G.	1.961	1.877	N/A	35	0.0273
ZnNi Alk LHE D.G.	1.960	1.876	N/A	45	0.0351
ZnNi Alk LHE D.G.	1.957	1.873	N/A	57	0.0445
ZnNi Alk LHE D.G.	1.958	1.874	N/A	27	0.0211
ZnNi Alk LHE D.G.	1.957	1.873	N/A	24	0.0187
ZnNi Alk LHE D.G.	1.957	1.873	N/A	40	0.0312
ZnNi Alk LHE D.G.	1.957	1.873	N/A	40	0.0312
ZnNi Alk LHE D.G.	1.958	1.874	N/A	33	0.0258
EPP Zn-Ni (Dipsol - 201)	1.962	1.875	N/A	420	0.3279
EPP Zn-Ni (Dipsol - 202)	1.962	1.875	N/A	453	0.3536
EPP Zn-Ni (Dipsol - 203)	1.962	1.875	N/A	1377	1.0749
EPP Zn-Ni (Metalast - 207)	1.962	1.875	N/A	1377	1.0749
EPP Zn-Ni (Metalast - 208)	1.962	1.875	N/A	420	0.3279
EPP Zn-Ni (Metalast - 209)	1.961	1.874	N/A	420	0.3279
SnZn (1st Batch)	1.960	1.876	<10min*	0	0
SnZn (1st Batch)	1.959	1.875	<10min*	0	0
SnZn (1st Batch)	1.958	1.874	<10min*	0	0
SnZn (1st Batch)	1.957	1.873	<10min*	0	0
SnZn (1st Batch)	1.953	1.869	<10min*	0	0
SnZn (1st Batch)	1.958	1.874	<10min*	0	0
SnZn (1st Batch)	1.953	1.869	<10min*	0	0
SnZn (1st Batch)	1.960	1.876	<10min*	0	0
SnZn (1st Batch)	1.959	1.875	<10min*	0	0

The only coating with better performance than the EPP coatings was AlumiPlate™ (electroplated Al), which was considered overall by the JCAT to be the best-performing Cd alternative. Note also that the EPP ZnNi performed better than the standard electroplated acid ZnNi or the new LHE ZnNi.

3.4.2. Fatigue

The fatigue of coated 4340 steel is shown in Figure 16. The three Sheffield sets of data points (in red) are the three batches shown in Table 5. The EPP specimens all show a debit relative to the uncoated material. There is little difference between the Zn-Ni and Zn-Mg specimens, except at the highest stress, where the Zn-Ni appears somewhat lower.

Standard electrolytic alkaline ZnNi is also known to cause a debit of about the same order [3], with a factor of two or three debit and an 11% reduction in endurance limit.

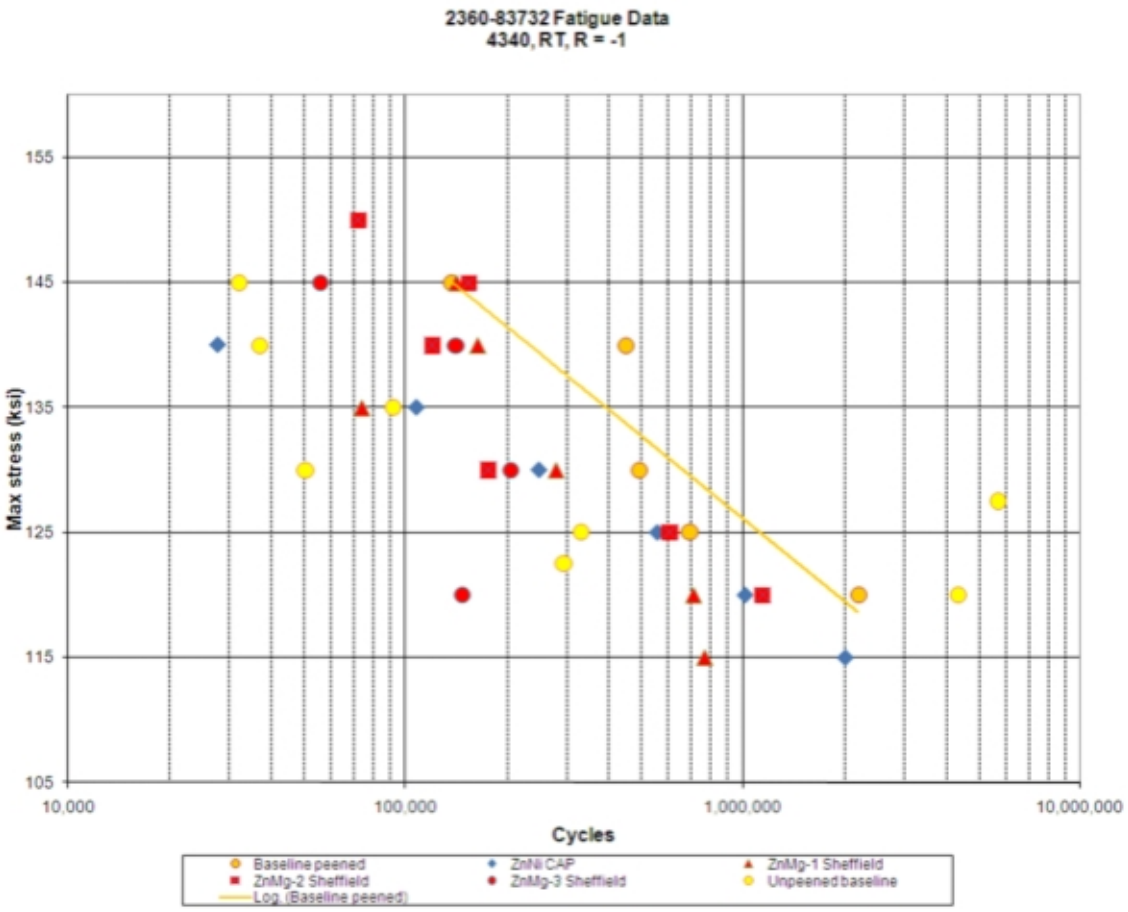

Figure 16. Fatigue of EPP-coated 4340 R=-1. Zn-Ni (CAP), Zn-Mg (Sheffield).

3.4.3. Corrosion

3.4.3.1. Zn-Mg coatings

Potentiodynamic polarization curves for Zn-Mg are shown in Figure 17. It is clear that as, a result of passivation, the region of passivity shifts from (-0.8 – -0.55) V to (-0.6 – -0.25) V (Figure 17a). This means that, compared with the as-deposited EPP coating, the open circuit potential of the coating is more electronegative than the steel and so provides sacrificial corrosion protection. The phosphate-silicate post-treatment promotes coating passivation of the coating at higher anodic potentials, around the corrosion potential of steel. Thus, should any galvanic coupling occur between the coating and the substrate, the coating corrosion would be inhibited by surface passivation; this should enhance the coating durability. Notice also that the region of passivity for the passivated EPP coatings is the same regardless of the coating open circuit potential (Figure 17b). The passive region appears to be controlled by the cathodic reaction, which is similar to the observation for EPP cleaned surfaces.

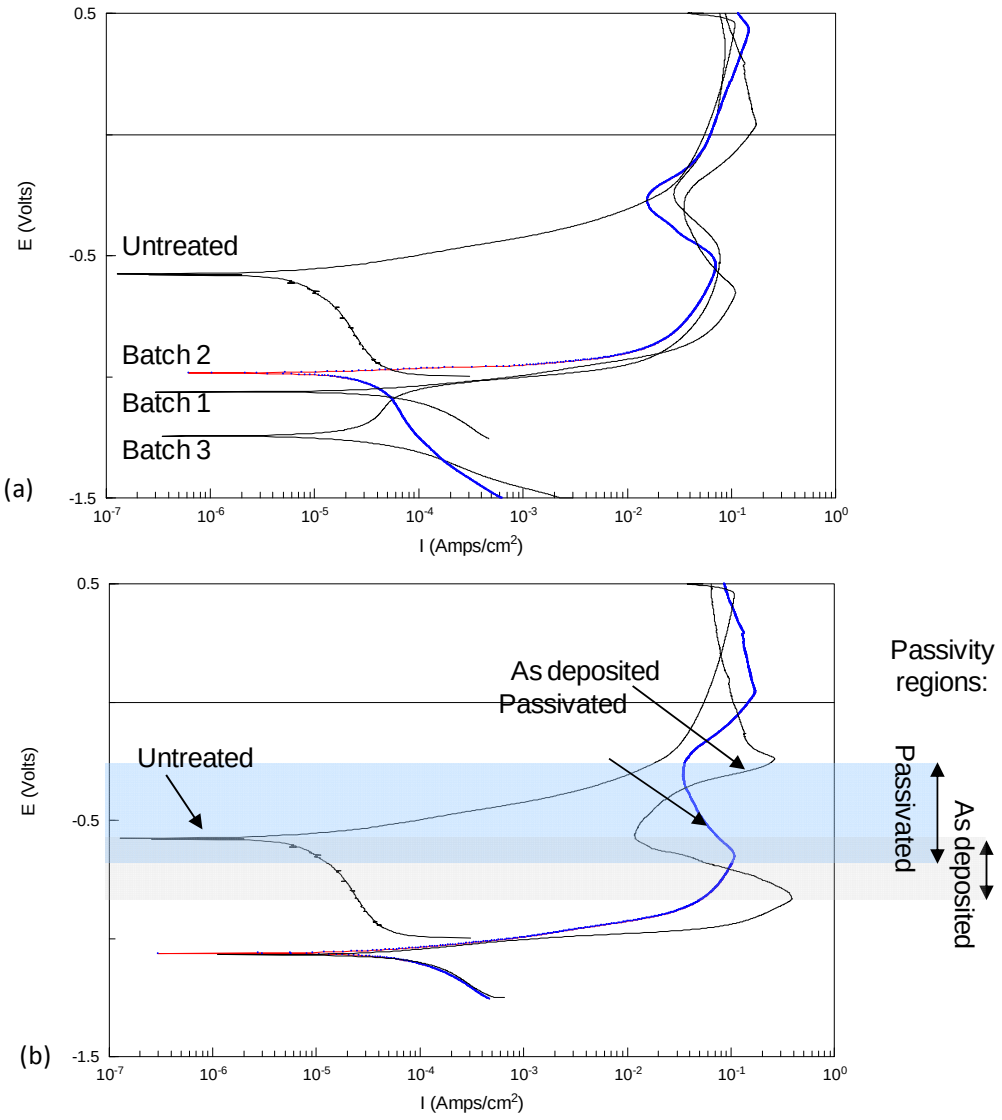

Figure 17. Potentiodynamic polarization curves in 3.5% NaCl solution of EPP Zn-Mg coatings phosphated and silicate sealed. (a) the passivation post-treatment (Batch 1) and (b) Mg salt content in the bath per Table 5 (Sheffield).

However, in B117 cabinet testing at NAVAIR PAX the Zn-Mg coatings failed rapidly (Figure 18), exhibiting white corrosion over most their surface after 144 hr, and red rust after 696 hr. Surfaces of some of these specimens are shown in Figure 19.

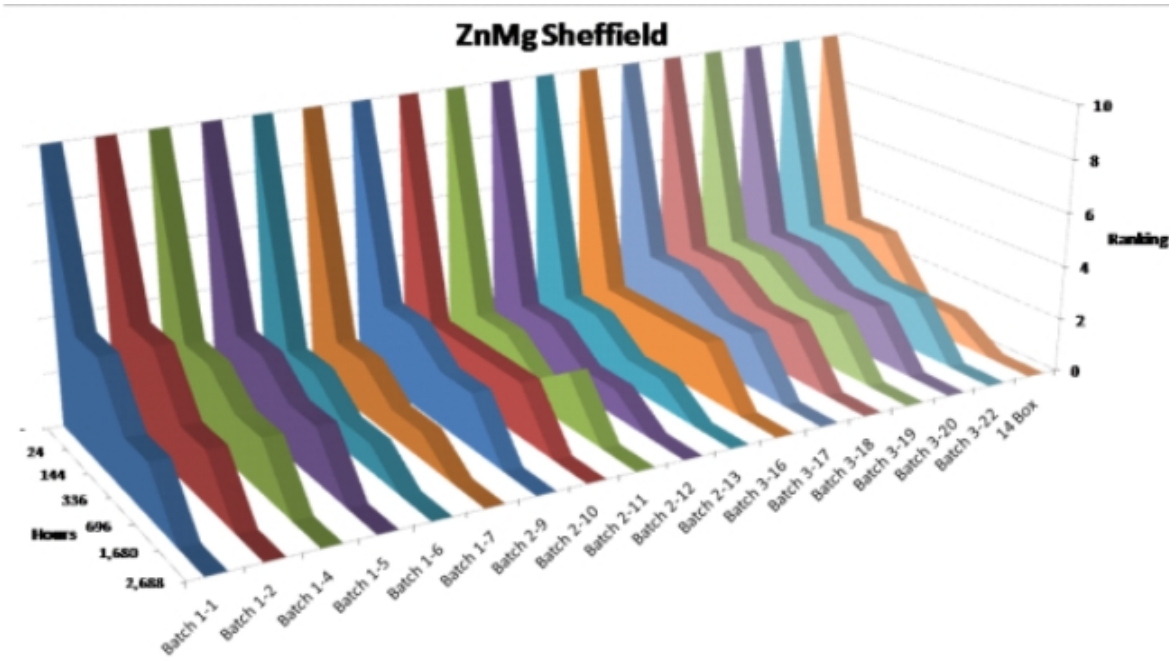

Figure 18. B117 Corrosion Ranking vs exposure time for Zn-Mg coatings on 4340, (Sheffield). Measured at PAX.

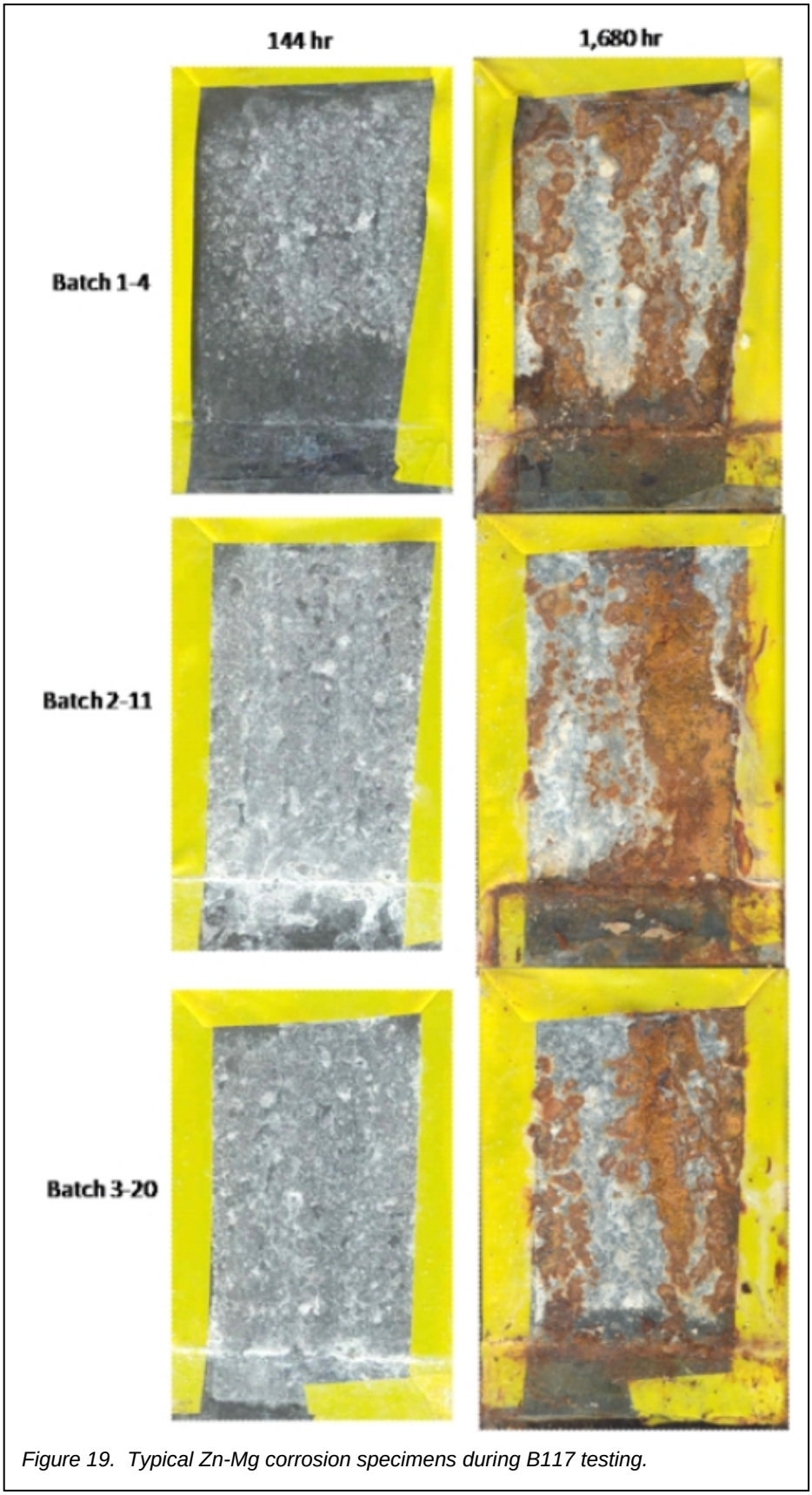

Figure 19. Typical Zn-Mg corrosion specimens during B117 testing.

3.4.3.2. Zn-Ni coatings

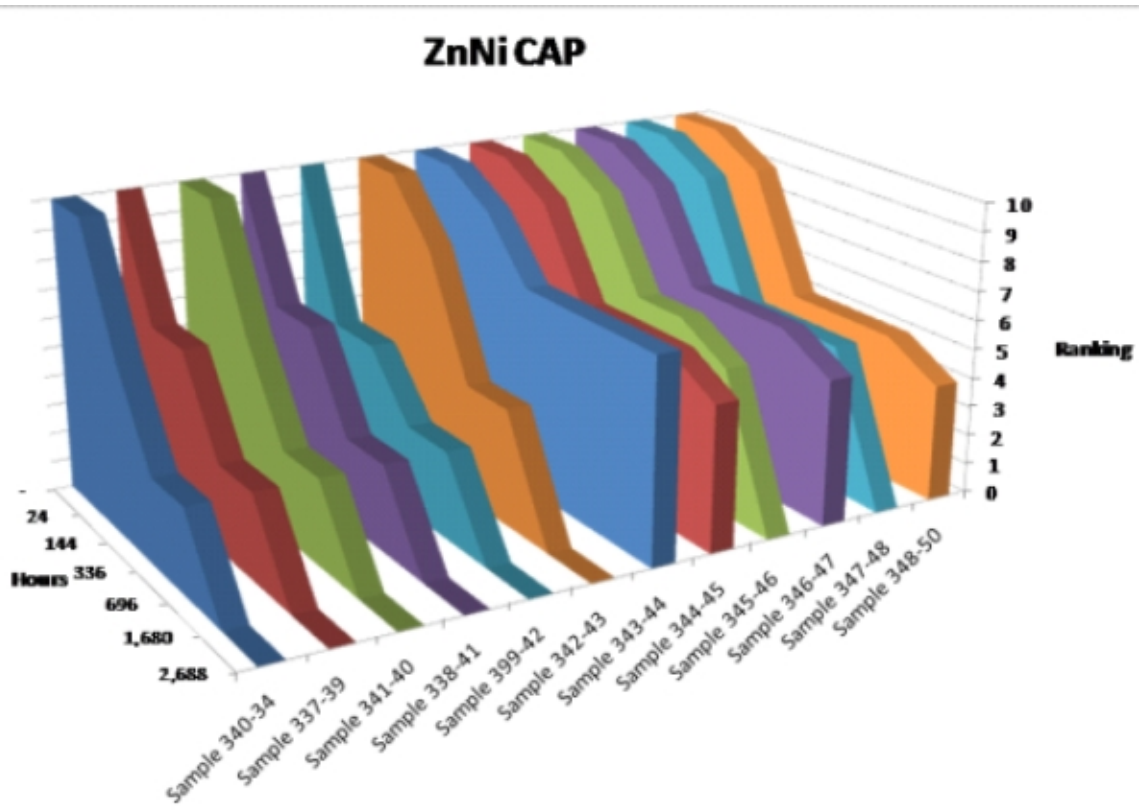

Figure 20. B117 Corrosion Ranking vs exposure time for Zn-Ni coatings on 4340 steel (CAP). Deposition conditions Table 4. Testing at NAVAIR PAX. Specimens 34-43 chromated, 44-50 TCP-sealed.

The Zn-Ni coatings performed better than the Zn-Mg coatings (see Figure 20). It is very interesting to note that the coatings sealed with the Metalast TCP-HF (trivalent chrome sealer developed by NAVAIR) performed better than those using the standard chromate conversion coating. The chromated coatings had failed completely by 1,680 hrs, whereas the trivalent-sealed coatings continued to perform quite well, in some cases still showing reasonable rankings at 2,688 hrs (16 weeks). Selected specimens are shown during the B117 test in Figure 21.

One coating, Sample 343-44, stands out for its exceptional performance. It transpires that this specimen was the last specimen treated, and it was sealed by carefully following the written procedure specified by Metalast. The previous specimens had been sealed by following a less careful set of verbal instructions from the company. This exemplifies the now well-known fact that trichrome treatments are less forgiving than most hexavalent treatments.

Given the porosity of the coatings it is unclear why they should perform so well in corrosion. CAP Technologies surmises, based on detailed EDX data obtained with EPP Ni coatings on steel, that the reason is alloying of the Ni with the Fe at the steel surface, forming a very corrosion-resistant surface layer. While this may be correct it does not explain why there should be such differences between the different sealing treatments, which we would not expect if the primary effect was creation of a CRES alloy. Or it may be that, as with the Keronite and Tagnite processes, mixed oxide deposition at the surface may improve corrosion resistance.

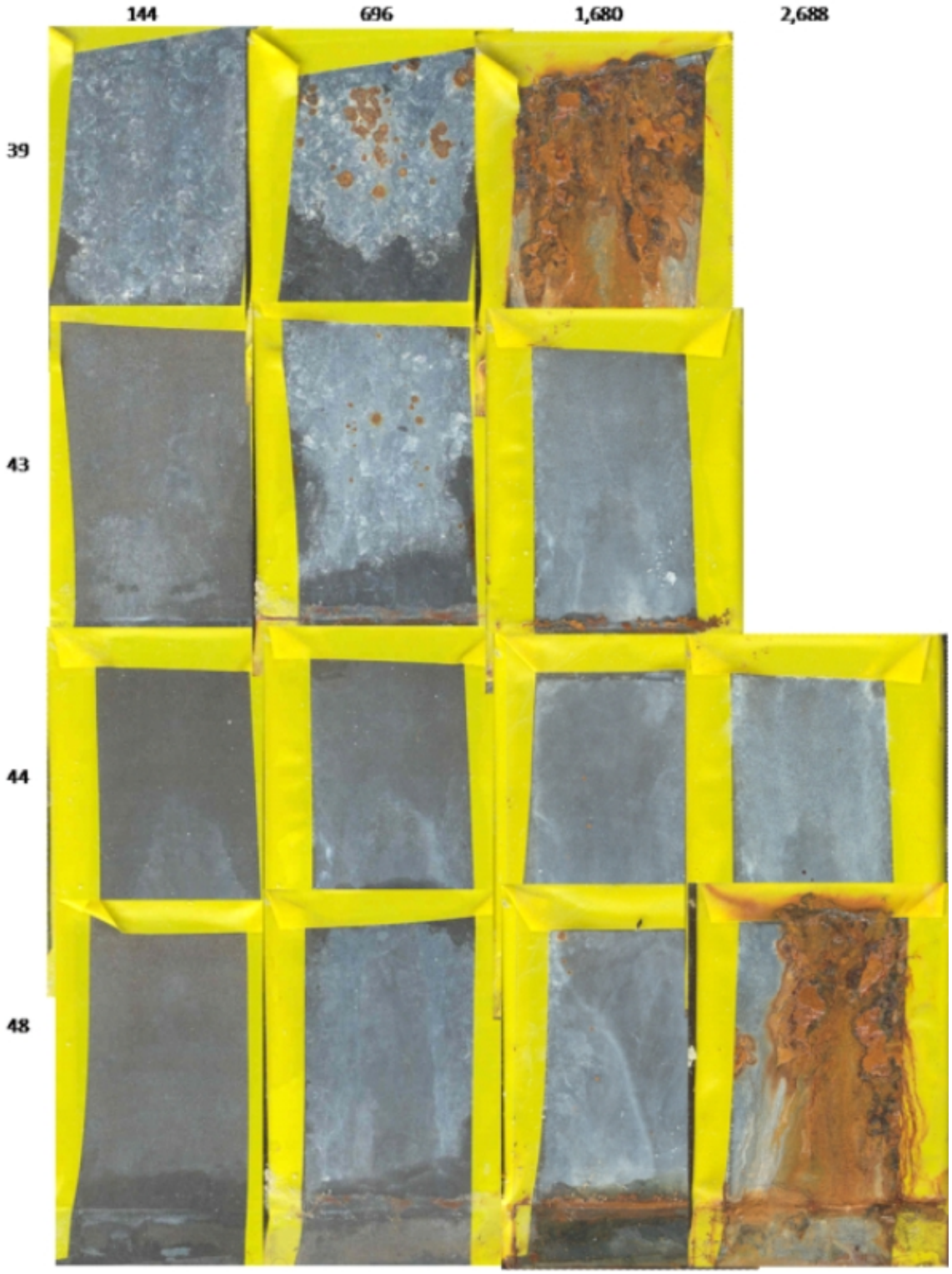

Figure 21. Zn-Ni specimens during B117 corrosion test. Specimen number at left, hours at top (CAP). Testing at NAVAIR PAX.

4. Evaluation of Suitability for DoD Use

EPP is an interesting technology, capable of cleaning substrates and depositing coatings using the same basic method, and even in the same deposition system, merely by flowing in a different electrolyte. Clearly, EPP coatings are very different from standard electroplates, and the EPP method has some distinct advantages and disadvantages:

Advantages	Disadvantages
Low volume of solution	Porous coating
Ability to clean and coat surface in one piece of equipment	Complex electrode shape or manipulation needed for complex components
Localized plating	Fatigue debit for coatings (but not for cleaning)
No hydrogen embrittlement	Difficult to plate entire complex shape once, inside and out
Usable for ODs or IDs	Anode hole erosion (equipment maintenance issue)
Rough surface for paint adhesion	High voltage equipment

The technique as tested in this program is well-suited to simple cylindrical or flat shapes, which is what it is most commonly used for (rebar, rod or wire, for example). It involves coating over a relatively small area (which could be increased with a larger power supply) using a standoff for the anode of about 1-3 cm. This makes it somewhat akin to brush plating or thermal spray in that it requires the anode to be kept (or designed to be) at a certain distance from the workpiece, and requires workpiece manipulation for large or complex components. There are very similar high voltage electrolytic coating methods (such as the Keronite™ and Tagnite™ processes) that take place in a bath. There is no inherent reason EPP could not be done in the same way, which would better accommodate complex components. This approach was not examined, but would appear to make more sense for complex components.

With its higher voltages and geometry restrictions, EPP will be more difficult and expensive to use than standard ZnNi electroplate. If pulse plating is used the equipment is more expensive still. The higher voltages do pose worker safety concerns, so that one could not, for example, use a tank with open bus bars as we do for standard electroplating. Because of this concern other high voltage processes such as Keronite use covered tanks.

The lack of hydrogen embrittlement is a distinct advantage, especially since it is the case both for cleaning and coating. In addition, the lack of fatigue debit makes EPP cleaning worth considering for some particularly difficult applications that occur with legacy components, such as coking in engines. It may be worth evaluating the process for specific cleaning problems, concentrating on how well it cleans and how the modified surface layer might affect fatigue or subsequent processing for the component alloys, as well as how it might impact subsequent overhaul cycles.

For EPP coatings, the fatigue debit is a distinct disadvantage, although it is similar to the debit seen for alkaline ZnNi. Thus it does not exclude its use for corrosion resistance of high strength alloys.

The nodular coating morphology and high porosity is inherent to the process. EPP may be a very good way of depositing a material that requires a large surface area, such as a catalyst, but for a corrosion-resistant coating we usually expect to need a continuous coating. Nevertheless the project showed that it is possible to produce ZnNi coatings that provide quite significant corrosion protection, in some cases comparable with standard electroplates. How it does this is an interesting technical question, and it suggests that more is happening than simply sacrificial corrosion protection. The porosity does suggest an interesting possibility, however, that one might obtain a very well-adhered, corrosion resistant coating system with a primer that infiltrates the porosity, followed by a topcoat.

What would have made EPP uniquely valuable would have been an ability to plate Al from aqueous solution. Unfortunately this project demonstrated the difficulty of doing that. While Al could be deposited, it was always deposited as hydroxide or oxide (in fact the deposition of surface oxides on Al is part of the Keronite™ process). This problem might, of course, be avoided with the use of non-aqueous solvents, but then it would have no advantage over the AlumiPlate™ process unless it could be done without the need for an enclosure, which is what makes the AlumiPlate process so capital-intensive. Spark machining, for example, is often done in an open tank under kerosene, which is insulating and inert for this process. If an Al-bearing salt were soluble in a non-aqueous fluid that did not need an enclosure, then it might be possible to deposit Al coatings using this

technology, depending on how the fluid conducted and hydrolyzed. However, it would be essential to eliminate air from the coating region, which would most likely require that the process be done under the liquid rather than in a jet or foam. The coating would still be porous, making it very different from electroplated Al, but since we have seen that even porous EPP coatings can be corrosion-resistant, such an approach may be worth pursuing.

We conclude that the EPP process has several disadvantages compared with standard cleaning and electroplating processes for the types of complex components that make up the typical depot workload. It does not have sufficient advantages to make it worthwhile developing for general DoD operations, but it may have some value for specific problems such as

- Difficult cleaning problems (engine coking or other legacy MRO cleaning issues). Any evaluation for this application should include careful evaluation of fatigue as well as ensuring that the modified surface does not present problems for subsequent MRO operations in the current or a subsequent MRO cycle.
- Coating of components where the porosity can be used to advantage, such as infiltrating a primer to improve paint adhesion.

For OEMs there may be additional possibilities:

- It would in principle be possible to infiltrate a lubricious material such as PTFE or silicone. Another possible application for this type of approach is to use EPP to deposit a layer of a hard alloy such as Ni or Ni-W, and infiltrate with PTFE. This is similar to some of the commercial electroless Ni processes that combine hard EN with PTFE. These are typical OEM rather than MRO processes.
- If alloying is the source of the unexpected corrosion resistance seen here, then it might be possible to use the method to alloy the surface for improved corrosion resistance. In a way this is already being done on magnesium alloys (Tagnite) and aluminum alloys (Keronite), but those processes might perhaps be improved with a deliberate alloy in addition to the multi-component oxide that the processes produce.

REFERENCES

1. A. Yerokhin, **X. Nie**, A. Leyland and A. Matthews, Characteristics of TiO_2 Coatings on Ti6Al4V Deposited by Micro-arc Oxidation, *Surf. and Coat Technol*., 130(2000)195-206
2. S. Gaydos, "ZnNi coatings and Al repairs", Workshop on Surface Finishing and Repair Issues for Sustainment of New Aircraft Systems, Tempe, AZ Feb (2008). http://www.hazmat-alternatives.com/Meetings.php
3. J. Osborne, "Validation of Alternatives to Electrodeposited Cadmium for Corrosion Protection and Threaded Part Lubricity Applications: Final Program Review" http://www.jgpp.com/projects/cadmium/documents/jtr_presentation.pdf

Electrolytic Plasma Technology:
Surface cleaning and coating deposition

Final Report

submitted by

Efstathios I. Meletis, Professor
The University of Texas Arlington
Materials Science and Engineering Department
P.O. Box 19031
Arlington, Texas 76019

Tel. (817)-272-2559
Fax (817) 272-2538
e-mail: meletis@uta.edu

and

E.O. Daigle, President
CAP Technologies, LLC
11725 Industriplex Blvd, Suite 4,
Baton Rouge, LA 70809

Tel: (225) 753 2200
Fax: (225) 753 2283
e-mail: eodaigle@captechnologiesllc.com

Period-of-performance: January 2005 - December 2007

Table of Contents

page

1. Background and Introduction....1
2. Objectives....3
3. Experimental....4
3.1 Electrolytic Plasma Processing....4
3.2 Testing Methods and Material Characterization....13
4. Cleaning Treatments....15
4.1 Processing Conditions....15
4.2 Surface Morphology and Composition....15
4.3 Metallography of Near Surface Layer....19
4.4 Microstructure Analysis....22
4.5 Microhardness Profile....26
4.6 Internal Stress Analysis....27
4.7 Hydrogen Content Analysis....29
4.8 EPT Cleaning of HE Specimens....31
4.9 EPT Cleaning of Fatigue Specimens....33
5. Coating Treatments....34
5.1 Zn Coatings....34
5.2 Zn-Al and Al Coatings....39
5.2.1 Screening Deposition Experiments....39
5.2.2 Deposition of Al-rich Coatings....45
5.3 Zn-Ni Coatings....69
5.3.1 Deposition and Characterization of Zn-Ni Coatings....69
5.3.2 Coating of Cylindrical Specimens....81
5.3.3 Hydrogen Embrittlement and Fatigue Testing and Evaluation....105
5.3.4 Coating of Flat Specimens....109
5.3.5 Salt Fog Corrosion Testing and Evaluation....117
6. Summary of Findings....122
Publications....123
References....124

1. Background and Introduction

Electrolytic Plasma Technology (EPT) is an emerging patented (CAP Technologies) surface engineering technique that can combine effective cleaning and coating of material surfaces in a single process. EPT also offers unrealistically high coating growth rates and unique characteristics, such as low cost, high efficiency, simplicity, high process flexibility and utilization of environmentally friendly precursor materials [1,2]. During processing, an electrical potential is applied between the workpiece material (cathode) and a counter electrode (anode) in an aqueous electrolyte. Above a critical voltage, fine bubbles comprising gaseous reaction products (H_2) generate on the cathode surface, and finally form continuous gaseous arcing plasma over the entire workpiece surface. Generation of a reducing plasma atmosphere and the subsequent collapsing of the generated bubbles result in effective surface cleaning (reduction and removal of oxides and surface deposits) and a desirable surface profile with microroughness. Also, the process has the ability to apply numerous metal/alloy coatings with excellent adhesion in an environmentally friendly manner.

The first attempts to use the electrolytic plasma discharge technique date back in the 1960's when CdNi has been deposited on cadmium anode in an electrolytic bath using spark discharge [3]. In the 1970's and 1980's parallel studies on oxide layer forming techniques have been developed in Russia [4-8] and Germany [9,10]. In parallel, researchers in US and China have become involved in the field and a few patents were awarded [11-13]. In the 90's, UK has become an important player in the field. Keronite Ltd. and Poeton™ are the main companies involved in electrolytic plasma processing. In the last years, interest in the field of electrolysis plasma research has grown significantly in Europe, Asia and US, but overall emphasis of groups are centered on performance evaluation, testing and characterization of plasma electrolytic oxidation coatings mostly on aluminum and magnesium [14-18]. Very few studies have been conducted on surface cleaning and metal coating deposition [2,19].

In the case of surface cleaning by EPT, the workpiece acts as cathode while a reducing gas (H_2) forms on its surface. The low electric conductivity of the gaseous envelope causes the concentration of voltage drop in the near workpiece area, and therefore, significant ohmic heating at the workpiece surface. This generates high local temperature in a very short time, resulting in the local melting of the workpiece surface. Meanwhile, the gaseous vapor plasma (H_2) effectively reduces oxide layers present and decomposes any organic hydrocarbon materials on the workpiece surface. Due to the high surface temperature followed by quenching, microstructural changes and formation of metastable structures can take place on the workpiece surface.

Moreover, EPT is an environmentally friendly technique for large area deposition of metal or alloy coatings with very high deposition rates (for example, more than 10 μm/min has been achieved for Zn coatings). In this situation, EPT is similar to conventional electroplating except for the much higher potential applied between the workpiece and counter electrode. The metal ions are accelerated by the electric field formed within the gaseous vapor arcing plasma surrounding the workpiece surface, and then transported to and condensed on the work piece surface and form metal coatings with high deposition rates. Due to local melting and particular surface profile generated

by the process, the coating material blends and keys with the substrate at the surface resulting in high adhesion.

2. Objectives

In the present project, EPT was utilized to clean and coat 4340 steel in an effort to assess its potential in developing alternative coating treatments for Cd coating replacement. The influence of the EPT cleaning process on the structure, hydrogen content, and properties such as hardness, hydrogen embrittlement (HE), fatigue, etc., was investigated. The effort concentrated on several potential coatings such as pure Al and Zn-Al and Zn-Ni coatings since they possess attractive characteristics for sacrificial corrosion protection of steel. The capability of EPT to produce these coatings was assessed. The coatings produced were characterized in terms of microstructure, properties and performance to fully evaluate their potential as Cd replacements.

3. Experimental

3.1 Electrolytic Plasma Processing

All processing in the present study was conducted in electrolytic plasma units located at CAP Technologies (Baton Rouge, LA). A typical unit is shown in Figure 1. The equipment is using the "foam" technology where the workpiece is surrounded by a foam rather than by a thin electrolyte layer. The equipment is capable of processing round and flat metal surfaces. In the course of the present work, various reactor configurations were developed and fabricated in order to allow processing of flat and rod shape specimens required for HE, fatigue and corrosion testing. Figures Figure 2-6 present some of the fabricated units. An important aspect of EPT is anode design. Figure 7 presents various representative types of anodes that have been fabricated during the course of the project. Specific cleaning and coating conditions are described in the next sections.

Most processing was conducted on hardened AISI 4340 steel coupons (24 mm in diameter and 1.5 mm thick) with a hardness of HR_c= 52.

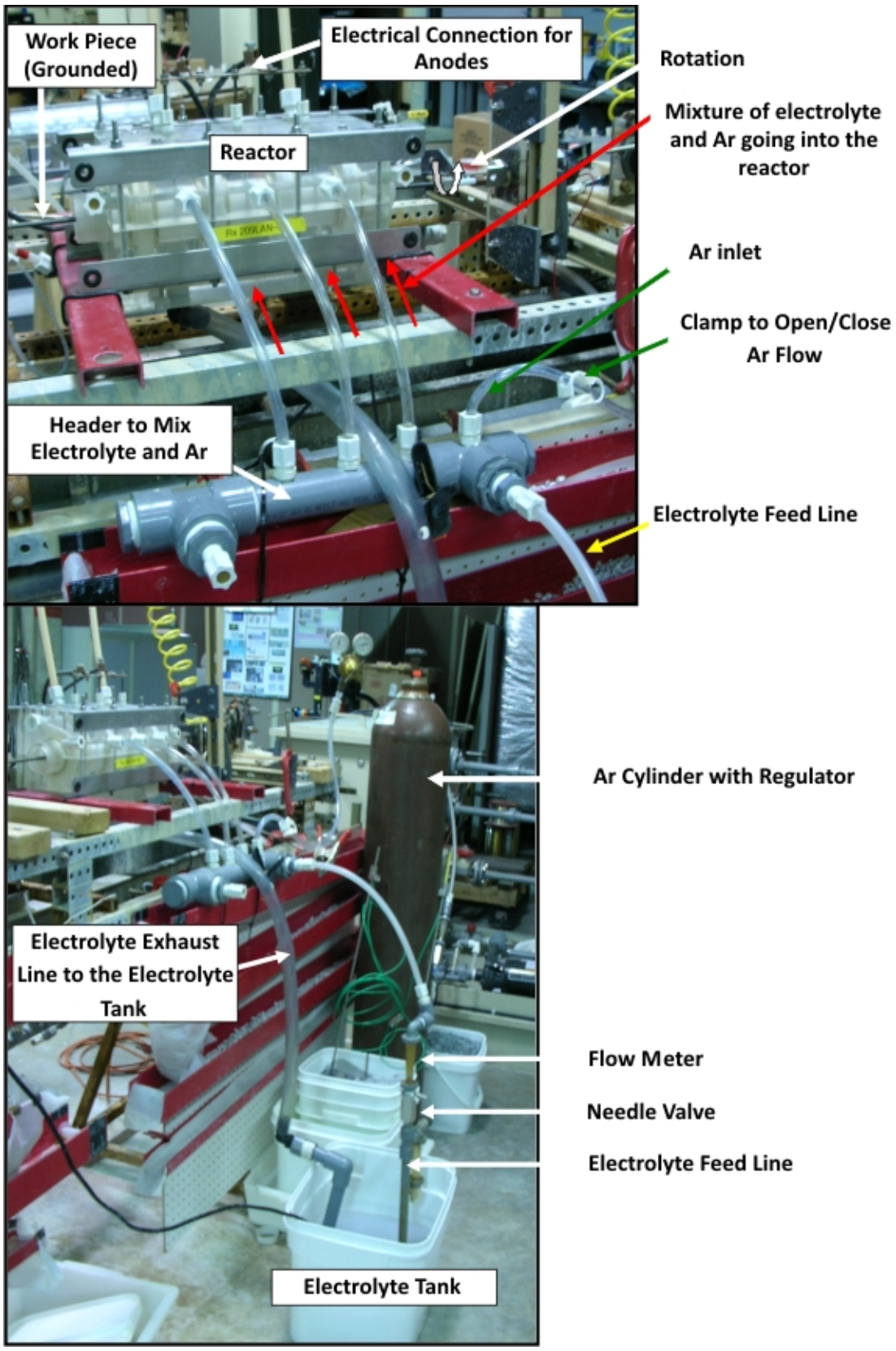

Figure 1 Processing unit at CAP Technologies used for cleaning and coating treatments.

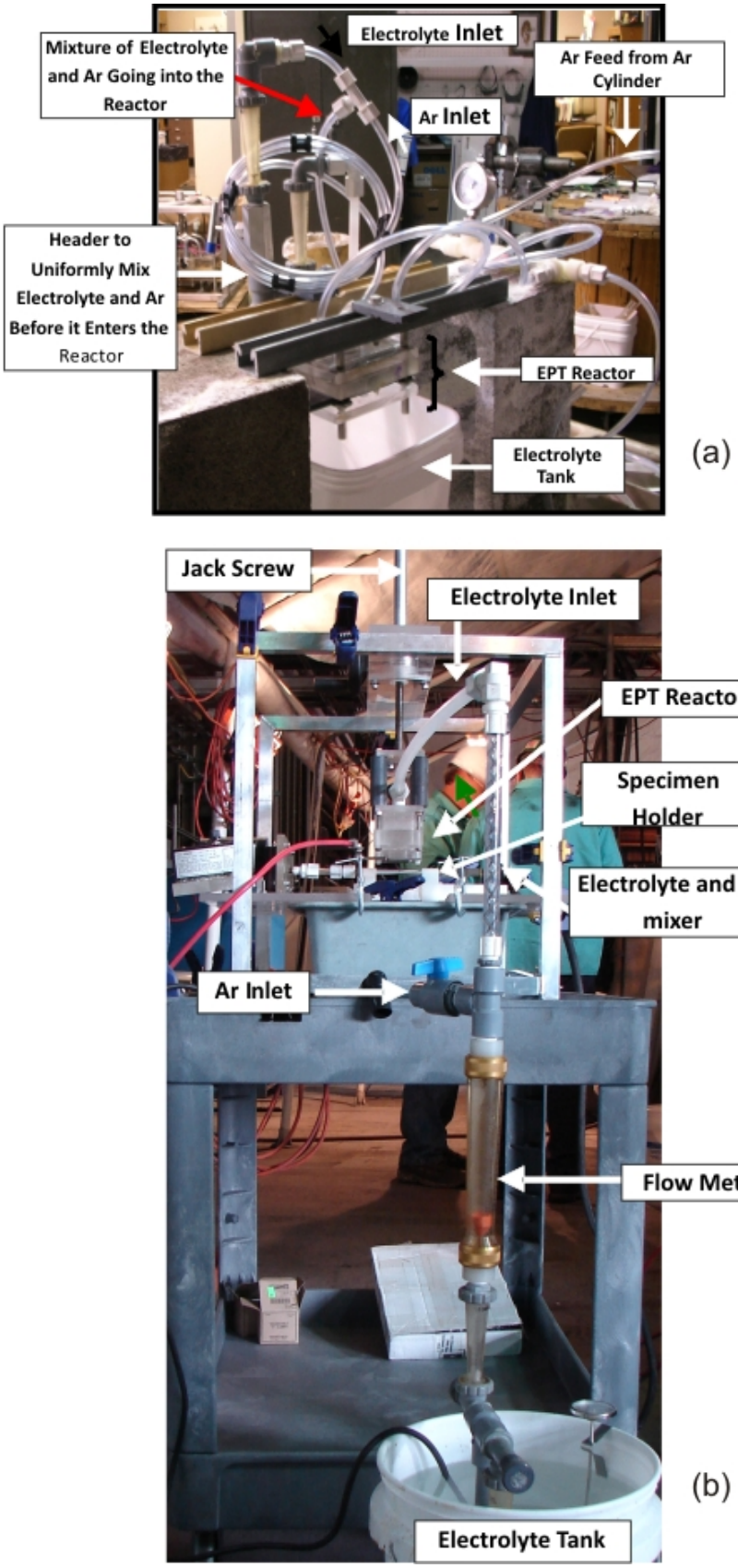

Figure 2 (a) Experimental setup used to deposit Zn-Al and Al coatings on 0.75" diameter, 4340 disc samples by using EPT. (b) EPT reactor that was designed to handle different types of specimen configuration.

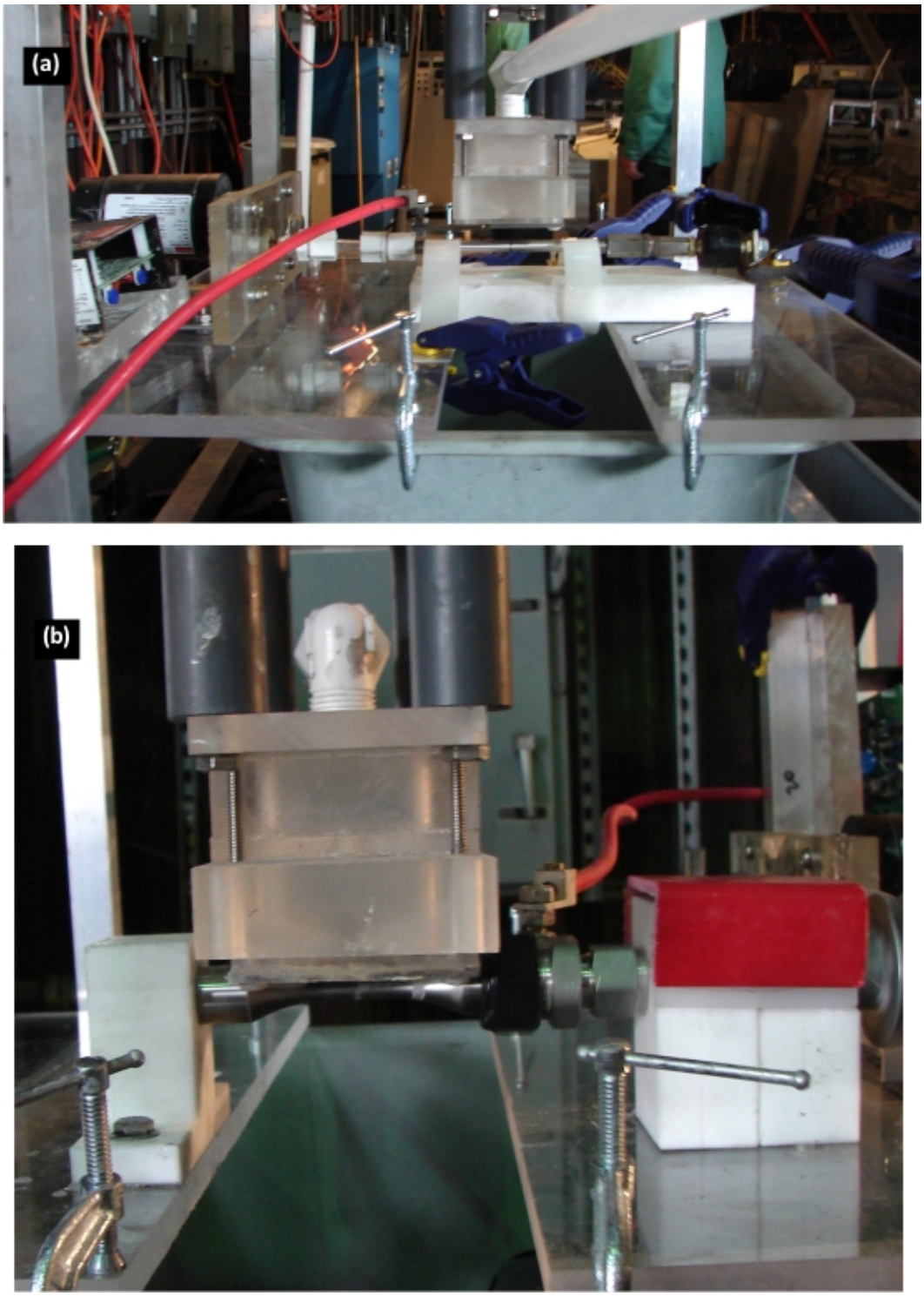

Figure 3 Experimental setup for: (a) HE and (b) Fatigue specimens.

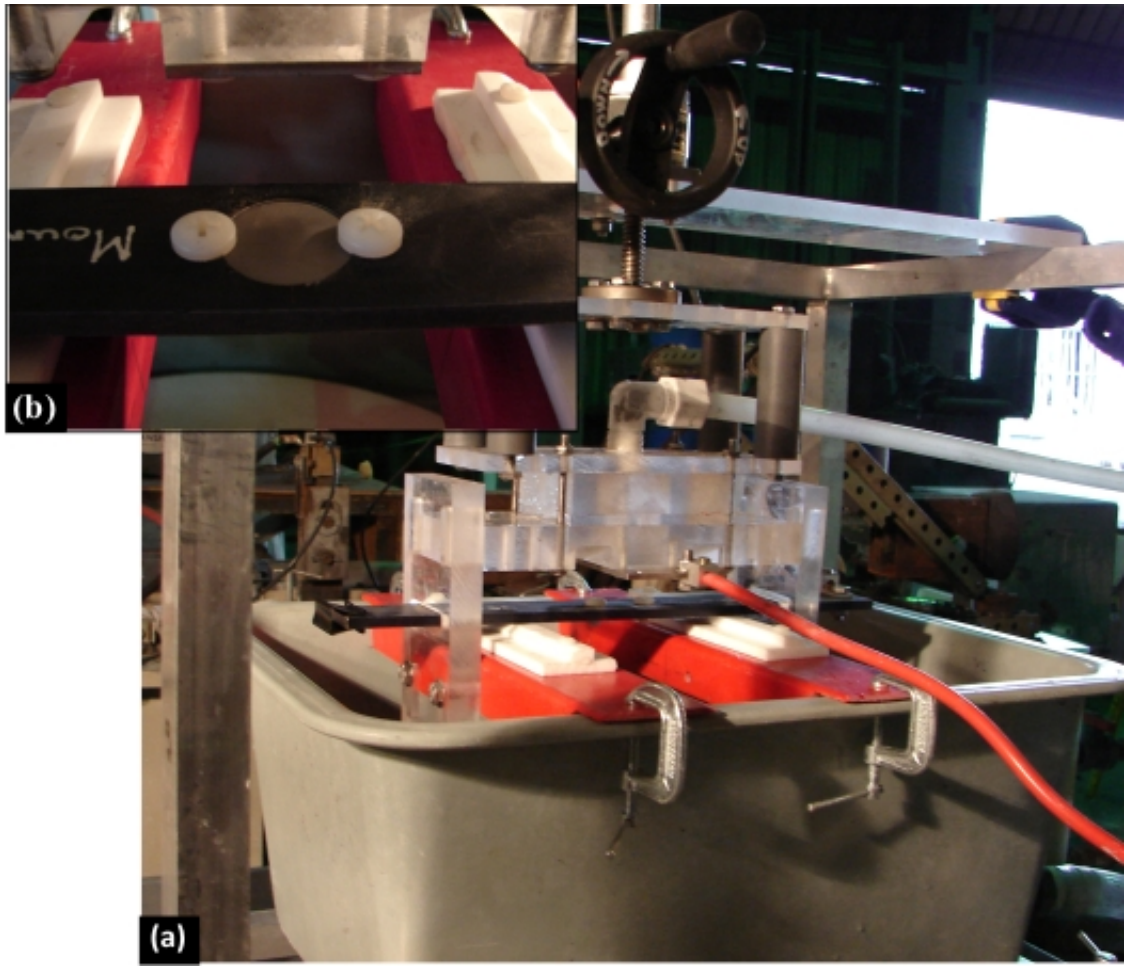

Figure 4 Flat disk specimen: (a) experimental setup and (b) specimen holder.

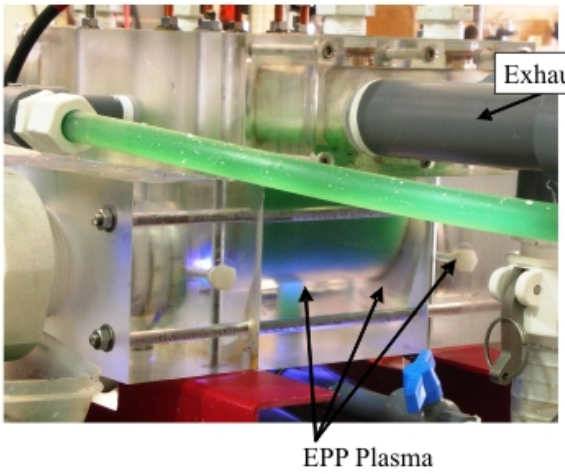

(a) Picture of V-8 with Plasma

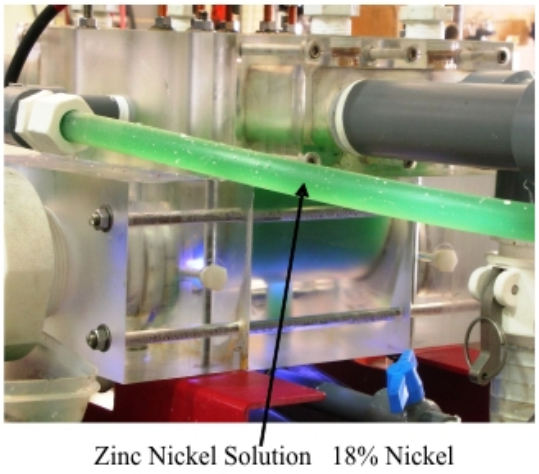

(c) V-8 Reactor with plasma

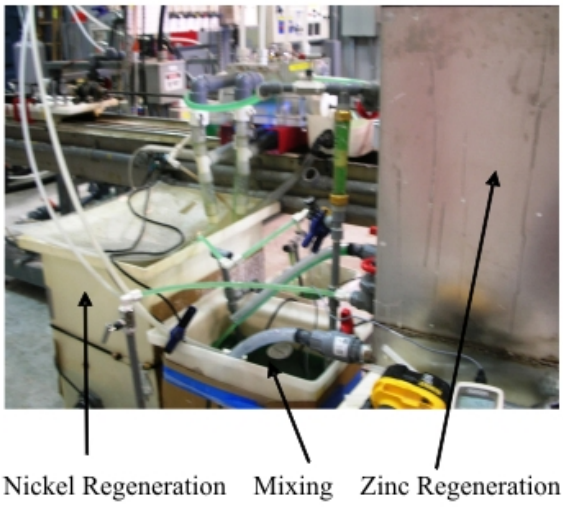

(b) Zn-Ni coating setup with the regeneration system

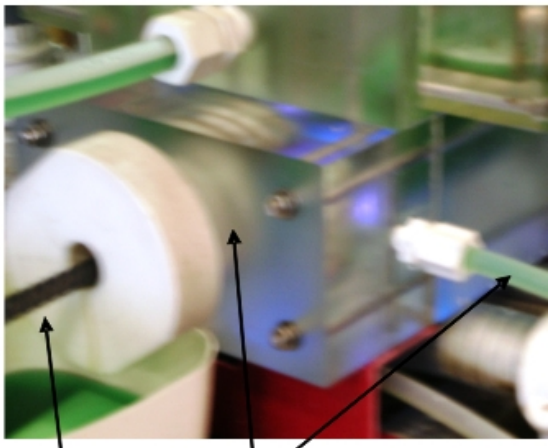

(d) V-8 Reactor with plasma

Figure 5. CAP reactor V-8 built to deposit Zn-Ni coatings.

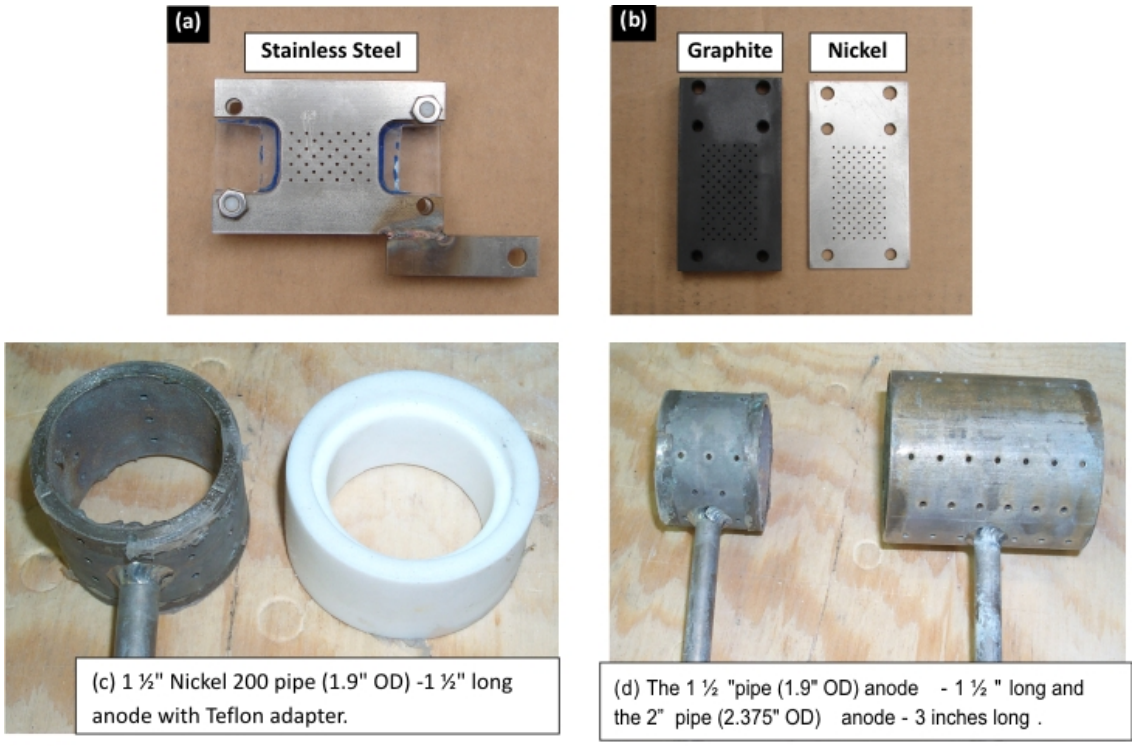
(a)
Stainless Steel
(b)
Graphite
Nickel
(c) 1 ½" Nickel 200 pipe (1.9" OD) -1 ½" long anode with Teflon adapter.
(d) The 1 ½ "pipe (1.9" OD) anode - 1 ½ " long and the 2" pipe (2.375" OD) anode - 3 inches long .
(e) Pt coated ring type anode for the 302 Reactor before testing.

Figure 6.

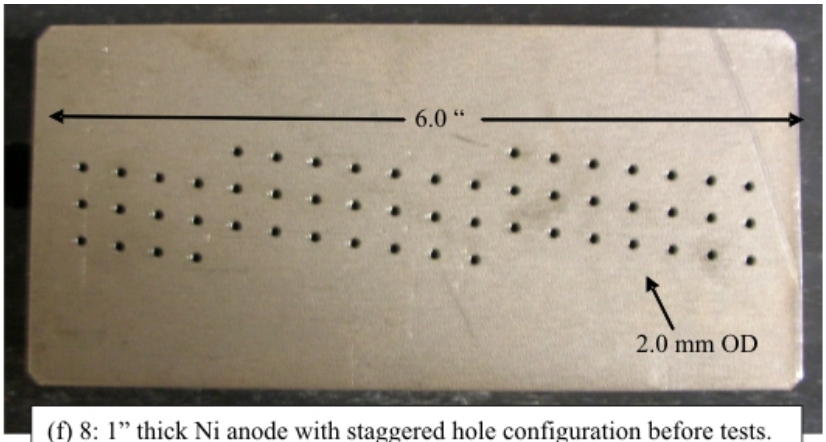

(f) 8: 1” thick Ni anode with staggered hole configuration before tests.

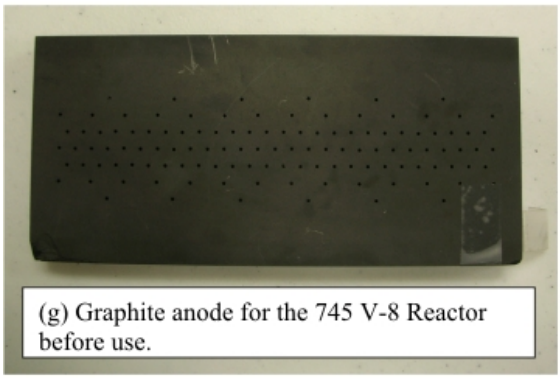

(g) Graphite anode for the 745 V-8 Reactor before use.

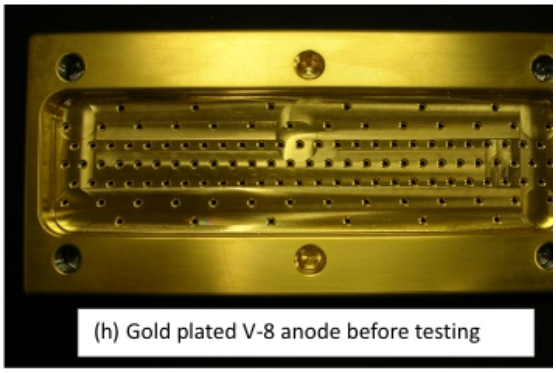

(h) Gold plated V-8 anode before testing

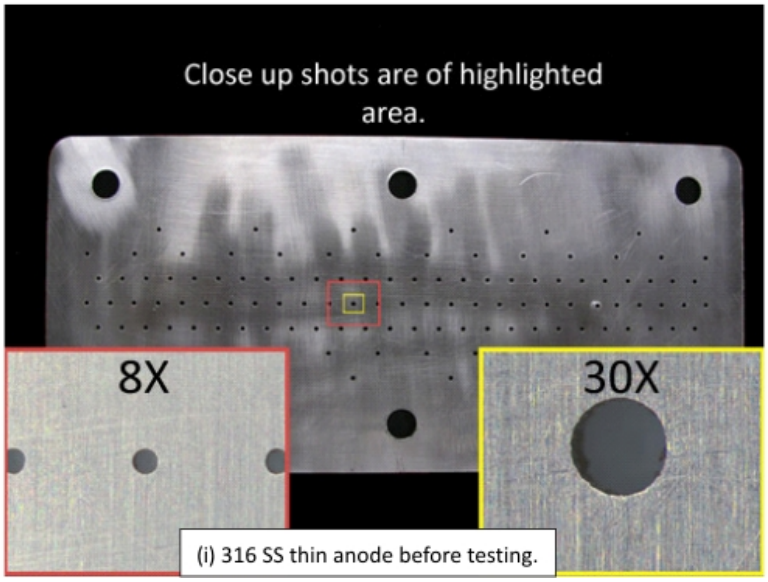

(i) 316 SS thin anode before testing.

Figure 6 Different representative types of anodes developed in the project along with their erosion.

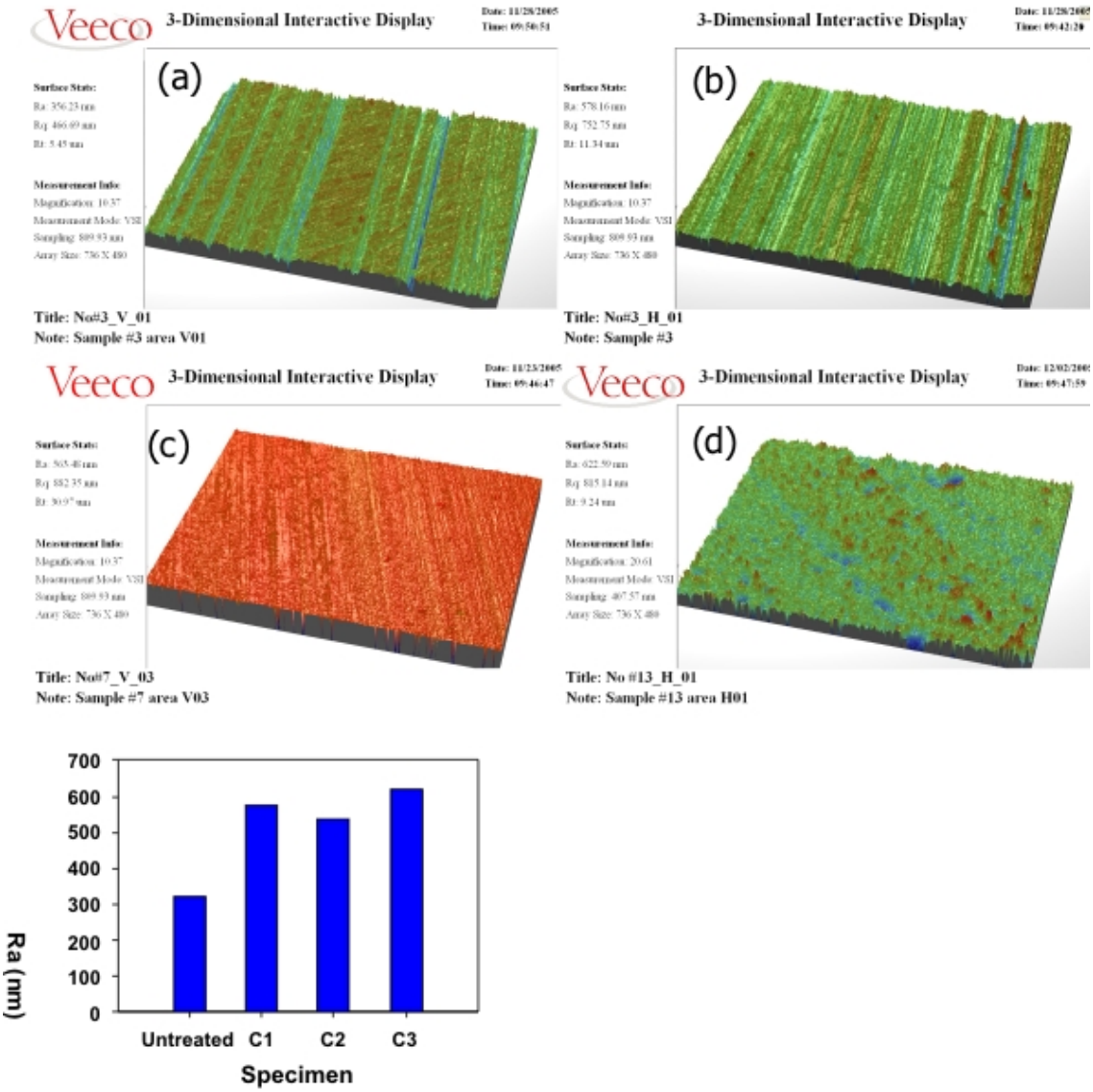

Figure 7 Surface roughness profiles and characteristics for untreated and cleaned 4340 steel under the three conditions shown in Table 1.

3.2 Testing Methods and Material Characterization

Several complementary techniques were employed to characterize the cleaned and coated steel specimens. The surface morphology and microstructure of the EPT-treated samples were characterized by scanning electron microscopy (SEM) with a typical acceleration voltage of 20 keV. X-ray energy dispersive spectroscopy (EDS) at a typical voltage of 10 keV was used to determine the composition, especially oxygen content in the surface layer. High-resolution (HR) SEM was conducted using a field emission microscope. Coating thickness was measured by examining cross sections. For the cross sectional observations, samples were mounted in epoxy, then ground and fine polished with 0.1 micron alumina as the final step. Samples were etched with 2.5 Nital (2.5% HNO_3 in Methanol). The surface roughness of EPT-treated specimens was characterized by profilometry.

The distribution of the microhardness along the cross section was determined using a Vickers microhardness indenter with a load of 25g. The specimens were first coated with electroless Ni in an electrolytic bath to retain their edge during polishing.

The microstructure and phase structure of the EPT-treated samples was studied using a JEOL 1200EX transmission electron microscope (TEM). Thin foils were prepared from cross sections and bright and dark field imaging along with electron diffraction was utilized to characterize the microstructure of the EPT-treated specimens.

The phase structure of the EPT-treated samples was also studied using a Siemens D500 x-ray diffractometer operated in the Bragg-Brentano mode. A Cu K_α radiation source was used for the x-ray diffraction (XRD) experiments with an accelerating voltage and filament current of 40 kV and 30 mA, respectively. Also, the chemical state of the various elements in selected coatings was studied by x-ray photoelectron spectroscopy (XPS).

The hydrogen content in the EPT-treated and untreated 4340 samples was measured by the nuclear reaction analysis (NRA) method. This is a nuclear method to obtain concentration and depth distributions for certain target chemical elements, especially for light elements. In order to determine hydrogen in 4340 steel, the mass 15 isotope of nitrogen interacts with hydrogen in the target if the nitrogen has energy of motion equal to 6.385 MeV. If the nitrogen beam of particles has precisely this energy and if it hits atoms of hydrogen on the surface of the sample, then gamma ray emission occurs. The gamma rays are measured and used to show the absolute concentration of H on the surface.

Cross sectional observations on selected cleaned and coated specimens were made using the focused ion beam (FIB) technique. In this technique, an ion beam is utilized to mill polish a selected cross section of the specimen followed by direct observation.

Potentiostatic and potentiodynamic corrosion experiments were conducted to characterize the corrosion behavior of the EPT-treated specimens. These tests were conducted in tap water and 3.5% NaCl solution under aerated and deaerated conditions. In the potentiostatic experiments, the corrosion potential was measured versus time until the potential was stabilized. In the potentiodynamic experiments, the potential was increased in steps while the corrosion current was measured. Corrosion rates were

calculated using Tafel extrapolation. All corrosion potentials were measured with respect to a saturated calomel electrode (SCE). Additional salt fog experiments were conducted on cleaned and Zn-Ni coated panels using an outside vendor.

4. Cleaning Treatments

4.1 Processing Conditions

This part of the study focused on determining effective cleaning conditions for 4340 steel surfaces. Based on previous experience with EPT, three different treatment conditions were selected for cleaning 4340 steel specimens. Table 1 presents the three different cleaning conditions selected for treating the 4340 steel surfaces. The treatments involved two different electrolytes that have been typically used previously for cleaning of steel surfaces.

Table 1 EPT Conditions for Cleaning 4340 Steel.

Processing Parameters	***Condition 1***	***Condition 2***	***Condition 3***
Voltage, V	**140**	**180**	**140**
Current, A	**6-7**	**6-7**	**5**
Treatment Time, sec	**10**	**30**	**15**
Electrolyte	**$NaHCO_3$**	**$NaHCO_3$**	**NH_4Cl**
Temperature, °C	**65**	**60**	**70**

4.2 Surface Morphology and Composition

Surface profilometry and SEM were employed to study surface morphology and characteristics of the untreated and EPT-cleaned 4340 steel under the three different conditions shown in Table 1. It was found that the surface morphology is strongly dependent on the electrolyte type, voltage, and treatment time. Figure 7 presents the 3-D surface appearance and the mean surface roughness value (R_a) of untreated and cleaned 4340 steel under the above three processing conditions. Also, Figures 8-10 present scanning electron micrographs showing the surface morphology and surface composition obtained by EDS of EPT-cleaned specimens under the three different processing conditions. The analysis showed that cleaning under *Condition 2* resulted in a rather uniform surface profile in terms of micro roughness and appearance.

More specifically, the specimens cleaned for 10 s in the electrolyte of $NaHCO_3$ (*Condition 1*) showed parallel rough wavelike features with a spacing of about 7.5-12.5 μm, Figure 8. Careful inspection of the high magnification image showed that smooth wavelike structures with a spacing of 0.5-1 μm exist between those rough features. These are produced by the continuous melting, freezing and remelting of the surface during the treatment. Quantitative analysis of the EDS spectra, Figure 8(c), shows that oxygen content was fairly low (only 0.26 wt%), indicating that 10s is sufficient to clean the steel surface. Also, the C content was found to be significantly lower than the nominal steel C content (0.4 wt%) and ranged from 0.1-0.15 wt%.

The specimens cleaned for 30 s in $NaHCO_3$ (*Condition 2*) exhibit an entirely different surface morphology, which consists of parallel linearly arranged valleys with a diameter of about 0.7-1.5 μm. High magnification image, Figure 9(b), shows droplet-like structures with a size of about 1.5 μm existing on the surface. Similarly, quantitative EDS analysis, Table 2, shows low O content for this cleaning treatment.

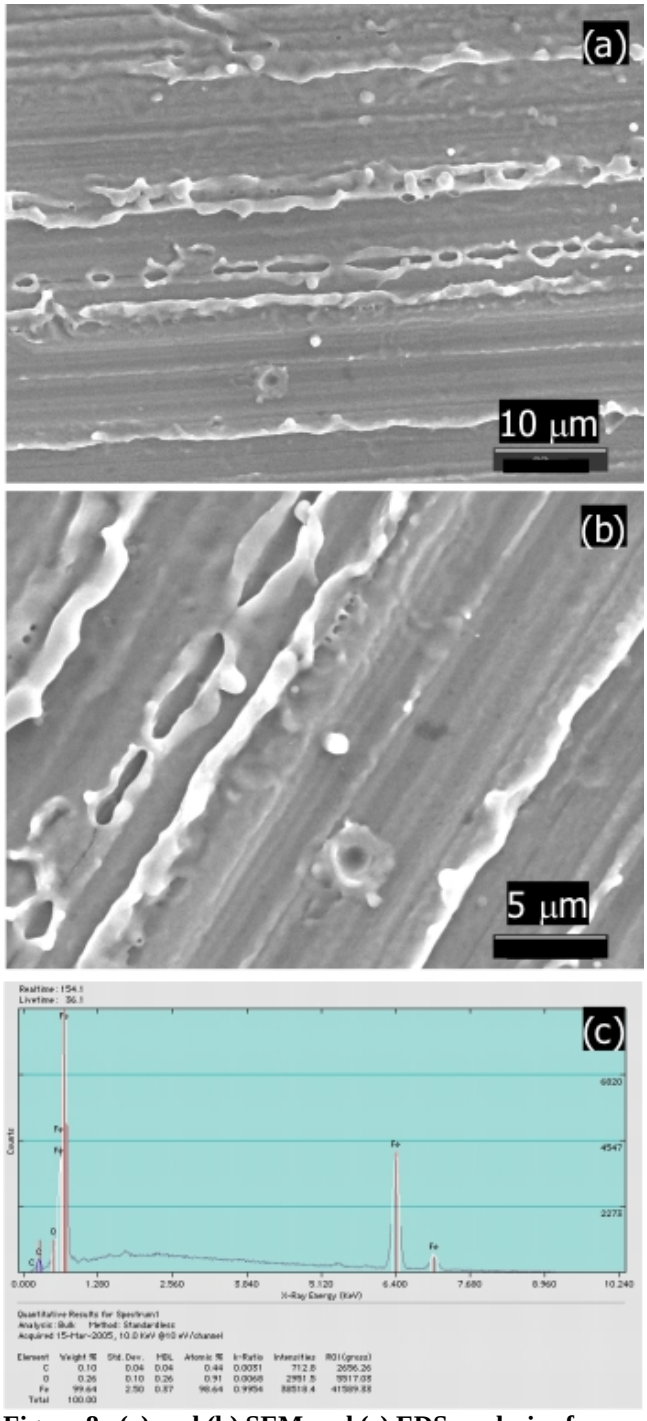

Figure 8 (a) and (b) SEM and (c) EDS analysis of 4340 steel treated by EPT for 10 s in NaHCO3 solution (Condition 1).

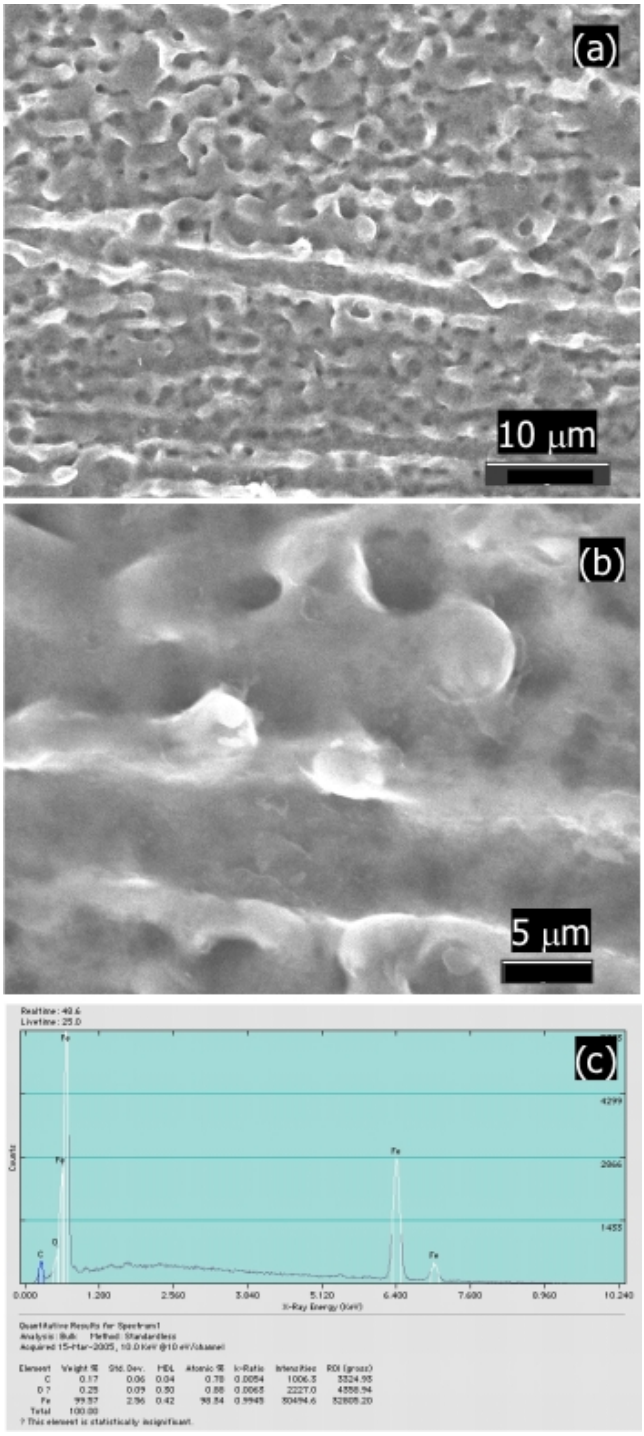

Figure 9 (a) and (b) SEM and (c) EDS analysis of 4340 steel treated by EPT for 30 s in NaHCO3 solution (Condition 2).

Table 2 Quantitative EDS results for EPT-cleaned 4340 Steel.

Processing Parameters	O Content		C Content		Fe Content	
	Wt %	At %	Wt %	At %	Wt %	At %
Condition 1	**0.1**	**0.44**	**0.26**	**0.91**	**99.64**	**98.64**
Condition 2	**0.17**	**0.78**	**0.25**	**0.88**	**99.57**	**98.34**
Condition 3	**0.09**	**0.42**	**0.32**	**1.09**	**99.59**	**98.49**

The surface morphology of the 4340 steel specimen cleaned with NH_4Cl for 15 s (*Condition 3*) exhibited a rather rough surface appearance, Figure 10. The entire surface comprises of large circular craters with a size of 10 μm surrounded with irregular shape or spherical molten droplet-like structures. The morphology consists of a three dimensional crater network. EDS analysis for this cleaning treatment also showed low O content.In order to evaluate the influence of the cleaning time on the surface morphology and microstructure of the 4340 steel, a specimen was cleaned using EPT for an extremely prolonged time of 20 min in $NaHCO_3$ solution. The surface morphology, Figure 11(a), exhibited a honeycomb-like structure, consisting of uniformly distributed valleys with a diameter of about 0.5-1.5 μm and spacing of 1.5-2 μm, and droplet-like structures, 0.7-2 μm in diameter. It appeared that the extensive cleaning treatment resulted in a steady-state in terms of surface morphology. As shown in the high magnification image, Figure 11(b), the droplets exhibit very smooth surface while some fine flaws with a size of 100-200 nm appear inside the valleys, which may result from the collapse of the hydrogen bubbles in the plasma. Quantitative analysis of the EDS indicates that there is no significant change in the C and O content on the specimen surface.

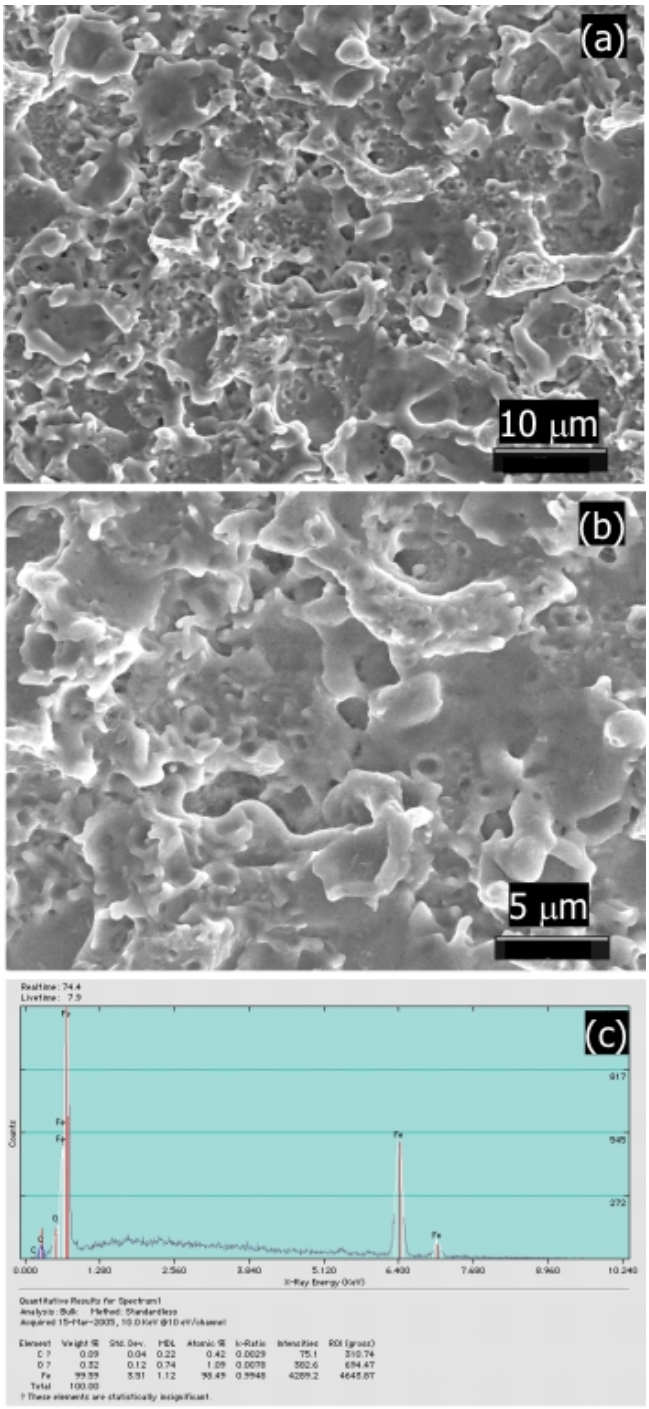

Figure 10 (a) and (b) SEM and (c) EDS analysis of 4340 steel treated by EPT for 15 s in NH4Cl solution (Condition 3).

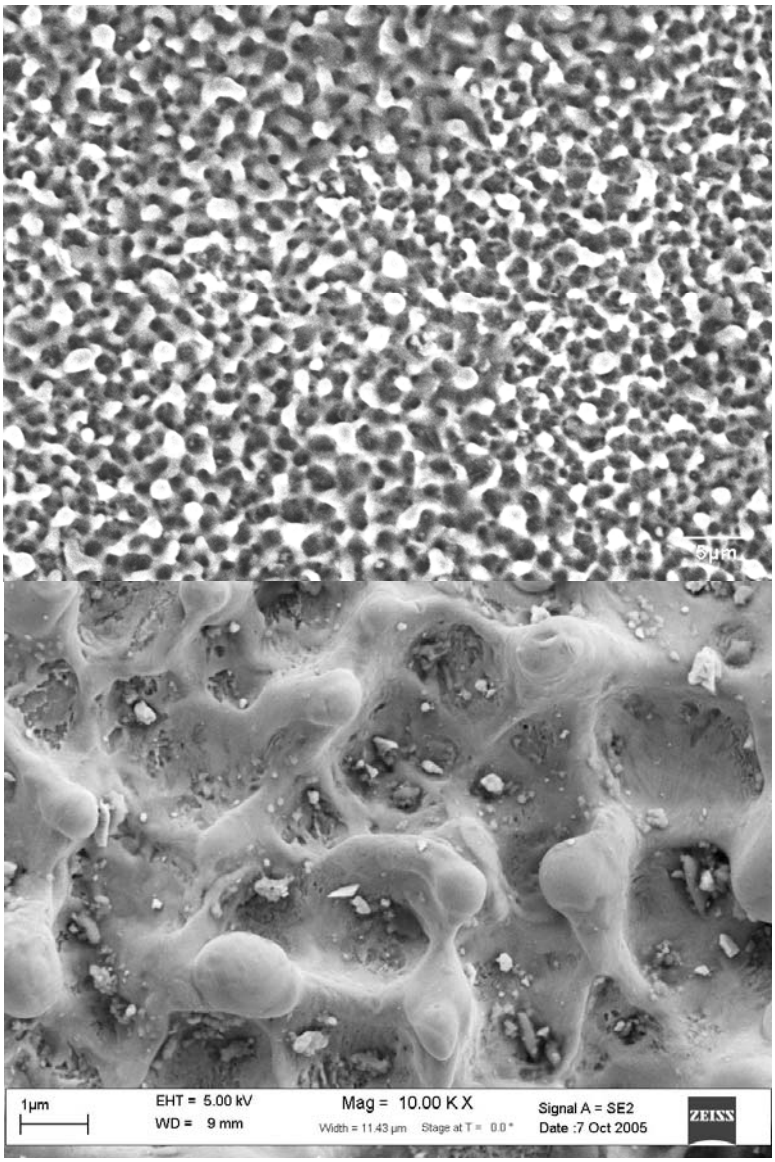

Figure 11 Scanning electron micrograph showing surface morphology of EPT-treated 4340 steel for 20 min under Condition 2.

Thus, for all three samples, there was no significant change on the surface composition measured by EDS at a voltage of 10 kV, Figures 8-10. The oxygen content was fairly low (0.25-0.32 wt %) for all treated samples, Table 2. Also, the C content was found to be significantly lower than the nominal steel C content (0.4 wt%) and ranged from 0.1-0.15 wt%. It should be noted that composition obtained by EDS is the average value within the excitation volume which extends down to a few microns below the surface. As a result, the surface C content is expected to be much lower than 0.1 wt.%. Thus, EPT was found to remove scale effectively from the surface and at the same time significantly reduce the amount of C at the surface.

Cleaning *Condition 2* was selected for treating the fatigue and HE specimens that were shipped and tested at Metcut Research Inc. (Cincinnati, OH) and Army Research Laboratory, respectively.

4.3 Metallography of Near Surface Layer

Cross sectional microstructure analysis was conducted for 4340 steel cleaned by all three different conditions. The samples were first mounted in epoxy, then ground and fine polished, followed by etching with Nital reagent (2.5% HNO_3 in methanol). For all specimens, the bulk morphology exhibited a needle shaped structure with a length of 0.5-5 μm and width of 200-500 nm, as shown in Figure 12(a). This is the typical morphology of the martensite phase. High magnification observations showed the existence of nanosize (<100 nm) spherical and rod-like cementite within the large martensite grains, Figure 12(b). This is a typical microstructure of tempered martensite.

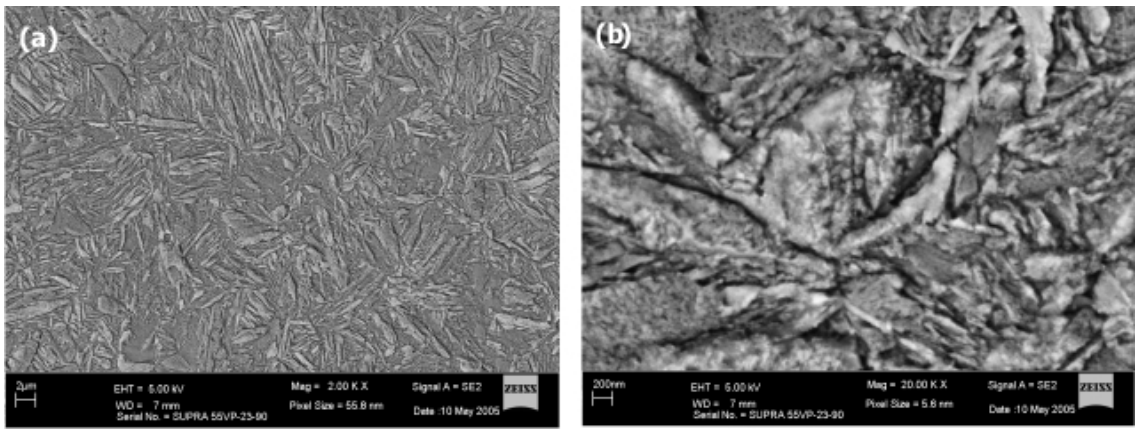

Figure 12 Scanning electron micrographs of bulk 4340 steel showing typical tempered martensite microstructure (a) overall and (b) high magnification images.

The sample cleaned for 10 s in $NaHCO_3$ solution (*Condition 1*) exhibits a relatively smooth surface, Figure 13. SEM observations showed the presence of a surface layer with a thickness of 0.8-1.5 μm. High magnification image demonstrated that this surface layer consists of nanosized particles, 50 -100 nm in diameter.

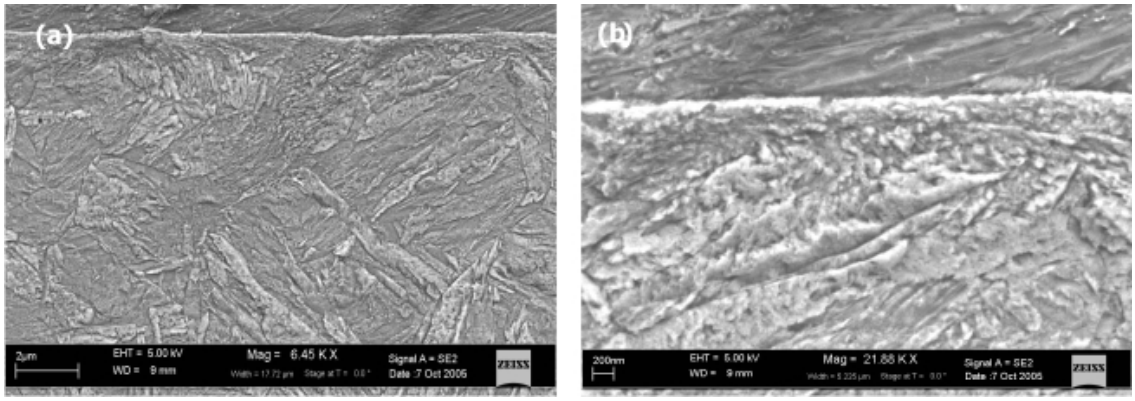

Figure 13 SEM from a cross section of 4340 steel treated by EPT for 10 s in NaHCO3 solution (Condition 1) (a) overall and (b) high magnification images.

For the sample cleaned for 30 s in $NaHCO_3$ solution (*Condition 2*), the surface was relatively rough. Features, about 200 nm high and 1.5 μm width, were observed on the surface, Figure 14. Furthermore, a surface layer, exhibiting a fine grain structure, with a thickness of about 1-2.5 μm was also distinguished. After careful inspection, it was

found that the surface layer comprises of two layers: top layer and subsurface layer. The top layer is featureless and amorphous-like, indicating amorphous or nanocrystalline structure. However, the subsurface layer consists of a fine-grained (about 10-40 nm) structure. The thickness of the top layer and subsurface layer is about 200-500 nm and 0.5-2 μm, respectively with the size of the features increasing gradually with depth.

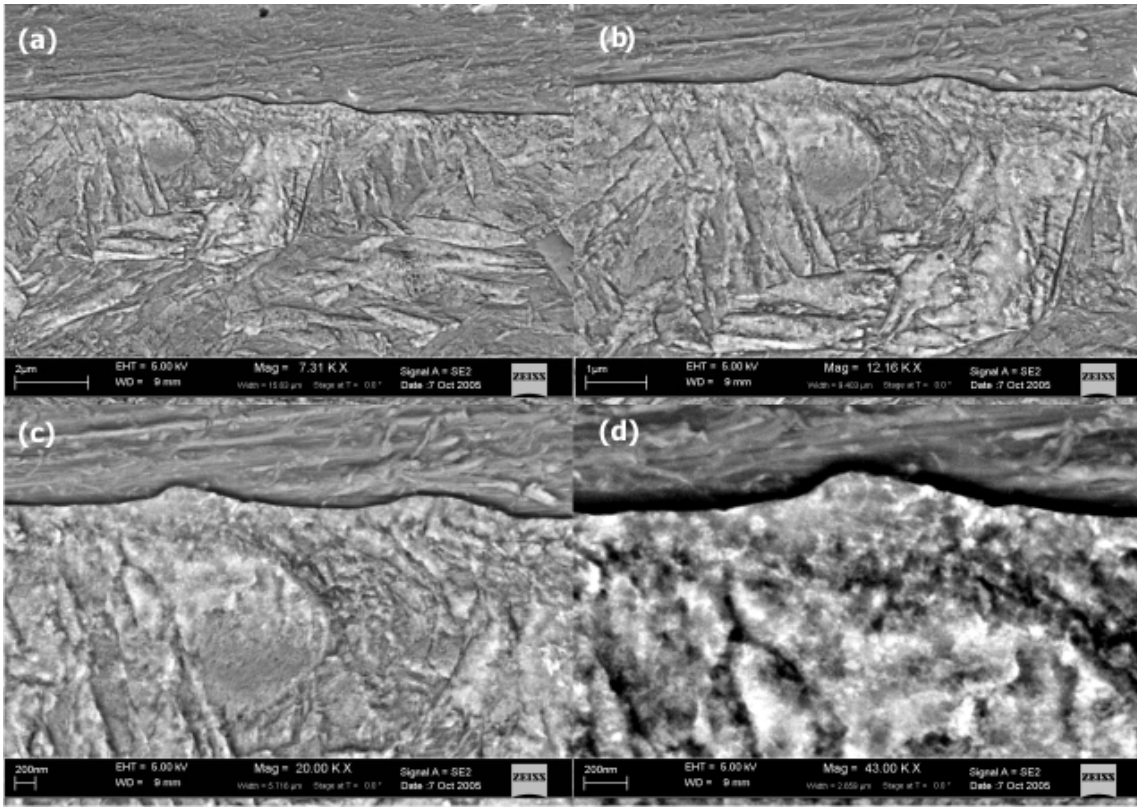

Figure 14 SEM from a cross section of 4340 steel treated by EPT for 30 s in NaHCO3 solution (Condition 2); magnification increases from (a) to (d).

The sample cleaned for 20 min under Conditions 2 exhibited a very interesting microstructure. Although, this sample also presents a two layer structure, the features in each layer are much larger, and the thickness for the top layer and subsurface layer increased to about 1.5-2 μm and 4-6 μm, respectively, Figure 15(a) and (b). In addition, a clear boundary between the top layer and the subsurface layer can be distinguished, Figure 15(c), which demonstrates signs of initial solidification. High magnification images show that the microstructure in the top layer consisted of three sub-layers, Figure 15(d). The top most layer with a thickness of about 150-300 nm exhibited an amorphous like structure. The second layer had a thickness of about 320-650 nm, which comprised of nanosized grains, about 25-90 nm in diameter. The third layer was very thick, about 1-1.5 μm. The grain size increased rapidly to about 130-180 nm. As compared with the top layer, the microstructure in the subsurface layer is very similar to that in the bulk. However, the grain size, 14 μm, is significantly larger than the grain size, 6 μm, in the bulk. The large grain size results from the prolonged exposure to local high temperature spikes during plasma treatment.

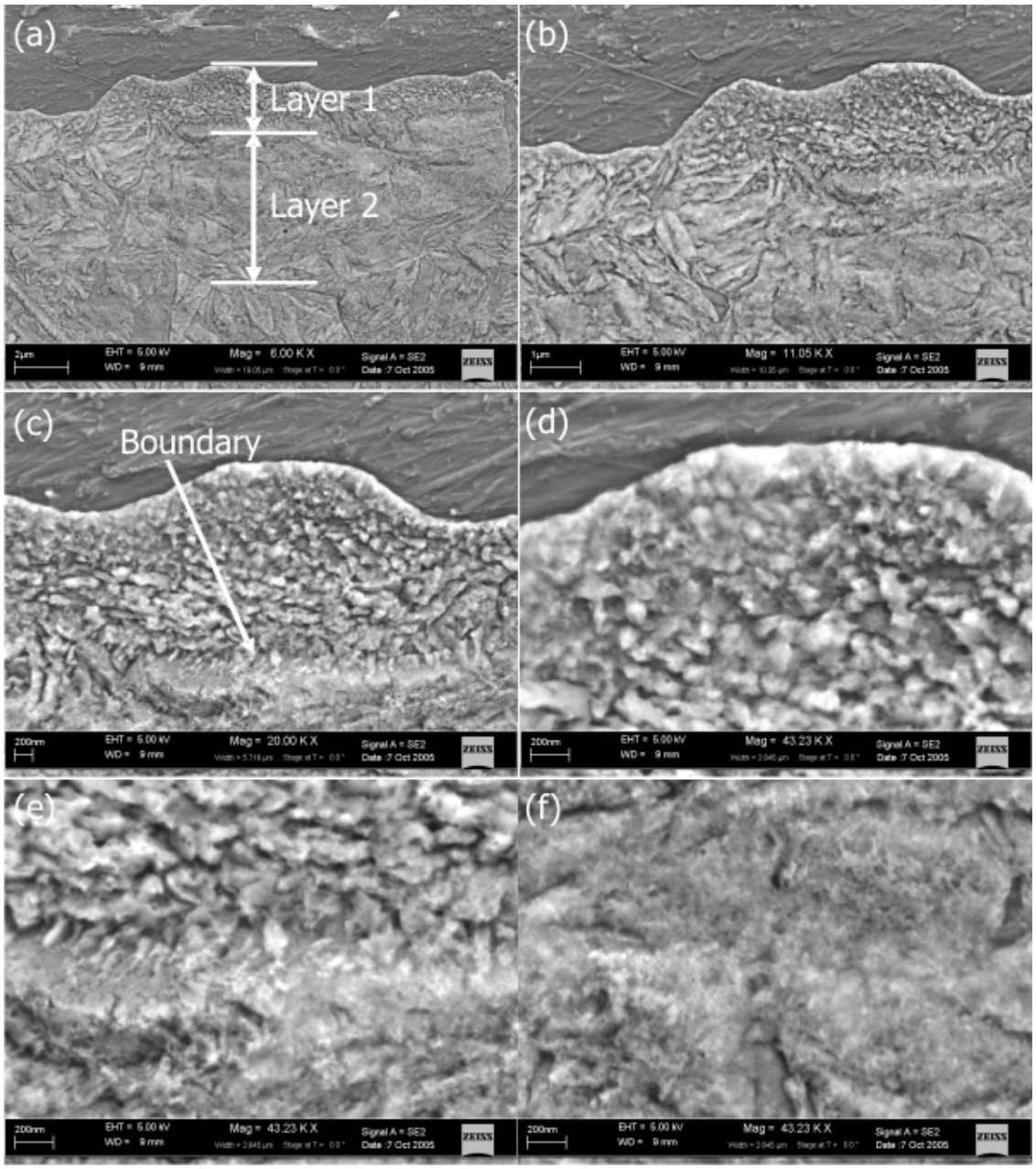

Figure 15 Cross sectional SEM images of 4340 steel treated by EPT for 20min in NaHCO3 solution. Two layers were distinguished from the bulk in Figs. (a-c). Figs. (d-f) show the high magnification images of the layer 1, boundary, and layer 2, respectively.

SEM observations of cross sections of 4340 steel treated with NH_4Cl solution (*Condition 3*) showed a similar microstructure. An obvious surface layer of about 2 μm thick, Figures 16(a) and (b), can be clearly distinguished with a microstructure entirely different from that of the bulk. This is similar to the microstructure of the 4340 steel treated in $NaHCO_3$ for 20 min. High magnification observations showed that the surface layer comprises of two layers: top layer and subsurface layer. The top layer was featureless and amorphous-like, indicating amorphous or nanocrystalline structure, Figure 16(c). However, the subsurface layer consists of a fine-grained (about 150 nm) structure.

The thickness of the top layer and subsurface layer was about 200-500 nm and 0.5-2 μm, respectively. The size of the features increased gradually with the distance away from the surface.

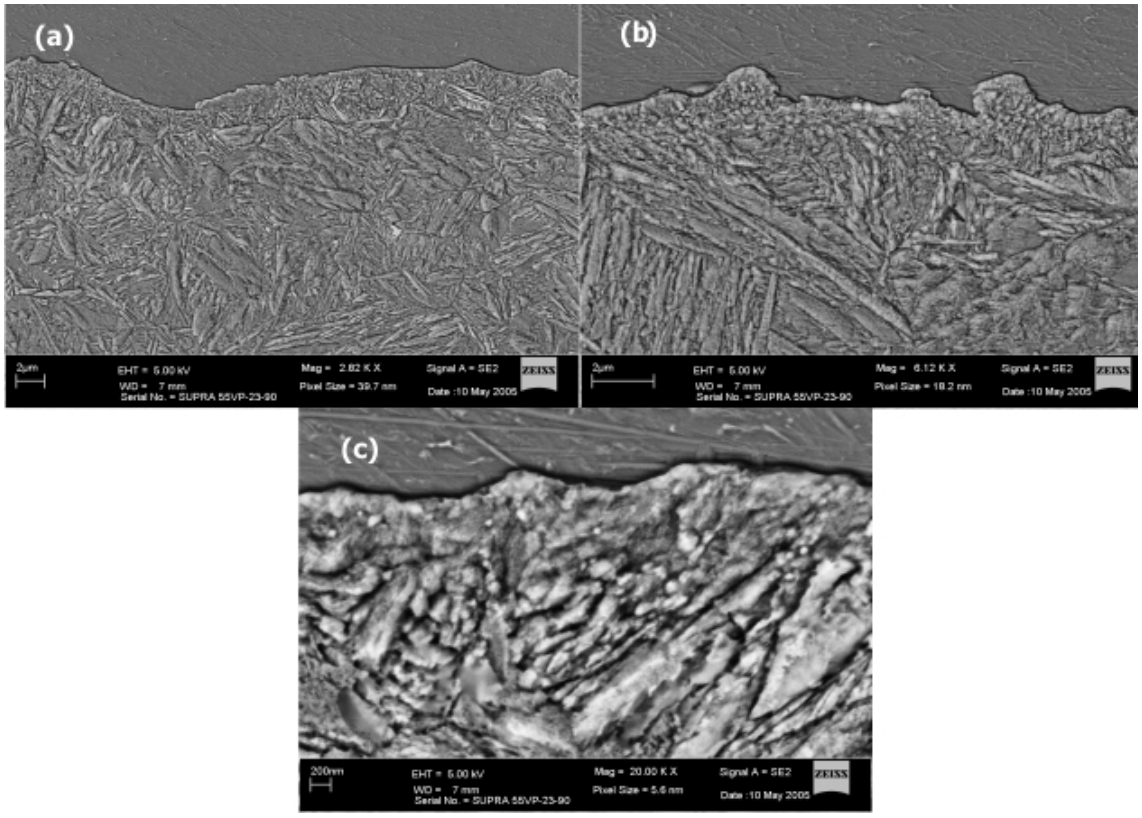

Figure 16 Cross sectional scanning electron micrographs of the EPT-treated surface layer under Condition 3 showing (a) and (b) a two-layered surface structure and (c) high magnification of top layer.

4.4 Microstructure Analysis

To investigate further the structure change caused by EPT treatment, TEM was used to study the fine structure of an EPT-treated specimen as well as the structure variation along its cross section. Figure 17 presents the plan view TEM images of the EPT cleaned specimen surface. It is interesting to note that even at high magnifications, a featureless, membrane-like structure formed on the top surface, Figure 17(a). Electron diffraction patterns, Figure 17(b), taken from this top layer exhibited three diffuse weak rings with a d-spacing of 0.2, 0.14, and 0.114 nm, corresponding to the (110), (200) and (211) plane, respectively, of α-Fe. The diffuse features indicate the existence of short ranged order in this top surface layer. Figures 17(c) and (d) present respectively, the electron diffraction pattern and a high magnification image of the feature that is near the top left corner in Figure 17(a). This feature lies below the top surface layer and is composed of nanosized crystals with a size of 10-70 nm. Its diffraction pattern also exhibits a ring-like morphology with occasional discontinuity. However, the rings are much sharper, indicating a better crystallinity than the top layer. The ring-like

morphology also demonstrates the nanosize of the grains. These rings also correspond to the (110), (200) and (211) plane of α-Fe. The high magnification TEM image, Figure 17(e), demonstrates that the area below the surface layer consists of irregular shaped sub-grains with a size of 10-20 nm. Interestingly, plate-like structures of 10 nm in length and 1-2 nm in width also appear in this region.

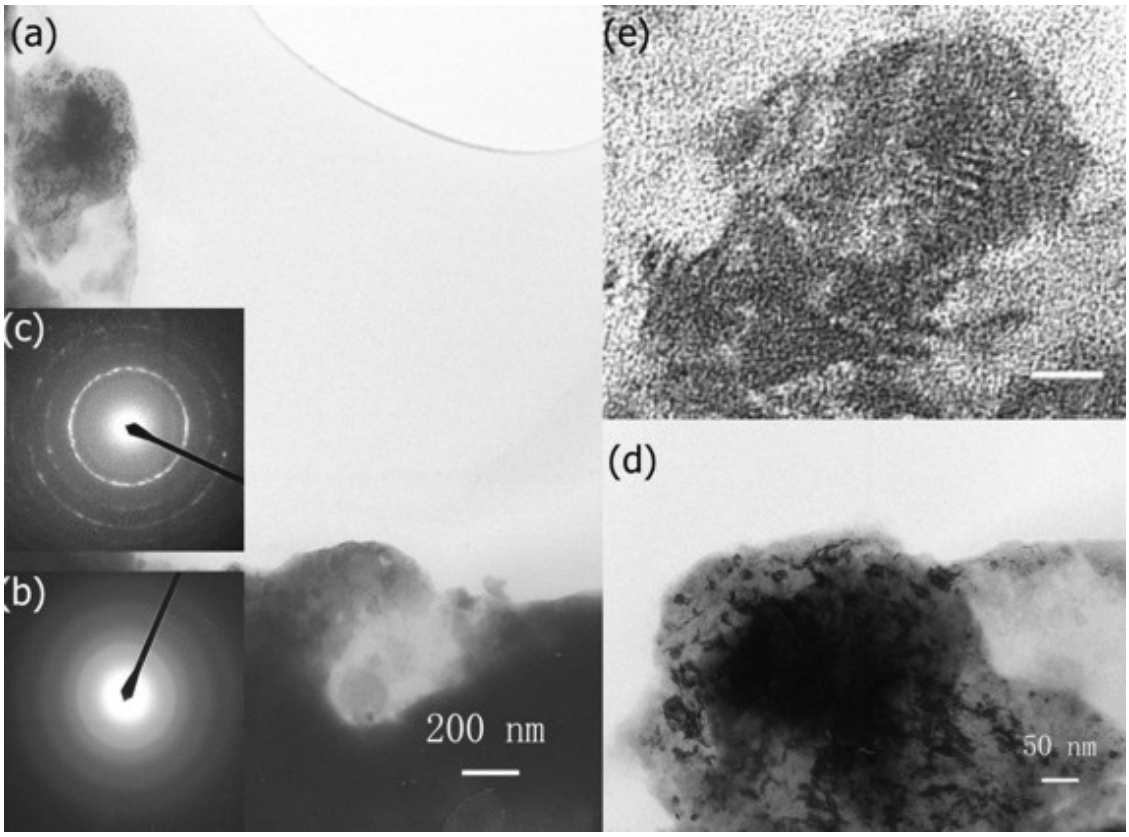

Figure 17 (a) Plan view TEM images of the EPT cleaned surface, (b) diffraction pattern from the membrane area, (c) diffraction pattern and (d) bright field TEM images of the dark area near the up corner at the left hand side of image (a), as well as the (d) hig

Figure 18 presents the bright field, dark field, and the selected area electron diffraction pattern of a region away from the EPT-treated surface (unaffected region). This region was found to consist of coarse needle shaped grains. Figure 18(a) shows a portion of a grain in this region. The width of the grain is measured to be 300 – 500 nm which is consistent with the SEM observations. The diffraction patterns exhibit a series of sharp discontinuous rings, which are designated to the (110), (200) and (211) plane of α-Fe. Two fairly weak continuous rings at a d-spacing of 0.25 and 0.178 nm could also be noted after careful inspection. These two rings correspond to the (200) plane of Fe_3C and the (200) plane of austenite, indicating existence of Fe_3C and austenite phase in the steel. This is also consistent with the aforementioned XRD results. The dark field TEM image, taken using a portion of the (110) plane of α-Fe and the (200) plane of Fe_3C, shows that the needle like structure is a mixture of finely divided ferrite and cementite. This is the typical structure of tempered martensite.

Cross sectional TEM observations, Figure 19(a), showed some characteristic features with a height of about 2 μm, on the top treated layer. After comparing with the surface morphology, it is evident that these features correspond to the interconnected droplet network on the specimen surface. The inset in the figure shows the diffraction patterns from this droplet and is very similar to that observed for the membrane structure, Figure 17. The weak and diffuse rings indicate again an amorphous structure with short range order.

A cross sectional TEM image close to the surface region is shown in Figure 19(b). Clearly, it demonstrates the presence of three different zones with different microstructure, which are named as *molten zone*, *solid-liquid zone* and *recrystallization zone*. The *molten zone* is a part of the droplet structure as shown in Figure 14(a) and is amorphous without any features. The thickness of the *solid-liquid zone* and *recrystallization zone* is about 400-600 nm and 1 μm, respectively. In the *solid-liquid zone*, dark particles with a size ranging between 10-100 nm are present with their

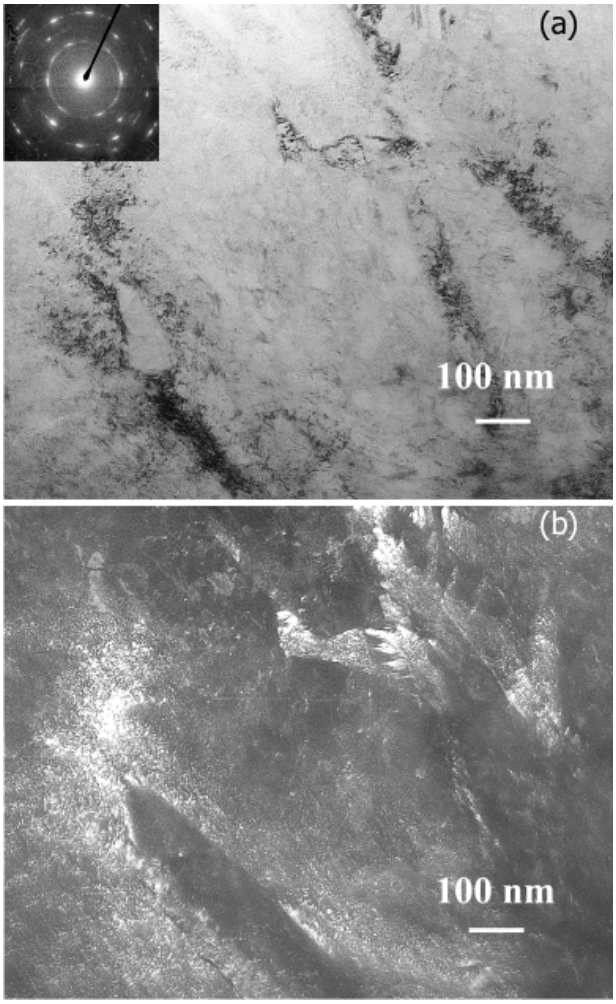

Figure 18 (a) bright field and (b) dark field TEM images of 4340 steel in the unaffected region. Inset shows the corresponding selected area diffraction

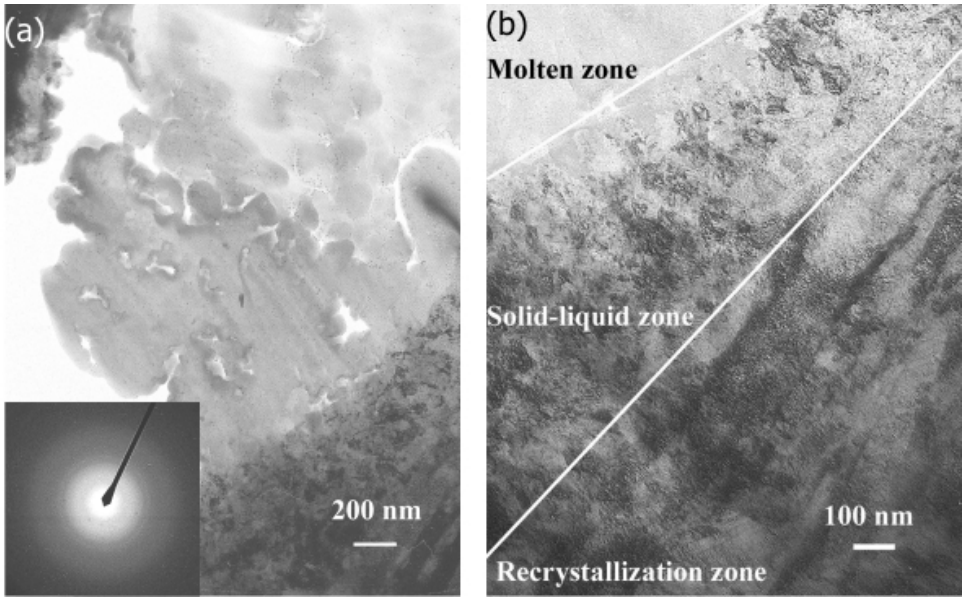

Figure 19 Cross sectional TEM images of (a) the surface region and (b) the near surface region of the EPT-treated sample. The inset in (a) is a diffraction pattern from the feature formed on the surface.

size increasing by moving away from the surface. The *recrystallization zone* exhibits a lath-like morphology with a width of 100-200 nm and length of 500-1000 nm.

Figure 20 shows high magnification bright field and dark field TEM images of the *solid-liquid zone*. The dark areas in the bright field image, Figure 20(a), exhibit a layered morphology with a width of 5-10 nm. Higher magnification observations, Figure 20(d), showed additional details of the layered structure with each layer being around 1-2 nm. The characteristic morphology of these features suggests the presence of ultra fine pearlite that formed during solidification. Interestingly to note that only two sharp diffraction rings, corresponding to the (110) and (211) plane of α-Fe, appears in the selected area electron diffraction pattern, Figure 20(c). No appreciable ring from Fe_3C was observed more than likely due to its small size and limited probe quantity.

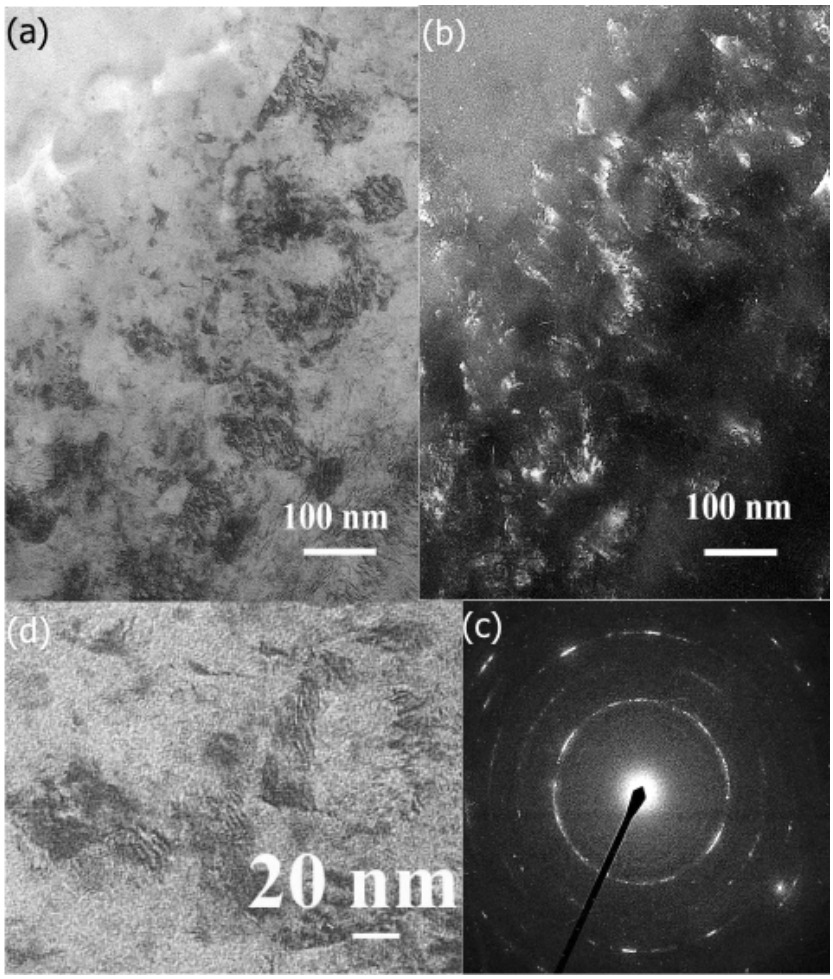

Figure 20 (a) Bright field and (b) dark field TEM images; (c) diffraction pattern of the liquid-solid zone; and (d) high magnification TEM image of a dark area shown in (a).

The *recrystallization zone* was found to compose of a lath structure. Interestingly, high magnification observations showed that the lath in the *recrystallization zone* exhibits a similar layered structure as that found in the *solid-liquid zone*. The thickness and the length of such layered plates are about 2-4 nm and 20-50 nm, respectively. However, some laths, as that shown in Figure 21(b), are composed of irregular arranged elongated particles with a size of about 3-5 nm in thickness and 10-30 in length. The inset in Figure

21(a) is the selected area electron diffraction pattern of the *recrystallization zone*. It is composed of a few sharp discontinuous rings arising from α-Fe. Interestingly, a weak ring corresponding to the (200) plane of Fe_3C could be distinguished after careful inspection, indicating the presence of nanosize Fe_3C particles in the *recrystallization zone*. Thus, the substructure more than likely is composed of fine pearlite that is a little coarser than the one observed in the *solid-liquid zone.*

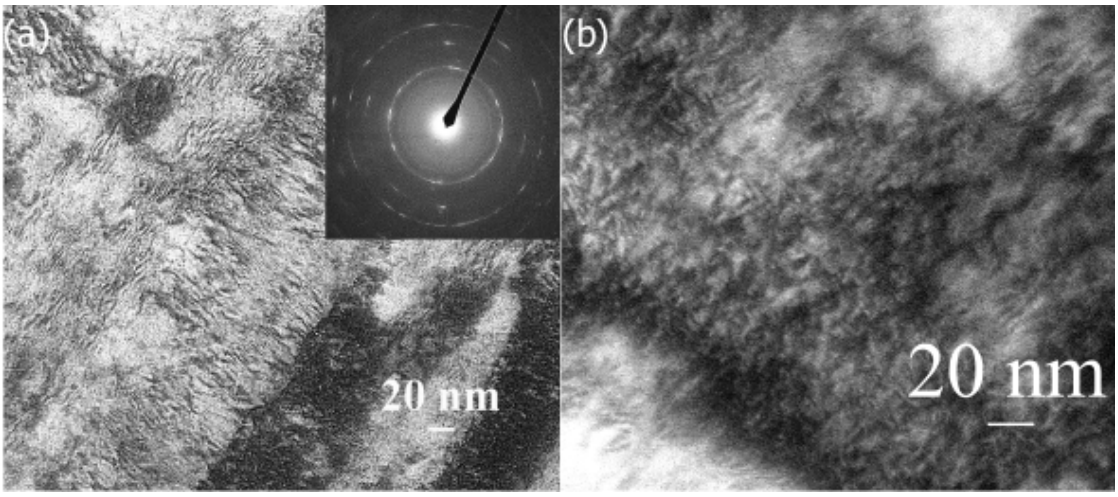

Figure 21 Different morphologies in the recrystallization zone. Inset shows the corresponding selected area diffraction pattern.

4.5 Microhardness Profile

The hardness distribution as a function of depth from the surface was measured using a Vickers microhardness indenter with a load of 25g. The microhardness distribution along the cross section is shown in Figure 22(a). In order to support the EPT-treated surface for the microhardness measurements, a Ni coating with a thickness of about 20 μm was deposited on the sample surface using electroless deposition. As shown, the hardness didn't change significantly with depth, although slightly lower hardness values (about HV 500) were measured in the near surface region as compared to those in

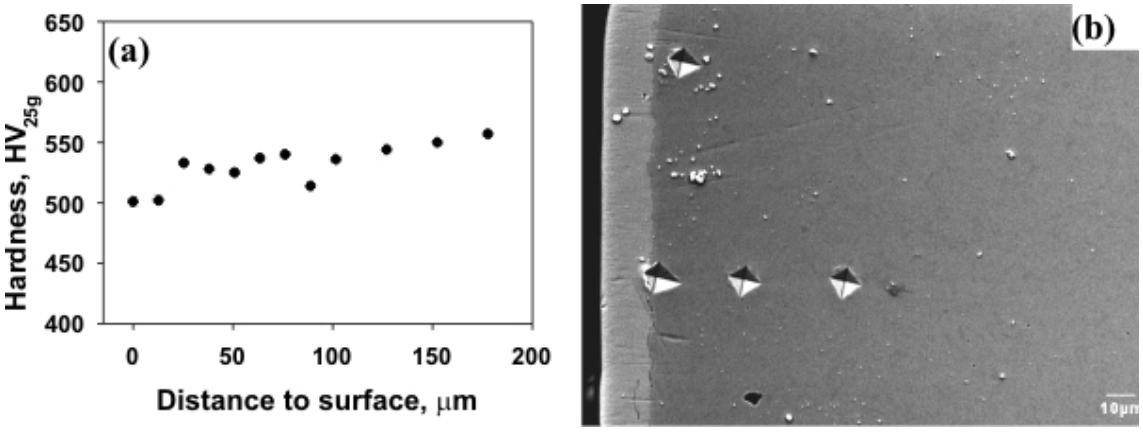

Figure 22 (a) Microhardness profile of EPT-cleaned 4340 steel and (b) scanning electron micrograph showing typical images of indentations.

the center region (about HV 550). It can be seen in the SEM image that the indentations close to the surface are deformed, Figure 22(b). In spite of the support of the hard and thick Ni coating, a longer diagonal length of the pyramid at the direction perpendicular to the surface is shown compared to that parallel to the surface. This may imply a somewhat softer surface layer.

4.6 Internal Stress Analysis

X-ray diffraction is a powerful method for determining phases, grain size, and stress in materials. Figure 23 presents x-ray diffraction patterns of EPT-treated and untreated 4340 steel in the 2θ range of 20-75°. There is no significant change in the diffraction pattern after EPT treatment. There are four broad peaks in this range at the diffraction angle of about 39.8°, 44.5°, 50.6° and 65°. According to the PDF files (#34-0001 and #31-0619), the first and third peaks correspond to the (002) plane of Fe_3C and the (200) plane of austenite, respectively. The short range XRD spectra, Figure 23(b), show that the second peak for the untreated sample is at 44.45°, which is smaller than the (110) peak, 44.67°, of α–Fe, but greater than the (101) peak, 44.18°, of martensite. However, the broad peak could be an overlap of the (101) and (110) peaks from BCT martensite and the (110) peak from α–Fe with BCC structure, indicating a tempered martensitic structure. For the EPT-treated sample, this peak shifts to a higher 2θ angle, 44.6°, which fits well with the (110) plane of α–Fe. As the penetration depth of x-rays in ferrite is only 2 μm, only the surface layer shown in Figure 16 contributes to the pattern for the EPT-treated sample. Thus, the structure changes from tempered martensite to α–Fe upon EPT treatment. In addition, there is an obvious shoulder at a 2θ angle of 43.7° in both curves as shown in Figure 23(b). This could arise from the overlap of the (102) peak of Fe_3C and the (111) peak of austenite.

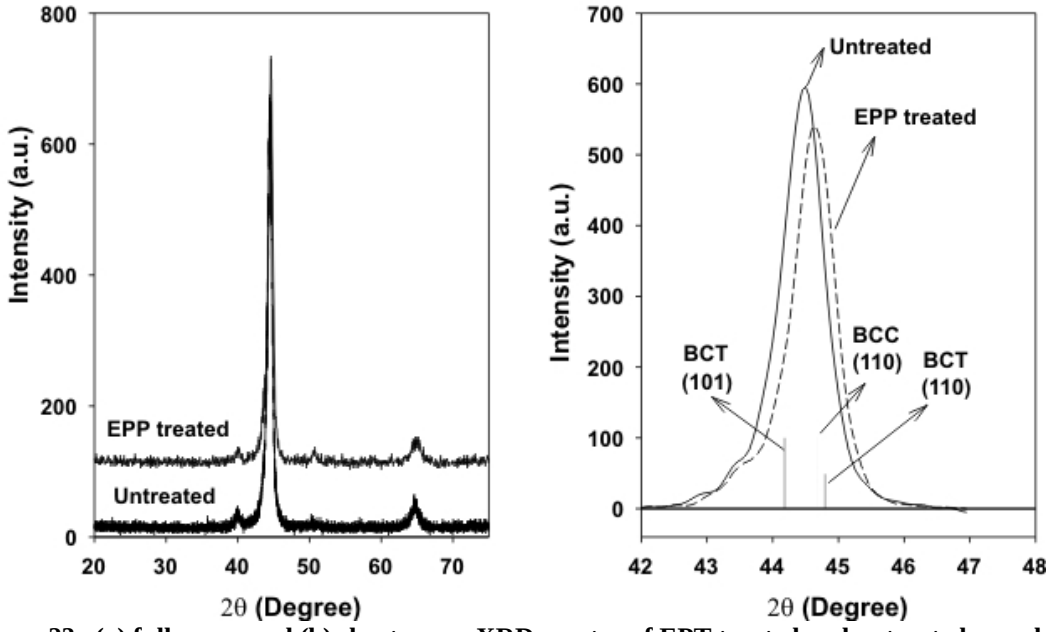

Figure 23 (a) full range and (b) short range XRD spectra of EPT treated and untreated samples.

In order to ascertain the phase structure at different depths, the glancing angle XRD technique was utilized. In this case, the penetration depth of x-ray diminishes with decreasing the angle of incidence. During the measurement, the incidence angle was fixed while the 2θ angle changed from 42° to 47°. It is interesting to see that the diffraction peak becomes broader and shifts to a lower diffraction angle with reducing the glancing angle. Figure 24(a) presents the peak center position and full width at half maximum (FWHM) of the (110) peak as a function of the glancing angle. The (110) peak center position decreases linearly with reducing the glancing angle, while the FWHM of the (110) peak increases linearly with reducing glancing angle down to 1° followed by a rapid increase. The grain size at different glancing angle was computed using the Scherer equation:

$$d = \frac{0.9\lambda}{B\cos\theta}$$

where d is the diameter of the grain, B is the FWHM of the diffraction peak, and θ is half of the diffraction angle. Meanwhile, the penetration depth (D_θ) of x-ray at different glancing angle (α) could be calculated by

$$D_\theta = 2\sin(\alpha)/\sin(22.5).$$

The grain size at different depth is plotted in Figure 24(b). It shows two distinct regions: top layer and subsurface layer. In the top layer (about 200 nm thick), the grain size is fairly small, but it increases rapidly with increasing depth. In the subsurface region, the grain size increases slowly, but monotonically with increasing depth. This is consistent with the SEM observations. It should be noted that the grain size calculated from the FWHM of the XRD peaks measured at higher glancing angles should be larger than the value shown in Figure 24 because both the surface region and sub-surface region contribute to the XRD pattern. Cross sectional TEM is necessary to obtain direct information about the change of grain size along cross section. As discussed about, the ultra-small grain size in the surface region could result from the rapid freezing of the local melting produced by the process. More than likely, the gradient of the temperature is responsible for the gradual change of the grain size.

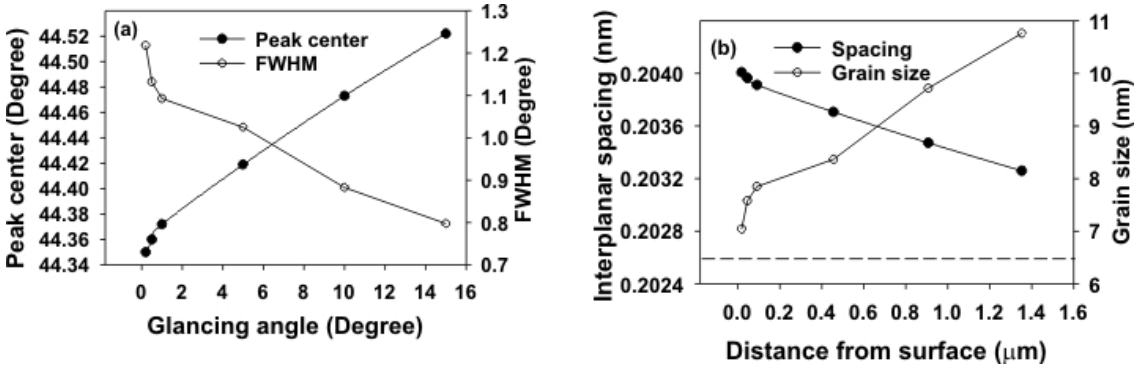

Figure 24 (a) Dependence of the peak center and FWHM of the XRD peak on the x-ray glancing angle and (b) calculated depth profile of interplanar spacing and grain size.

Interplanar spacing was obtained from the positions of the diffraction peaks using Bragg's law. The interplanar distance and grain size at different distance from the surface were calculated and also plotted in Figure 24(b). The dotted line in the graph is

the interplanar distance of α-Fe obtained from PDF standard files. It can be seen that the interplanar distance decreases linearly with increasing distance from surface. The larger interplanar spacing in the near surface region indicates the presence of a higher compressive stress, and the decrease of interplanar spacing implies a reduction of compressive stresses with depth.

In order to investigate the existence of a compressive stress and obtain qualitative information about the internal stress in the EPT-treated surface layer, the standard $d_{hkl}(\psi)$ *versus* $sin^2(\psi)$ method was used to measure the internal stress. For the stress measurement, the (310) ferrite reflection was used due to its high diffraction angle (about 116.4°) and relatively high intensity. During measurement, the sample surface was tilted 0-30° (ψ angle) and a θ-2θ scan was conducted in the 2θ range of 110-120°. The calculated $(d_\psi - d_0)/d_0$ *vs* $sin^2(\psi)$ is plotted in Figure 25. As shown, the $(d_\psi - d_0)/d_0$ decreases linearly with increasing $sin^2(\psi)$, indicating a compressive stress. According to the $sin^2(\psi)$ method, for cubic structures the stress (σ) in a thin layer in a state of equi-biaxial stress could be computed by the following equation

$$\frac{d_{hkl}(\psi) - d_0}{d_0} = \sigma[\frac{1+\nu}{E}\sin^2(\psi) - \frac{2\nu}{E}],$$

where d_0 is the stress-free lattice parameter, $d_{hk}l(\psi)$ is the lattice spacing measured with surface tilted ψ angle, ν and E are the Poisson's ratio and elastic modulus, which are 0.29 and 200 GPa for 4340 steel, respectively. From this equation, the internal stress in the surface layer can be calculated after obtaining the slope of the $(d_\psi - d_0)/d_0$ vs. $sin^2(\psi)$ plot. The internal stress is calculated to be -1.8 GPa. The negative sign indicates that the stress in the surface layer is compressive.

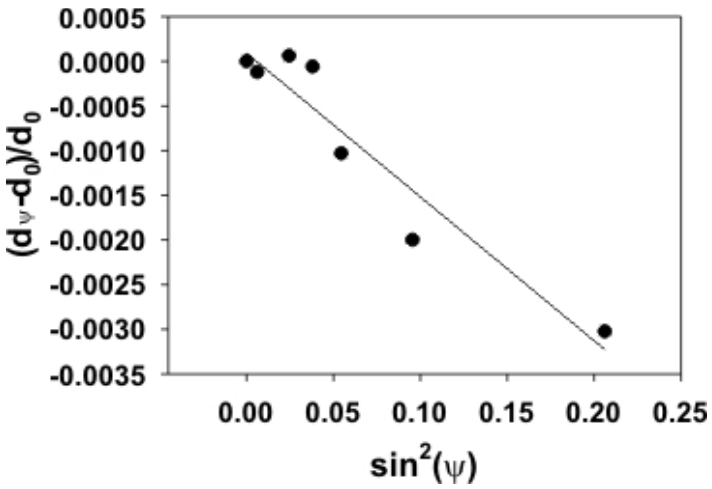

Figure 25 Fig. 25 (d -d0)/d0 vs. sin2( ) plot for the (310) ferrite reflection.

4.7 Hydrogen Content Analysis

The hydrogen content at the surface region of the electrolytic plasma processed 4340 steel cleaned under three different conditions and untreated steel was measured using the NRA method. The influence of the electrolyte on the hydrogen content was also studied. Figure 26 presents the H variation as a function of depth for untreated 4340 steel (base line) and EPT-treated 4340 steel in $NaHCO_3$ solution for 10 s and 30 s. It is evident that for the 10 s treatment the two profiles are merely the same showing that the EPT treatment does not increase the H content in the surface region. The higher H content at

the surface is an effect caused by humidity and is typically observed in many materials. The profile for the specimen cleaned under *Condition 2* shows a somewhat higher H content for a depth of about 100 nm from the surface. Beyond that, both profiles remain the same. The slight difference in H content between *Condition 1* and *Condition 2* can be attributed to longer treatment time and higher voltage used in *Condition 2*. A longer treatment time is expected to increase the interaction between the plasma and the surface whereas a higher voltage is expected to influence the chemical species in the plasma and may have an effect on the amount of H that may be trapped in the surface region.

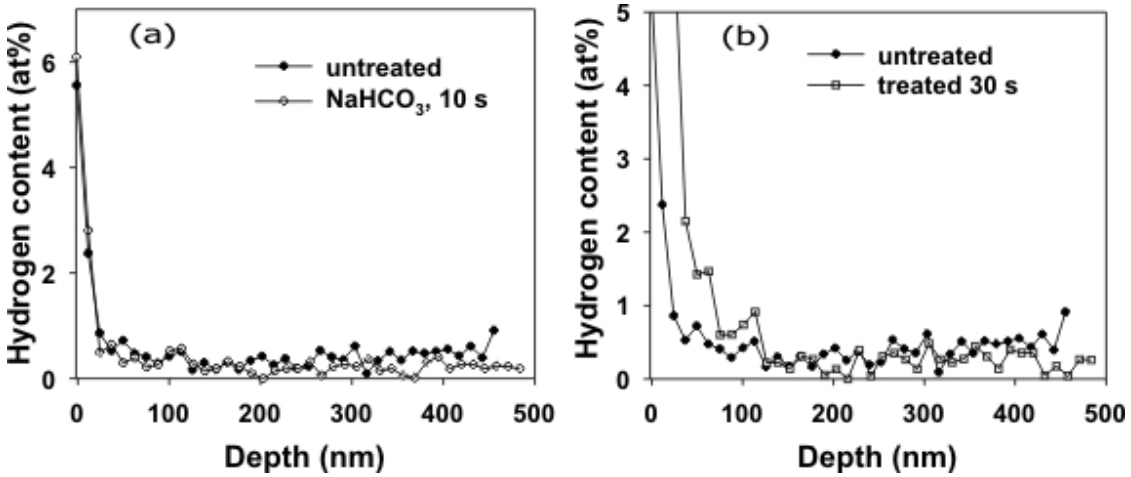

Figure 27 Depth profile of hydrogen content in 4340 steel treated in NaHCO3 under Condition 1 and Condition 2.

The H profile for the specimen treated under *Condition 3* was similar to that treated under *Condition 2*, Figure 27. It exhibited a thin layer of about 200 nm with a somewhat higher H content. Beyond that depth, the profiles of treated and untreated specimens were merely the same. Even though a direct comparison cannot be made due to different treatment processing time involved, the profile in Figure 27 seems to indicate that the type of electrolyte may also be important.

Thus, the H analysis indicates that processing conditions in terms of applied voltage and type of electrolyte affect the plasma characteristics that in turn may influence the H interaction with the surface of the material. However, it is important to note that the layer/region with higher H content is very small (100-200 nm from the surface) and the amount of H in this region is

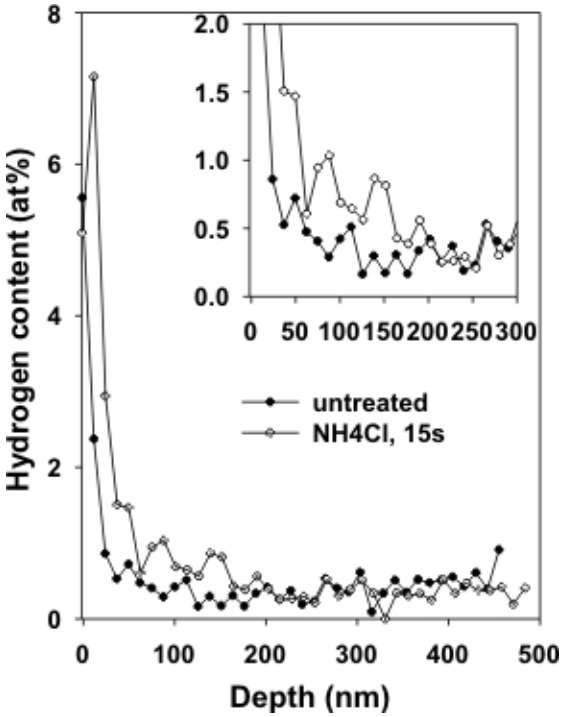

Figure 26 Hydrogen depth profile in 4340 steel treated in NH4Cl under Condition 3.

also limited (~0.5-1 at% higher than the untreated concentration). Taking both of the above factors together, it is evident that the total amount of H is probably insignificant.

4.8 EPT Cleaning of HE Specimens

In this stage of the project, EPT cleaning was conducted in notched HE specimens. There was concern that the cleaning action may have not reached the root of the 60^o notch thus, additional cleaning experiments were conducted using specimens with a wider notch to resolve any possible HE issue. Twenty HE specimens with 60° angle notch were received. Ten of these specimens were sent for center less grinding to open the angle of the notch to 90°. The root of the notch was not touched while grinding. The objective was to clean the HE specimens with 90° notch by EPT, and analyze the quality of the cleaning at the root of the notch. Some "dummy" HE specimens were also manufactured, using a lathe, with 60° and 90° notches to establish the plasma conditions on the EPT unit. Five HE specimens (three with 90^o groove and two with 60^o groove) were processed under various conditions shown below and analyzed using SEM and EDS.

HE06-1	90^o groove	140V, ~ 5A, 0.3GPM, 80 rpm (rotation), 30 sec
HE06-2	90^o groove	140V, ~ 5A, 0.3GPM, 40 rpm (rotation), 30 sec
HE06-3	90^o groove	175V, ~ 5A, 0.3GPM, 80 rpm (rotation), 30 sec
HE06-4	60^o groove	175V, ~ 5A, 0.3GPM, 80 rpm (rotation), 30 sec
HE06-5	60^o groove	140V, ~ 5A, 0.3GPM, 80 rpm (rotation)$^+$

$^+$ ran for many minutes. This sample was used to establish the plasma.

SEM/EDS analysis at the root of the notch for the 90^o groove specimens showed very low oxygen content that was comparable to that at the outer specimen surface showing that cleaning had taken place, Figure 28. For all cleaned specimens the O and C content is significantly reduced as compared to as-received specimens, Table 3. Also, in the specimens with 90^o groove, the C and O content in the root of the notch was significantly less compared with the 60^o groove. Thus, opening the notch angle allowed access of the plasma to the root of the notch.

Table 3 EDS results from the root of the notch of EPT-cleaned specimens.

		C		Fe		O	
		wt%	at%	wt%	at%	wt%	at%
Untreated sample		5.45	16.21	79	51.06	14.67	32.73
HE06-1		0.35	1.54	97.85	92.52	1.8	5.94
HE06-2		0.72	3.07	96.67	88.59	2.61	8.34
HE06-3		0.73	3.07	96.37	87.7	2.91	9.23
HE06-4		1.85	7.19	92.9	77.5	5.25	15.3
HE06-5		1.18	4.64	93.6	79.8	5.22	15.53

The root of the notch was analyzed in the processed specimens and it was decided to process the HE specimens with condition HE06-1 and HE06-3. Three specimens were treated with each condition (total 6 specimens). The processed samples were shipped and

tested for HE at Anachem Laboratory. All specimens passed the test: 75% NFS (Notch Fracture Strength), 200 hours. Specimens were step loaded up to 95% NFS where rupture occurred at the notch while all specimens survived 90% test.

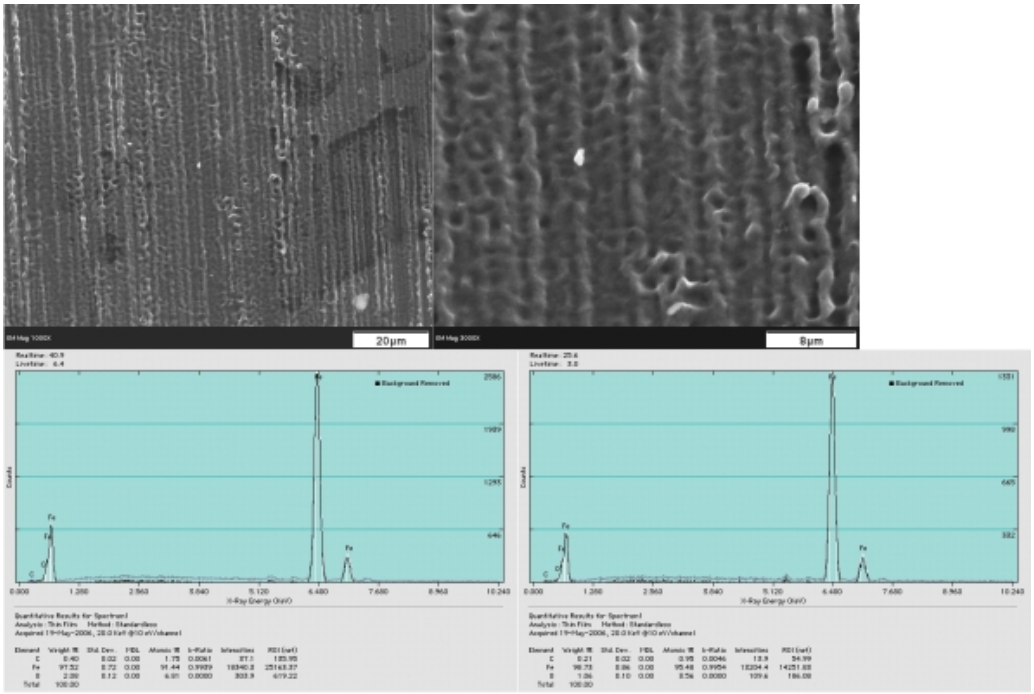

Root of the notch:

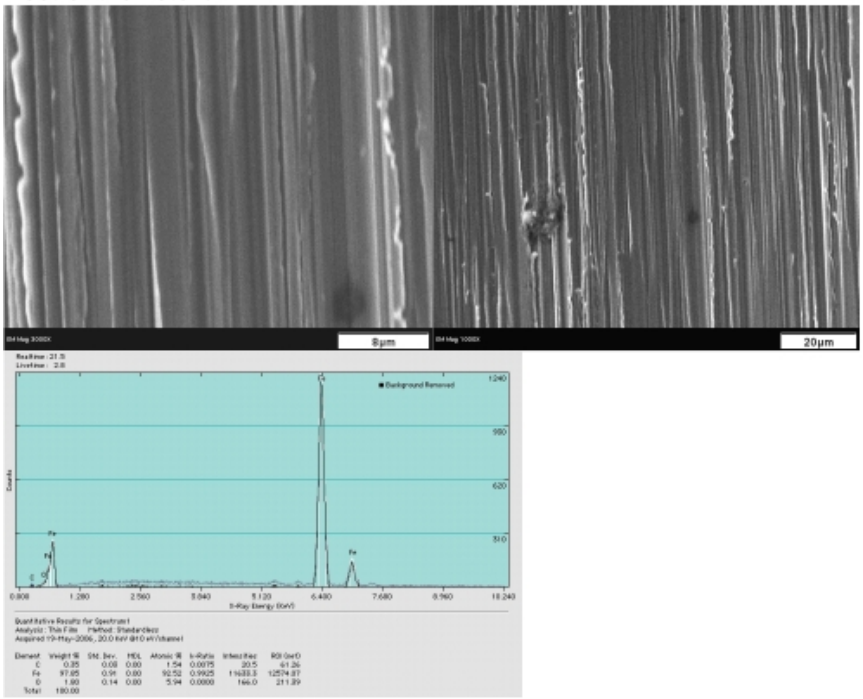

Figure 28 Morphology and EDS analysis of surface and root of the notch of EPT-cleaned specimens prepared for HE testing.

4.9 EPT Cleaning of Fatigue Specimens

EPT-cleaned specimens that were processed initially showed a small fatigue debit. This was attributed to either surface softening (removal of carbon from the near surface region) or surface roughening (causing stress concentration at valleys) occurring during treatment. Currently, Cd coated components are typically shot peened prior to coating. Thus, a similar treatment was applied to a set of fatigue specimens in order to compare EPT processing on the same base. Forty shot peened fatigue test specimens were received. Ten specimens were cleaned by EPT under the same conditions as the HE specimens and shipped to Metcut Research, Inc. for fatigue testing. Figure 29 shows the EPT-cleaned specimens. It was found that shot peened and EPT-cleaned specimens exhibit affordable fatigue behavior without major debit.

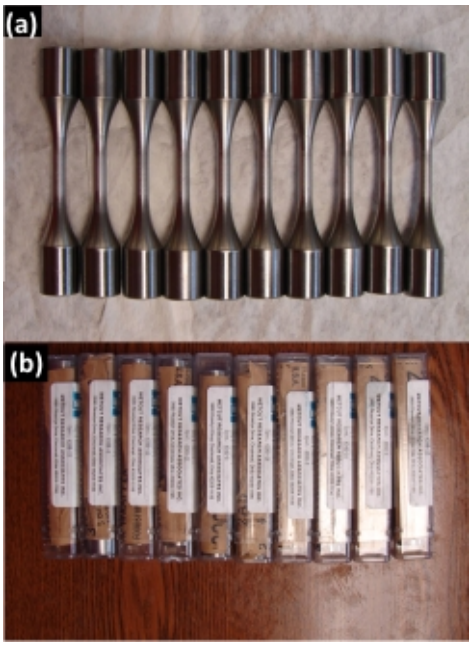

Figure 29 Fatigue specimens: (a) EPT cleaned; and (b) Packed for shipping to Metcut Research, Inc.

5. Coating Treatments

5.1 Zn Coatings

Coatings of metallic Zn have generally been regarded as the most popular and economical means of protecting iron and steel products from corrosion because Zn acts as a sacrificial anodic coating. If the coating is damaged, Zn will be anodic to iron and steel, and will preferentially corrode providing protection. Generally, Zn coatings are produced on iron and steel products in industry by hot dip galvanizing, continuous line galvanizing, electro-galvanizing, zinc plating, mechanical plating, and zinc spraying. However, all these techniques have, more or less, the environmental and work safety problems, such as emission of toxic vapors and waste poisonous streams, as well as the elevated processing temperature.

Zn coatings were deposited using an electrolytic bath with 23 % $ZnSO_4.7H_2O$. Processing voltage, current, flow rate, and temperature was 150-180 V, 25-30 A, 3.2 lit/min, and 75-80 °C, respectively.

Visually, the Zn coatings appear dull gray in color with a matte finish. Under SEM, at low magnification, Figure 30(a), the coating surface exhibits a faceted pyramidal-shaped cluster with a size of about 200-500 nm. However, high magnification images, Figure 30(b), show that these clusters are composed of densely packed nanoparticles with a size of about 15 nm.

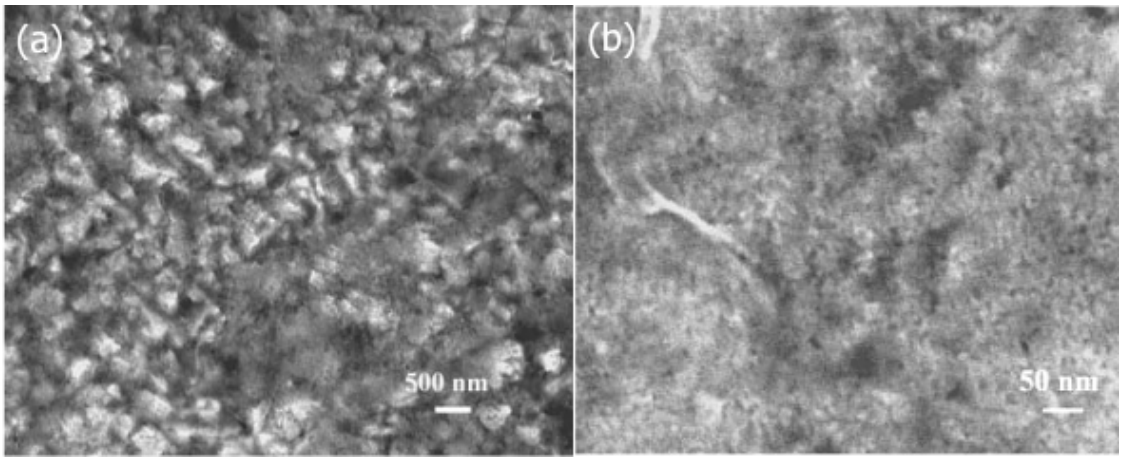

Figure 30 Typical SEM images of EPT-deposited Zn coating.

During deposition, Zn^{2+} ions are predominantly transported to the steel surface through the collapse of the hydrogen bubble on which the ions ride. The rapid collapse of the hydrogen bubble during EPT deposition corresponds to an extremely high transportation rate for Zn^{2+} ions. An instantaneous super-saturation condition for Zn^{2+} ions will form on the steel surface, corresponding to a high nucleation rate, thus the nuclei don't have enough time to grow before a new nucleus forms on its surface. As a consequence, nanocrystalline Zn coatings form.

To evaluate the cross sectional structure of the Zn coatings, FIB studies were conducted. Figure 31 illustrates the cross sectional FIB secondary electron image of the Zn coating. It is interesting to note in the low magnification image, Figure 31(a), that the Zn coating consists of two layers: a dense base layer with a thickness of about 1-2 μm and a porous top layer with a thickness of about 2-3 μm. The formation of the porous top layer is believed to result form the collapsing of the bubbles as well as the degassing of the gases encapsulated in the Zn coating. In the EPT processing, hydrogen plasma continuously forms on the growing coating surface. The extremely high temperature of the plasma will melt the previously deposited Zn coating, eliminating voids in the Zn coating, and, therefore, leading to the formation of dense base layer. The existence of an obvious interface between those two layers further supports the aforementioned suggestion. The high magnification image, Fig. 31(b), demonstrates that the base layer is composed of nanocrystals with a size of about 12-50 nm, and thus the Zn coating is strongly bonded to the steel substrate. No obvious defects exist in the interface between Zn coating and steel substrate. The formation of nanocrystals results more than likely from the nonequilibrium quenching process of the molten Zn coating.

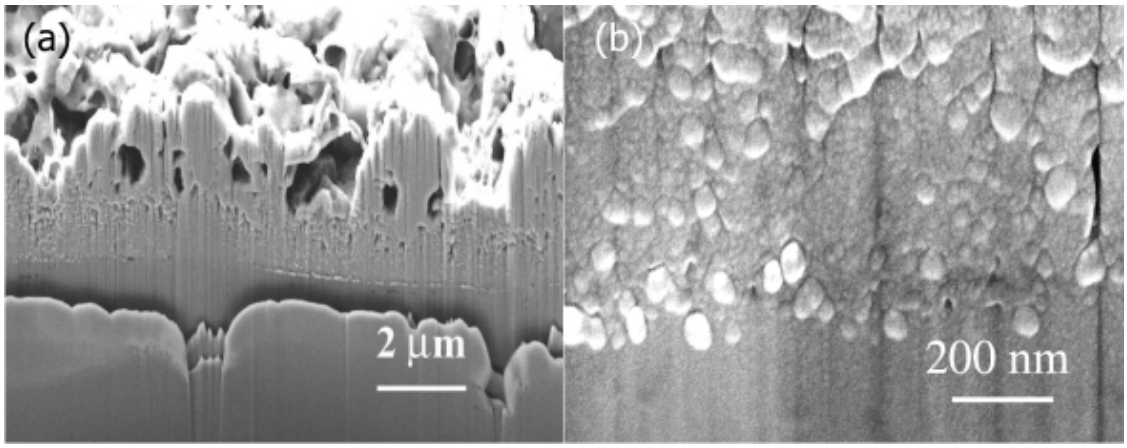

Figure 31 Typical cross sectional FIB images of EPT deposited Zn coating.

TEM was used to further explore the crystalline structure and microstructure of the Zn coatings. Plan view TEM, Figure 32, shows that the Zn coatings consist of irregular shaped clusters with a size of about 50-300 nm. However, high magnification dark field TEM, Figure 32(b), demonstrates that those clusters are comprised of nanosized Zn crystals with a size of 5- 20 nm. The inset in Figure 32(b) presents the selected area electron diffraction pattern of the Zn coating in which there are four rings with a d-spacing of 0.26, 0.24, 0.21, and 0.16 nm, corresponding to the (002), (100), (101), and (102) plane of Zn with a hexagonal crystal structure, respectively. The ring like feature of the diffraction pattern indicates the small size of the Zn grains.

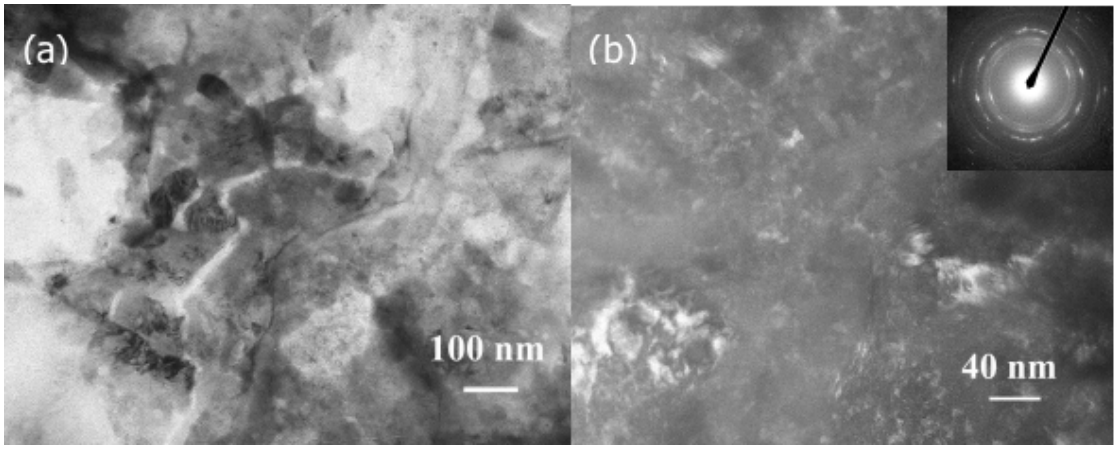

Figure 32 Plan view (a) bright field and (b) high magnification dark field TEM images of a Zn coating. Inset shows the corresponding selected area electron diffraction pattern.

Figure 33 provides cross sectional TEM images of the Zn coating. As shown in Figure 33(a), the Zn coatings are comprised of columnar like clusters with a size of about 350-550 nm. This is consistent with the SEM observations. High-resolution bright field and dark field TEM images demonstrate that the clusters are composed of nanosized sub-columns with a size of 22-40 nm. Also, the sub-columns consist of nano-grains with a size of 5-20 nm. The electron diffraction pattern shown in Figure 33(b) as an inset, indicates that the deposited Zn coatings have a hexagonal crystal structure.

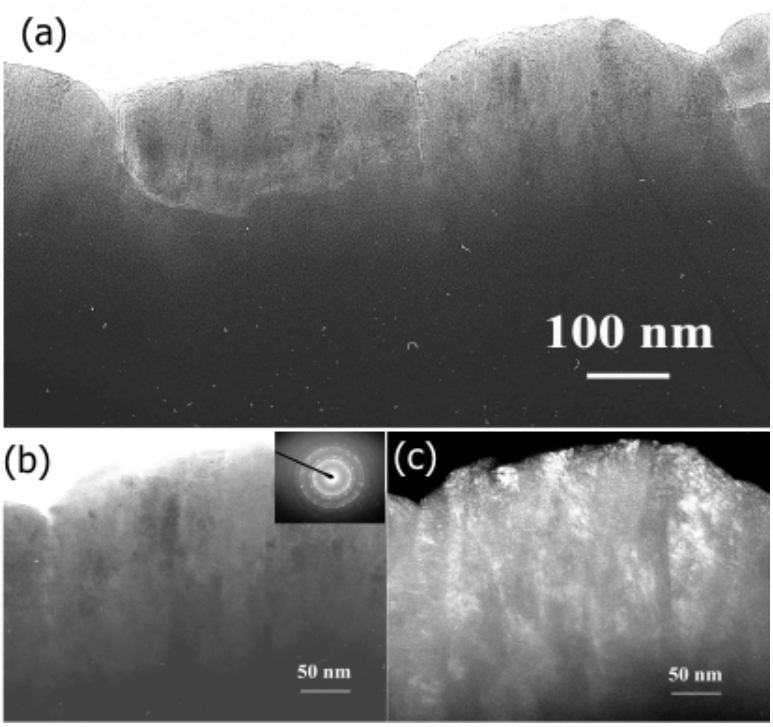

Figure 33 Typical cross sectional TEM images of a Zn coating (a) low magnification, (b) high magnification bright field and (c) dark field. Inset shows the electron diffraction pattern.

A standard XRD θ-2θ scan was performed to ascertain the crystal structure of the Zn coatings. Figure 34(a) depicts the typical XRD pattern of the Zn coating. According to the PDF files, as shown, the peaks could be indexed to Zn with a hexagonal structure and Fe with a BCC structure. The peaks from Fe arise from the steel substrate. It is interesting to note that the intensity ratio of the (101) peak to (002) peak is 9.97, which is much higher than the ratio of 1.89 from randomly oriented Zn powder (JCPDS #04-0831). This indicates that the Zn coatings exhibit a (101) preferred orientation.

In addition, a 2θ scan with a fixed glancing angle of 0.5-15° was conducted to investigate the phase structure of the coatings at different depth because the penetration depth of the X-ray decreases with reducing glancing angle. Figures 34(b) and (c) exhibit the typical XRD patterns at a glancing angle of 5 and 1°, respectively. As compared with the XRD pattern from the θ-2θ scan, the relative intensity of the peak from Fe decreases with reducing glancing angle, and eventually disappears at a glancing angle below 1°, indicting a gradient distribution of the α-Fe phase over the cross section of the Zn coating. Furthermore, a gradual broadening of the peak from Zn is unambiguously observed with reducing glancing angle. To quantify the change of the peak position and width with glancing angle, the XRD (101) peak of Zn from different glancing angle was fitted with Gaussian function. There is no significant change in the peak position, while the FWHM of the (101) peak of Zn increases almost linearly from 0.19 to 0.57 ° as the glancing angle is reduced from 21.6 to 0.5°, as shown in Figure 35. It is well accepted that the broadening of the XRD peak could result from the decrease of the grain size or the strain in the coating. The grain size could be calculated using Scherer equation: $d = \frac{0.9\lambda}{B\cos\theta}$, where d is the diameter of the grain, B is the FWHM of the diffraction peak, and θ is half of the diffraction angle.

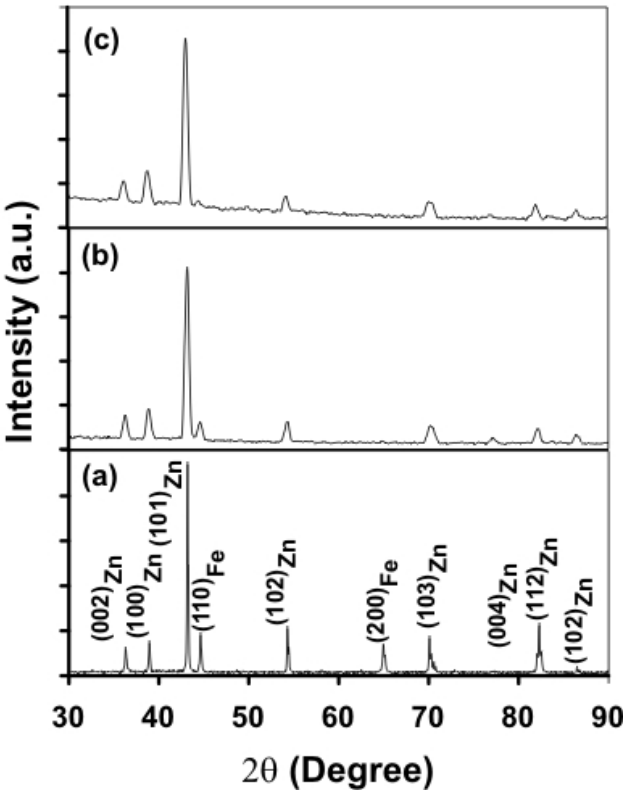

Figure 35 XRD patterns of Zn coatings from (a) a θ-2θ scan and a 2θ scan with a glancing angle of (b) 5 and (c) 1°, respectively.

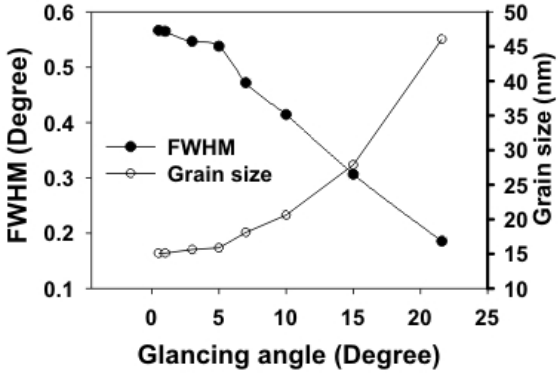

Figure 34 Dependence of the FWHM of the (101) peak of Zn and the calculated grain size of Zn coating on the glancing angle.

The calculated average grain size at different glancing angle is also shown in Figure 35. At a glancing angle of below 5°, the grain size of the Zn coating is only about 15 nm. At such a small glancing angle, only the top surface of the Zn coating contributes to the XRD pattern, implying the nano size of the grain on the top surface layer of the Zn coating. This is consistent with the grain size measured by TEM. The gradual increase of the grain size with glancing angle indicates a gradual increase of grain size with depth.

The internal stress in the EPT-deposited Zn coatings was measured by a standard $d_{hkl}(\psi)$ versus $sin^2(\psi)$ method using XRD, where ψ is the angle between the diffraction plane and the sample surface and $d_{hk}l(\psi)$ is the lattice spacing measured at different ψ angle. In this study, the (114) Zn reflection was used. A θ-2θ scan was performed in the 2θ range of 112-120 ° at different ψ angle of 0-30°. Figure 36 present the $(d_\psi-d_0)/d_0$ vs $sin^2(\psi)$ curve, which exhibits a slight but linear increase of $(d_\psi-d_0)/d_0$ with $sin^2(\psi)$, indicating the existence of small tensile stress in the Zn coating. According to the $sin^2(\psi)$ method, for cubic structures, the stress (σ) in a thin layer in a state of equi-biaxial stress could be computed by the following equation:

$$\frac{d_{hkl}(\psi)-d_0}{d_0}=\sigma[\frac{1+\nu}{E}\sin^2(\psi)-\frac{2\nu}{E}],$$

where d_0 is the stress-free lattice parameter, ν and E are the Poisson's ratio and elastic modulus, which are 0.35 and 96.5 GPa for Zn, respectively. By getting the slope of the $(d_\psi-d_0)/d_0$ vs. $sin^2(\psi)$ plot, the internal stress in the Zn coating was calculated to be only 108 MPa. The positive sign indicates that the tensile nature of the stress in the Zn coatings, which is common for metallic films or coatings deposited by different techniques.

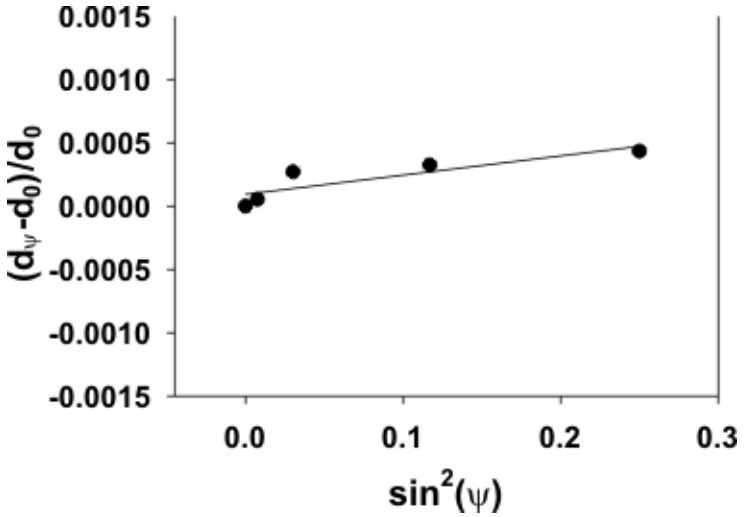

Figure 36 (d_ψ-d0)/d0 vs. sin2(ψ) plot for the (114) Zn reflection.

5.2 Zn-Al and Al Coatings

Zn-Al coatings, especially Al-rich or pure Al coatings, are very attractive for corrosion protection of steels. In the present study, screening deposition experiments were conducted first to identify the relationship between deposition parameters and ability to produce Al-rich coatings.

5.2.1 Screening Deposition Experiments

(a) Zn-Al Coatings

Zn-Al coatings were deposited using an electrolytic bath with 23 % $ZnSO_4.7H_2O$ and $Al_2(SO_4)_3.14H_2O$. Steel wires with a diameter of 1.6 mm were used as substrate. Different combinations of anode material and electrolyte bath composition were used for Zn-Al coating deposition. The detailed deposition parameters associated with electrolytic bath and deposition are shown in Table 4. The amount of Al salt in the electrolyte was increased up to 99% relative to Zn salt, keeping the total concentration of the salt ~ 23%. No compensation was given for Zn depletion due to deposition of coating, so Al/Zn ratio shown in Table 3 may be higher than indicated as per electrolyte composition due to preferential deposition of Zn. Also, in case of Al anode tests, dissolution of Al anodes may have increased Al content in the electrolyte even higher. Depositions were conducted at the lowest possible voltage allowed by the anode-electrolyte combination.

Table 4 Parameters associated with electrolytic bath and deposition.

Sample	Gas Through the Seals	Anode Material	Bath Condition			Processing Parameters*		
			Al Salt	Zn Salt	Al/Zn	Voltage, V	Current , A	Time, Sec
Zn-Al 0.3[+]	**Air**	**Ni**	**92.5**	**7.5**	**4.9**	**145**	**25-30**	**22.5**
Zn-Al 1.3	**Air**	**Al**	**92.5**	**7.5**	**4.9**	**150**	**28**	**22.5**
Zn-Al 2.3	**Air**	**Al**	**95**	**5**	**7.6**	**155**	**20 -25**	**22.5**
Zn-Al 3.3	**Air**	**Al**	**97.5**	**2.5**	**15.6**	**190**	**20**	**22.5**
Zn-Al C1.3	**Air**	**Graphite**	**97.5**	**2.5**	**15.6**	**150**	**23**	**22.5**
Zn-Al C2.5	**Air**	**Graphite**	**99**	**1**	**39.5**	**160**	**20**	**37.5**
Zn-Al Ni1.5	**Air**	**Ni**	**99**	**1**	**39.5**	**160**	**20**	**37.5**
Zn-Al Ni2.5	**Air**	**Ni**	**97.5**	**2.5**	**15.6**	**150**	**20**	**22.5**
Zn-Al Ni3.3	**Ar**	**Ni**	**97.5**	**2.5**	**15.6**	**160**	**20**	**22.5**

[+] Zn-Al 0.3 is the sample that had Al ~1.37 wt% (~ 3 at%)

* For each specimen other processing conditions were same: electrolyte temperature 75 – 85 ^oC, flow rate 3.2 lit/min.

The surface morphology and the composition of the Zn-Al coatings were investigated by SEM and EDS. Table 5 presents the composition of the deposited Zn-Al coatings. EDS analysis showed a high Fe content which is contributed from the substrate due to the small thickness of the coating. To obtain clearly the impact of different

parameters on the coating composition, the interaction of the substrate contribution has been removed from the EDS analysis. In general, the increase of Al salt content from 92.5% to 99% leads to a significant decrease in the Zn/Al ratio. No obvious conclusion can be drawn for the influence of the anode materials on the change of the Zn/Al ratio in the coatings. High content of Ni was detected in the coatings deposited from Ni anode. In addition, high oxygen content was observed in all coatings.

Figures 37 and 38 illustrate the surface morphology of the Zn-Al coatings. It is obvious that all the coatings with high Zn content are porous and consist of faceted crystalline clusters. On the contrary, the coatings with high Al content exhibit a dense amorphous like morphology.

Table 5 Composition of the coated surface

Sample	Composition of the Coated Surface (At %)					
	O	Al	S	Ni	Zn	Zn/Al
Zn-Al 0.3^{+}	21.90	3.10	1.50	12.50	61.10	19.71
Zn-Al 1.3	20.05	1.05	1.15	0.00	77.75	74.05
Zn-Al 2.3	49.53	5.80	3.27	0.00	41.47	7.15
Zn-Al 3.3	64.35	13.50	4.85	0.00	17.35	1.29
Zn-Al C1.3	23.00	2.40	0.95	0.00	73.70	30.71
Zn-Al C2.5	83.67	12.73	1.97	0.00	1.53	0.12
Zn-Al Ni1.5	65.00	7.15	3.30	14.55	9.95	1.39
Zn-Al Ni2.5	30.00	4.25	1.10	12.70	52.00	12.24
Zn-Al Ni3.3	34.50	5.87	1.80	16.00	41.90	7.14

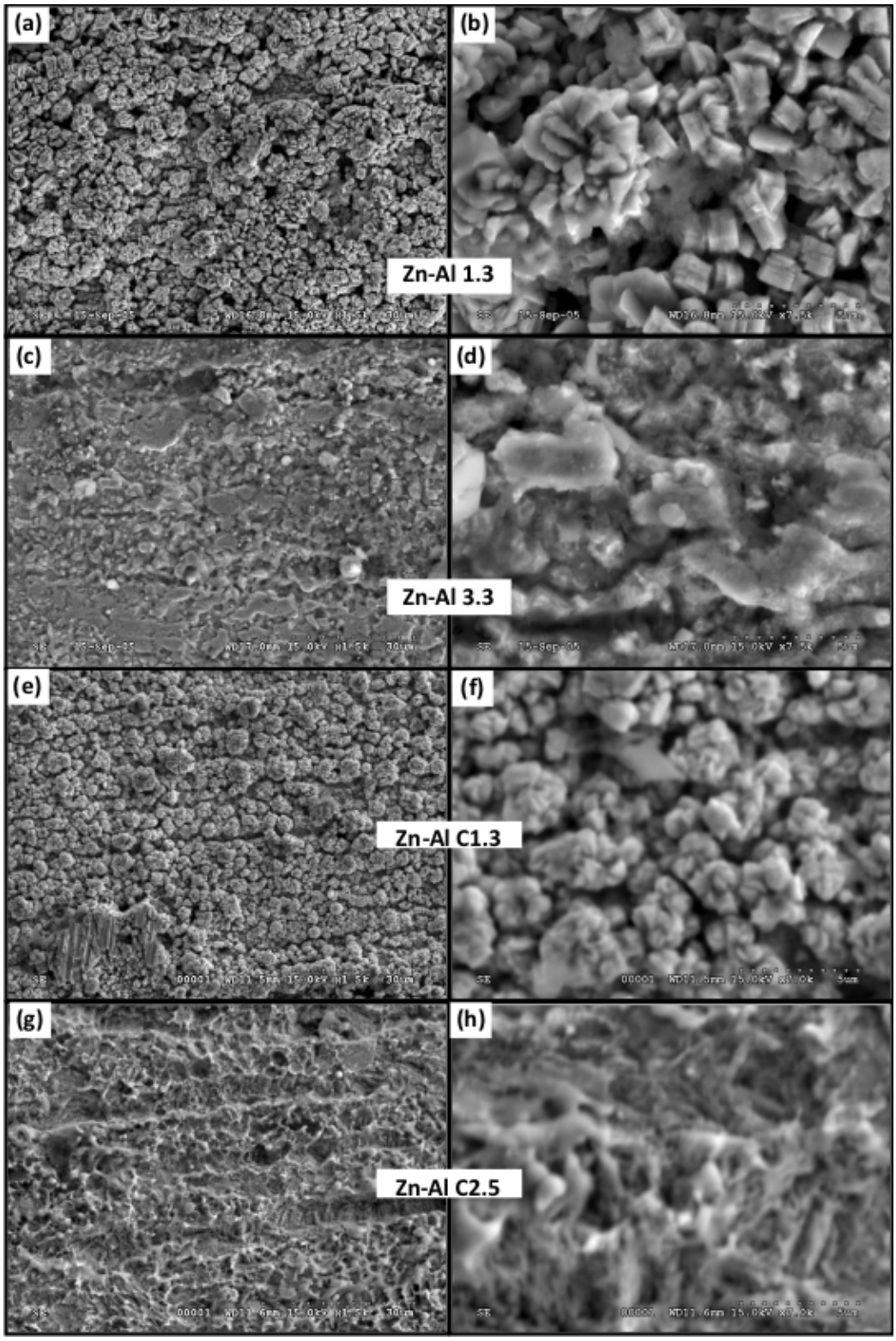

Figure 37 Surface morphology of Zn-Al: (a)&(b) Zn-Al 1.3; (c)&(d) Zn-Al 3.3; (e)&(f) Zn-Al C1.3; and (g)&(h) Zn-Al C2.5.

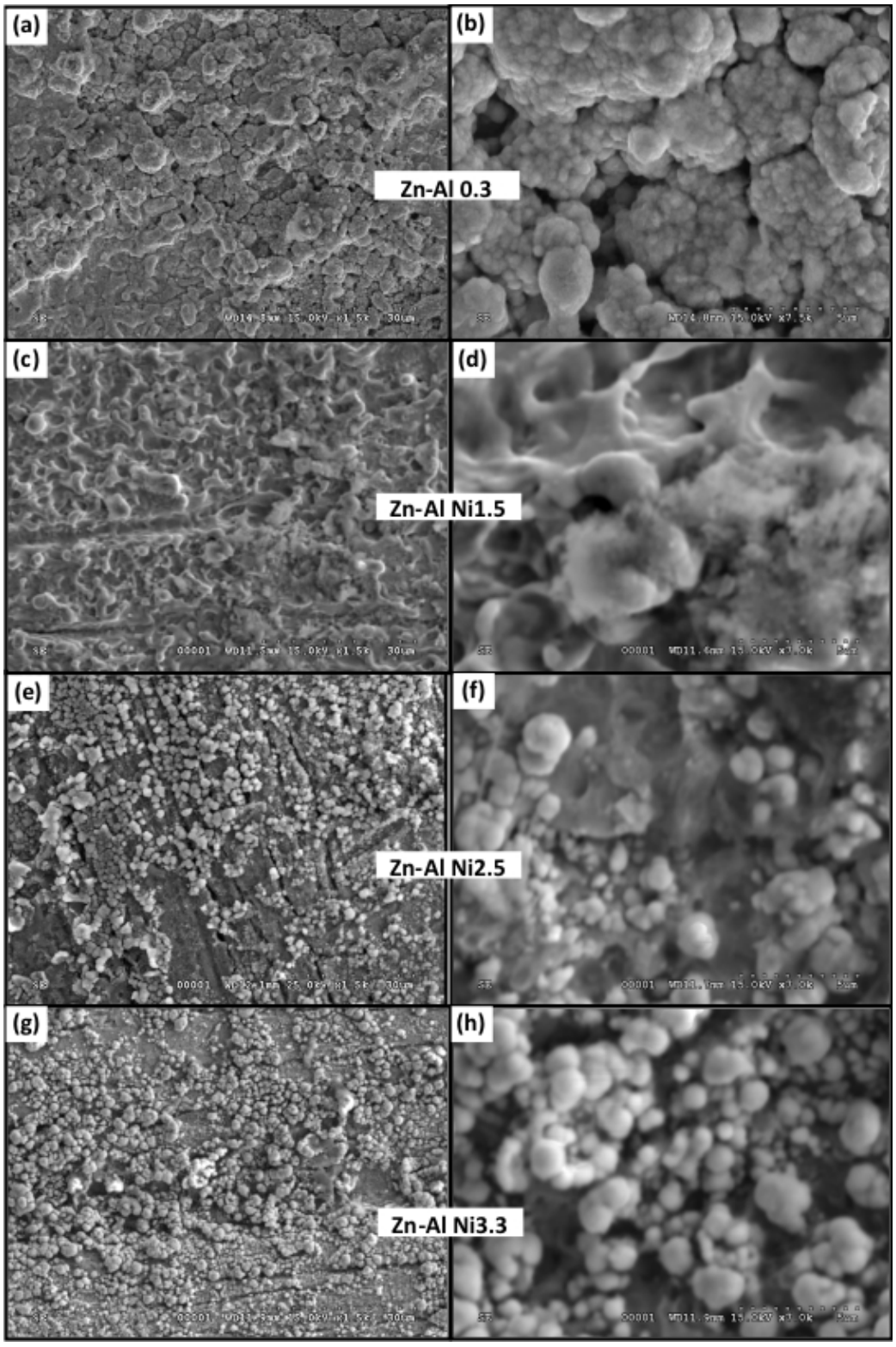

Figure 38 Surface morphology of Zn-Al: (a)&(b) Zn-Al 1.3; (c)&(d) Zn-Al 3.3; (e)&(f) Zn-Al C1.3; and (g)&(h) Zn-Al C2.5.

(b) Al Coatings

Pure Al coatings were deposited from $Al_2(SO_4)_3.14H_2O$ solution. Steel wires with a diameter of 1.6 mm were used as substrate. The percentage of $Al_2(SO_4)_3.14H_2O$ salt was varied from 5% to 20%. Also, in one test Ar (Al 5.2) was flown through the seals of the cell, instead of air. All the samples were processed using Al anodes except Al C1.1 in which a graphite anode was used. Table 6 gives the bath condition, processing parameters (V, A) and composition of the coated surface. Depositions were performed at the lowest possible voltage allowed by the anode-electrolyte combination. As shown in Table 6, with the increase of Al salt content in the solution there is no significant change in the coating composition. In addition, high oxygen content was also noticed in all Al coatings. Figure 39 shows the surface morphology of the deposited Al coatings. There is no significant change in the surface morphology in all of the Al coatings, which exhibit a dense amorphous-like morphology.

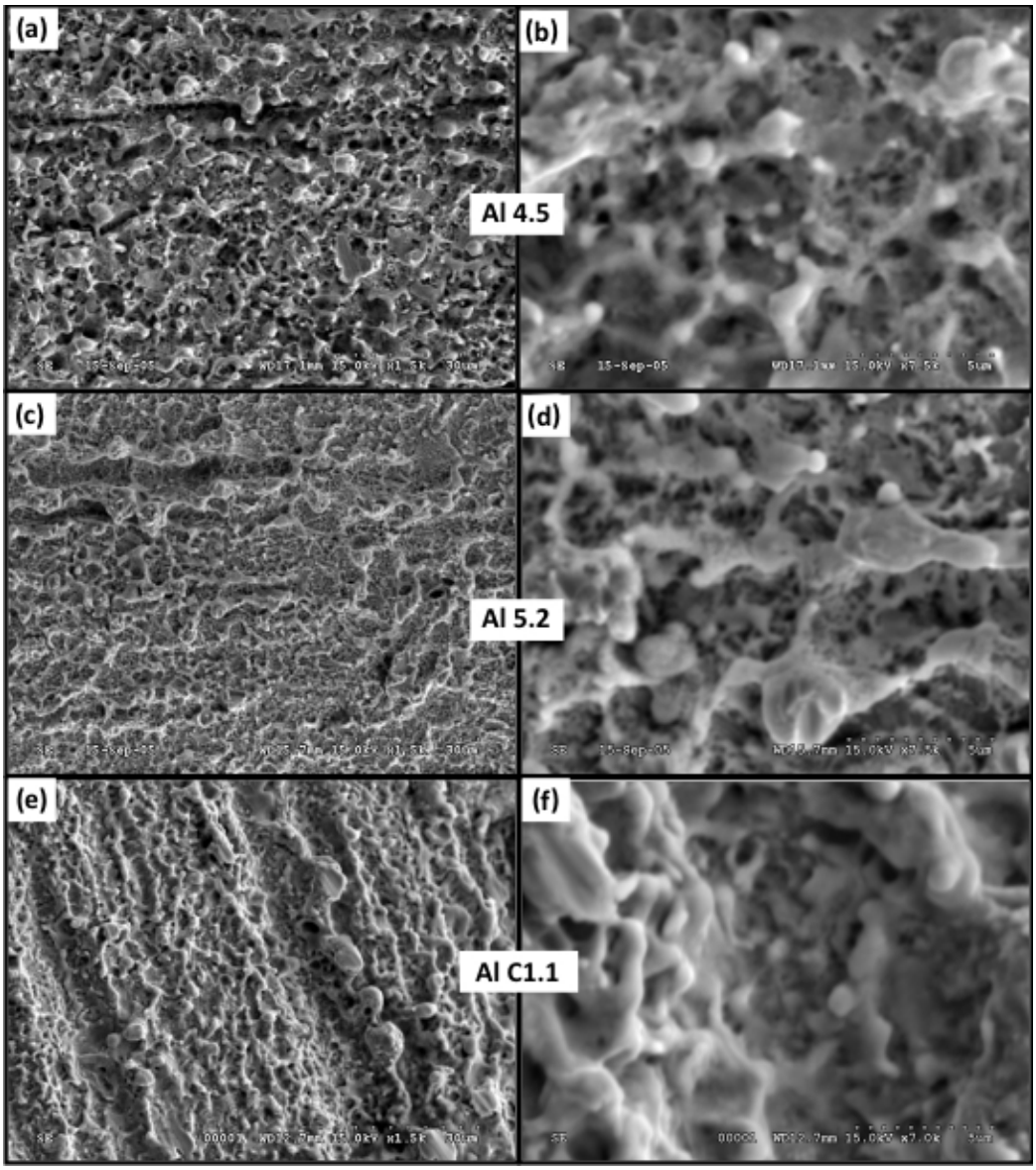

Figure 39 Surface morphology of Al coatings: (a)&(b) Al 4.5; (c)&(d) Al 5.2, and (e)&(f) Al C1.1.

Table 6 Parameters associated with electrolytic bath, deposition and composition of the coated surface.

Sample	Gas through the seals	Anode Material	Bath Composition wt% of Al Salt	Processing Parameters*			Composition of the Coated Surface (at %)					
				Voltage, V	Current, A	Processing Time, Sec	O	Na	Al	Si	S	Fe
Al 1.5	Air	Al	5	215/220	15	37.5	14.58	1.72	5.91	0.64	0.81	76.31
Al 2.5	Air	Al	10	205	15	37.5	16.45	0.94	6.99	0.50	0.77	74.34
Al 3.5	Air	Al	15	200	15	37.5	17.63	1.23	7.26	0.50	0.68	72.68
Al 4.5	Air	Al	20	185	15-20	37.5	16.55	1.18	6.84	0.65	0.71	74.39
Al 5.2[+]	Ar	Al	20	185	15-20	15	6.11	0.62	1.00	0.47	0.27	91.53
Al C1.1	Air	Graphite	23	160	~ 30	7.5	9.73	2.98	2.51	0.35	0.00	88.08

***** For each specimen other processing conditions were same: electrolyte temperature 75 – 80 ^{o}C, flow rate 3.2 lit/min. Al C1.1 was deposited at electrolyte temperature of 60 ^{o}C.

[+] Al5.2; deposition time for this sample was only 15 sec due to wire breakage.

The EDS analysis showed that all the coatings have a high O content. In order to ascertain the bonding characteristics of the deposited coatings, XPS was conducted for the Al C1 coating (Al coating). The coating was sputter-cleaned for 5 min before measurement. Figure 40 presents the high-resolution Al *2p* and O *1s* XPS spectra. The spectra were fitted using a Gaussian function. The center of the Al *2p* and O *1s* peak was fitted to be 74.6 eV and 530.7 eV, respectively, which corresponds to the binding energy of Al *2p* and O *1s* in AlOOH. It is important to note that the XPS analysis shows that Al is deposited as a hydroxide rather than an oxide. This chemical state of Al is expected to be more desirable for corrosion protection purposes.

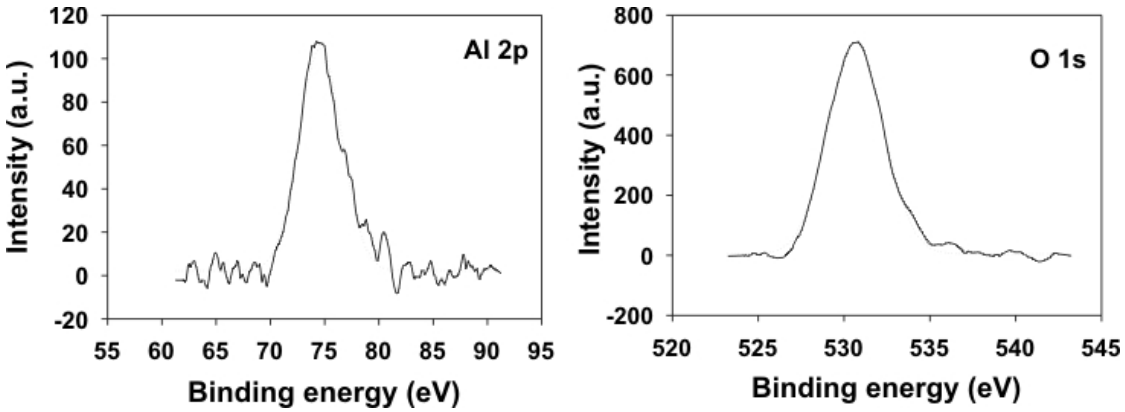

Figure 40 Al 2p and O 1s XPS spectra of the Al C1 coating.

5.2.2 Deposition of Al-rich Coatings

The previous screening deposition experiments showed that increasing the Al salt content in the solution results in an increase in the Al content in the coatings. Also, high Fe content was observed from the EDS results, indicating that the coatings deposited in 20-30 s were very thin. In an attempt to deposit thicker Al-rich coatings, another set of experiments was designed.

Rods (0.25 in in diameter) of 4340 steel were used as substrate for Al-rich coating deposition. The electrolytic baths used for the deposition were a mixture of $ZnSO_4.7H_2O$ and $Al_2(SO_4)_3.14H_2O$. Five series of deposition experiments were conducted at different combinations of processing parameters. The detailed bath conditions and processing parameters are shown in Table 7. In order to evaluate the influence of the anode material on the structure, composition and morphology of the deposited coatings, Ni, Al, and graphite anodes were used in different trials. In some trials, Ar was mixed in the electrolyte during EPT deposition to prevent the oxidization of the deposited coatings. Different combination of anode material and electrolyte bath composition was used for Zn-Al coating deposition. The amount of Al salt in the electrolyte was increased up to 99% relative to Zn salt, keeping the total concentration of the salt ~ 23%. No compensation was given for Zn depletion due to deposition of coating, so Al/Zn ratio shown in Table 6 may be higher than indicated as per electrolyte composition due to preferential deposition of Zn. Also, in case of Al anode tests, dissolution of Al anodes may have increased Al content in the electrolyte even higher. Depositions were conducted at the lowest possible voltage allowed by the anode-electrolyte combination.

For all the tests, fresh electrolyte was made each time. Furthermore, the same electrolyte was used for tests conducted in "one" series of experiments. The sequence of the sample deposited with an electrolyte (in one series of tests) was the same as the one shown in the Table 7. This may be important for analysis as no compensation was given to the electrolytic bath due to loss or addition of metal ions due to coating deposition or anode dissolution, respectively.

Before coating deposition, the substrates were EPT-cleaned using 12% $NaHCO_3$ electrolyte. Figure 41 shows a picture of the substrates after cleaning. The as-received 4340 steel surface showed a black color, while the cleaned steel surface exhibits a much brighter gray color. Figure 42 shows a picture of the coated specimens after five different series of experiments. Generally, all coatings showed a gray color, with different variations of contrast.

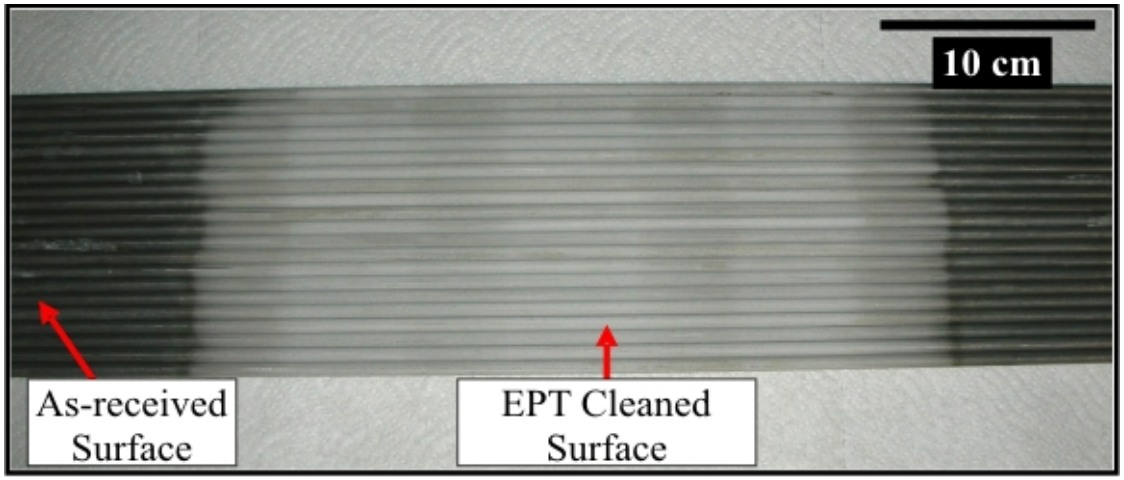

Figure 41 EPT-cleaned 4340 rod samples.

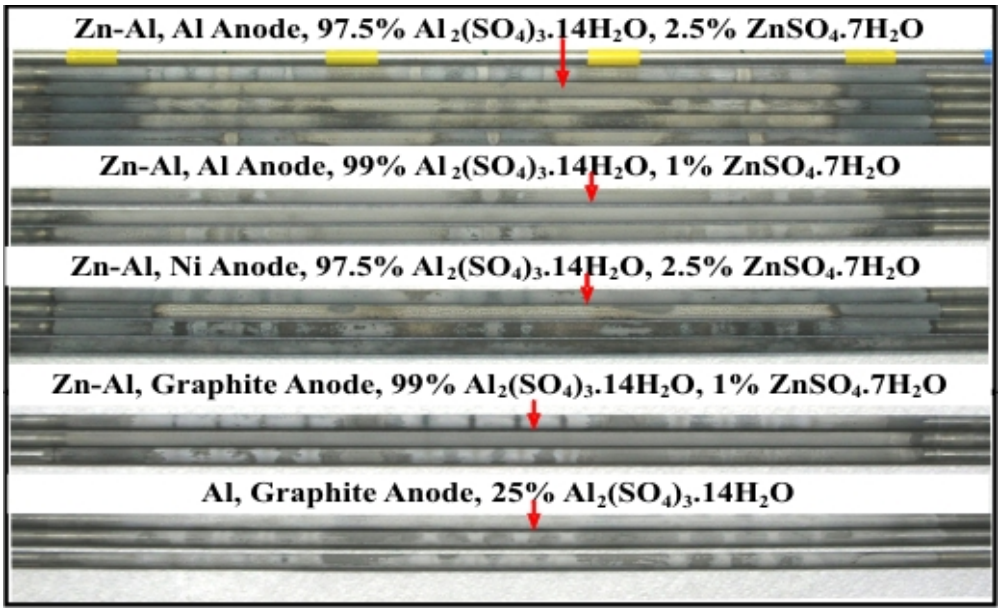

Figure 42 EPT-coated 4340 rod samples. Zn-Al samples represent Zn-Al coatings and Al sample represent Al coating deposited on 4340 substrate.

Table 7 Parameters associated with electrolytic bath and deposition.

Sample Code	Ar Through Electrolyte	Anode Material	Bath Condition (Wt %)			Processing Parameters*		
			Al Salt	Zn Salt	Al/Zn	Voltage V	Current A	Time Min
Zn-Al-Al1	Yes	Al	97.5	2.5	15.6	190	45-50	2
Zn-Al-Al2	No	Al	97.5	2.5	15.6	190	38	2
Zn-Al-Al3	Yes	Al	97.5	2.5	15.6	190	50	5
Zn-Al-Al4	No	Al	99	1	39.5	200	30	2
Zn-Al-Al5	Yes	Al	99	1	39.5	200	35-40	2
Zn-Al-Al6	Yes	Al	99	1	39.5	200	45	5
Zn-Al Ni1	Yes	Ni	97.5	2.5	15.6	160	50-55	2
Zn-Al Ni2	No	Ni	97.5	2.5	15.6	160	45	2
Zn-Al Ni3	Yes	Ni	97.5	2.5	15.6	160	50-55	5
Zn-Al Ni4[+]	Yes	Ni	97.5	2.5	15.6	160	50	2
Zn-Al C1	Yes	Graphite	99	1	39.5	170	50-55	2
Zn-Al C2	No	Graphite	99	1	39.5	170	35	2
Zn-Al C3[‡]	Yes	Graphite	99	1	39.5	170	45-50	5
Al C1	Yes	Graphite	25	-	-	170	50-55	2
Al C2	No	Graphite	25	-	-	170	40	2
Al C3	Yes	Graphite	25	-	-	170	50-55	5

** For each specimen other processing conditions were same: electrolyte temperature 70 – 80 ^{o}C, flow rate 5 lit/min.*

[+] rotation and linear motion was given during deposition.

[‡] Speed of rotation was higher as compared to all other tests.

The composition of the Zn-Al coatings deposited by EPT was obtained by EDS. In order to minimize the effect of the 4340 steel substrate, an acceleration voltage of 10 keV was used. The results are shown in Table 8. It should be noted that the Fe content varied from 9-92 at% indicating a wide variation in coating thickness. Also, all coatings have high oxygen content, which is related to the Al content. However, the Al:O atomic ratio was about 1:1 and much higher than that in the screening experiments.

Table 8 Zn-Al coating composition measured by EDS.

Sample Code	Ar flow	Anode Material	Coating composition, at%					
			Al	C	Fe	O	Zn	S
Zn-Al-Al1	Yes	Al	35.3	7.14	10.79	39.37	2.05	2.94
Zn-Al-Al1E			1.64	1.26	76.29	3.43	5.94	0.76
Zn-Al-Al2	No	Al	18.14	4.04	51.83	16.24	3.49	5.36
Zn-Al-Al3	Yes	Al	18	4.34	12.95	16.55	34.34	5.42
Zn-Al-Al4	No	Al	1.95	1.28	92.13	3.48	0.09	1.07
Zn-Al-Al4e			3.14	2.54	86.82	5.49	0.36	1.66
Zn-Al-Al5	Yes	Al	12.95	1.56	73.76	9.04	1.06	1.64
Zn-Al-Al6	Yes	Al	15.85	2.65	62.06	12.01	5.69	1.73
Zn-Al Ni1	Yes	Ni	29.02	1.68	36.46	16.84	13.27	2.74
Zn-Al Ni2	No	Ni	2.51	1.42	84.42	3.94	7.01	0.69
Zn-Al Ni3	Yes	Ni	38.07	4.82	16.11	35.4	2.69	2.91
Zn-Al Ni4^{+}	Yes	Ni	27.68	6.39	9.03	26.16	25.95	4.8
Zn-Al C1	Yes	Graphite	40.31	2.89	6.79	46.16	0.56	3.3
Zn-Al C2	No	Graphite	1.5	2.46	91.42	2.96	0.21	1.45
Zn-Al C3‡	Yes	Graphite	15.37	4.87	26.87	12.27	33.34	7.27
Al C1	Yes	Graphite	42.16	2.41	10.16	42.09	0	3.17
Al C2	No	Graphite	35.69	5.1	32.28	23.47	0	3.46
Al C3	Yes	Graphite	20	3.13	55.03	17.87	0	2.24

For all the coatings deposited for the same time, an increase of the Al salt content leads to an increase in the Fe content, indicating a thinner coating. For the coatings deposited with Ar purging through the electrolyte, the Fe content is significantly lower, indicating a higher deposition rate. It is interesting to note that all the coatings deposited for 5 min exhibit very high Zn content. This is attributed to depletion of Al in the solution in the initial stages of deposition.

Figure 43 presents the surface morphology of Zn-Al coatings deposited from an electrolyte of 97.5% Al salt with Al anode. As shown, the coatings deposited for 2 min with Ar purging through the electrolyte consist of large particles (4-8 μm), but the coatings deposited without Ar purging exhibit much smaller particles, 1-3 μm in diameter. However, the coatings deposited for 5 min exhibit quite different morphology, which consist of a mixture of large and

small particles with a size of 150-250 nm. EDS analysis shows that the small particles have high Zn content.

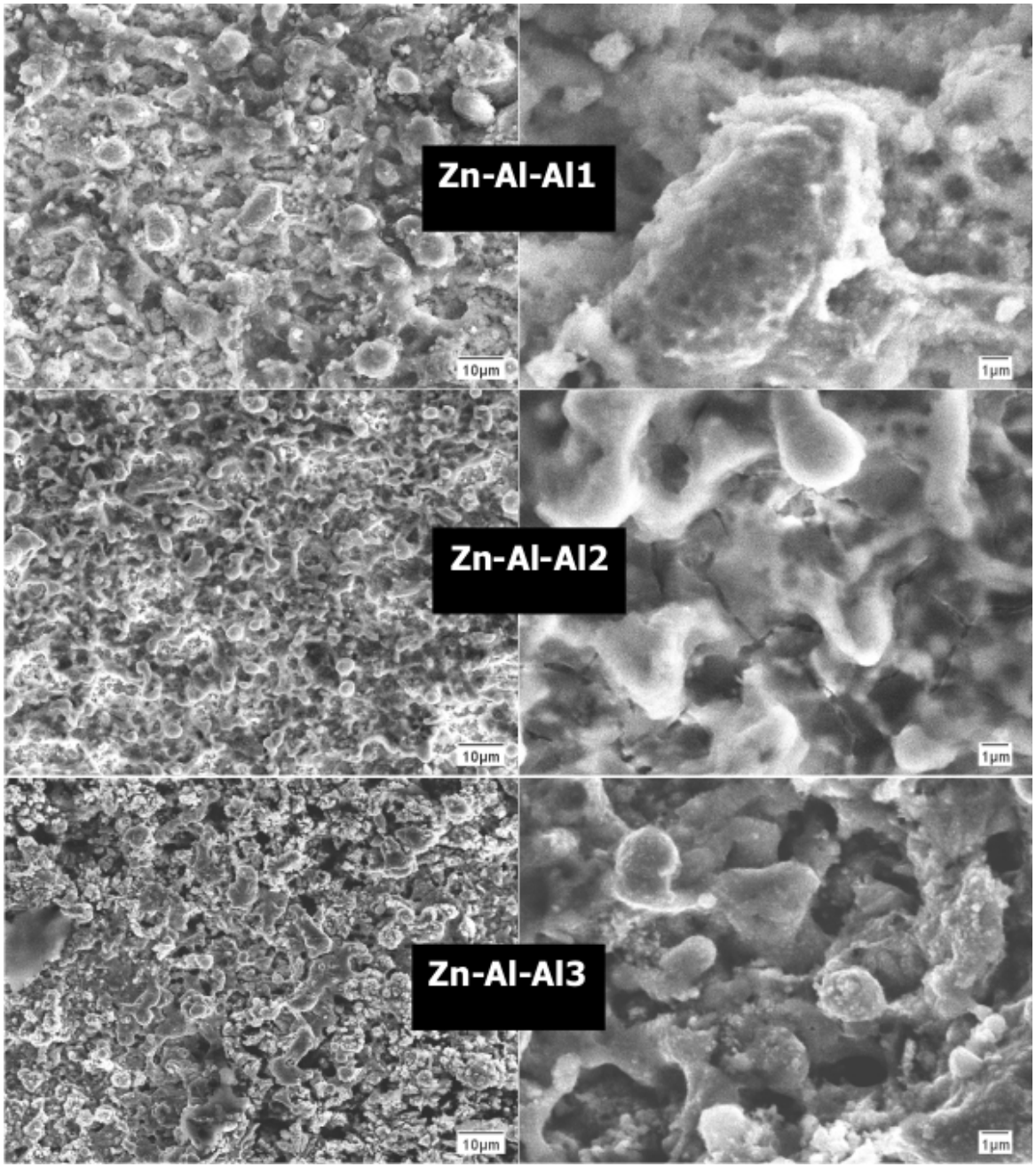

Figure 43 Surface morphologies of Zn-Al coatings deposited from an electrolyte of 97.5% Al salt with Al anode

For the coatings deposited from 99% Al salt, the morphology, Figure 44, exhibits a porous network, which is similar to that of the EPT-cleaned steel substrate, indicating that the deposited coatings are very thin. This is consistent with the EDS results, showing high Fe content. The coatings deposited for 5 min exhibit a similar morphology as the Zn-Al-Al1 coating.

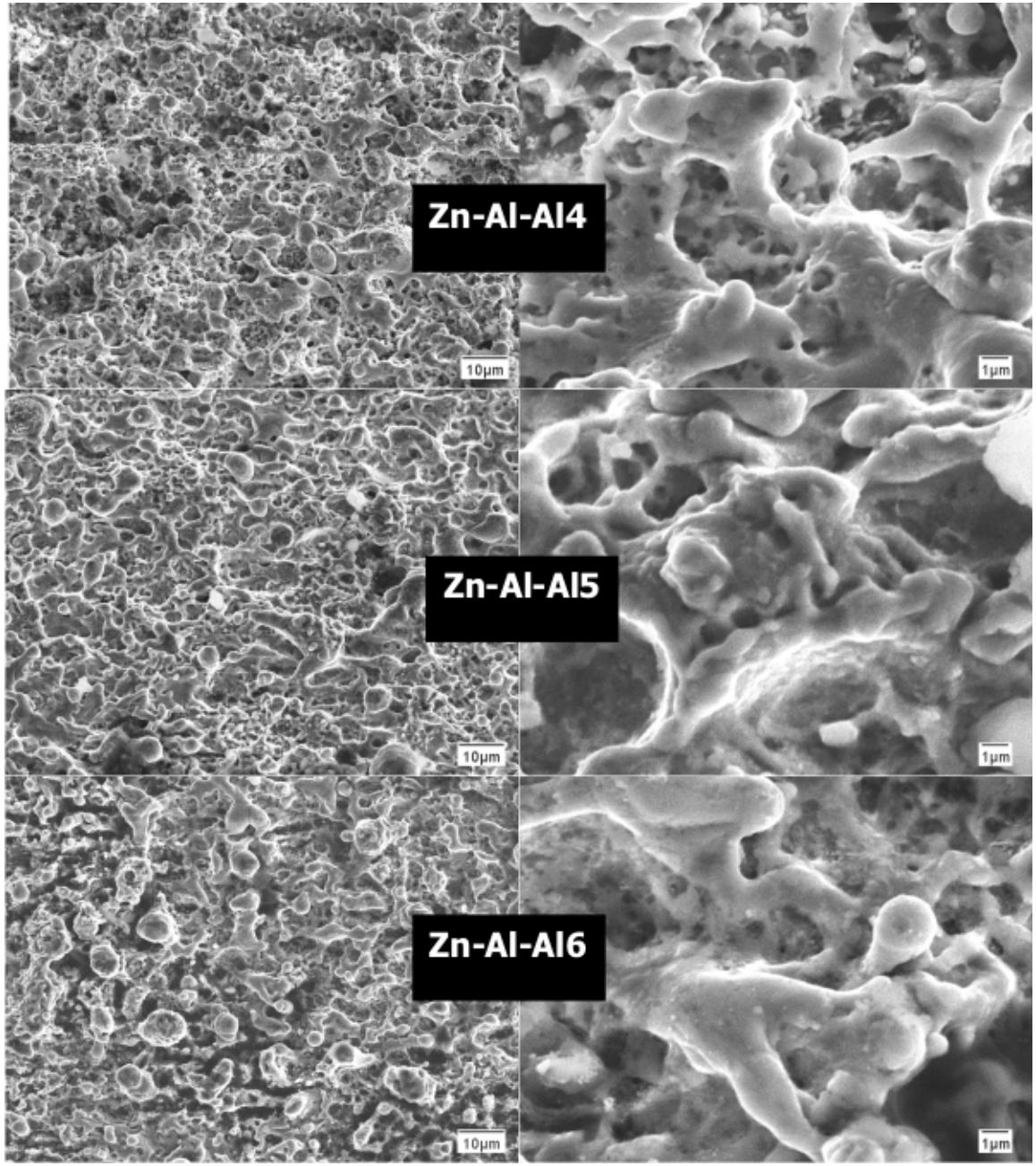

Figure 44 Surface morphologies of Zn-Al coatings deposited from an electrolyte of 99 % Al salt with Al anode.

When Ni was used as an anode, all the coatings deposited for 2 min contained high Zn, but the coatings deposited for 5 min contained high Al. This is contrary to the results from the coatings deposited using Al anode. The morphology of these coatings is shown in Figure 45. This seems to indicate that Ni catalyses Zn deposition and fast consumption of Zn in the initial stages of deposition.

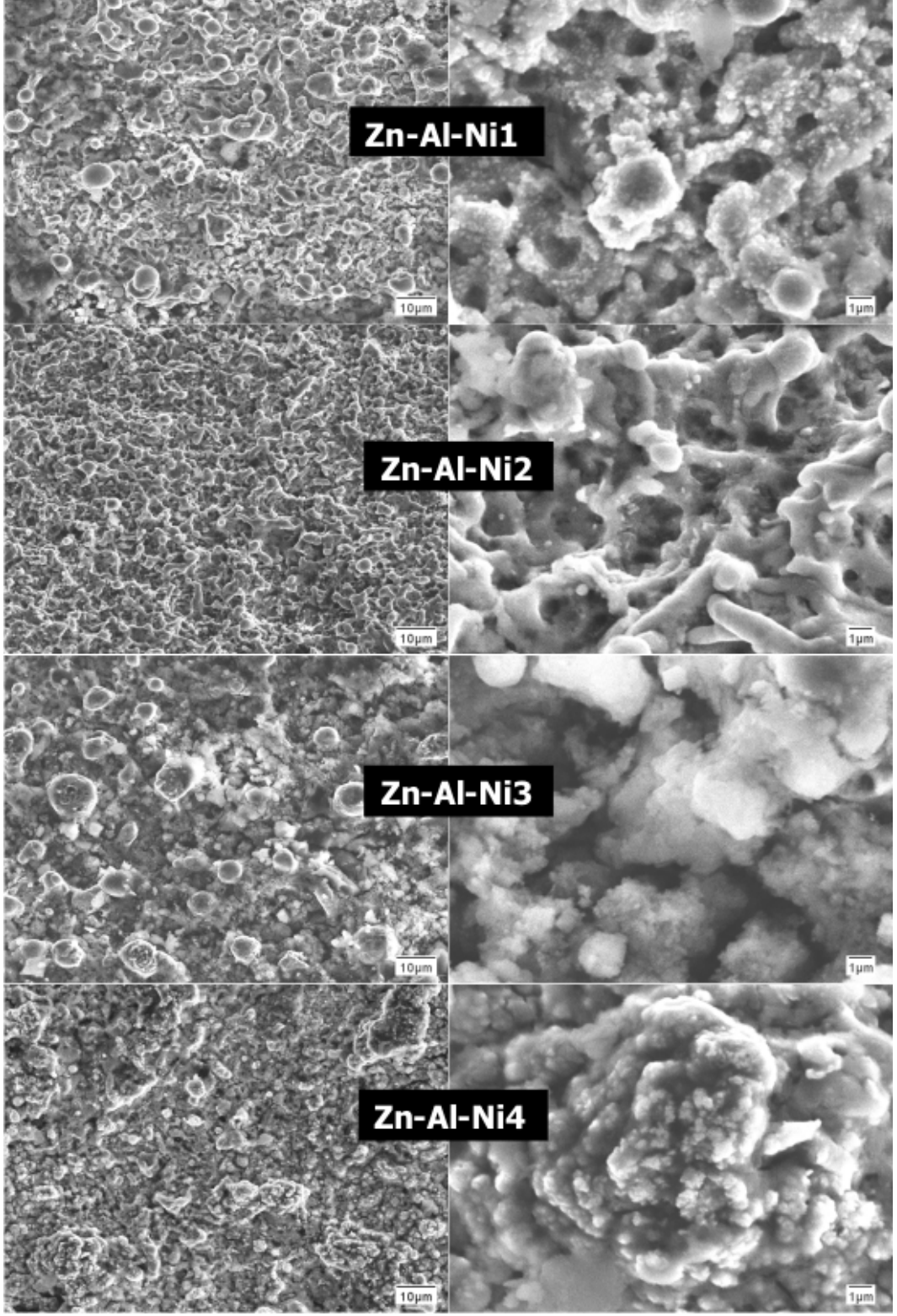

Figure 45 Surface morphology of Zn-Al coatings deposited from an electrolyte of 97.5 % Al salt with Ni anode.

The morphology, Figure 46, for the series of coatings deposited using graphite as anode is similar to that for the coatings using Al anode. Short deposition time with Ar flow through the electrolyte results in the formation of large particles, while long deposition time results in the co-existence of large particle and nanosized particle.

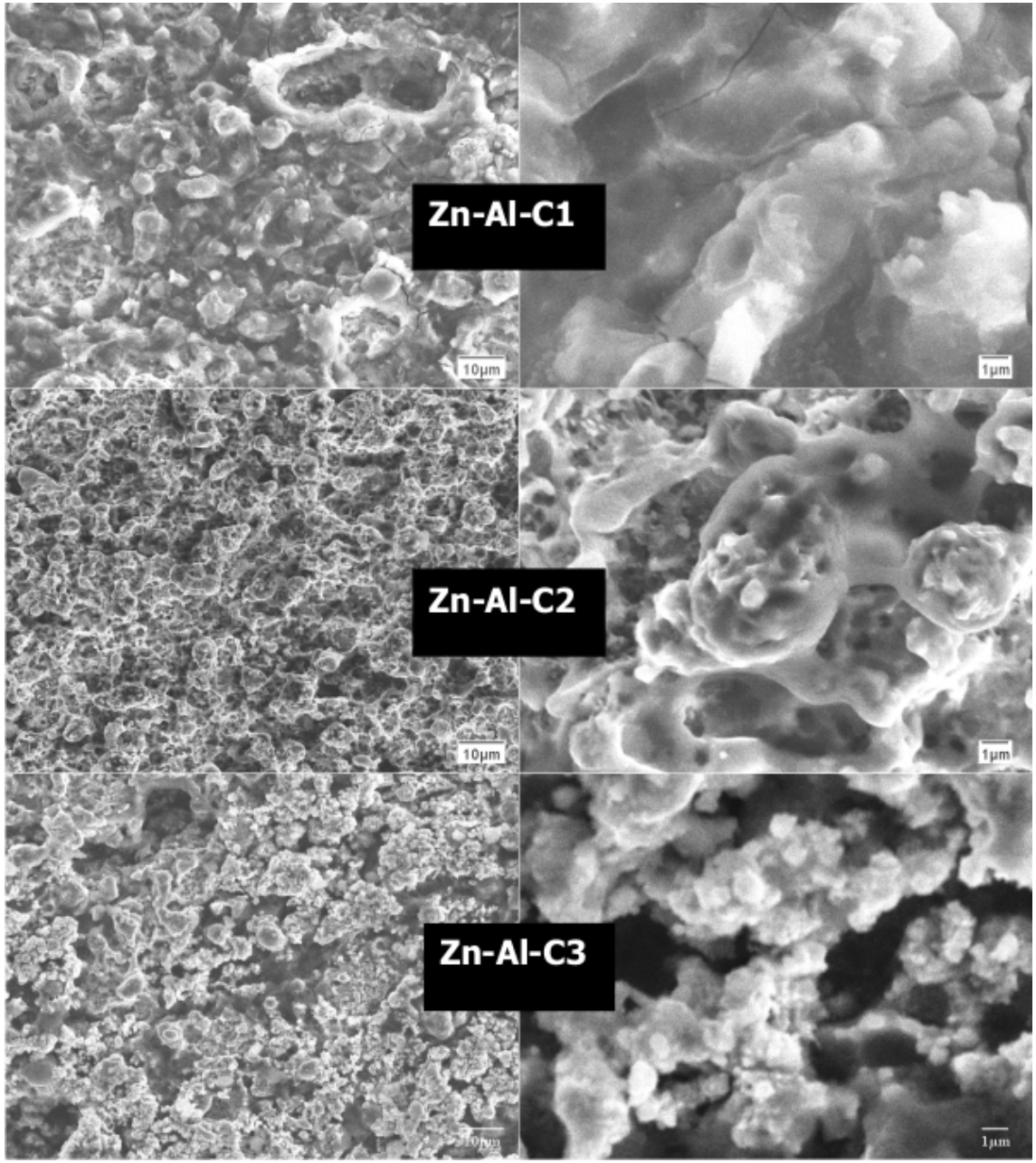

Figure 46 Surface morphology of Zn-Al coatings deposited from an electrolyte of 99 % Al salt with graphite anode.

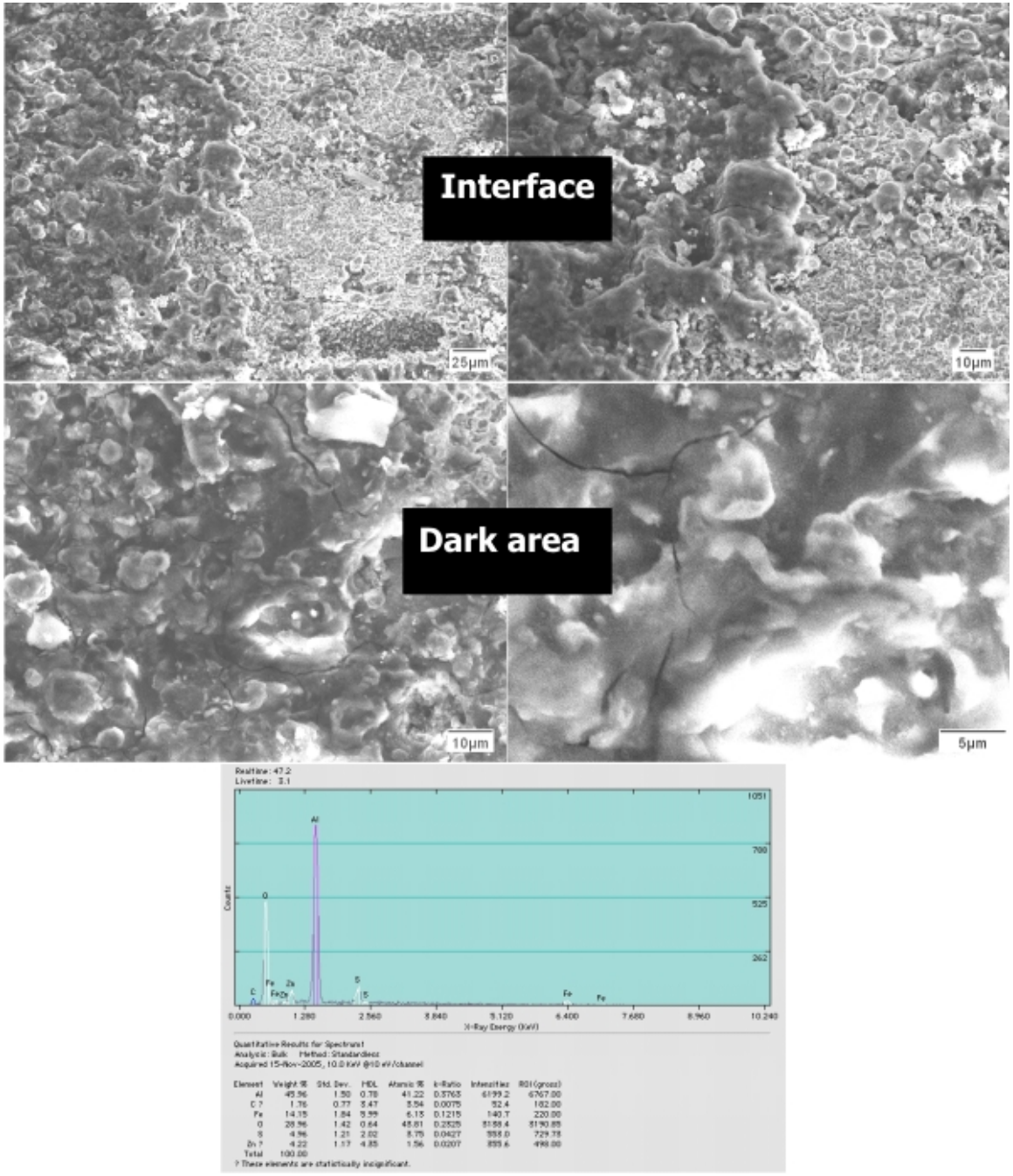

Figure 47 Interface and morphology in the dark area of the Zn-Al-C3 sample.

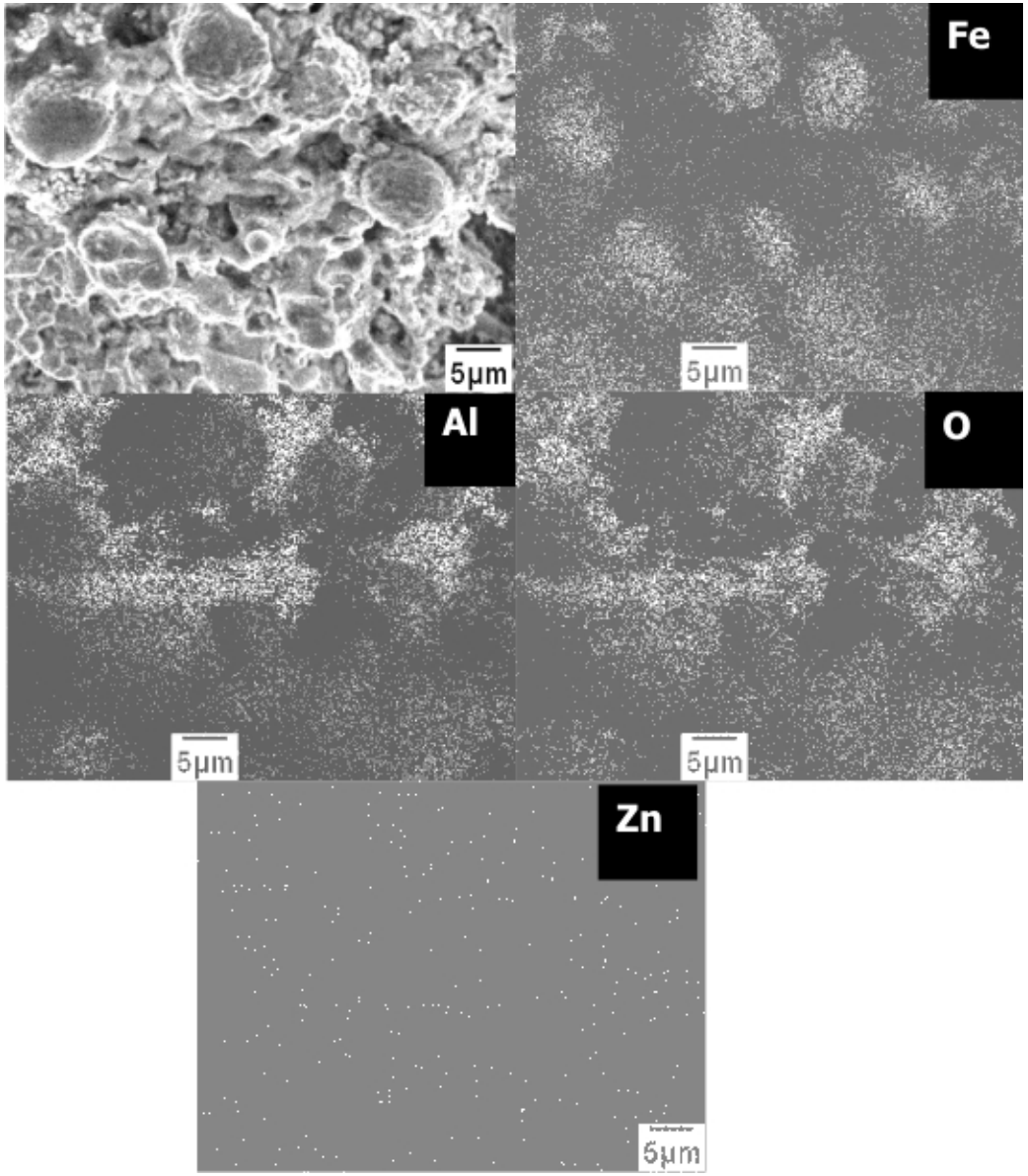

Figure 48 EDS mapping of the Zn, Fe, Al, and O elements in Zn-Al-C3 sample

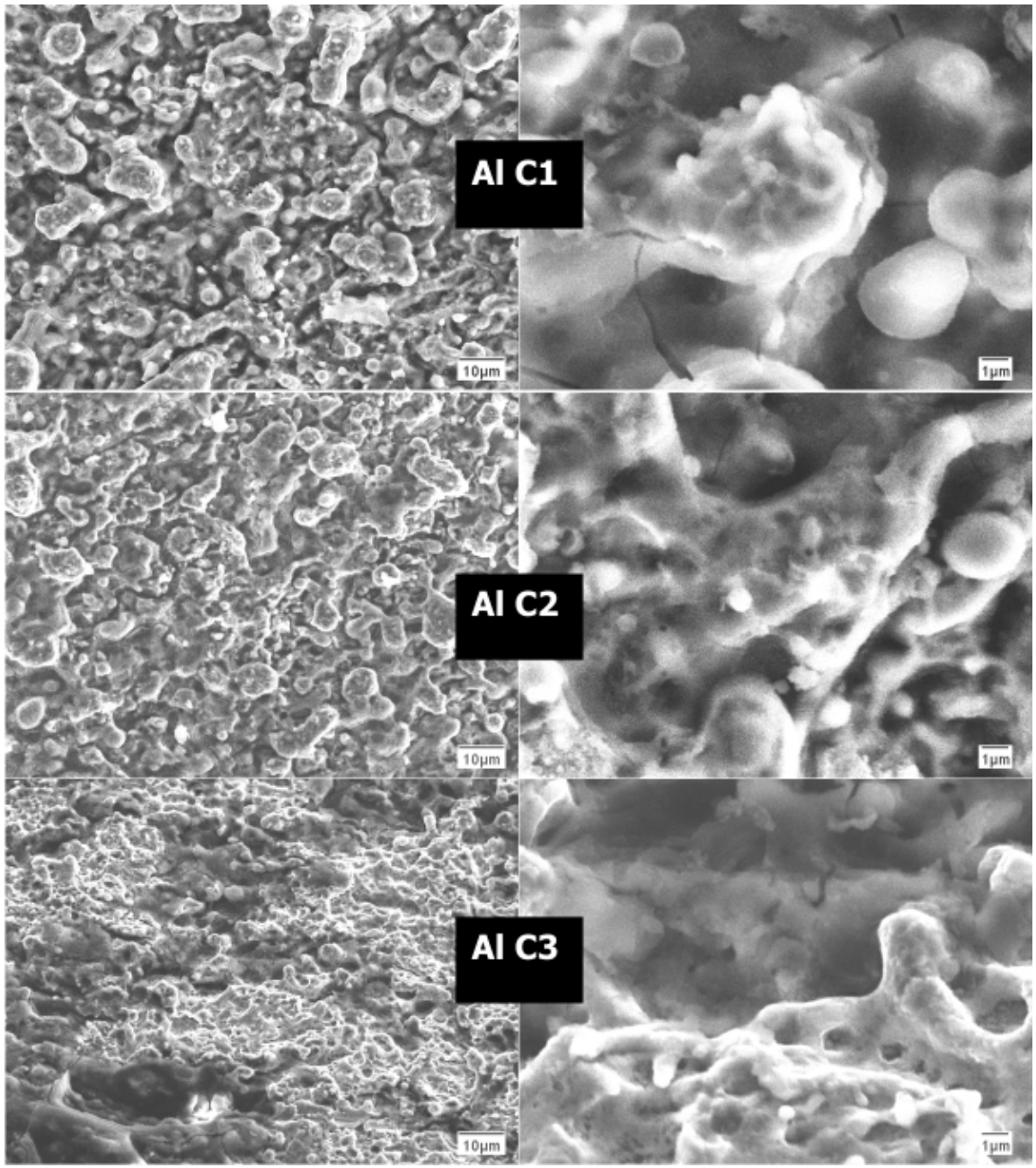

Figure 49 Surface morphology of Al coatings deposited with graphite anode.

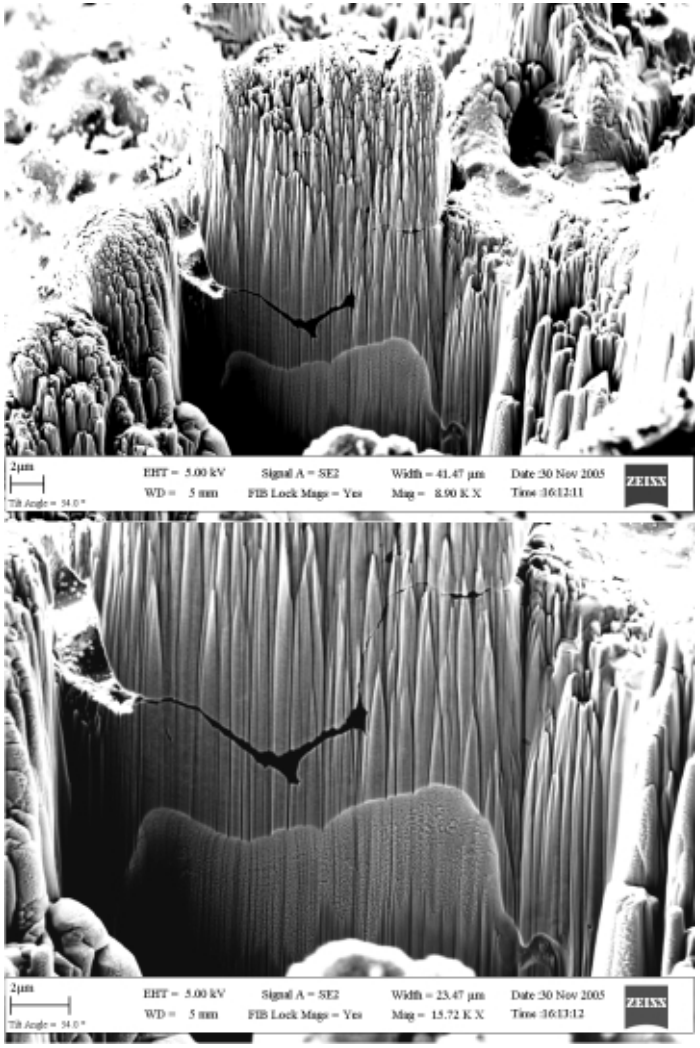

Figure 50 FIBs images of Al C1 coatings.

(a) First Group of Deposition Experiments

In this part, Zn-Al and Al coatings were deposited on 4340 strip and disk specimens that were prior cleaned by EPT. Ar was purged through the distribution chamber to form a shield around the plasma. Fresh electrolyte was made for deposition using $ZnSO_4.7H_2O$ and $Al_2(SO_4)_3.14H_2O$ as Zn salt and Al salt, respectively. For Zn-Al coating the total % of metal salt ($Al_2(SO_4)_3.14H_2O$ + $ZnSO_4.7H_2O$) was ~ 23%.

Three deposition conditions that have been identified from the last series of experiments were applied to deposit Zn-Al and Al coatings. The detailed processing parameters for disc and strip specimens are shown in Table 9. Figure 51 shows the appearance of coated specimens. Tables 10 and 11 present the compositional analysis of the disc and strip specimens, respectively. Approximate coating thickness was estimated based on the Fe content present in the EDS

analysis. Depending on processing conditions, the coating thickness ranged from ~1 – 6 µm for 2 minutes deposition time.

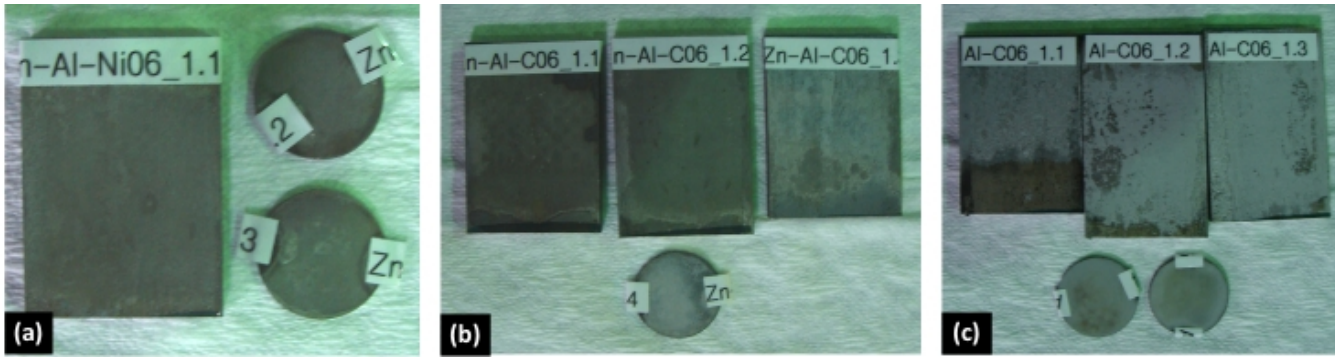

Figure 51 (a) Zn-Al coating deposited using Ni anode; (b) Zn-Al coating deposited using graphite; and (c) Al coating deposited using graphite anode.

The oxygen content was relatively high for all specimens. Some discrepancies were observed, i.e., no Zn deposition when a Ni anode was used. Also, when a graphite anode was used, Zn was deposited only on disc specimens but not on strips. Furthermore, SEM/EDS results showed that the thickness and Zn/Al ratio for the coating on disk and strip substrate differ significantly even with the same deposition parameters. The relatively low Al content in these tests is not consistent with the deposition experiments on cylindrical specimens where a high Al content was obtained (last section). Thus, these results show that the reactor and anode design is critical in the Zn-Al and Al deposition process. Also, deposition of Al-containing coatings is very sensitive to processing parameters and small deviations may have a significant effect. Certain modifications were made in the reactor and anode and a systematic study of processing parameters was conducted to try to better understand this deposition process (next section).

Scanning electron micrographs presenting the coating morphology and representative EDS results for all three Zn-Al and Al coatings are shown in Figure 52. SEM observations showed that the pure Al coatings were relatively dense and featureless and they were several μm thick (4-6 μm). The Zn-Al coatings deposited using a Ni anode exhibited a porous structure, which was comprised of flower-like clusters with a size of about 500 nm-3 μm. These clusters consisted of nanosize faceted grains with a size of about 100-200 nm. The Zn-Al coatings

Al-C06-1.4

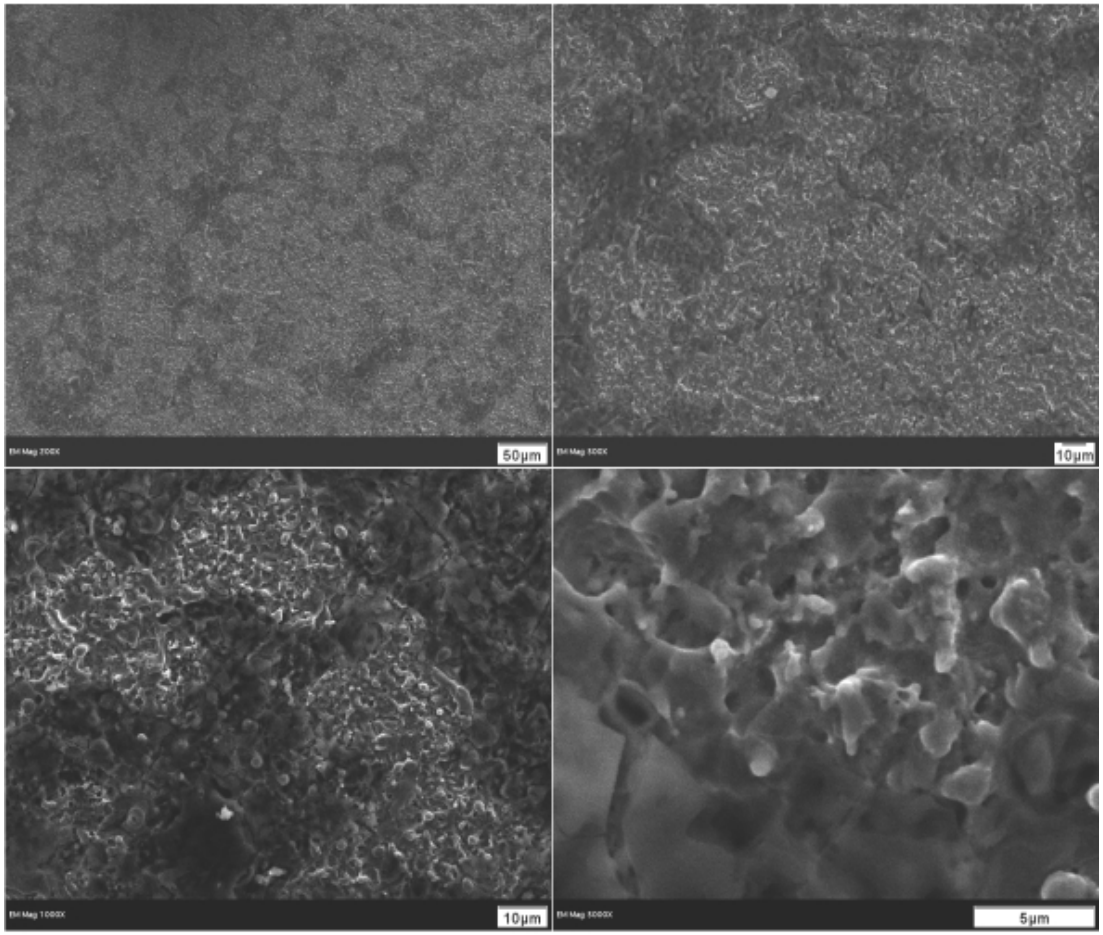

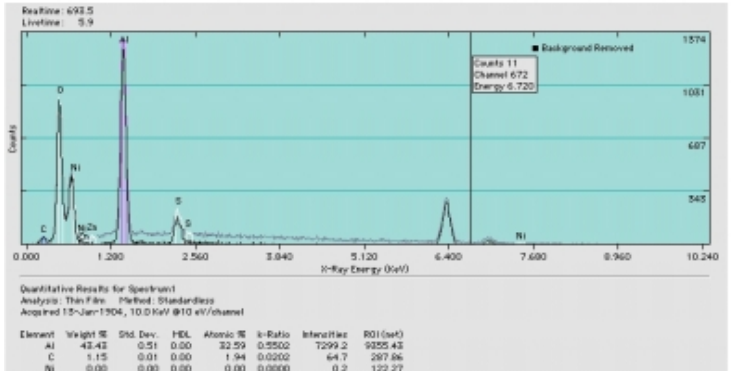

deposited using a graphite anode, were also relatively thin and characterized with high porosity. Thus, certain differences in characteristics (thickness, density, composition) of coatings deposited on cylindrical and flat specimens were observed and attributed to differences in specimen size (small disc, strip and cylinder) and geometry (cylindrical vs flat) affecting the processing conditions.

Table 9 Parameters associated with electrolytic bath and deposition of Zn-Al and Al on flat specimens.

Sample Code	Ar Through Electrolyte	Anode Material	Bath Condition Wt.%			Processing Parameters*		
			Al Salt	Zn Salt	Al/Zn	Voltage V	Current A	Time Min
[+]Zn-Al-Ni06-1.x	Yes	Ni	97.5	2.5	15.6	185	20	2
[+]Zn-Al-C06-1.x	Yes	Graphite	99	1	39.5	185	20	2
[+]Al-C06-1.x	Yes	Graphite	25	-	-	190	20	2

[+] x = 1, 2… that represents the number of repeats with the condition.

** Flow rate was ~ 3 lit/min and temperature of the electrolyte was maintained between 65 °C - 75 °C.*

Table 10 EDS results for Zn-Al and Al coated disks using 15 keV accelerating voltage.

Samples	Al		C		Ni		O		S		Zn		Fe	
	wt. %	at. %	wt. %	at. %	wt.%	at.%	wt. %	at. %	wt. %	at. %	wt. %	at. %	wt. %	at. %
Al-C06-1.4	27.30	25.82	0.72	1.52	-	-	33.54	53.51	4.49	3.57	-	-	33.94	15.56
Zn-Al-C06-1.4	9.44	12.17	5.51	15.99	-	-	14.27	31.05	1.60	1.73	45.89	24.48	23.29	14.58
Zn-Al-Ni06-1.3	1.23	1.95	2.44	8.68	1.06	0.77	7.59	20.30	1.66	2.22	-	-	86.01	66.07

The data is the average of three readings taken at different places on the coating surface at 200X magnification.

Samples	Al		C		Ni		O		S		Zn		thickness
	wt. %	at. %	wt. %	at. %	wt. %	at. %	wt. %	at. %	wt. %	at. %	wt. %	at. %	µm
Al-C06-1.4	43.53	32.64	1.14	1.91	-	-	48.17	60.92	7.14	4.50	-	-	~6
Zn-Al-C06-1.4	14.74	16.56	7.20	18.30	-	-	19.29	36.52	2.18	2.08	56.57	26.60	~2
Zn-Al-Ni06-1.3	11.59	7.28	23.11	33.05	1.98	0.58	47.54	50.77	15.64	8.48	-	-	~3

The compositions shown are those of the coating without including Fe from the substrate. The coating thickness was estimated from the Fe content in the analysis.

Table 11 EDS results for Zn-Al and Al coated strips using 10 keV accelerating voltage.

Samples	Al		C		Ni		O		S		Zn		Fe	
	wt. %	at. %	wt. %	at. %	wt. %	at. %	wt. %	at. %	wt. %	at. %	wt. %	at. %	wt. %	at. %
Al-C06-1.3	35.38	29.49	0.92	1.72	-	-	41.02	57.68	6.36	4.47	0.22	0.08	16.12	6.58
Zn-Al-C06-1.2	1.28	2.16	0.81	3.05	-	-	6.71	19.02	2.11	2.98	0.03	0.02	89.07	72.77
Zn-Al-Ni06-1.1	1.17	1.93	1.26	4.72	0.81	0.62	7.15	19.92	1.59	2.22	0	0	88.01	70.59

The data is the average of three readings taken at different places on the coating thickness at 200X magnification.

Samples	Al		C		Ni		O		S		Zn		thickness
	wt. %	at. %	wt. %	at. %	wt. %	at. %	wt. %	at. %	wt. %	at. %	wt. %	at. %	µm
Al-C06-1.3	43.00	32.30	1.13	1.90	-	-	48.05	60.87	7.76	4.90	0.08	0.03	~4
Zn-Al-C06-1.2	28.98	23.92	16.93	31.36	-	-	10.32	14.35	43.77	30.38	0.01	0.01	~1
Zn-Al-Ni06-1.1	12.22	8.32	13.69	21.11	6.0	1.92	50.93	58.74	17.16	9.91	0	0	~2

The compositions shown are those of the coating without including Fe from the substrate. The coating thickness was estimated from the Fe content in the analysis.

The crystalline structure of the Al and Zn-Al coatings was ascertained by XRD. For both types of coating, two strong and broad peaks at a 2θ range of 12-20° were observed, Figure 53. Careful inspection showed that these peaks are asymmetric. This asymmetry indicates that the peaks originate from different phases. After comparing with standard diffraction patterns, it was found that these peaks could be a mixture of the (020) peak, with a 2θ of 14.5° of AlO(OH) and the (002) peak, with a 2θ of 18.3° of $Al(OH)_3$ as shown in Figure 53. The intensities of these two peaks are comparable suggesting similar amounts of these hydroxides in the coating. These results are consistent with the XPS analysis conducted on these coatings showing that Al is present as hydroxide or oxyhydroxide and not as an oxide. In addition, three sharp peaks at 2θ values of 44.7°, 65° and 82.5° could be seen in the XRD patterns of both samples. These peaks fit well with the (110), (200) and (211) peak of α-Fe, indicating that they are from the steel substrate. This is consistent with the small thickness of the coatings and the EDS results. Finally, the XRD from the Zn-Al coating shows that Zn is present mostly as a Zn hydroxide, $Zn(OH)_3$ and Zn(OH), and only a small portion of Zn is present in the metallic state (shoulder in the main Fe peak). Thus, the results show that under the present conditions, the coatings consist of hydroxides.

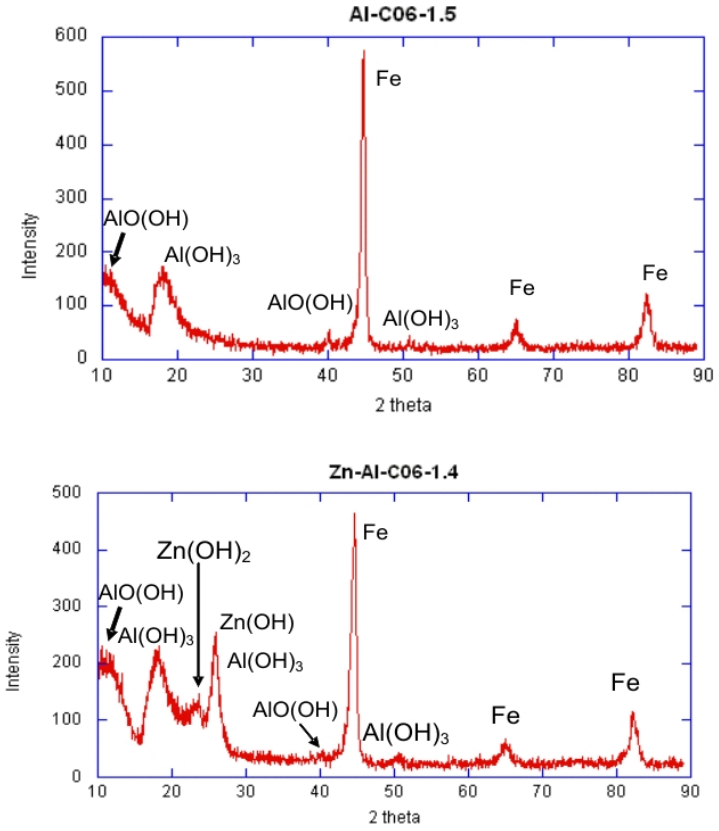

Figure 53 XRD phase analysis for Al and Zn-Al coatings.

(b) Second Group of Deposition Experiments

A systematic approach to deposition of Al was initiated by mainly varying the processing voltage, electrolyte composition and processing time. Tables 12 and 13 provide all the experimental details for this group of tests. A broad range of processing parameters was investigated first, Table 12. Based on these results, the refinement experiments followed up shown in Table 13. All deposition experiments were performed on 15" wide, strip specimens by keeping the size of the treated area constant. Specimens were first cleaned by EPT using 12% $NaHCO_3$ electrolytic solution. Figures 54 and 55 show the appearance of the specimens after the Al deposition experiments described in Tables 12 and 13, respectively. Figure 56 shows representative EDS spectra taken from the surface of Al coated specimens deposited under the conditions outlined in Tables 12 and 13. Table 14 summarizes the EDS results of the elemental composition analysis. A

high Fe content indicates a very thin coating. The estimated coating thickness is shown only for relatively thick coatings in these tables.

A summary of the findings from this group of deposition experiments has as follows. Low (180 V) or high (210 V) voltage does not produce continuous coatings. Also, increasing deposition time (2 and 5 min experiments) under these conditions does not have a significant effect on coating thickness. Best coatings in terms of uniformity and thickness were obtained with 190 V and to a lesser extend with 200 V. Increasing processing time in this case from 2 to 5 minutes caused a minor increase in coating thickness. Presence of sodium sulfate in the electrolyte was found to improve uniformity but inhibited coating thickness. It was interesting to note that coatings produced with sodium sulfate present in the solution contained no oxygen. Sodium sulfate is basically a "cleaning" solution so it is expected to have some "cleaning" action on the process that reduces and removes oxygen but at the same time prevents deposition of thicker coatings by similar reduction of the metallic ions. Sodium sulphate and Al powder was added in the bath for one experiment and produced a more uniform coating. The intention was to provide an additional source of Al with the expectation to melt and deposit it on the surface during processing. Since both, sodium sulfate and Al powder were present, the possible role of Al powder could not be determined. Such possible effect was investigated with the second set of experiments shown in Table 13. A voltage of 190 V produced relatively thicker and uniform coatings and thus the experiments of the second set were conducted only under this voltage.

The second set of deposition experiments showed that addition of Al power even though it does not increase coating thickness, it improves uniformity. Also, increasing processing time from 2 to 5 minutes had only a moderate effect in increasing coating thickness (from ~3 to ~4 μm).

Another modification made to the deposition unit was to introduce the inert gas atmosphere around the plasma zone rather than at the exit. This arrangement dries the specimen before being exposed to the ambient atmosphere by removing any liquid as it exits the plasma zone. Coating of the entire specimen surface was achieved with some variation in the coating thickness. This was attributed to the way the inert gas was supplied around the plasma zone. Figure 57 shows a cross section of such a specimen with a coating thickness of about 3-4 μm. Thus, aluminum coating is feasible and its uniformity can be ensured by optimizing the reactor design. For example, the location where the inert gas is delivered in the unit seems to be important.

Future work: the reactor will be redesigned such that the gas is introduced along the ends of the plasma zone. Inert gas is expected to extinguish the plasma on exit so that there will be no ambient air between the plasma and the inert gas.

Table 12 Processing parameters for the second group of Al coating deposition.

Sample Code	Processing Conditions						Electrolyte Composition	Coating morphology
	Voltage V	Current A	Flow Rate Lit/min	Temp. °C	Time, min	Gap mm		
Al-180V-2m	180	15	2.5	70	2.0	8	$AlSO_4 + Na_2SO_4$	poor coverage, very thin coating, high oxy
Al-180V-5m	180	15	2.5	70	5.0	8	$AlSO_4 + Na_2SO_4$	
Al-190V-2m*	190	10	2	70	2.0	6.2	$AlSO_4$	90% coverage, relative thick, high oxygen
Al-190V-5m*	190	11	2	65	5.0	6.3	$AlSO_4$	
Al-190V-2m2	190	10	2	70	2.0	6.3	$AlSO_4$	
Al-200V-2m	200	13	2	65	2.0	6.3	$AlSO_4$	very poor coverage, islands feature, high c
Al-200V-5m	200	13	2	68	5.0	6.3	$AlSO_4$	
Al-200V-2m2	200	13	2	65	2.0	6.3	$AlSO_4 + Na_2SO_4$ + Al powder	uniform coverage, very thin coating, no ox
Al-200V-2m3	200	15	2	70	2.0	8	$AlSO_4 + Na_2SO_4$	
Al-210V-15s	210	15	2.5	65	0.25	8	$AlSO_4 + Na_2SO_4$	
Al-210V-2m	210	17	2.5	70	2	8	$AlSO_4$	
Al-210V-5m	210	15	2.5	65	5	8	$AlSO_4$	
Al-225V-2m2	225	13	2.5	65	2.0	8	$AlSO_4 + Na_2SO_4$ + Al powder	

** higher linear speed as compared to rest of the samples.*

Table 13 Follow up deposition tests based on best results of those shown in Table 12.

Sample Code	Processing Conditions						Bath Conditions
	Voltage V	Current A	Flow Rate l/min	Temperature °C	Time, min	Gap mm	
Al-190V-2m	190	15	2.5	65-70	2.0	6.2	$AlSO_4$
Al-190V-5m	190	15	2.5	65-70	5.0	6.3	$AlSO_4$
Al-190V-Static	190	15	2.5	65-70	2.0	6.3	$AlSO_4$
Al-190V-2m2	190	15	2.5	65-70	2.0	6.3	$AlSO_4$ + Powder

Table 14 EDS results for Al coating deposited under the conditions shown in Tables 5 and 6.

Code	Al		C		O		S		Fe		Thickness
	wt. %	at. %	wt. %	at. %	wt. %	at. %	wt. %	at. %	wt. %	at. %	μm
Al-180V-5m	0.64	1.30	0.15	0.67	0.32	1.09	0.27	0.46	98.62	96.48	~2
Al-190-2m	26.80	37.00	0.25	0.78	6.92	16.10	2.90	3.37	62.82	42.23	~3
Al-190-5m	32.57	41.65	0.21	0.62	9.35	19.94	3.07	3.30	54.78	34.48	~4
Al-200V-2m	17.66	27.64	0.17	0.62	3.93	10.37	1.98	2.62	76.23	58.73	~4
Al-200V-5m	17.96	28.23	0.15	0.54	4.02	10.66	1.82	2.40	76.04	58.15	~4
Al-200V-2m2	18.55	11.01	57.34	76.28	0.05	0.05	20.79	10.38	~99	~99	<1
Al-210V-15s	17.04	9.95	59.34	78.05	0.06	0.06	22.67	11.33	~99	~99	<1
Al-210-2m	14.79	8.33	64.95	81.93	0.12	0.11	19.75	9.35	~99	~99	<1
Al-210V-5m	14.49	8.92	53.63	74.00	0.04	0.04	29.08	15.03	~99	~99	<1
Al-225V-2m2	19.86	11.86	55.68	74.88	0.04	0.04	20.41	10.3	~99	~99	<1

The data is average of three readings taken at different places.

Code	Al		C		O		S		Fe		Thickness
	wt. %	at. %	wt. %	at. %	wt. %	μm	wt. %	at. %	wt. %	at. %	μm
Al-190V-2m-set2	23.86	34.26	0.15	0.50	6.48	15.68	2.36	2.85	67.14	46.72	~3
Al-190V-2m2-set2	22.08	32.84	0.13	0.50	5.37	13.43	2.25	2.82	70.15	50.43	~3
Al-190V-5m-set2	29.36	39.31	0.15	0.45	8.03	18.13	2.50	2.80	59.95	39.30	~4
Al-190V-static	6.51	12.05	0.06	0.25	1.47	4.59	0.59	0.92	91.36	82.17	~1

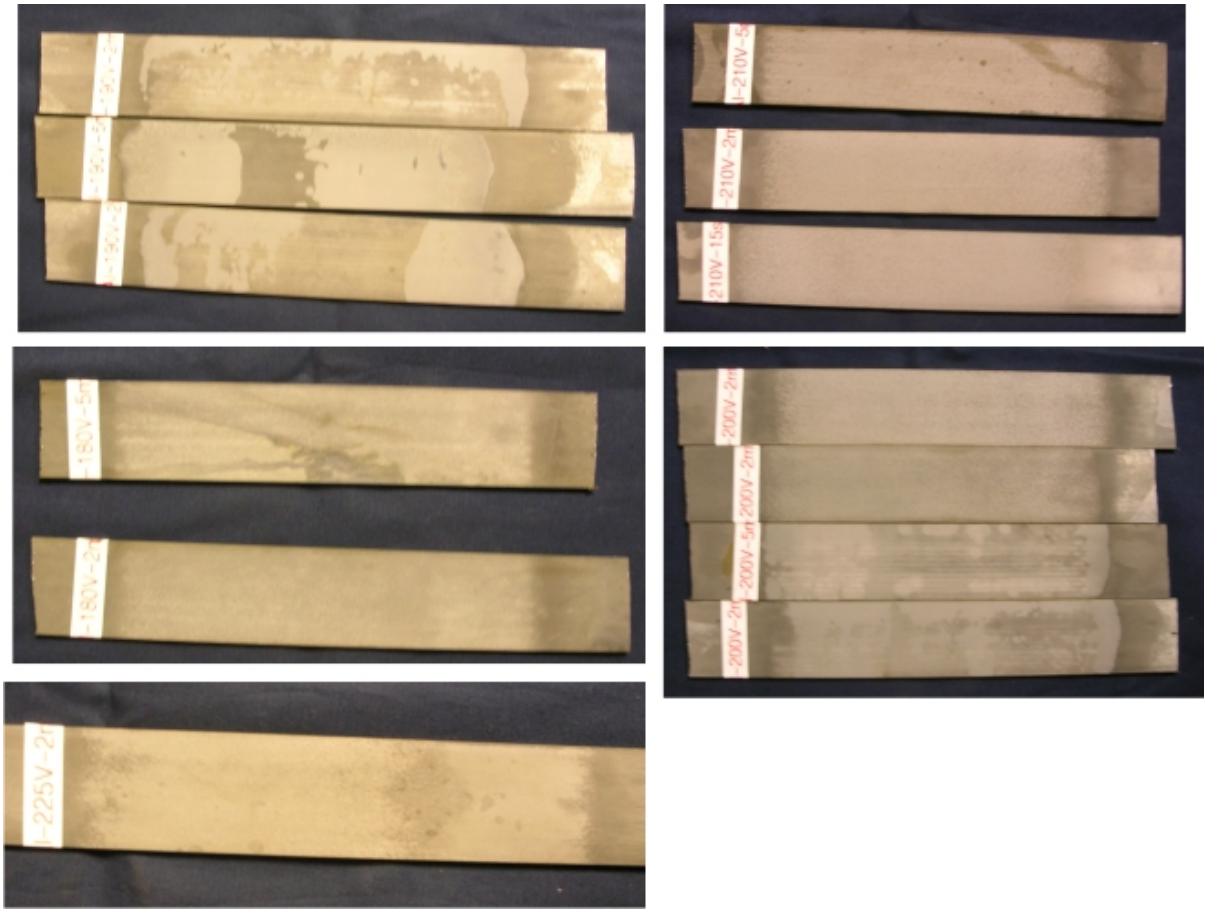

Figure 54 Appearance of Al coated specimens from the second group of experiments deposited under the conditions shown in Table 12.

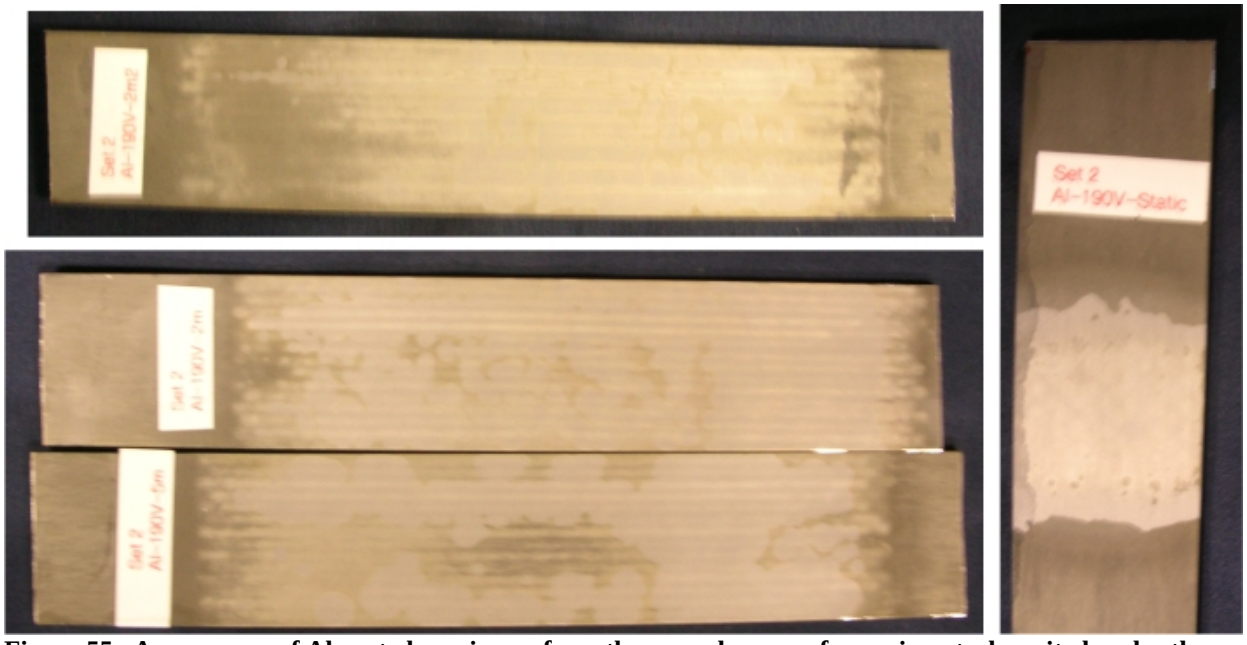

Figure 55 Appearance of Al coated specimens from the second group of experiments deposited under the

Al-180V-5m

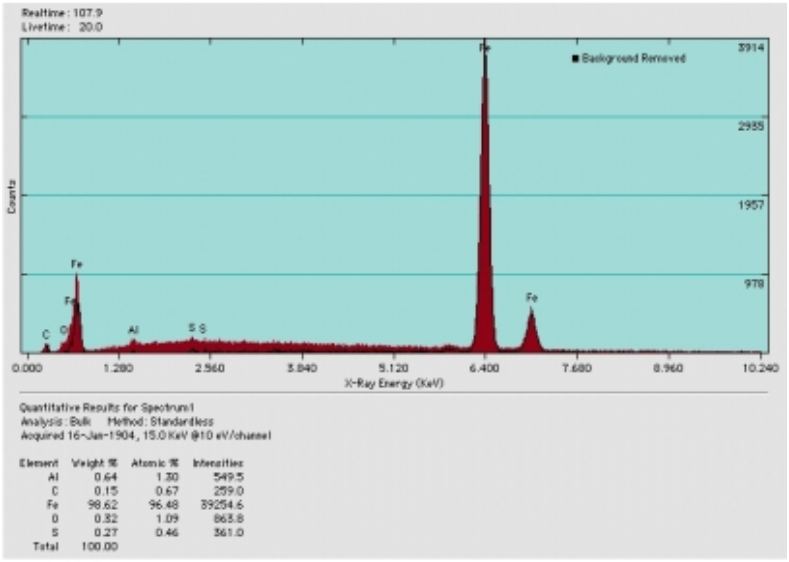

Al-190V-2m

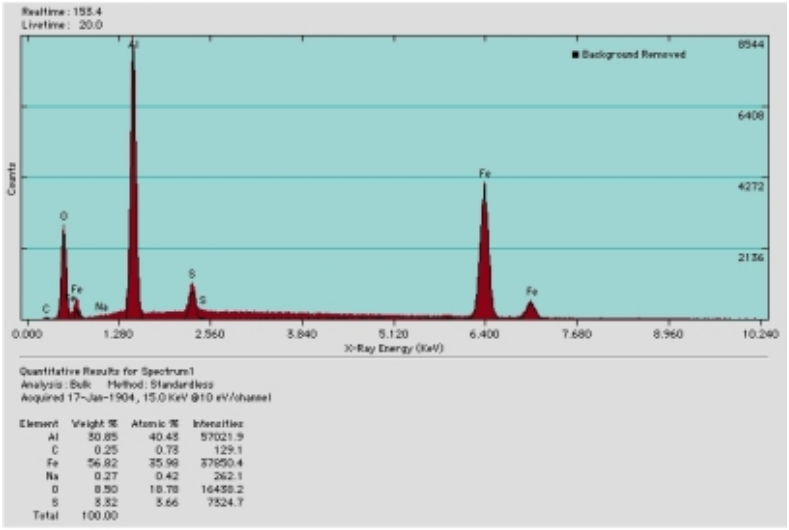

Al-190V-static

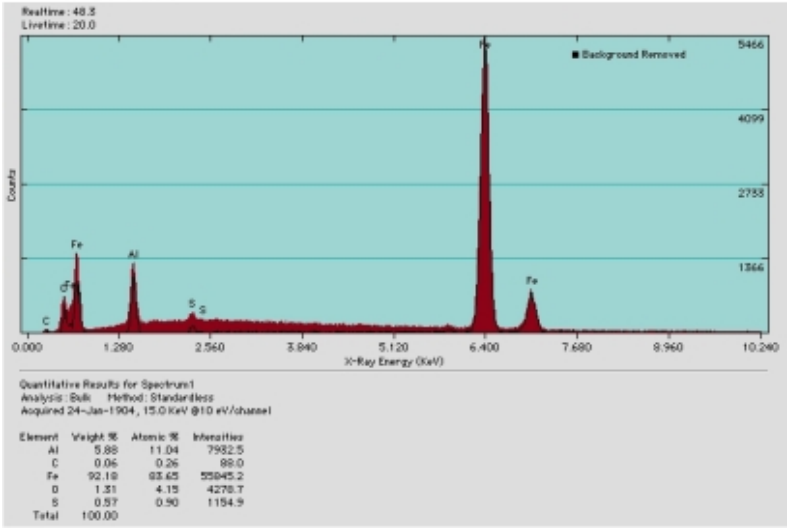

Figure 56 Typical EDS spectra from all Al deposited coatings in the second group of experiments.

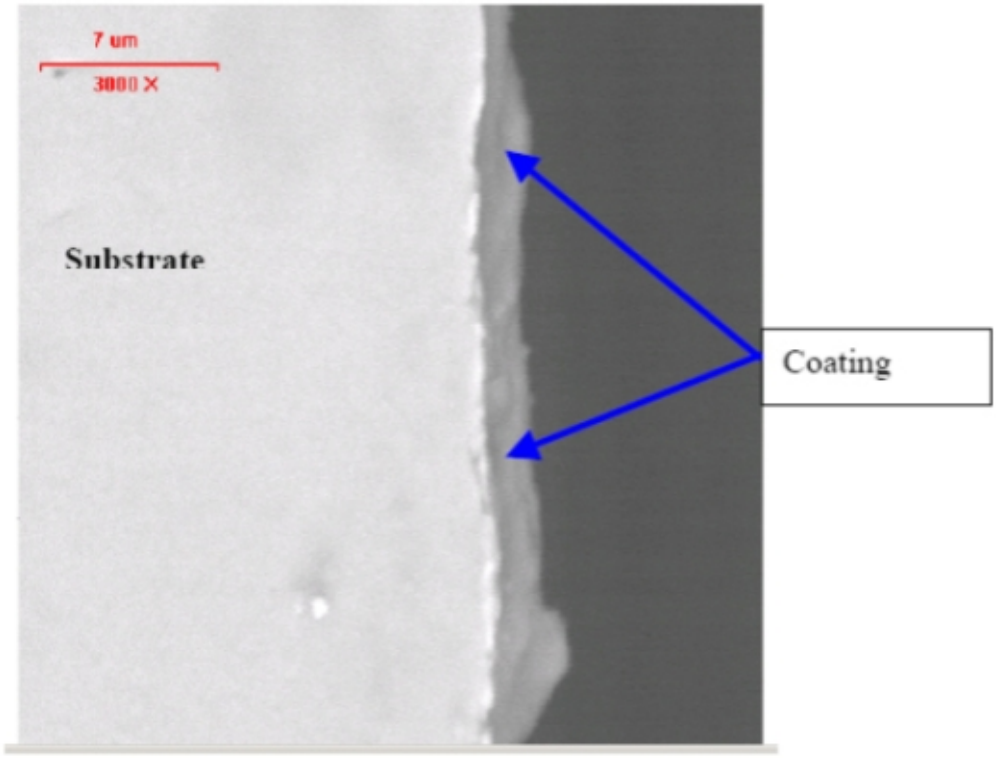

Figure 57 Backscatter scanning electron micrograph of a specimen cross section showing the Al coating.

5.3 Zn-Ni Coatings

5.3.1 Deposition and Characterization of Zn-Ni Coatings

Using a previously established pattern for process parameters, 6 sets of Zn-Ni coated samples (Zn-Ni-S1 to S6) were produced on 4340 steel strip and disc specimens, Table 15. All coated specimens except two (Zn-Ni 1a and Zn-Ni 2a) were deposited at a gap of 5 mm between the anode and the work piece (cathode). The latter two specimens were coated at a gap of 10 mm. The gap was changed to observe its effect on composition and morphology of the coatings. The electrolyte mix was $ZnSO_4.7H_2O$ and $NiSO_4.6H_2O$ for Zn and Ni salt for a total of 17% metal salt. The ratio of Zn/Ni salt was varied as shown in Table 15. About 3% Na_2SO_4 was added to increase the conductivity of the electrolyte solution. The processing parameters were: voltage 200 V, current ~ 10 A, flow rate 1 lit/min, bath temperature 65 ^oC – 75^oC, deposition time 2 min.

Table 15 Parameters associated with electrolytic bath of Zn-Ni coatings.

Sample Code	Bath Condition (Wt %)			Ni content, g/lit
	Zn Salt	Ni Salt	Zn/Ni	
Zn-Ni-S1.x	97.5	2.5	39.7	0.95
Zn-Ni-S2.x	98	2	49.9	0.76
Zn-Ni-S3.x	98.5	1.5	66.8	0.57
Zn-Ni-S4.x	96	4	24.4	1.52
Zn-Ni-S5.x	95	5	19.3	1.9
Zn-Ni-S6.x	92.5	7.5	12.6	2.85
Zn-Ni-1a	98	2	49.9	0.76
Zn-Ni-2a	97.5	2.5	39.7	0.95

x = 1, 2… represents the number of repeats for each condition. S denotes strip. Zn-Ni 1a and Zn-Ni 2a were deposited at a gap of 10 mm, where as rest of the samples were deposited at a gap of 5 mm.

All Zn-Ni coated specimens exhibited a uniform appearance, Figure 58. Analysis of the coated strips was conducted using SEM in conjunction with EDS. Figures 59-62 show different surface morphologies exhibited by the Zn-Ni coatings. Also, typical EDS spectra are shown in these figures. Examinations showed similar surface morphology for all the Zn-Ni coated specimens. Some coatings showed a mixture of nodular and needle-shaped grains when observed at high magnifications. The needles tend to be present in a higher amount for coatings deposited with higher Ni salt bath content. Also, SEM micrographs of specimen Zn-Ni 1a showed nodular morphology with high density suggesting that electrode gap plays a major role in deposition.

EDS analysis showed that the coatings are thick (20-30 microns) containing 10-30 at.% oxygen and 1.5 – 4.5 at.% sulfur (from the salt in the electrolyte) while Ni content was relatively stable at around 10 at.%. Table 16 summarizes the composition of the coatings based on the EDS analysis.

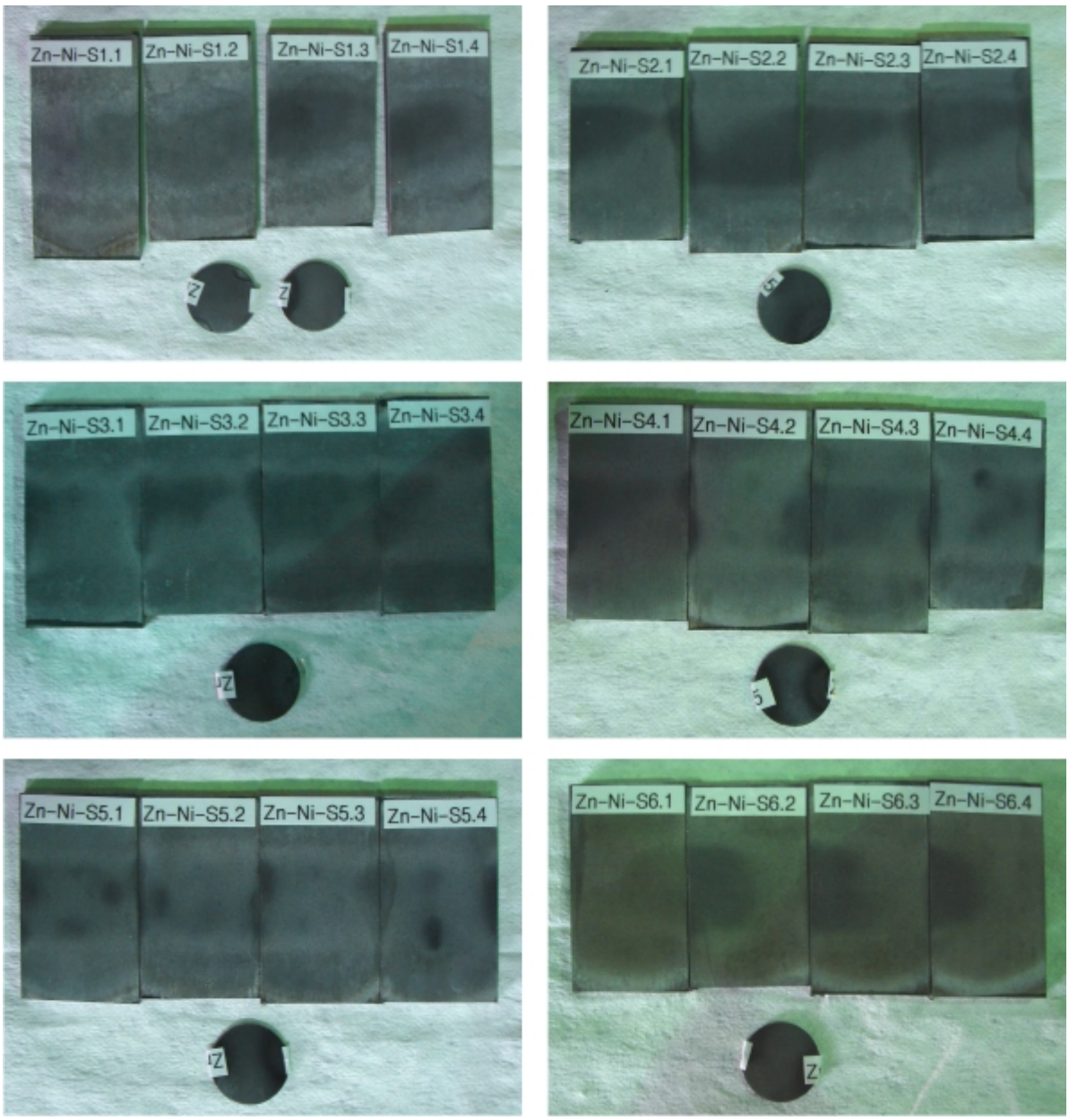

Figure 58 Surface appearance of the six sets of Zn-Ni coatings. Deposition conditions are shown in Table 15.

Table 16 Chemical composition for Zn-Ni coatings from EDS analysis using 15keV.

Code	C		Ni		O		S		Zn		Fe	
	wt. %	at. %	wt. %	at. %	wt. %	at. %	wt. %	at. %	wt. %	at. %	wt. %	at. %
Zn-Ni-S1.3	2.20	8.28	9.30	7.19	9.75	27.53	3.31	4.68	75.43	52.32	0.91	0.73
Zn-Ni-S2.3	1.35	6.05	10.14	9.31	4.18	13.83	1.99	3.29	82.34	67.53	5.45	5.14
Zn-Ni-S3.1	2.68	10.94	12.05	10.04	5.62	16.34	1.63	2.50	77.20	58.46	0.83	0.72
Zn-Ni-S4.1	0.67	3.23	13.86	13.74	2.25	8.18	0.84	1.52	82.38	73.33	1.66	1.72
Zn-Ni-S5.1	6.29	22.69	12.18	9.00	6.47	17.56	1.18	1.60	73.78	48.98	1.31	0.72
Zn-Ni-S6.1	4.16	13.87	10.76	7.33	12.94	32.38	3.44	4.30	68.63	42.03	0.57	0.41

Code	O		S		Fe		Ni		Zn	
	wt.%	at.%	wt.%	at.%	wt.%	at.%	wt.%	at.%	wt.%	at.%
Zn-Ni-1a	4.84	16.96	0.69	1.21	0.38	0.38	6.79	6.49	87.29	74.94
Zn-Ni-2a	6.46	21.38	2.00	3.31	2.84	2.69	7.80	7.04	80.90	65.58

The data is average of three readings taken at different places of 4340 strip at 200X magnification.

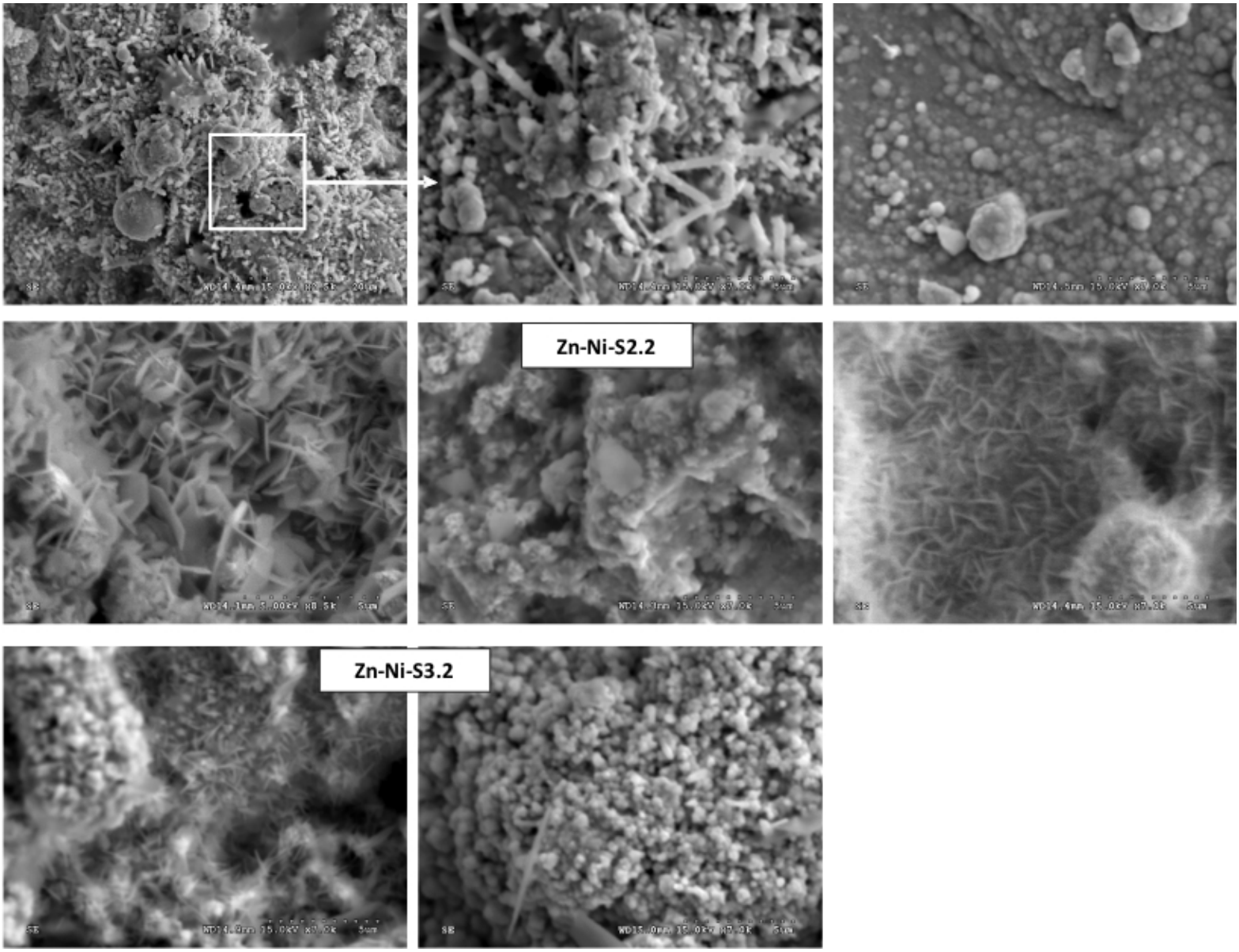

Figure 59 Surface Morphology of Zn-Ni coatings. It can be seen that the Zn-Ni coatings exhibit different surface morphologies with in a specimen and with different specimens. Two prominent features can be defined as needle shaped and nodular.

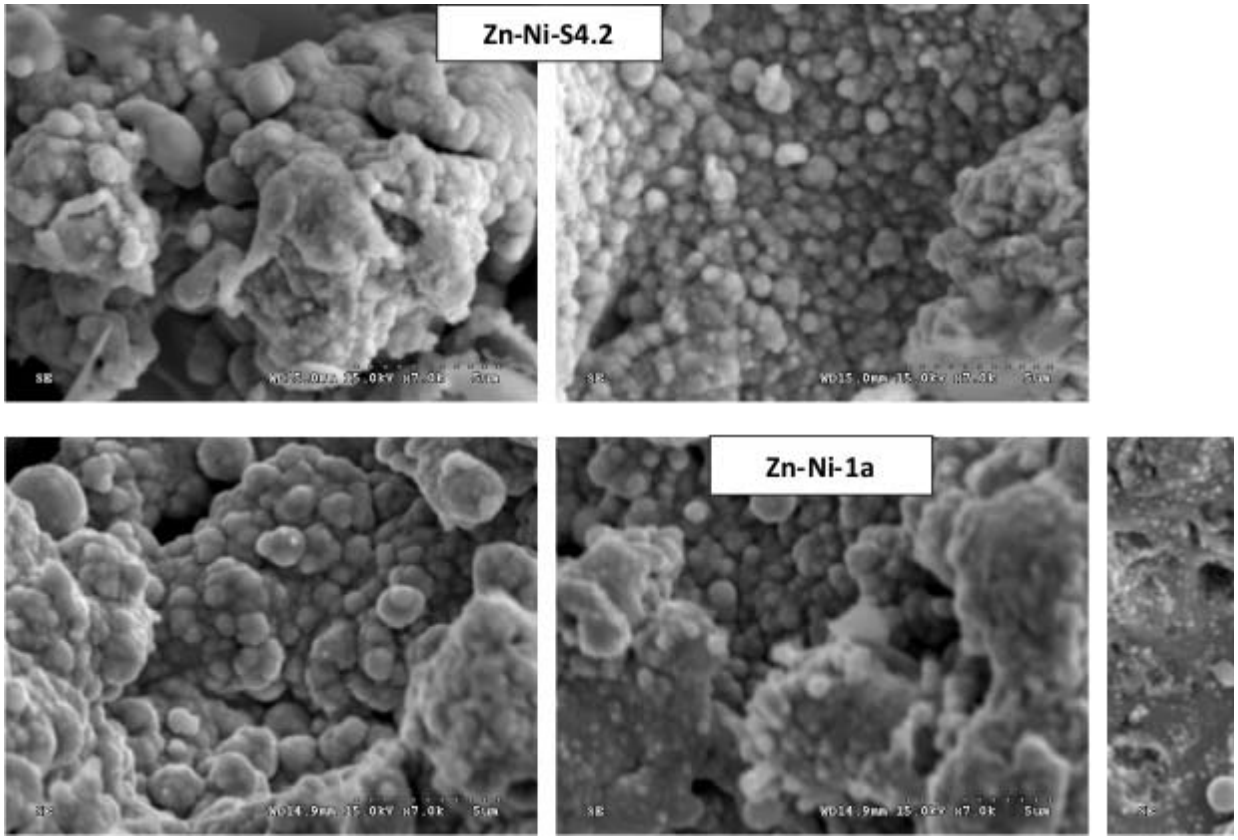

Figure 60 Surface Morphology of Zn-Ni coatings. Mostly nodular type morphology was seen in these two specimens.

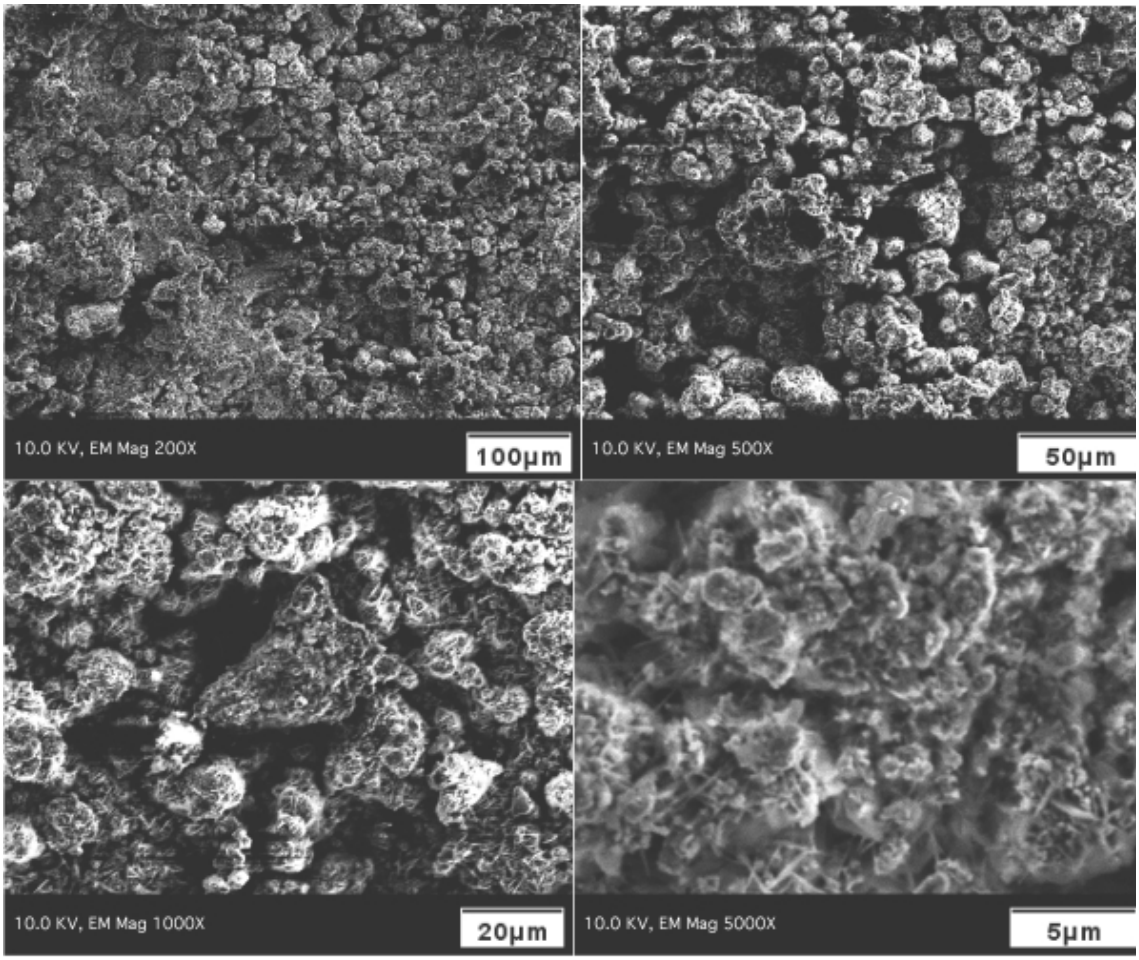

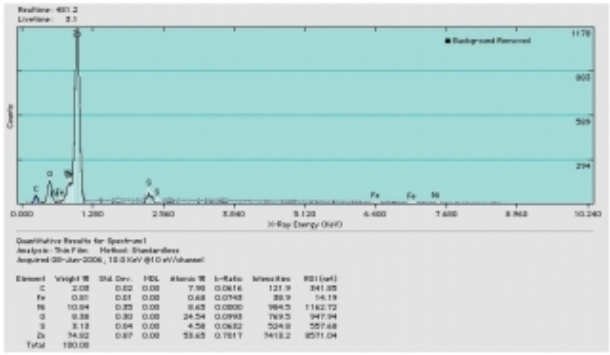

Figure 61 Scanning electron micrographs showing surface morphology of Zn-Ni coatings on strips, and typical EDS spectra for these Zn-Ni coatings.

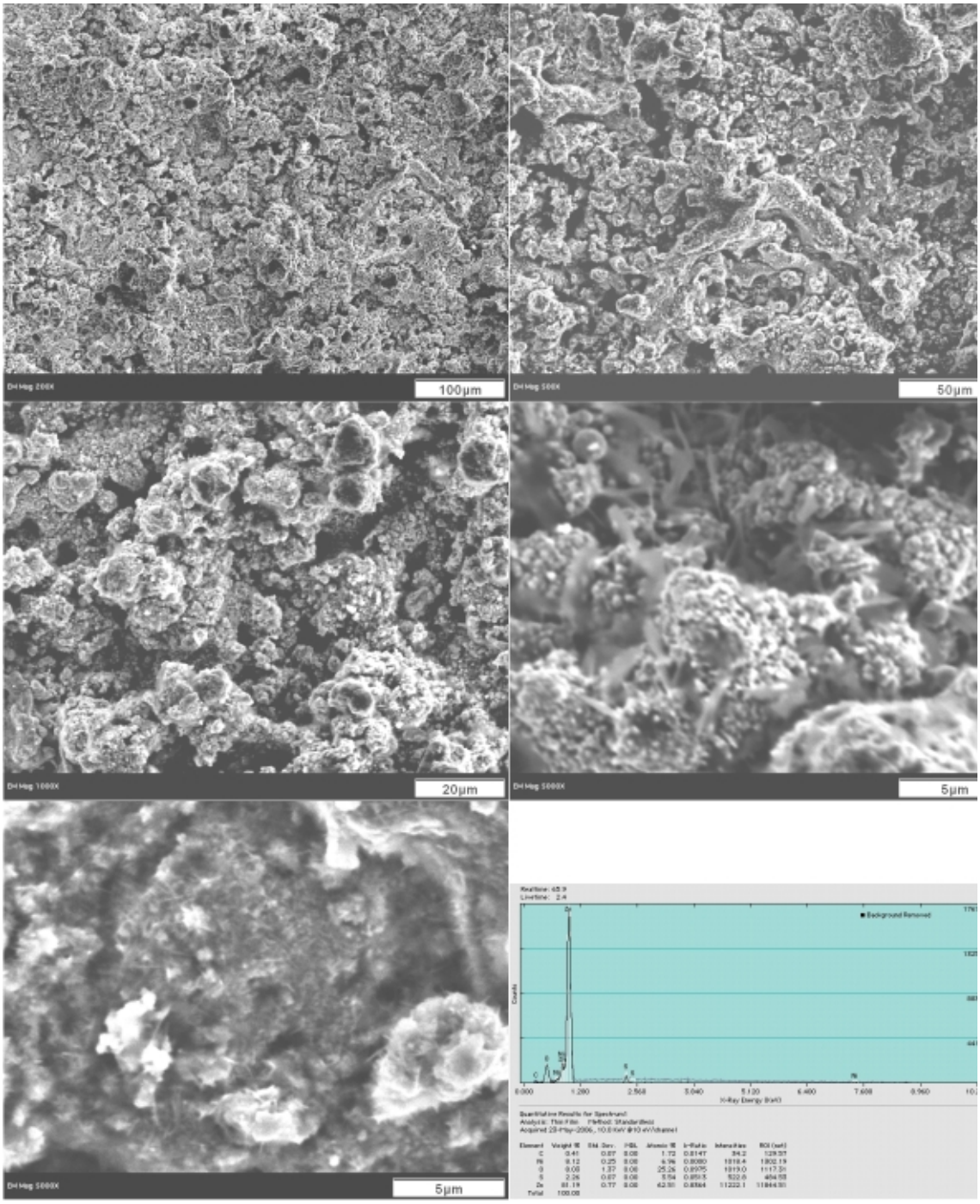

Figure 62 Scanning electron micrographs showing typical surface morphology of Zn-Ni coatings on disc specimens and corresponding EDS spectra.

XRD pattern analysis, Figure 63, indicated that the main phase is γ-Zn-Ni. SEM analysis of Zn-Ni coated samples using a higher electrode gap (10 mm) showed less surface uniformity compared to the previous samples (coated with a smaller electrode gap, 5 mm). Also, examinations at high magnification showed spherical shaped grains and total absence of the needle feature.

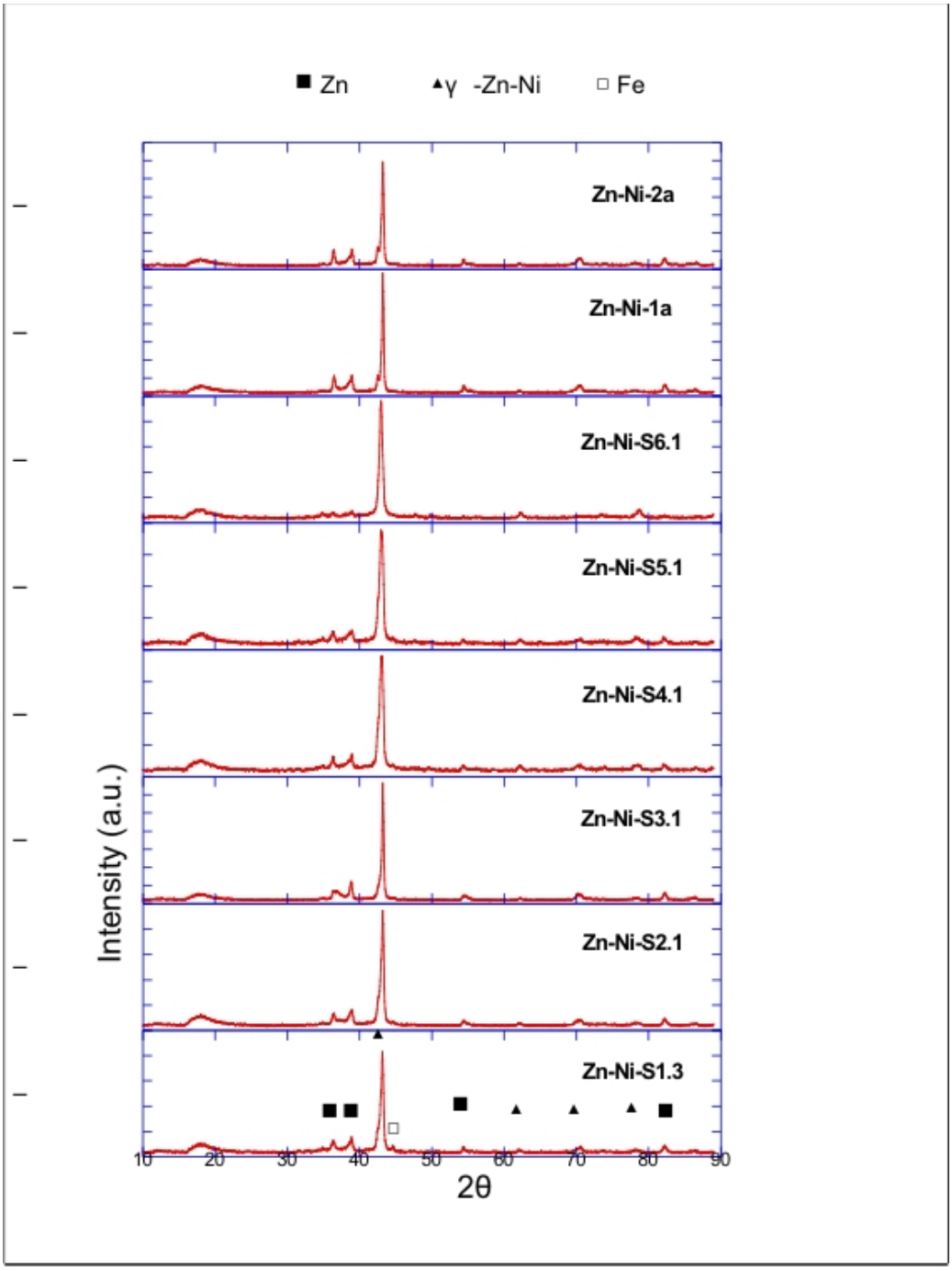

Figure 63 Summary of X-ray diffraction results for Zn-Ni coatings.

Potentiostatic and potentiodynamic polarization tests were performed on all Zn-Ni coated specimens using tap water and 3.5% NaCl solution at room temperature. Figures 64 and 65 show the variation of the corrosion potential as a function of time. The corrosion potential was monitored until it was stabilized (~6 h). For both environments, all coatings show an active behavior (potential moves to active range) with the corrosion potential in the range of -800 to -1000 mV (SCE). In view of the value of the corrosion potential of steel in these environments (~ -660 mV), it is expected that the Zn-Ni coatings will act as sacrificial anodes and provide protection to the steel structure. A similar role is played by the Cd coatings used currently.

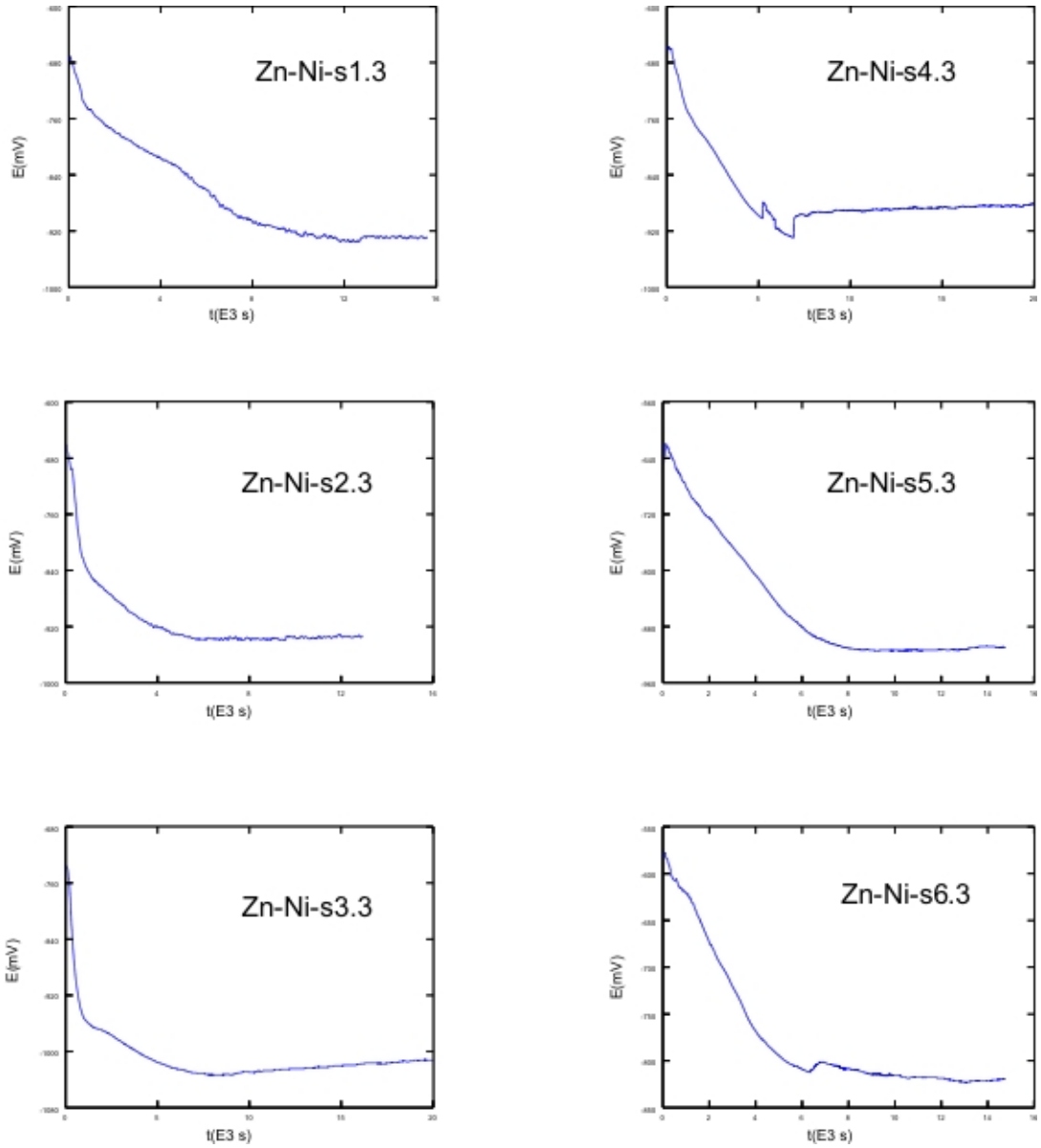

Figure 64 Ecorr vs Time for Zn-Ni-S1.3 – 6.3 samples in tap water.

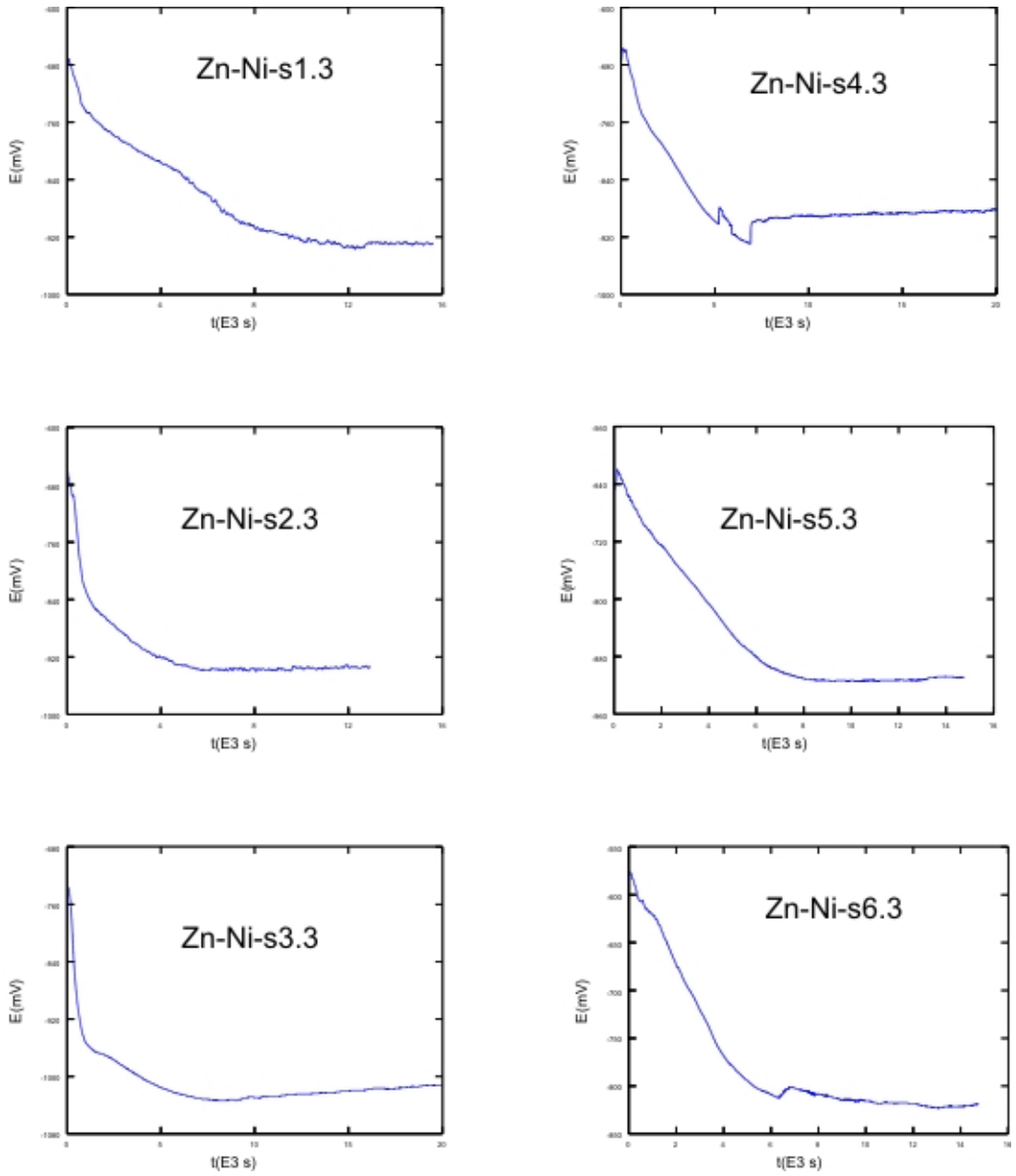

Figure 65 Ecorr vs Time for Zn-Ni-S1.3 – 6.3 samples in 3.5% NaCl.

Figures 66 and 67 present the anodic polarization behavior of the Zn-Ni coatings. All coatings showed an active behavior compared to the range of the corrosion potential of steel. This clearly shows that the present Zn-Ni coatings can provide anodic protection to the underlying 4340 steel. Corrosion rates were calculated from the anodic polarization experiments and the corrosion characteristics are summarized in Table 17.

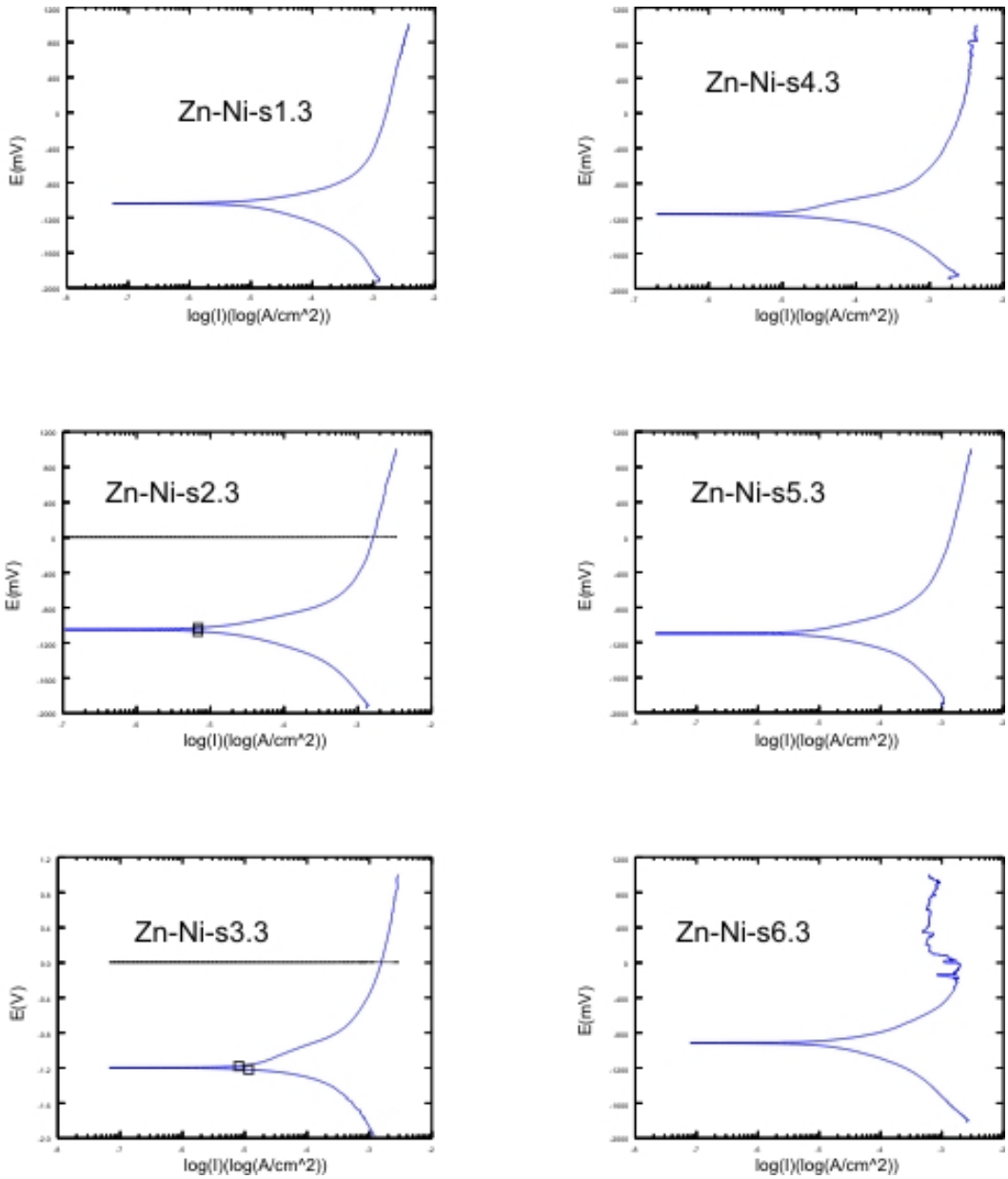

Figure 66 Anodic polarization behavior of Zn-Ni-S1.3 – 6.3 samples in tap water.

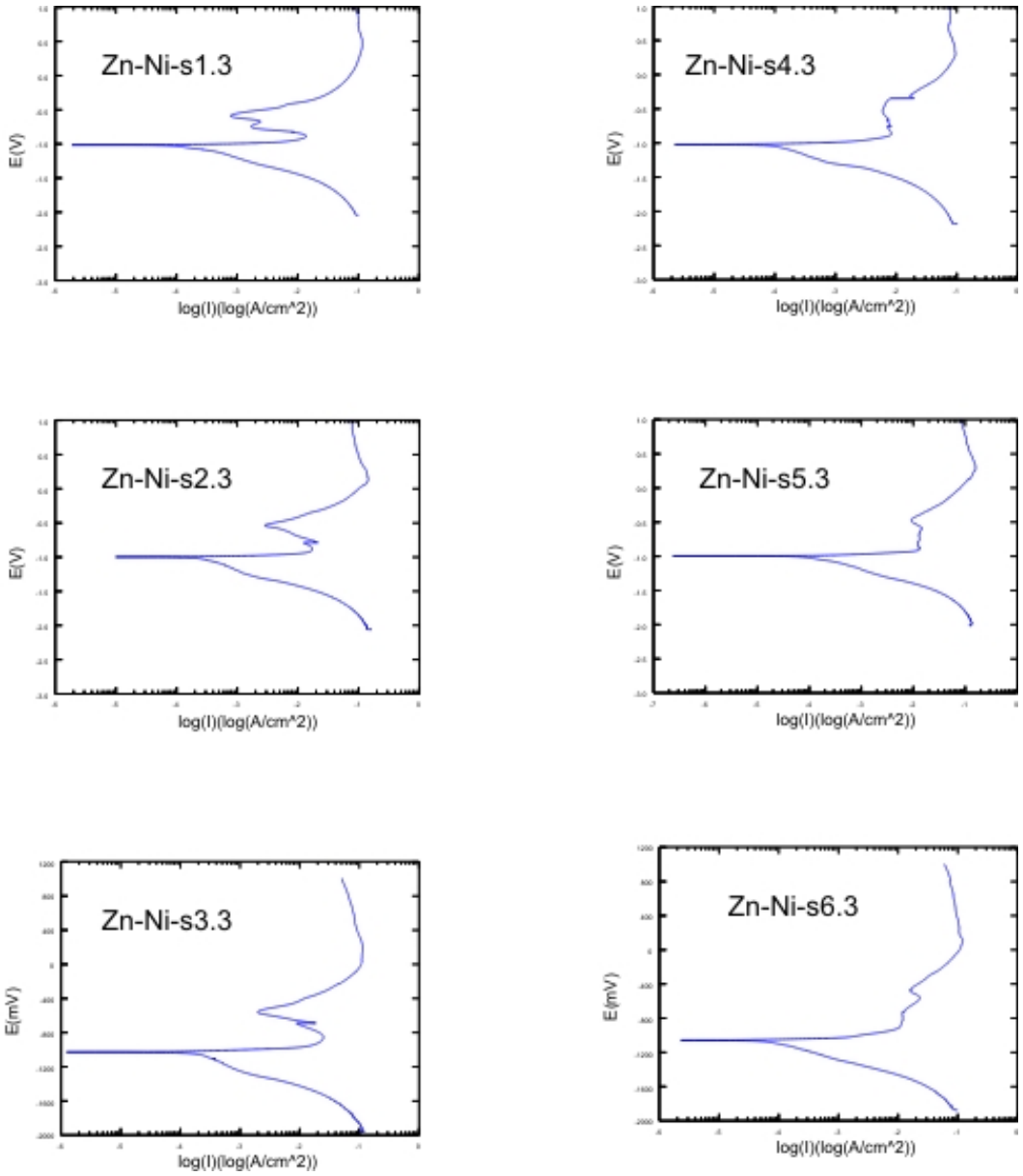

Figure 67 Anodic polarization behavior of Zn-Ni-S1.3 – 6.3 samples in 3.5% NaCl.

Table 17 Corrosion potential and corrosion rate of Zn-Ni coatings.

Sample	**E [mV]**		**I_{corr}** [mA/cm^2]	
	tap water	NaCl 3.5%	tap water	NaCl 3.5%
Zn-Ni-1.3	-0.940	-1.040	0.04	4.0
Zn-Ni-2.3	-0.940	-1.050	0.04	6.8
Zn-Ni-3.3	-1.020	-1.060	0.09	2.2
Zn-Ni-4.3	-0.900	-1.050	0.08	2.5
Zn-Ni-5.3	-0.920	-1.020	0.04	2.1
Zn-Ni-6.3	-0.820	-0.980	0.06	1.6

5.3.2 Coating of Cylindrical Specimens

(a) Preliminary Study

Several dummy HE notched, round specimens and fatigue specimens were Zn-Ni coated at CAP Technologies under various conditions (first batch of Zn-Ni coated samples). This preliminary study was conducted in order to ensure proper deposition conditions for the cylindrical HE and fatigue specimens. Three (3) HE dummy samples were analyzed at UTA. The first was a HE small sample coated with Zn-Ni coating (named HE small sample); the second was a HE large sample coated with Zn-Ni coating (named HE large sample); the third one was a HE large sample coated with Zn-Ni coating and then treated with Metalast TCP-HF conversion coating which was applied one week after the Zn-Ni coating was deposited. The surface was activated with 1% nitric acid for 30 seconds and rinsed before applying the conversion coating (named HE large sample with conversion coating). All the deposition parameters for the Zn-Ni are shown in Table 18.

Microstructure of first batch of Zn-Ni coatings on cylindrical specimens

The surface morphology and representative chemical composition of the coating on the large HE sample conducted by SEM in conjunction with EDS are shown in Figure 68. The Zn-Ni coating on this sample was mainly composed of a uniform nodular phase, Fig. 68(a). This coating showed a small amount of flake phase at a high magnification, Fig. 68(b). EDS analysis showed that the coating contained about 32 at. % oxygen and 10 at.% Ni. The Zn and Ni relative contents are 75.51 at. % and 24.49 at.%, respectively, regardless of all other elements in the coating. The ratio of Zn and Ni of the nodular phase was 76.57:23.43 or about 3:1, Fig. 68(b). EDS analysis on the flake phase showed some Fe and S. However, the ratio of Zn and Ni of the flake phase was 76.55:23.45 which is also close to 3:1, Fig. 68(c). Thus, more than likely the coating is composed of γ-Zn-Ni phase similar to that observed in the coating on the flat samples.

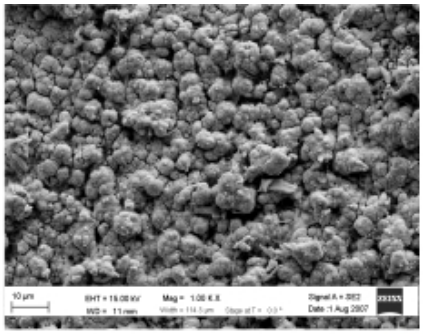

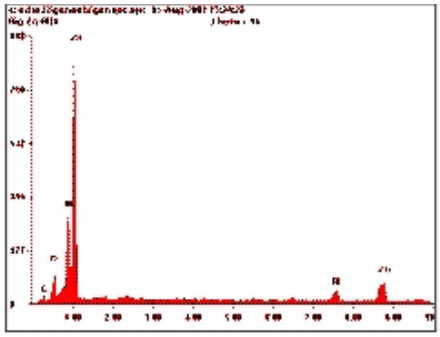

Element	Wt %	At %
NiK	22.56	24.49
ZnK	77.44	75.51

Element	Wt %	At %
C K	09.33	26.88
O K	14.74	31.88
NiK	17.29	10.19
ZnK	58.64	31.05

(a)

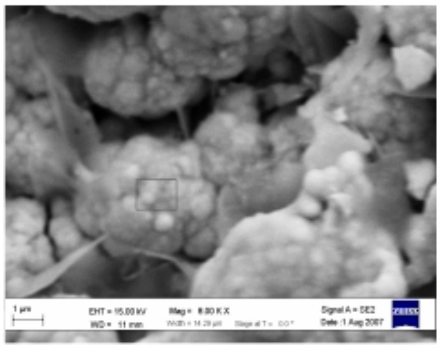

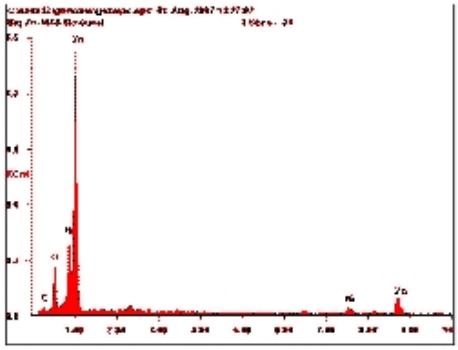

Element	Wt %	At %
NiK	21.56	23.43
ZnK	78.44	76.57

Element	Wt %	At %
C K	12.48	28.19
O K	27.21	46.15
NiK	13.24	06.12
ZnK	47.08	19.55

(b)

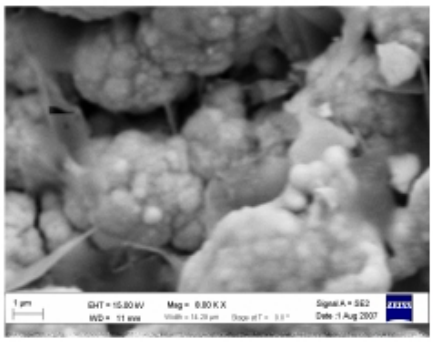

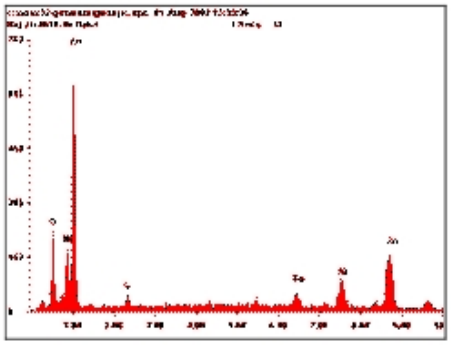

Element	Wt %	At %
NiK	21.58	23.45
ZnK	78.42	76.55

Element	Wt %	At %
O K	15.99	42.22
S K	02.30	03.03
FeK	06.66	05.04
NiK	16.90	12.16
ZnK	58.15	37.56

(c)

Figure 68 Surface morphology and representative chemical composition of the coating on the HE large sample.

The surface morphology and representative chemical composition of the coating on the small HE sample are shown in Fig. 69. The Zn-Ni coating on this sample was composed of a nodular phase and a flake phase which is present at a much higher percentage than that in the coating on the HE large sample. The zinc and nickel ratio is about 3:1 (relative contents are 74.87 at. % and 25.13 at. %, respectively, regardless of all other elements in the coating), Fig. 69(a). This is very close to the ratio of the coating on the HE large sample.

The cross-section SEM analysis of the HE large sample and HE small sample under 2000x and 4000x magnification showed a continuous but somewhat porous structure with a thickness of 4~5 μm, while the coating on the HE small sample showed a dense and continuous structure with a thickness of 1~2 μm. The coating on the HE small sample is thinner but denser than that on the HE large sample.

The phase structure of the coatings on the HE large sample and HE small sample was studied by X-ray diffraction. Figure 70(a) shows that all peaks on the XRD patterns of the two coatings were associated to Fe and γ_1 phase (γ-Ni_5Zn_{21}) which is corresponding to the nodular phase from the surface morphology and no clear difference could be found from the two patterns. However, the XRD patterns at the 2θ range of 30-50° for the two samples showed a clear difference. A more pronounced peak at 44.2° 2θ most likely corresponding to γ_2 phase (γ-$NiZn_3$), was present in

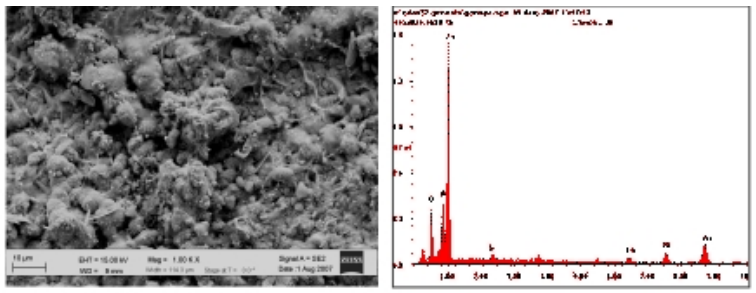

Element	Wt %	At %
NiK	23.16	25.13
ZnK	76.84	74.87

Element	Wt %	At %
O K	27.52	58.80
S K	3.39	3.60
FeK	6.43	3.94
NiK	14.62	8.52
ZnK	48.03	25.13

(a)

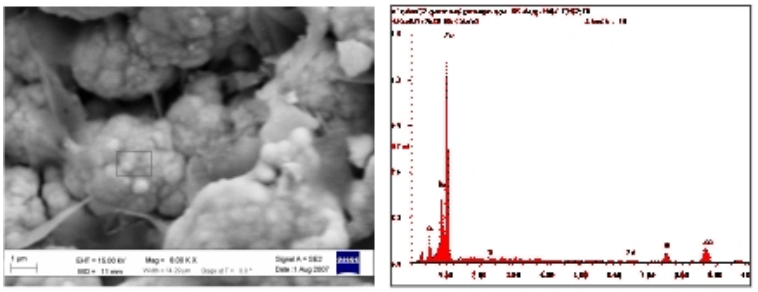

Element	Wt %	At %
NiK	23.60	25.60
ZnK	76.40	74.40

Element	Wt %	At %
O K	16.19	42.65
S K	2.35	3.09
FeK	3.87	2.92
NiK	18.31	13.15
ZnK	59.29	38.19

(b)

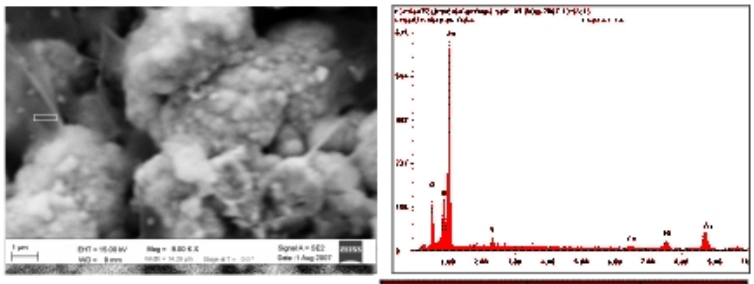

Element	Wt %	At %
NiK	21.54	23.41
ZnK	78.46	76.59

Element	Wt %	At %
O K	27.55	58.62
S K	4.64	4.93
FeK	3.71	2.26
NiK	13.84	8.03
ZnK	50.25	26.16

(c)

Figure 69 Surface morphology and representative chemical composition of the coating on the HE small sample.

the XRD pattern of the coating on the small HE sample while a much smaller peak appeared at this angle for the HE large sample, Fig. 70(b). Comparing the difference of the relative content of the nodular and flake phases in the Zn-Ni coatings on the two samples, this γ_2 phase could be associated with the flake phase.

Table 18 Deposition parameters for the three HE specimens.

Sample	pH	Conductivity (mS @ °C)	Electrolyte temp (°C)	Voltage (V)	Current (Amps)	Rotation (RPM)	Dwell time (s)
158	3.4	42 @ 85	85	190	50	6	20
160	3.0	45 @ 86	86	190	50	6	20
161	2.9	47 @ 85	85	190	50	6	20

Note: 158: small HE sample with Zn-18%Ni coating; 160: large HE sample with Zn-18%Ni coating; 161: large HE sample with Zn-18%Ni coating/Metalast TCP-HF conversion coating.

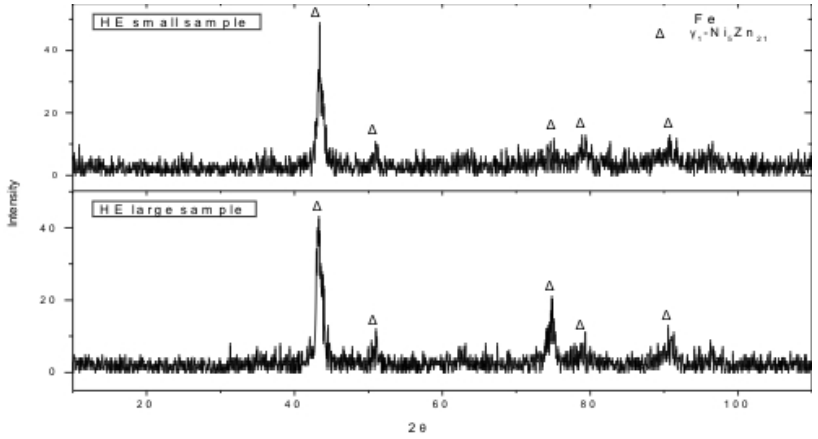

(a)

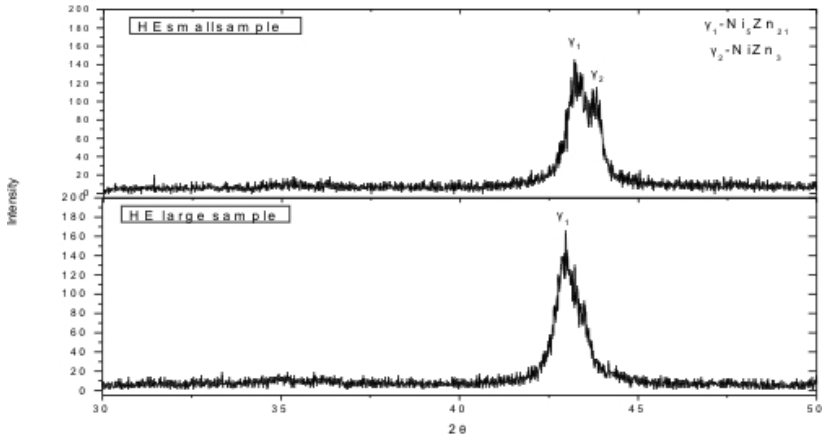

(b)

Figure 70 . X-ray diffraction patterns of the HE samples: a) 2θ range of 10-110° and b) 2θ range of 30-50°.

Corrosion testing of the first batch of Zn-Ni coatings on cylindrical specimens

The variation of the corrosion potential as a function of time for specimens 158 (small HE) and 160 (large HE) in tap water is shown in Fig. 71(a). The large HE sample exhibited a higher potential than that of the small HE sample. The large HE sample potential stabilized at around -350 mV, while the small HE sample stabilized at -485 mV. The anodic polarization behavior of the Zn-Ni coatings in tap water at room temperature is presented in Figure 71(b). The anodic polarization response is consistent with the potential measurements with the large HE sample exhibiting more noble behavior than that of the small HE sample. This difference can be attributed either to the presence of Fe and S in the large HE sample or to its lower percentage of the γ_2 phase present.

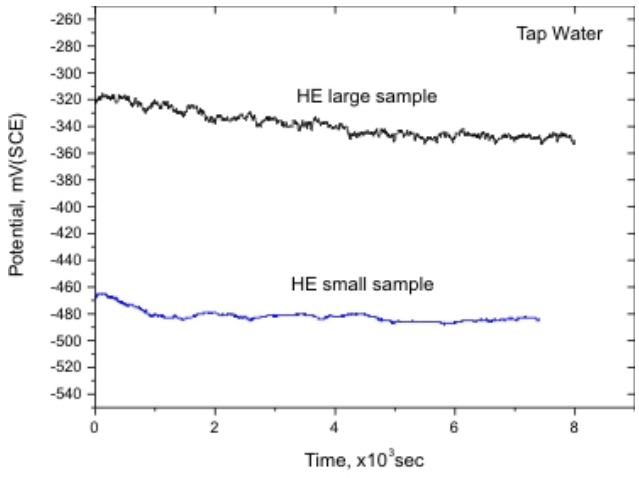

(a)

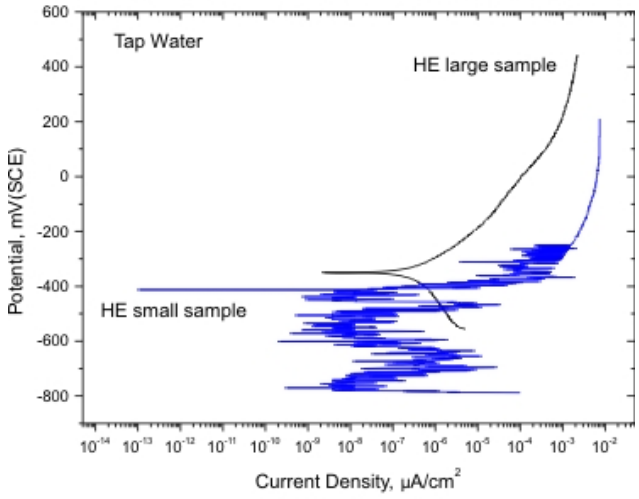

(b)

Figure 71 (a) Ecorr vs Time Anodic polarization behavior of the HE samples in tap water.

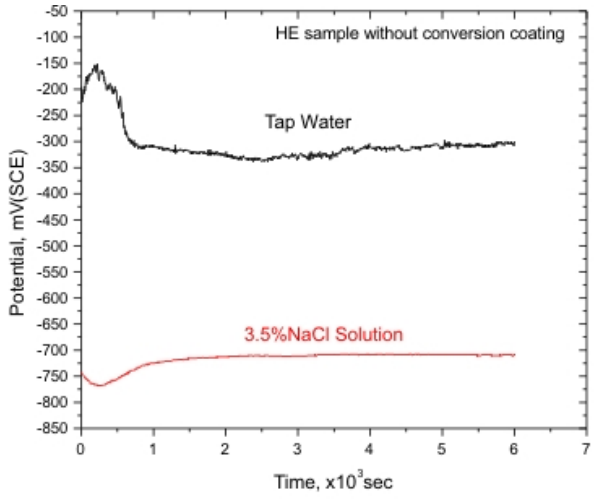

(a)

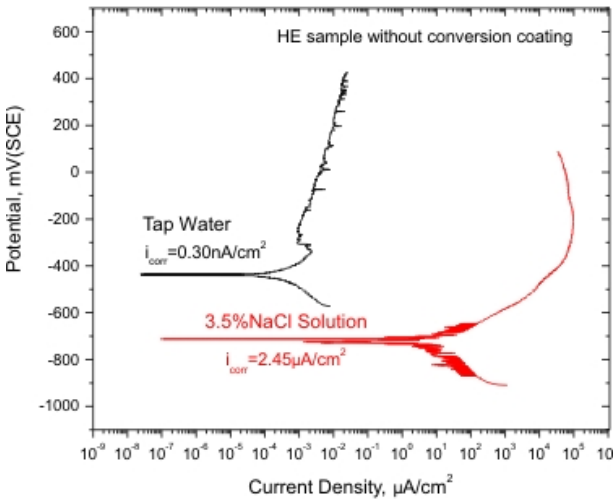

(b)

Figure 72 (a) Ecorr vs Time and (b) anodic polarization behavior of the large HE sample with Zn-18%Ni coating in tap water and 3.5% NaCl solution.

The variation of the corrosion potential of the large HE sample with Zn-Ni as a function of time was performed using tap water and 3.5% NaCl solution at room temperature, Fig. 72(a). In tap water the sample stabilized at around -300 mV, while in the 3.5% NaCl solution it stabilized at around -710 mV, Fig. 72(a). Apparently, the latter solution is more aggressive resulting in a lower potential. The anodic polarization behavior of the sample in tap water and 3.5% NaCl solution at room temperature is presented in Figure 72(b). The corrosion rate of the sample in tap water was 0.30 nA/cm^2, while the corrosion rate of the coating in the 3.5% NaCl solution was 2.45 μA/cm^2. These differences are consistent with the fact that the NaCl is a more aggressive electrolyte.

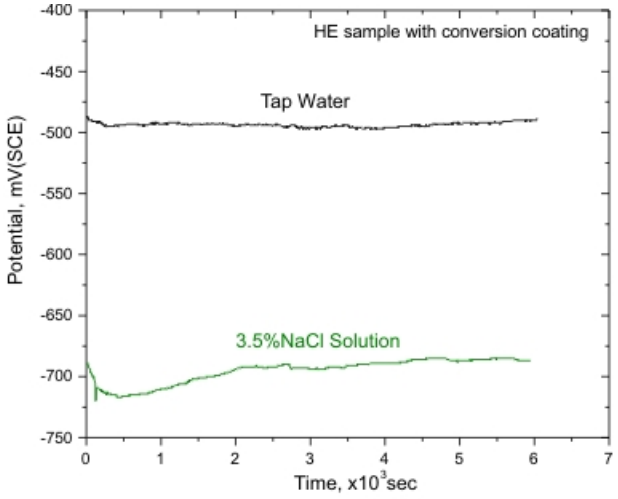

(a)

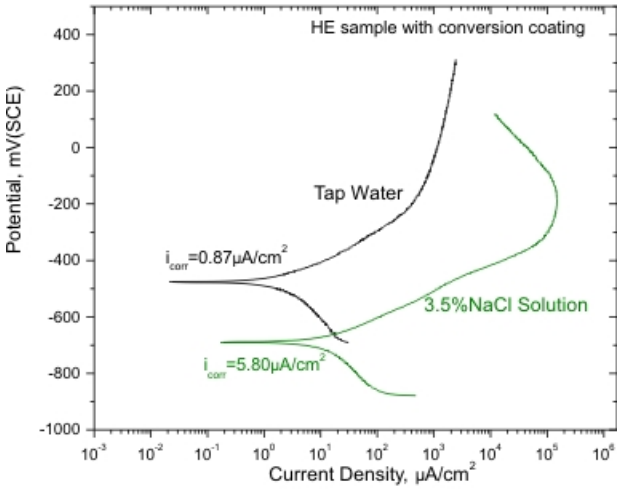

(b)

Figure 73 (a) Ecorr vs Time and (b) anodic polarization behavior of the large HE sample with Zn-18%Ni and TCP-HF treatment in tap water and 3.5% NaCl solution.

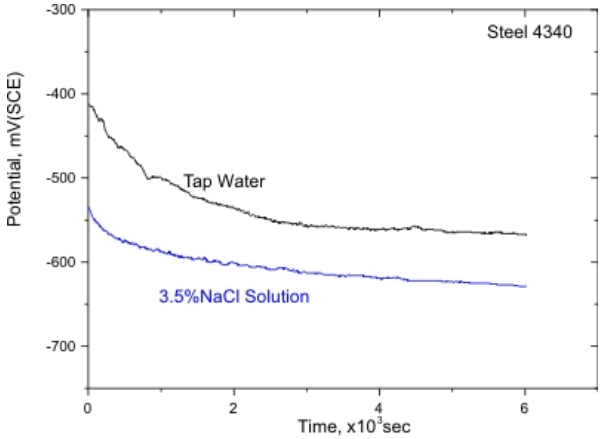

(a)

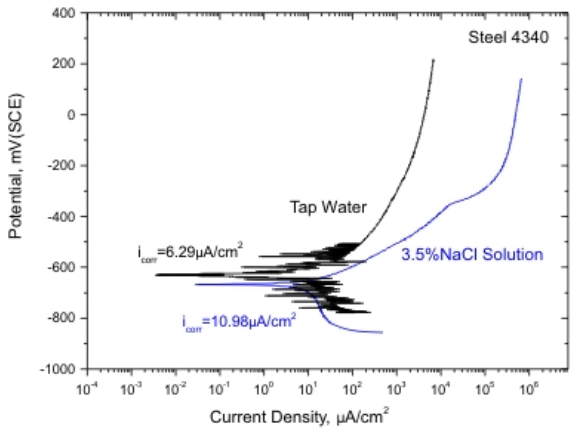

(b)

Figure 74 (a) Ecorr vs Time and (b) anodic polarization behavior of 4340 steel in tap water and 3.5% NaCl solution.

The variation of the corrosion potential with time of the large HE sample with Zn-18%Ni treated with Metalast TCP-HF in tap water and 3.5% NaCl solution is shown in Fig. 73(a). In tap water, the sample stabilized at around -490 mV, while for the 3.5% NaCl solution it stabilized at around -690 mV. Similarly, the anodic polarization behavior in NaCl was more active compared to that in tap water, Fig. 73(b). The corrosion rate in tap water was 0.87 $\mu A/cm^2$, while that in the 3.5% NaCl solution was 5.80 $\mu A/cm^2$. Metalast found to cause surface activation of the sample moving its response to a more direction.

The variation of the corrosion potential with time of 4340 steel was performed using tap water and 3.5% NaCl solution, Fig. 74(a). In tap water, the potential stabilized at around -570 mV, while in the 3.5% NaCl solution, it stabilized at around -630 mV. The anodic polarization behavior of the steel in tap water and 3.5% NaCl solution is presented in Fig. 74(b). The corrosion rate of the steel in tap water and 3.5% NaCl solution was 6.29 $\mu A /cm^2$ and 10.98 $\mu A/cm^2$, respectively.

To compare the corrosion properties of the coated samples with that of 4340 steel, the corrosion potentials and the anodic polarization graphs were plotted together. Fig. 75 clearly shows that the corrosion potential of steel is anodic with respect to that of the large HE sample and the one treated with Metalast. Thus, these coatings at the present Ni content don't qualify as sacrificial coatings for 4340 steel. The corrosion potential of the coated samples in NaCl solution was found to be anodic with respect to steel. The anodic polarization behavior in tap water is in agreement with the corrosion potential results with 4340 steel exhibiting higher corrosion rate than that of the coated samples, Fig. 76. Specifically, the corrosion rates in tap water were: large HE sample without conversion coating (0.30 nA/cm^2) < large HE sample with conversion coating (0.87 $\mu A/cm^2$) <4340 Steel (6.29 $\mu A /cm^2$). In NaCl solution, the behavior showed a similar trend: large HE sample without conversion coating (2.45 $\mu A/cm^2$) < large HE sample with conversion coating (5.80 $\mu A/cm^2$) <Steel 4340 (10.98 $\mu A /cm^2$).

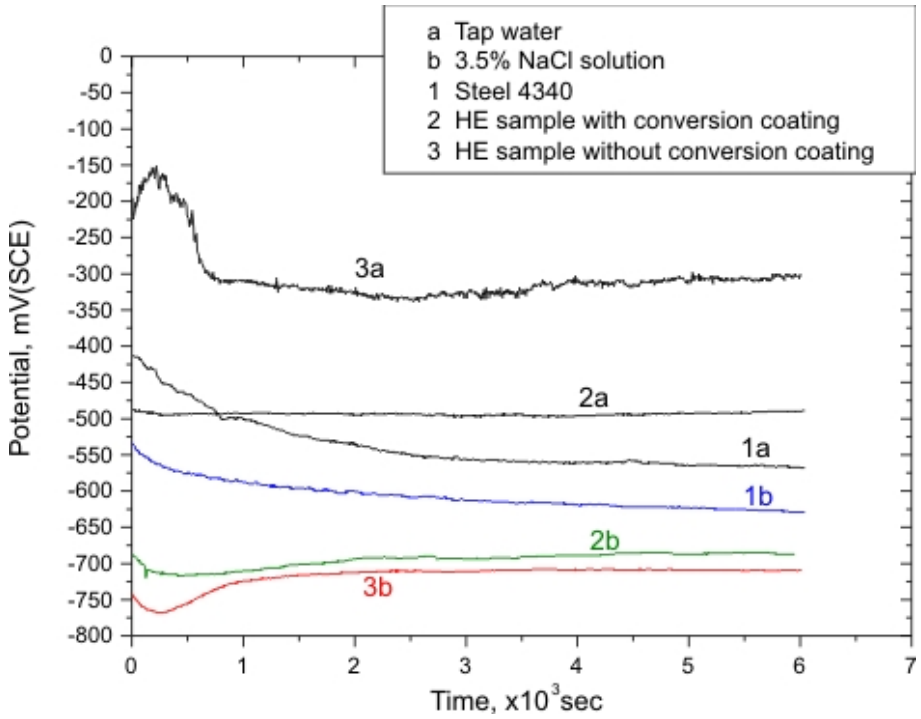

Figure 75 Ecorr vs Time for the steel 4340 and the large HE large sample with Zn-18%Ni coating with/without conversion coating in tap water and 3.5% NaCl solution: 1a) Steel 4340 in tap water, 2a) Zn-18%Ni coating with conversion coating in tap water, 3a) Zn-18

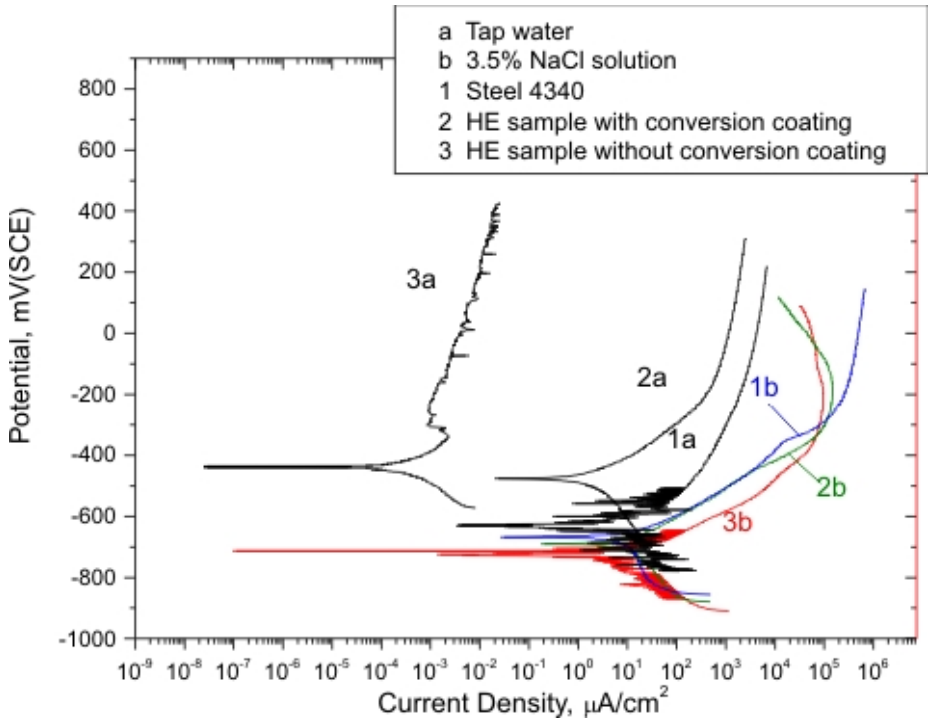

Figure 76 Anodic polarization behavior of the steel 4340 and the large HE large sample with Zn-18%Ni with/without conversion coating in tap water and 3.5% NaCl solution: 1a) Steel 4340 in tap water, 2a) Zn-18%Ni coating with conversion coating in tap water, 3a)

Conclusions

The SEM/EDS and XRD analyses and the corrosion testing results showed that the relative content of Zn and Ni in the coatings deviated from the Ni and Zn concentration in the electrolyte. The Zn-Ni coatings were composed of nodular and flake phases with high Ni content (~25% Ni). All the Zn-18%Ni coatings with/without Metalast TCP-HF conversion coating are not protective for the steel 4340 substrate due to their high Ni content.

(b) Deposition of second batch of Zn-Ni Coatings with <25 at% Ni

Additional cylindrical HE and fatigue specimens were Zn-Ni coated at CAP Technologies with lower Ni salt content in the electrolyte in order to reduce the Ni content below the 25 at.% level (second batch). All specimens were EPT cleaned prior to coating treatments. Five specimens were analyzed at UTA; namely three small HE and two fatigue samples. The deposition conditions for these Zn-Ni coatings are listed in Table 19.

Table 20 summarizes the chemical composition of all five samples. Fig. 77 shows a typical EDS spectrum from the fatigue sample 274 with Zn-Ni/no conversion coating. Based only on the Zn and Ni content, Table 20 shows that the present coatings had a significantly lower Ni content compared to the previous batch. The surface morphology of all five samples was examined by SEM and representative morphologies are shown in Figs. 78-82. The coating of the sample 274 was mainly composed of a nodular phase with a small amount of the flake phase. Sample 275 was composed entirely of a nodular phase without any visible flake phase even at 5000x magnification, 82. On the surface of sample 232 only a nodular phase could be seen, while a mixture of a nodular and a flake phase was evident on the surface of samples 222 and 244. The flake phase of the coating on the sample 244 was more uniform than that on sample 222, Fig. 78-80.

The variation of the corrosion potential with time and the anodic polarization behavior in tap water and 3.5% NaCl solution for samples 222, 232, 244, 274, 275 and 4340 steel is shown, respectively in Figs. 83-88. In addition, the variation of the corrosion potential with time for all specimens is shown in Fig. 89. Similarly, the anodic polarization behavior for all specimens in tap water and 3.5% NaCl solution is shown in Figs. 90 and 91, respectively. The stabilized corrosion potentials and the corrosion rates for all specimens are listed in Table 21.

The corrosion potential results in tap water show that all specimens exhibited an anodic potential with respect to that of steel (-533 mV) except specimen 275 (-504 mV) that was more noble than steel. This particular specimen had the highest Ni content reaffirming the previous observations that high Ni content promotes nobility and does not qualify for a sacrificial coating for steel. Also, specimen 274 exhibited a corrosion potential (-536 mV) similar to that of steel and does not qualify either for such an application. In the NaCl environment only specimen 274 exhibited a higher potential (-713 mV) than that of steel (-728 mV) with specimens 275 and 244 being the closest to

that of steel in this environment. Thus, based on the laboratory corrosion results coatings 244, 274 and 275 do not qualify for sacrificial coatings. Note that these three coatings had the highest Ni content among the five coatings of the second batch.

The anodic polarization testing for the remaining two coatings 222 and 232 showed a similar low corrosion rate in tap water (3-3.5 $\mu A/cm^2$) and NaCl solution (~5 $\mu A/cm^2$). This suggests that besides providing protection, these two coatings may have a long life time in these environments.

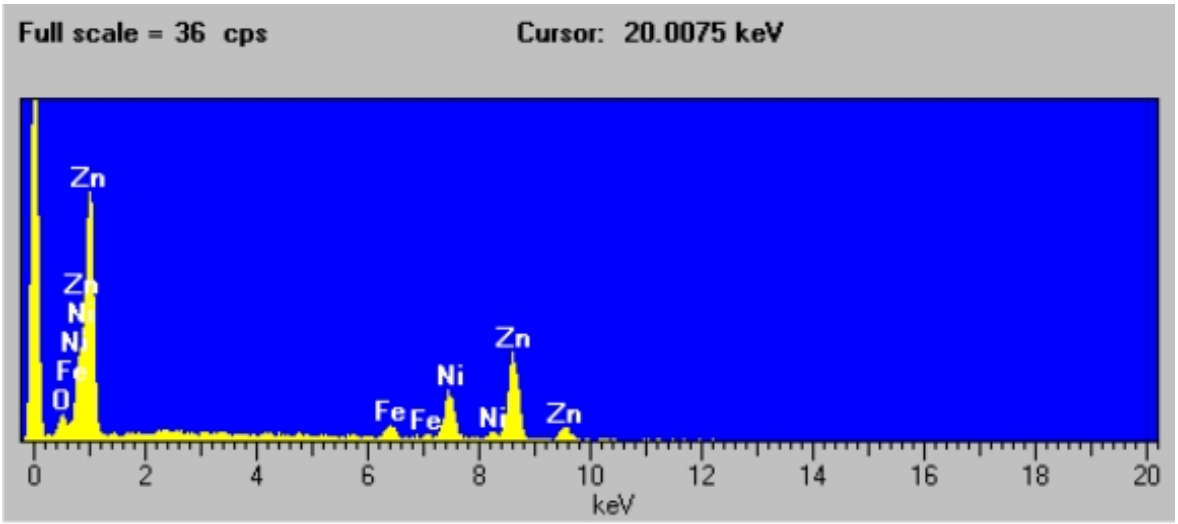

Figure 77 Typical EDS spectrum of Zn-Ni coating without conversion treatment (fatigue sample 274).

Table 19 Deposition parameters of the second batch of cylindrical specimens.

Sample	Type of coating	pH	Conductivity (mS @ °C)	Electrolyte temp (°C)	Voltage (V)	Current (Amps)	Rotation (RPM)	Dwell time (sec)
222 HE small	Zn-18%Ni/Metalast	2.8	29 @ 84	84	190	50	6	20
232 HE small	Zn-18%Ni/Dipsol	2.7	32 @ 85	85	190	45	6	20
244 HE small	Zn-18%Ni/no conversion coating	2.7	32 @ 85	85	190	45	6	20
274 Fatigue	Zn-16%Ni/no conversion coating	2.9	36 @ 85	85	195	55	6	20
275	Zn-16%Ni/no	2.8	37 @ 85	85	195	55	6	20

Table 20 Chemical composition of the specimens shown in Table 19.

	222		232		244		274		275	
	at.%	wt.%	at.%	wt.%	at.%	wt.%	at.%	wt.%	at.%	wt.%
O	42.88	15.86	25.49	7.92	45.38	17.29	35.89	12.36	48.63	19.43
Fe	1.83	2.36	3.74	4.05	1.21	1.61	2.67	3.21	4.44	6.19
Ni	11.63	15.79	14.57	16.62	12.88	18.01	14.25	18.01	13.42	19.67
Zn	43.66	65.99	56.21	71.40	40.53	63.09	47.19	66.42	33.52	54.72
Ni	20.77	19.05	20.21	18.53	24.18	22.27	22.84	21.00	28.04	25.92
Zn	79.23	80.95	79.79	81.47	75.82	77.73	77.16	79.00	71.96	74.08

Table 21 Corrosion potential and corrosion rate of the second batch Zn-Ni coated

Sample #	Corrosion potential, mV		Corrosion rate, μA/cm^2	
	Tap water	3.5% NaCl	Tap water	3.5% NaCl
4340 steel	-533	-728	9.20	320.88
222	-587	-768	2.83	5.03
232	-571	-811	3.50	5.06
244	-600	-754	2.03	15.63
274	-536	-713	2.37	10.91
275	-504	-757	0.33	7.11

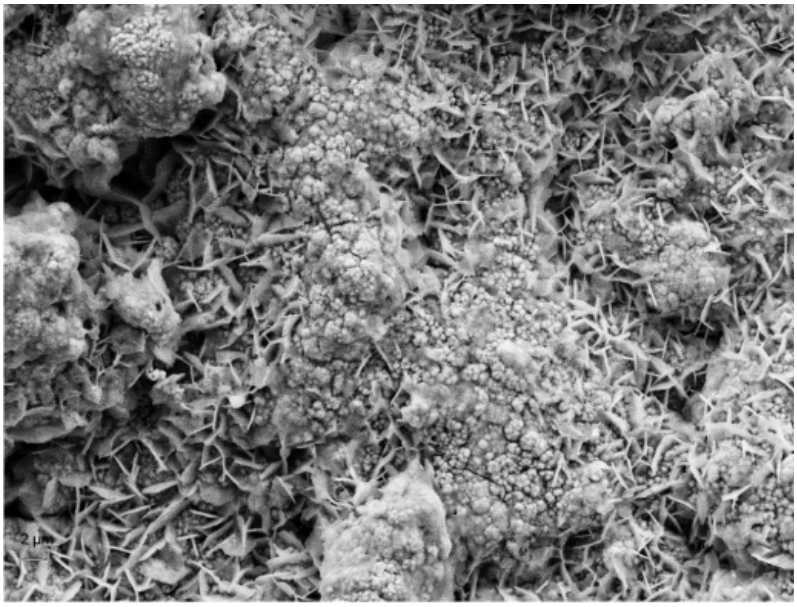

Sample 222, 2000x

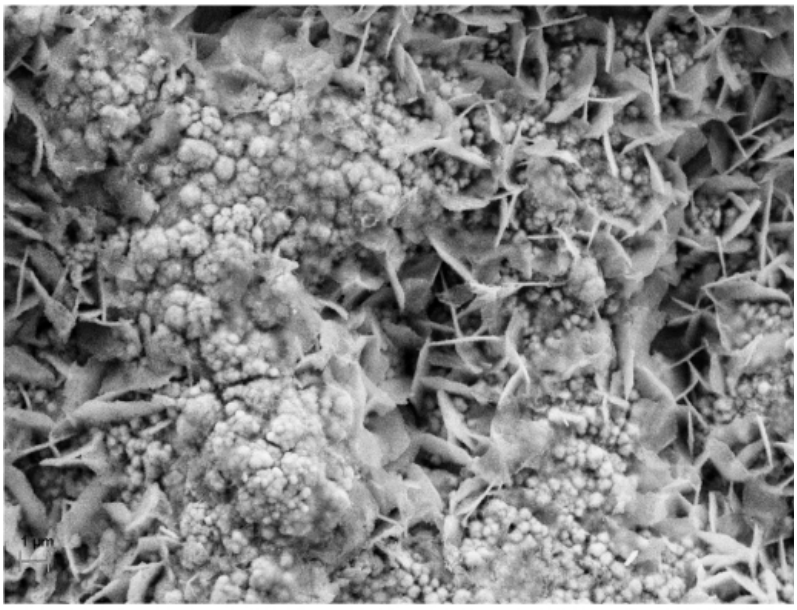

Sample 222, 4000x

Figure 78 SEM images of HE sample 222 with Zn-Ni/Metalast TCP-HF.

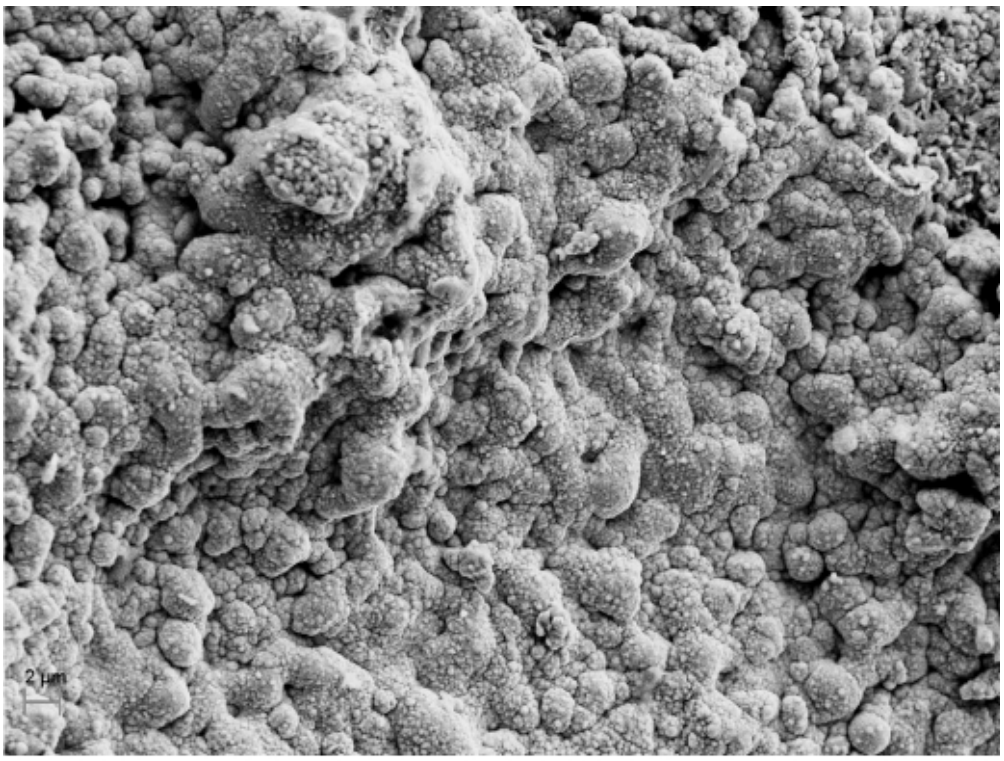

Sample 232, 2000x

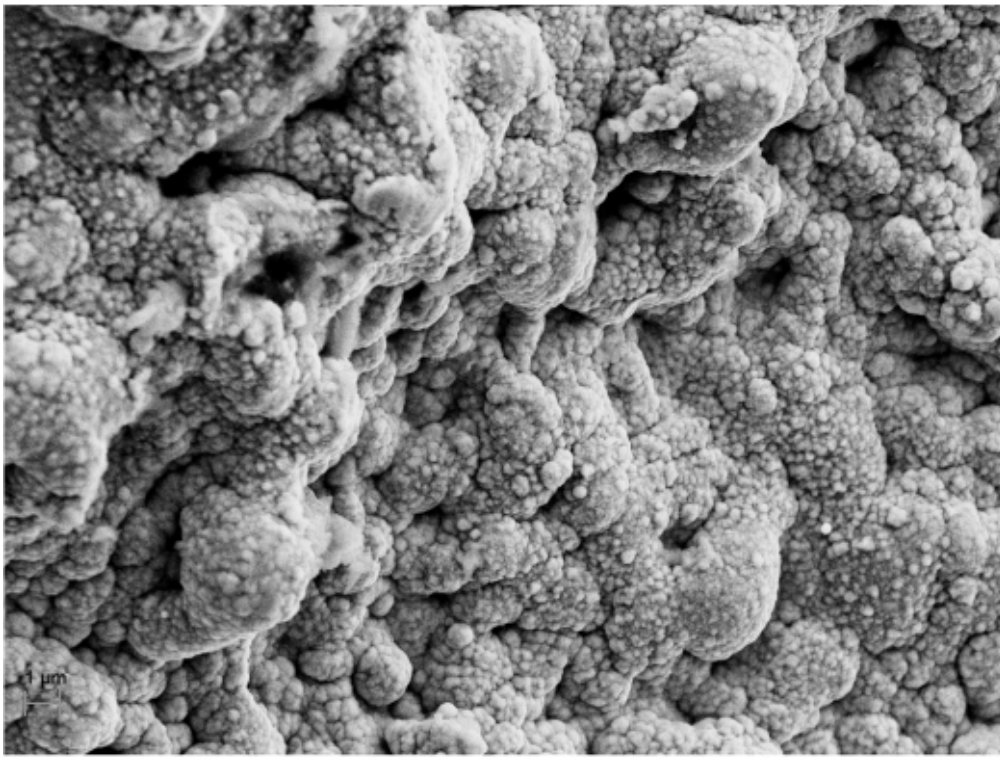

Sample 232, 2000x

Figure 79 SEM images of HE sample 232 with Zn-Ni/Dipsol.

Sample 244, 2000x

Sample 244, 4000x

Figure 80 SEM images of HE sample 244 with Zn-Ni/no conversion coating.

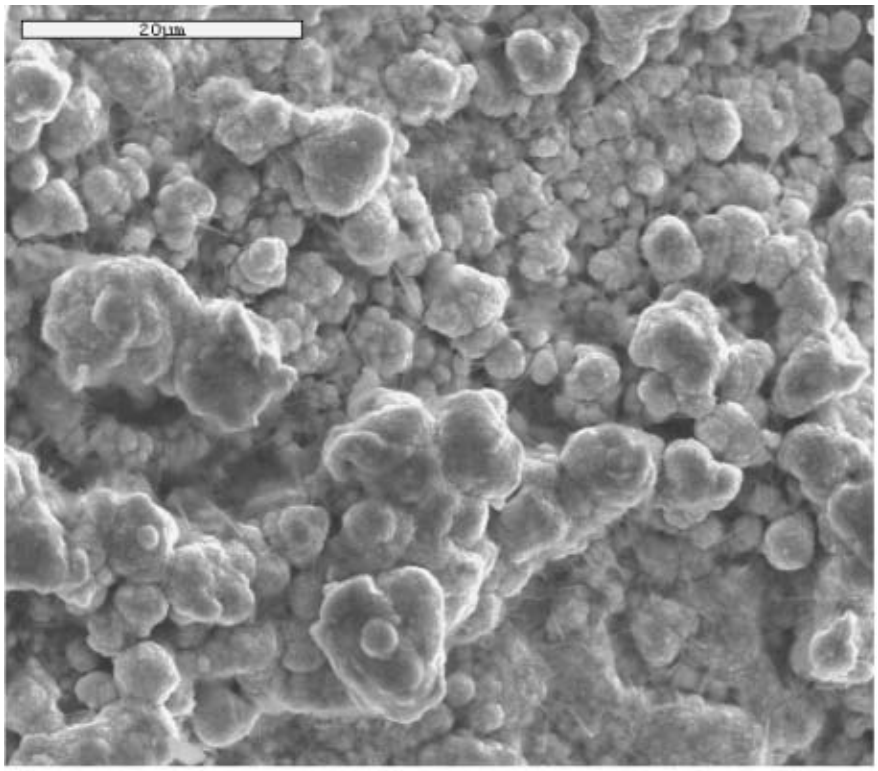

Sample 274, 2000x

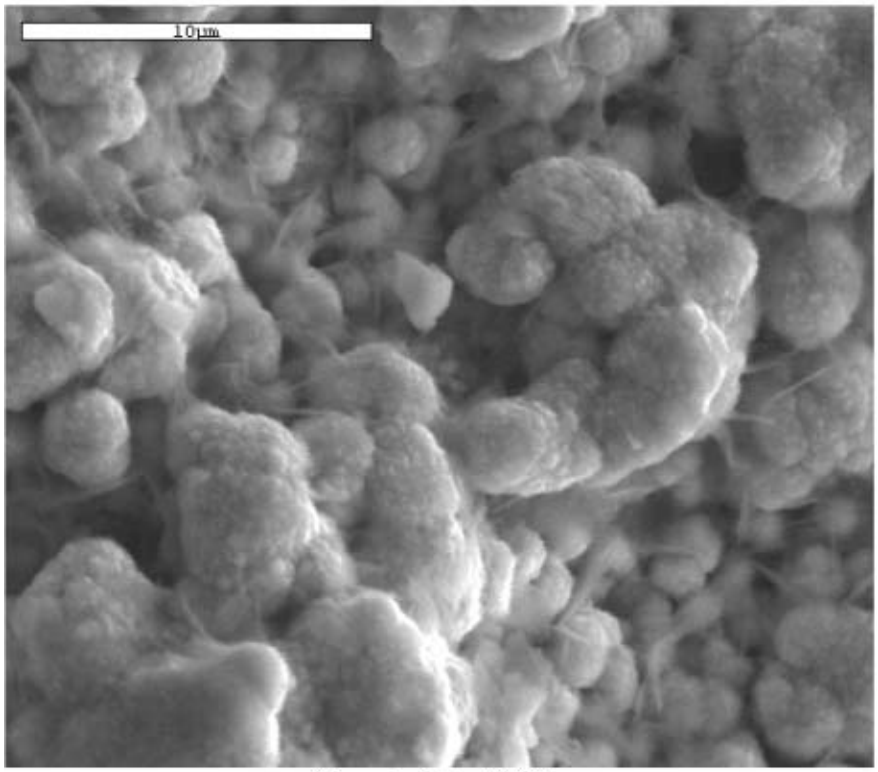

Sample 274, 5000x

Figure 81 SEM images of fatigue sample 274 with Zn-Ni and without conversion coating.

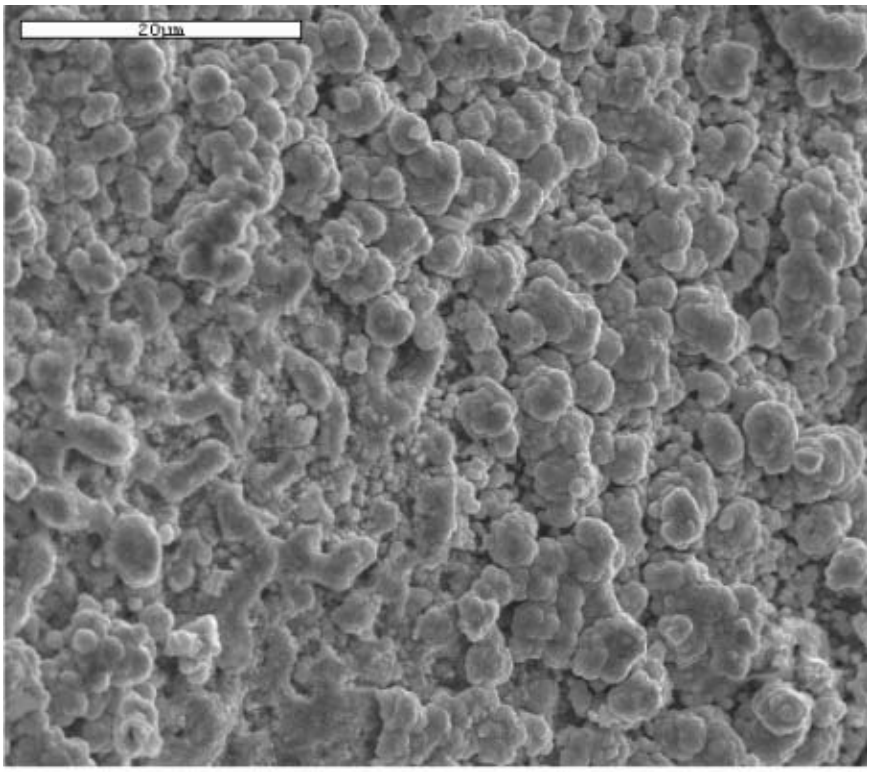

Sample 275, 2000x

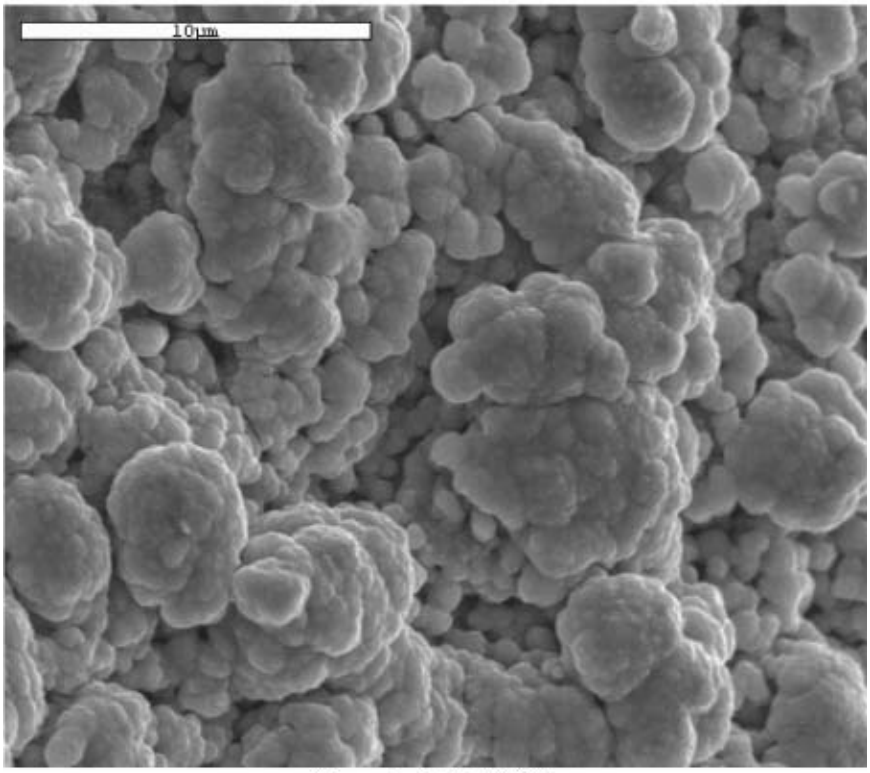

Sample 275, 5000x

Figure 82 SEM images of fatigue sample 275 with Zn-Ni and Dipsol coating.

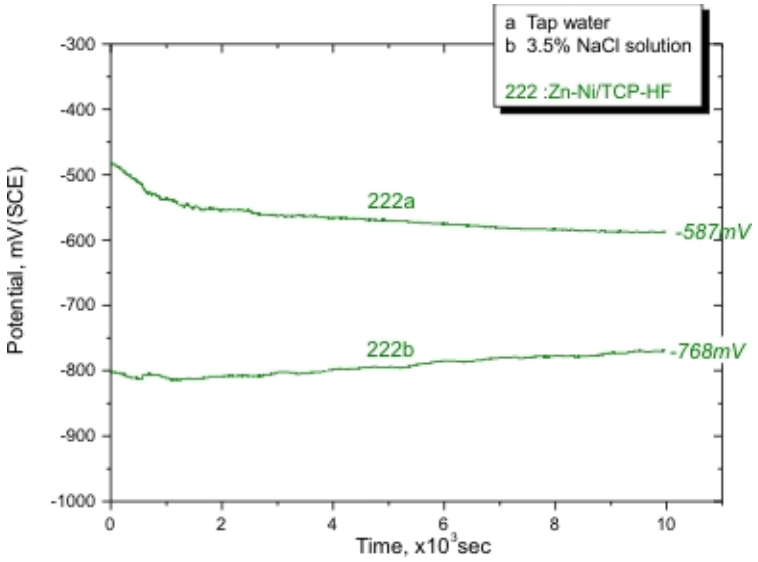

(a)

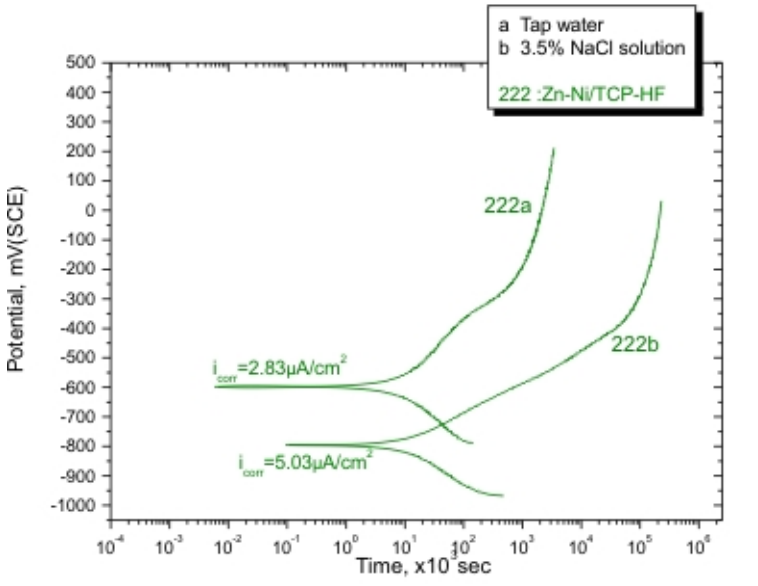

(b)

Figure 83 . (a) Ecorr vs Time and (b) anodic polarization behavior for the HE sample 222 with Zn-Ni/TCP-HF in tap water and 3.5% NaCl solution.

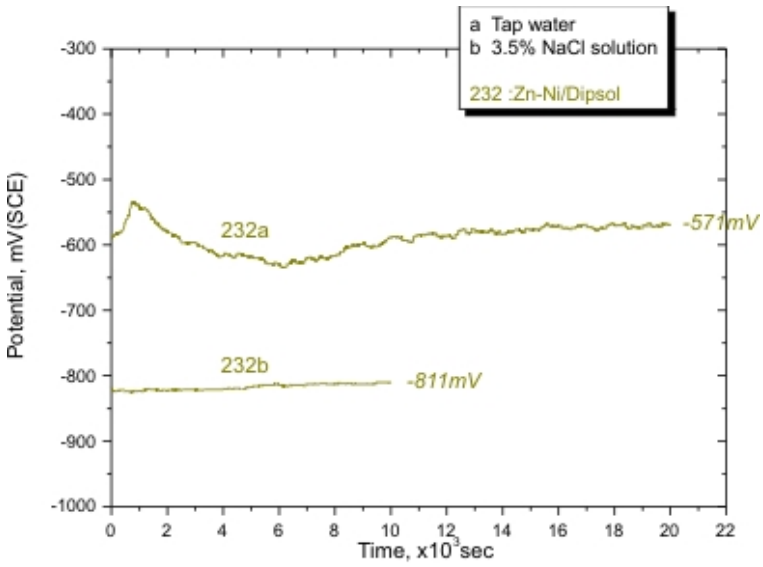

(a)

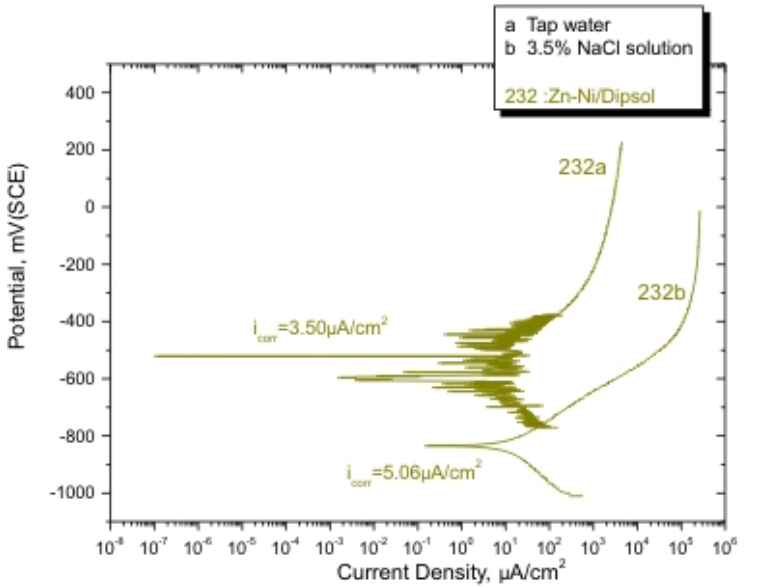

(b)

Figure 84 (a) Ecorr vs Time and (b) anodic polarization behavior for the HE sample 232 with Zn-Ni/Dipsol in tap water and 3.5% NaCl solution.

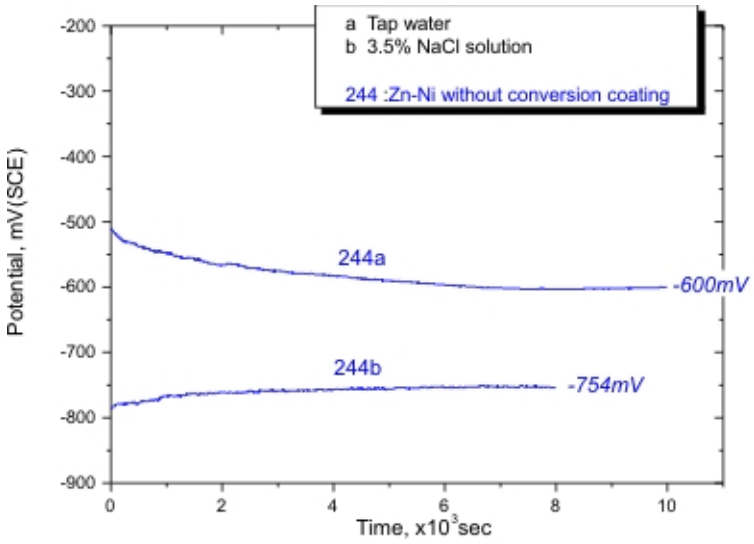

(a)

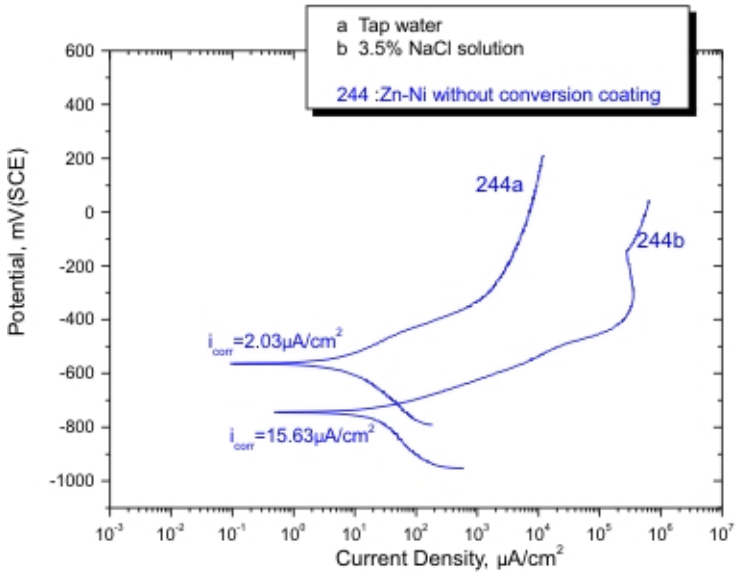

(b)

Figure 85 (a) Ecorr vs Time and (b) anodic polarization behavior for the HE sample 244 with Zn-Ni/no conversion coating in tap water and 3.5% NaCl solution.

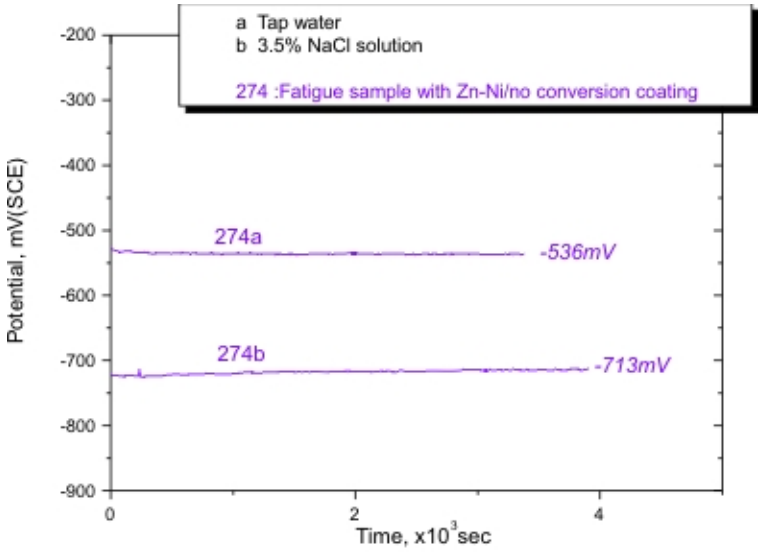

(a)

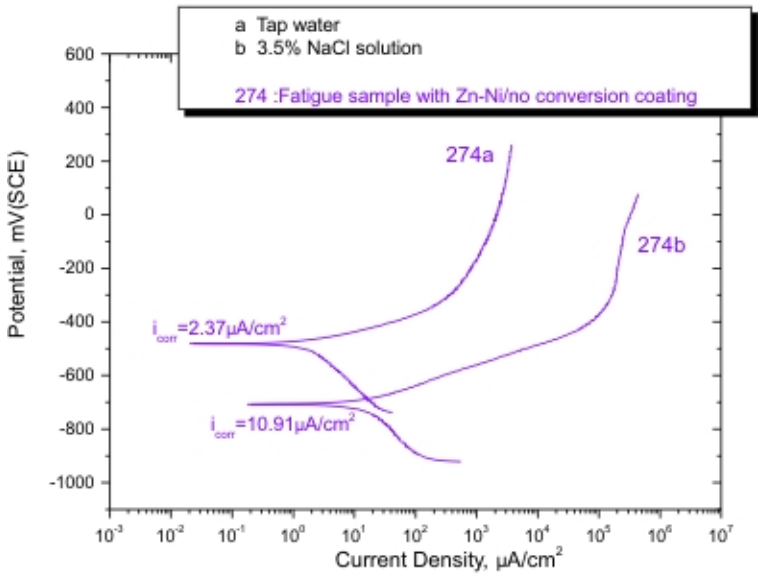

(b)

Figure 86 (a) Ecorr vs Time and (b) anodic polarization behavior for the fatigue sample 274 with Zn-Ni/no conversion coating in tap water and 3.5% NaCl solution.

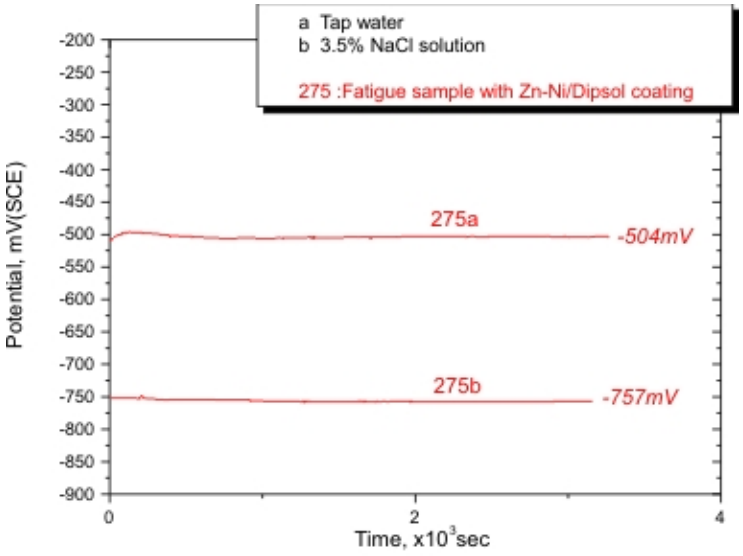

(a)

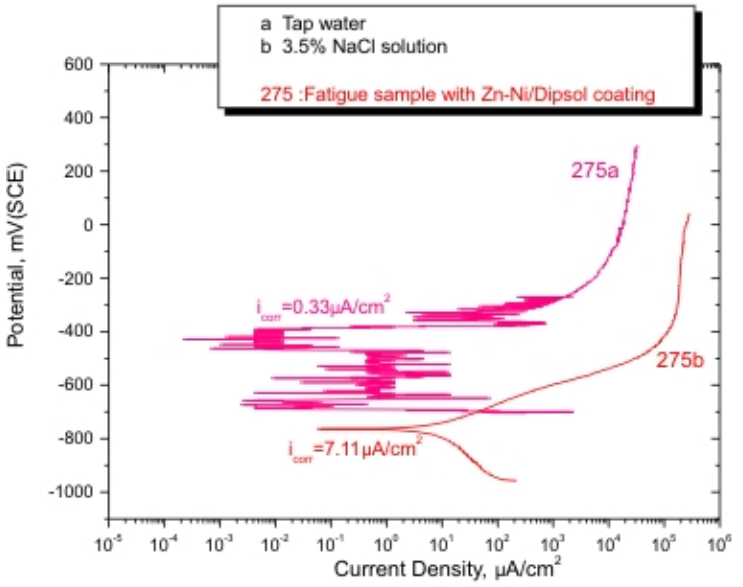

(b)

Figure 87 (a) Ecorr vs Time and (b) anodic polarization behavior for the fatigue sample 275 with Zn-Ni/Dipsol coating in tap water and 3.5% NaCl solution.

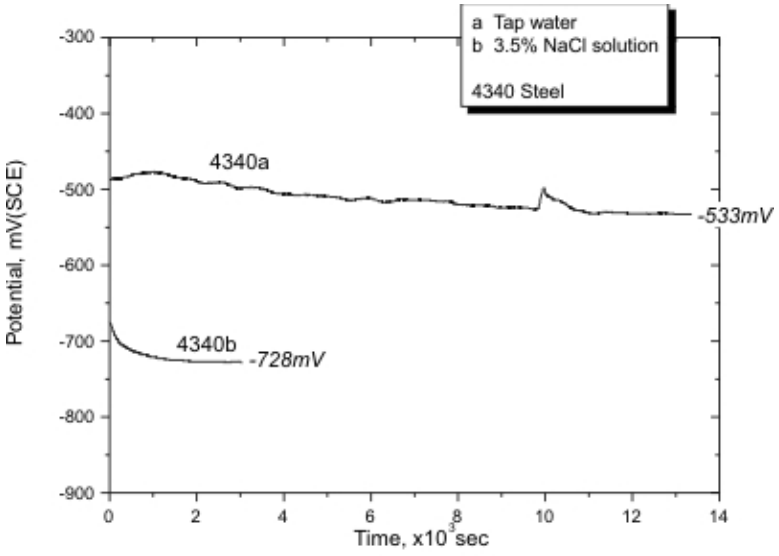

(a)

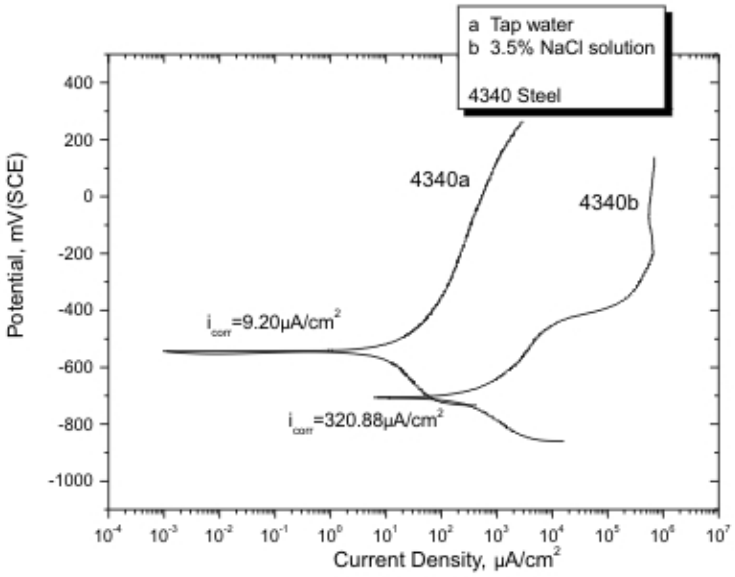

(b)

Figure 88 (a) Ecorr vs Time and (b) anodic polarization behavior for the 4340 steel in tap water and 3.5% NaCl solution.

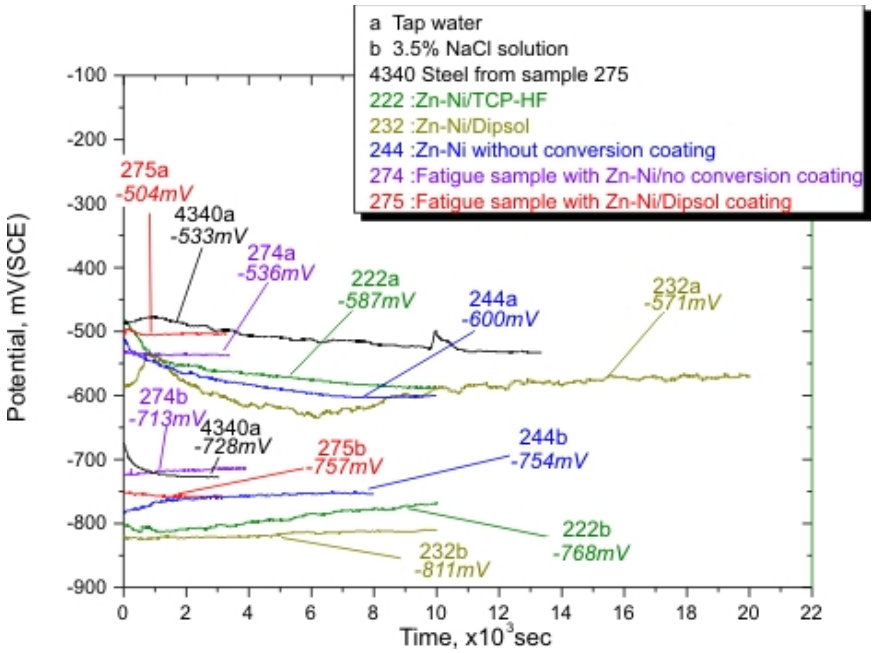

Figure 89 Ecorr vs Time for samples tested in tap water and 3.5% NaCl solution: 4340a) Steel 4340 in tap water; 222a) HE sample with Zn-Ni/TCP-HF in tap water; 232a) HE sample with Zn-Ni/Dipsol in tap water; 244a) HE sample with Zn-Ni/no conversion coating in tap water; 274a) fatigue sample with Zn-Ni/no conversion coating in tap water; 275a) fatigue sample with Zn-Ni/Dipsol coating in tap water; 4340b) Steel 4340 in 3.5% NaCl solution; 222b) HE sample with Zn-Ni/TCP-HF in 3.5% NaCl solution; 232b) HE sample with Zn-Ni/Dipsol in 3.5% NaCl solution; 244b) the HE sample with Zn-Ni/no conversion coating in 3.5% NaCl solution; 274b) the fatigue sample with Zn-Ni/no conversion coating in 3.5% NaCl solution; 275b) the fatigue sample with Zn-Ni/Dipsol coating in 3.5% NaCl solution.

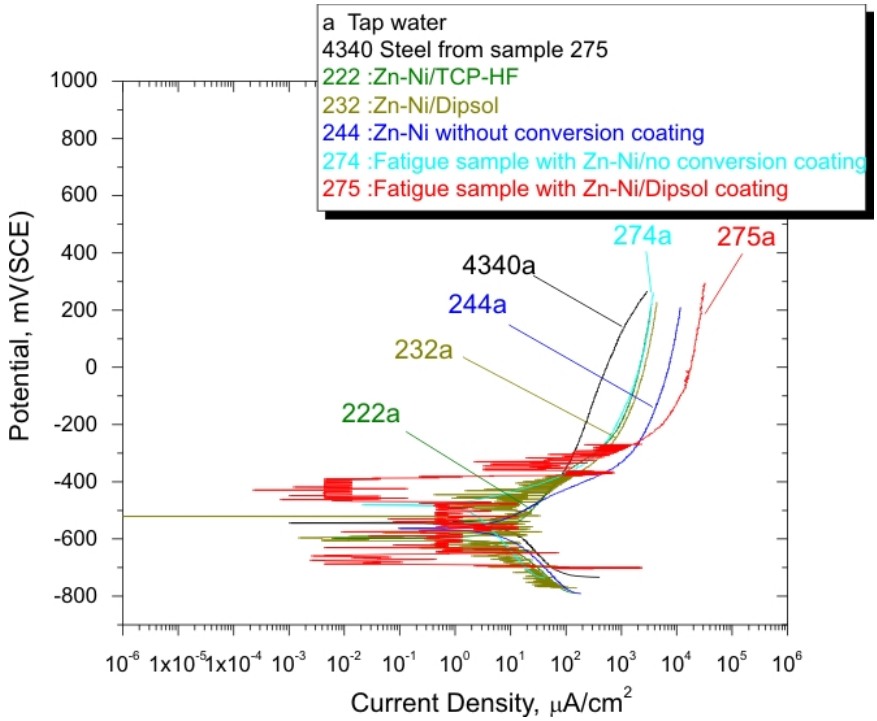

Figure 90 Anodic polarization behavior of samples tested in tap water: 4340a) Steel 4340; 222a) HE sample with Zn-Ni/TCP-HF; 232a) HE sample with Zn-Ni/Dipsol; 244a) the HE sample with Zn-Ni/no conversion coating; 274a) fatigue sample with Zn-Ni/no conversion coating; 275a) fatigue sample with Zn-Ni/Dipsol coating.

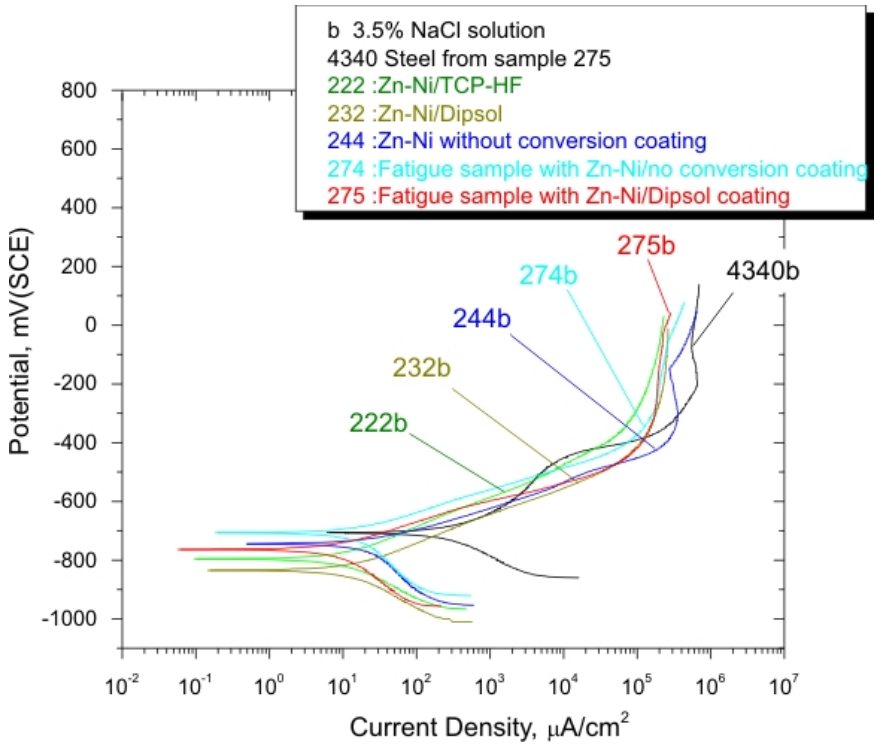

Figure 91 Anodic polarization behavior of samples tested in 3.5% NaCl solution: 4340b) Steel; 222b) HE sample with Zn-Ni/TCP-HF; 232b) HE sample with Zn-Ni/Dipsol; 244b) HE sample with Zn-Ni/no conversion coating; 274b) fatigue sample with Zn-Ni/no conversion; 275b) fatigue sample with Zn-Ni/Dipsol coating.

5.3.3 Hydrogen Embrittlement and Fatigue Testing and Evaluation

(a) Hydrogen Embrittlement Testing

Twelve C-ring HE specimens were EPT-cleaned and Zn-Ni coated with conditions determined from the previous section. Following Zn-Ni coating, six specimens were treated with Metalast TCP-HF and six with Dipsol [I-Z 2585]. These specimens were shipped to US Army Research Laboratory (Scott Grendahl) for testing and HE evaluation. The specimens were tested according to ASTM-F-519 and GM 9540P. The results reported are copied below:

Table 22 outlines the time until failure for the ASTM-F-519 Type 1d specimens, when loaded to 75% of UTS (0.099 inches of deflection), and exposed to ambient laboratory conditions. The specimens were inspected for failure after 12 hours, 15 hours, 20 hours, 24 hours, and then after each additional 24 hour period. The specimens did not fail and are currently still under load.

Table 22 Time Until Failure for 75% Loaded Type 1D Specimens.

Specimen Identification	Beginning Width	Final Width at Fracture	Hours Until Failure
Plasma Al (Dipsol - 204)	1.962	1.863	1680 - not failed
Plasma Al (Dipsol - 205)	1.962	1.863	1680 - not failed
Plasma Al (Dipsol - 206)	1.962	1.863	1680 - not failed
Plasma Al (Metalast - 210)	1.962	1.863	1680 - not failed
Plasma Al (Metalast - 211)	1.962	1.863	1680 - not failed
Plasma Al (Metalast - 212)	1.961	1.862	1680 - not failed

The EPT Zn-Ni coated specimens are indicated as Plasma Al.

Table 23 outlines the time until failure for the ASTM-F-519 Type 1d specimens, when loaded to 65% of UTS, and cycled in GM 9540P for the EPP Dipsol and Metalast processes as well as for other relevant cadmium replacement coatings performed by ARL under a different program. The specimens were inspected for failure periodically or when audible cracking was heard. **Discussion:** The ability of the specimens to withstand the 75% load for at least 200 hours constitutes passing IAW ASTM-F-519 for a coating or plating process. The 65% loading level and exposure to GM 9540P corrosion cycles data demonstrate that the EPP coatings and process is far better than most prospective cadmium replacement coatings at reducing hydrogen embrittlement risk on high strength steel. It is believed that the Alumiplate results were superior to the rest due to that superior barrier coating properties of Alumiplate and not entirely representative of coatings with scratches or inherent defects, as the specimens other than the EPP data were for entirely coated specimens.

Conclusion: The EPP processes tested under this program passed the requirements for coatings and processes and do not significantly contribute to hydrogen embrittlement failure, when tested IAW ASTM-F-519.

(b) Fatigue Testing

Twelve cylindrical fatigue specimens were EPT-cleaned and Zn-Ni coated with the same conditions as those used for the HE specimens. These specimens were shipped to Metcut Research, Inc. for fatigue testing. Fig. 92 presents the fatigue results along with those for untreated 4340 steel. Overall, the Zn-Ni coated specimens showed a small fatigue debit.

Table 23 Time Until Failure for Type 1d Hydrogen Embrittlement Specimens.

Specimen Identification	Beginning Width	Final Width at Fracture	Hours Until Failure	Raw GM 9540P Minutes	GM 9540P Cycles
LHE Cd	1.958	1.874	N/A	163	0.1272
LHE Cd	1.957	1.873	N/A	480	0.3747
LHE Cd	1.960	1.876	N/A	129	0.1007
LHE Cd	1.956	1.872	N/A	123	0.0960
LHE Cd	1.959	1.875	N/A	176	0.1374
LHE Cd	1.952	1.868	N/A	138	0.1077
LHE Cd	1.958	1.874	N/A	480	0.3747
LHE Cd	1.957	1.873	N/A	480	0.3747
LHE Cd	1.953	1.869	N/A	85	0.0664
IVD Al	1.962	1.878	N/A	38	0.0297
IVD Al	1.960	1.876	N/A	22	0.0172
IVD Al	1.960	1.876	N/A	33	0.0258
IVD Al	1.960	1.876	N/A	19	0.0148
IVD Al	1.959	1.875	N/A	31	0.0242
IVD Al	1.959	1.875	N/A	24	0.0187
IVD Al	1.956	1.872	N/A	480	0.3747
IVD Al	1.958	1.874	N/A	29	0.0226
IVD Al	1.958	1.874	N/A	30	0.0234
Al Sputter	1.958	1.874	N/A	135	0.1054
Al Sputter	1.955	1.871	N/A	480	0.3747
Al Sputter	1.960	1.876	N/A	480	0.3747
Al Sputter	1.957	1.873	N/A	480	0.3747
Al Sputter	1.959	1.875	N/A	480	0.3747
Al Sputter	1.956	1.872	N/A	36	0.0281
Al Sputter	1.956	1.872	N/A	480	0.3747
Al Sputter	1.958	1.874	N/A	480	0.3747
Al Sputter	1.952	1.868	N/A	511	0.3989
Alumiplate	1.964	1.880	N/A	42273	33
Alumiplate	1.956	1.872	N/A	7686	6
Alumiplate	1.959	1.875	N/A	38430	30
Alumiplate	1.958	1.874	N/A	20	0.0156
Alumiplate	1.956	1.872	N/A	46116	36
Alumiplate	1.956	1.872	N/A	37149	29
Alumiplate	1.957	1.873	N/A	47397	37
Alumiplate	1.959	1.875	N/A	28	0.0219
Alumiplate	1.953	1.869	N/A	56364	44
ZnNi Acid Boeing	1.958	1.874	N/A	25	0.0195
ZnNi Acid Boeing	1.957	1.873	N/A	38	0.0297
ZnNi Acid Boeing	1.958	1.874	N/A	110	0.0859
ZnNi Acid Boeing	1.953	1.869	N/A	50	0.0390
ZnNi Acid Boeing	1.958	1.874	N/A	44	0.0343
ZnNi Acid Boeing	1.958	1.874	N/A	35	0.0273
ZnNi Acid Boeing	1.952	1.868	N/A	29	0.0226
ZnNi Acid Boeing	1.959	1.875	N/A	190	0.1483
ZnNi Acid Boeing	1.961	1.877	N/A	37	0.0289
ZnNi Alk LHE D.G.	1.960	1.876	N/A	124	0.0968
ZnNi Alk LHE D.G.	1.961	1.877	N/A	35	0.0273
ZnNi Alk LHE D.G.	1.960	1.876	N/A	45	0.0351
ZnNi Alk LHE D.G.	1.957	1.873	N/A	57	0.0445

ZnNi Alk LHE D.G.	1.958	1.874	N/A	27	0.0211
ZnNi Alk LHE D.G.	1.957	1.873	N/A	24	0.0187
ZnNi Alk LHE D.G.	1.957	1.873	N/A	40	0.0312
ZnNi Alk LHE D.G.	1.957	1.873	N/A	40	0.0312
ZnNi Alk LHE D.G.	1.958	1.874	N/A	33	0.0258
Plasma Al (Dipsol - 201)	1.962	1.875	N/A	420	0.3279
Plasma Al (Dipsol - 202)	1.962	1.875	N/A	453	0.3536
Plasma Al (Dipsol - 203)	1.962	1.875	N/A	1377	1.0749
Plasma Al (Metalast - 207)	1.962	1.875	N/A	1377	1.0749
Plasma Al (Metalast - 208)	1.962	1.875	N/A	420	0.3279
Plasma Al (Metalast - 209)	1.961	1.874	N/A	420	0.3279
SnZn (1st Batch)	1.960	1.876	<10min*	0	0
SnZn (1st Batch)	1.959	1.875	<10min*	0	0
SnZn (1st Batch)	1.958	1.874	<10min*	0	0
SnZn (1st Batch)	1.957	1.873	<10min*	0	0
SnZn (1st Batch)	1.953	1.869	<10min*	0	0
SnZn (1st Batch)	1.958	1.874	<10min*	0	0
SnZn (1st Batch)	1.953	1.869	<10min*	0	0
SnZn (1st Batch)	1.960	1.876	<10min*	0	0
SnZn (1st Batch)	1.959	1.875	<10min*	0	0

Note: CAP Zn-Ni coatings are denoted as: Plasma Al.

4500829135

Cyclic Fatigue Data
4340 (peened + Zn-Ni coating)
smooth - 3/4 hyd grip

Dynamic Ratio : R = -1.0 Frequency : 59 Hz
Test Temperature : 75 °F Waveform : Sinusoidal

Project No. : **2360-83732** -21-265-01 **-04**

Test Number	Specimen Number	Diameter (in)	Stress Max (ksi)	Stress Alt (ksi)	Cycles	Actual Frequency (Hz)	Results	Test Hours	Test Machine
4-265-03	4340-32	0.2500	140	140	27,752	29, 10	F, G, SS	0.7	60059
5-265-03	4340-45	0.2500	130	130	248,310	10, 20, 29	F, G, SS	3.2	60059
6-265-03	4340-46	0.2499	120	120	1,013,198	29, 59	F, G, SS	9.5	60059
17-265-03	7	0.2499	135	135	107,604	29	F, G, S	1.0	60059
21-265-03	8	0.2500	125	125	556,413	20, 59	F, G, SS	2.6	60059
22-265-03	10	0.2499	115	115	2,005,242	29	Removed	19.2	60059
	12								
	15								
	17								
	20								
	22								
	29								

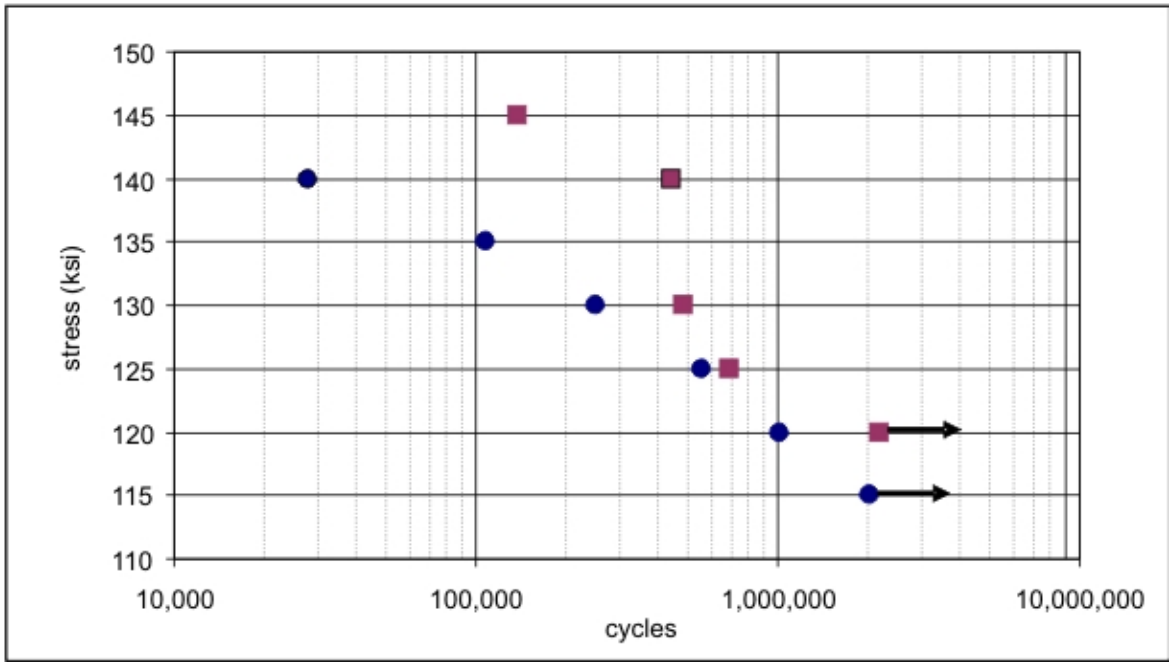

Figure 92 Fatigue testing parameters and fatigue response of the EPT Zn-Ni coated 4340 steel (circles) and untreated 4340 steel (squares).

5.3.4 Coating of Flat Specimens

Several flat panels were Zn-Ni coated at CAP Technologies and evaluated for ensuring coating composition, uniformity and thickness prior to coating the flat panels for salt fog corrosion testing. Six specimens were received at UTA for microstructural characterization and laboratory corrosion evaluation. Three samples (sample # 333, 334 & 335) were coated with Zn-12% Ni with no conversion coating treatment, one sample (sample # 336) was coated with Zn-12% Ni and then treated with Dipsol I-Z 258, one sample (sample # 349) was coated with Zn-12% Ni and treated with Metalast TCP-HF and one sample (sample # 351) was coated with Zn-16% Ni with no conversion coating treatment. The deposition parameters for the Zn-Ni coatings were listed in Table 24.

The chemical composition of the above six samples is presented in Table 25, and Fig. 93 shows a typical EDS spectrum of the fatigue sample 334 with Zn-Ni/no conversion coating. The surface morphology and the cross sections of all samples are shown in Fig. 94-99. All coatings were mainly composed of a nodular phase with very little flake phase present. As noted earlier, presence of the flake phase is associated with high Ni content. All coatings had a Ni content below 18-19% except sample 351 that intentionally was deposited with higher Ni content.

The variation of the corrosion potential with time and the anodic polarization behavior of all samples and the 4340 steel in tap water and 3.5% NaCl solution are shown in Figs. 100 and101, respectively for aerated (lab air) and deaerated testing conditions. The stabilized corrosion potentials and the corrosion rates for all specimens for both, aerated and deaerated conditions are listed in Table 26.

For lab air testing, the results showed that all specimens exhibited an active potential with respect to steel in tap water. However, in NaCl solution only specimens 333 and 336 exhibited a more active potential than steel, Fig. 100(a). In fact these were the specimens with the lowest Ni content, Table 25, confirming the early findings. Similarly, for deaerated testing conditions, only specimens 333 and 336 were found to exhibit an active potential with respect to steel in both tap water and NaCl solution.

The corrosion rates calculated from the anodic polarization graphs are shown in Table 25. For lab air testing in tap water and NaCl solution, the above two specimens exhibited comparable rates around 4-6 $\mu A/cm^2$. These values are consistent with the values obtained from the second batch of Zn-Ni coated cylindrical specimens.

Table 25 Deposition parameters for the six flat samples.

Sample	Type of coating	pH	Conductivity (mS @ °C)	Electrolyte temp (°C)	Voltage (V)	Current (Amps)	Rotation (RPM)	Dwell time (sec)
333 Flat bar	Zn-12%Ni/no conversion coating	3.9	36 @ 85	85	195	20	N/A	60
334 Flat bar	Zn-12%Ni/no conversion coating	3.9	39 @ 85	85	195	20	N/A	60
335 Flat bar	Zn-12%Ni/no conversion coating	3.9	39 @ 85	85	195	20	N/A	60
336 Flat bar	Zn-12%Ni/Dipsol	3.8	36 @ 85	85	195	20	N/A	60
349 Flat bar	Zn-12%Ni/Metalast	3.7	40 @ 85	85	195	20	N/A	60
351	Zn-16%Ni/no	3.6	42 @ 85	85	195	20	N/A	60

Table 24 Chemical composition and thickness of the six flat samples.

	333		334		335		336		349		351	
	wt	at	wt	at	wt	at	wt	at	wt	at	wt	at
C	18.87	47.48	23.09	47.48	19.50	43.56	21.74	48.08	14.59	37.64	15.40	37.39
O	20.32	22.07	13.70	22.07	14.91	26.30	14.22	23.99	14.46	28.01	16.90	31.01
Ni	9.74	6.67	12.42	6.67	14.38	7.15	11.00	5.34	12.79	6.76	17.25	8.71
Zn	51.07	23.77	50.79	23.77	51.21	22.99	53.04	22.59	58.15	27.59	50.45	22.90
Ni	13.51	14.81	17.34	18.91	19.05	20.74	15.41	16.83	16.55	18.08	23.78	25.78
Zn	86.49	85.19	82.66	79.70	80.95	79.26	84.59	83.18	83.45	81.92	76.22	74.22
thickness (μm)	40(80)		10(50)		20(70)		15(50)		10(60)		10(50)	

Table 26 Corrosion potential and corrosion rate for the flat Zn-Ni coated samples. [In light blue is the 4340 steel potential and in green coatings that are anodic to steel.]

Sample #	CORROSION POTENTIAL (mV)				CORROSION RATE (μA/cm^2)			
	LAB CONDITION		DEAERATED (Ar)		LAB CONDITION		DEAERATED (Ar)	
	Tap Water	3.5% NaCl	Tap Water	3.5% NaCl	Tap Water	3.5% NaCl	Tap Water	3.5% NaCl
333	-596	-759	-649	-833	3.92	4.18	2.43	2
334	-577	-731	-612	-747	4.64	5.5	1.52	1.9
335	-568	-712	-651	-741	3.51	6.52	1.36	1.89
336	-599	-879	-784	-862	4.55	5.88	1.08	3.56
349	-563	-715	-564	-757	9.19	3.01	3.89	2.53
351	-564	-698	-561	-765	?	?	0.83	0.87
4340 Steel	-533	-728	-575	-760	9.2	320.88	1.35	0.92

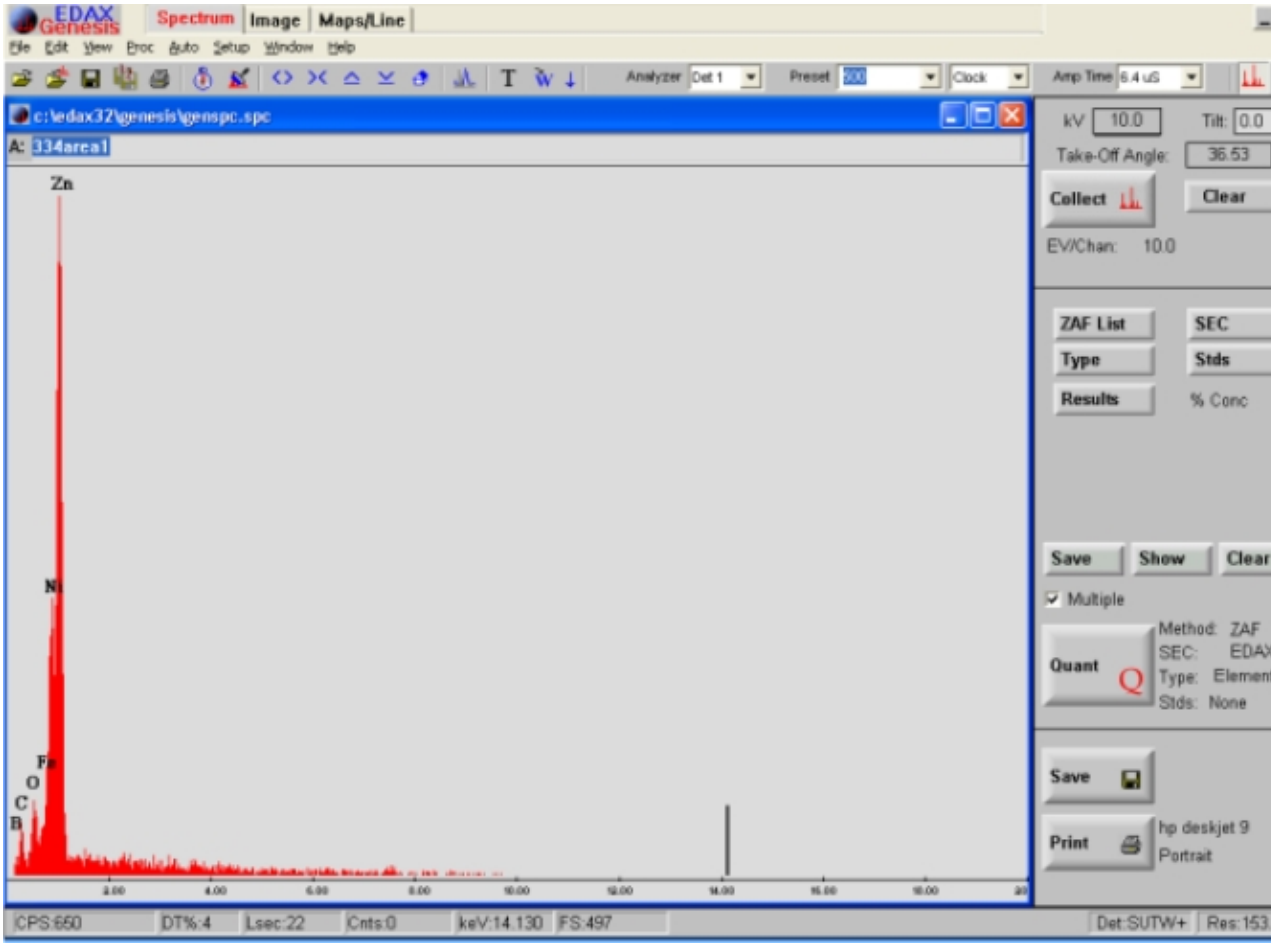

Figure 93 Typical EDS spectrum of Zn-12%Ni without conversion coating (sample 334)

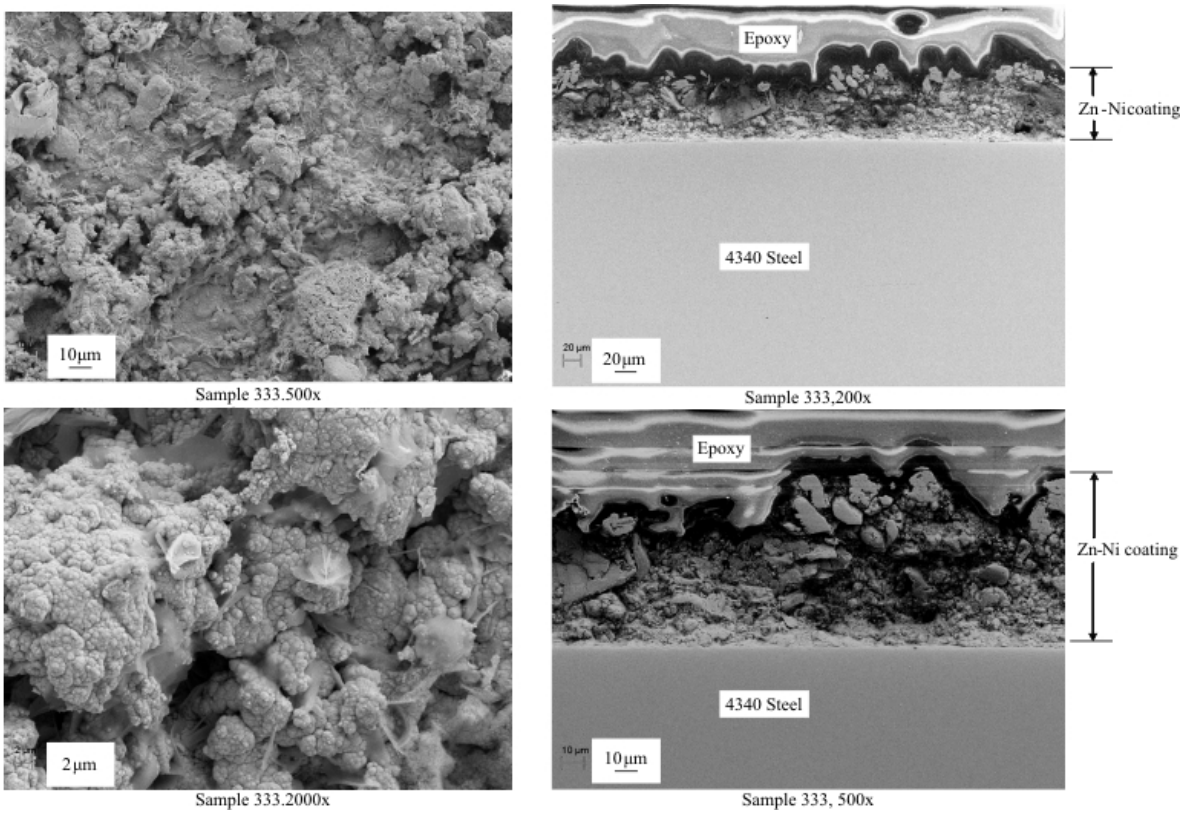

Figure 94 SEM surface and cross sectional images of sample 333 with Zn-12% Ni/no conversion coating.

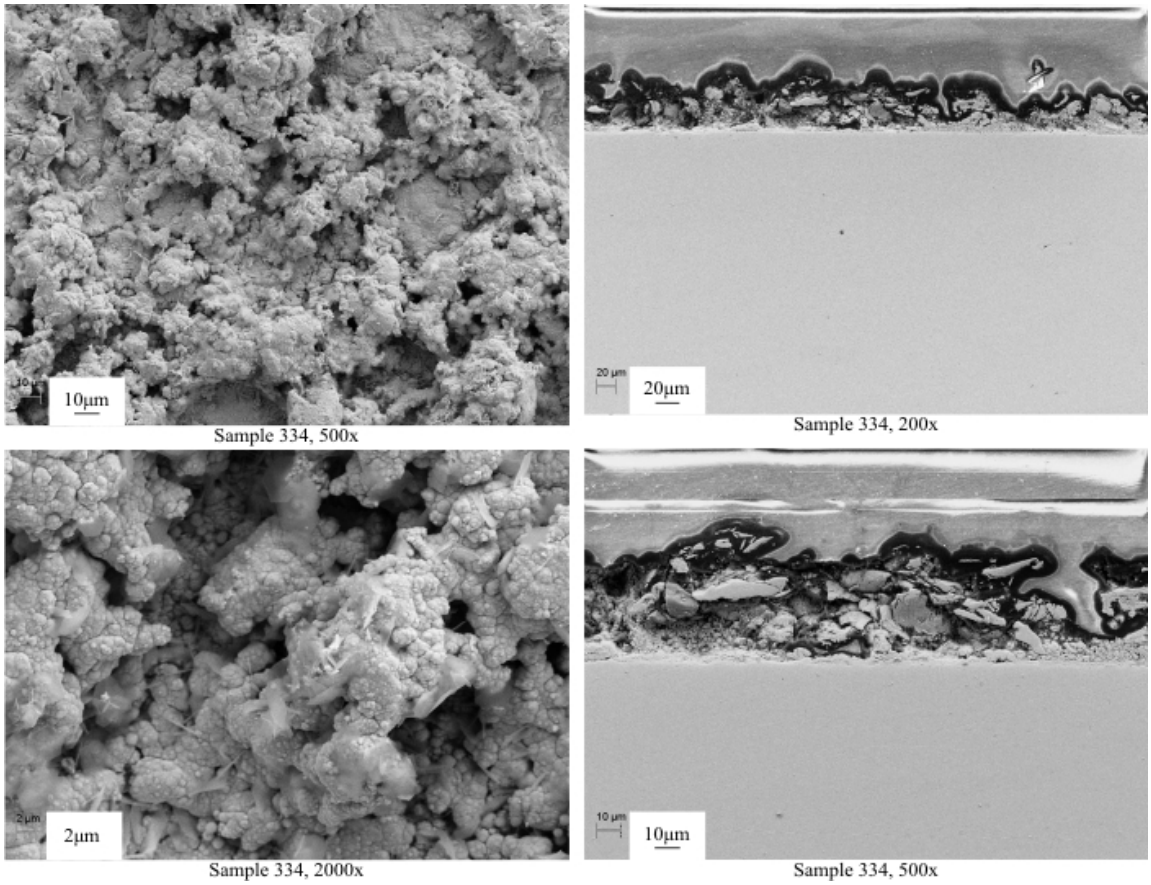

Figure 95 Surface and cross sectional SEM images of sample 334 with Zn-12%Ni/no conversion coating.

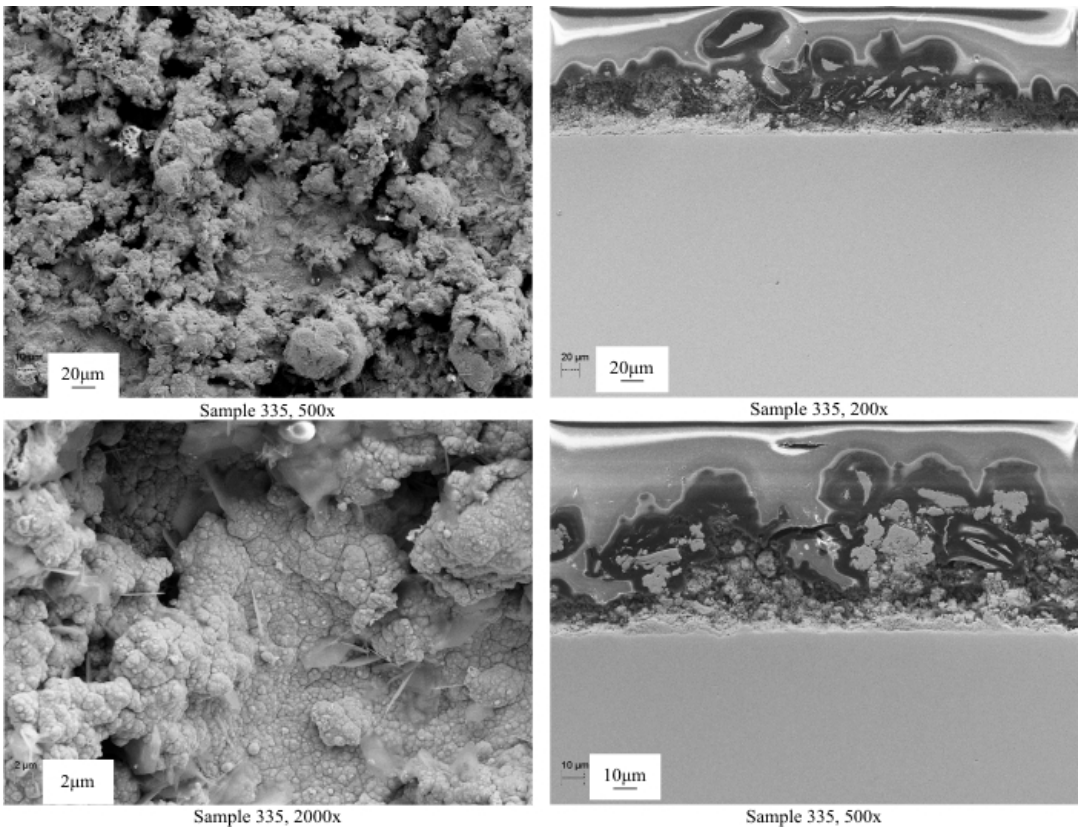

Sample 335, 500x Sample 335, 200x

Sample 335, 2000x Sample 335, 500x

Figure 96 Surface and cross sectional SEM images of sample 335with Zn-12% Ni/no conversion coating.

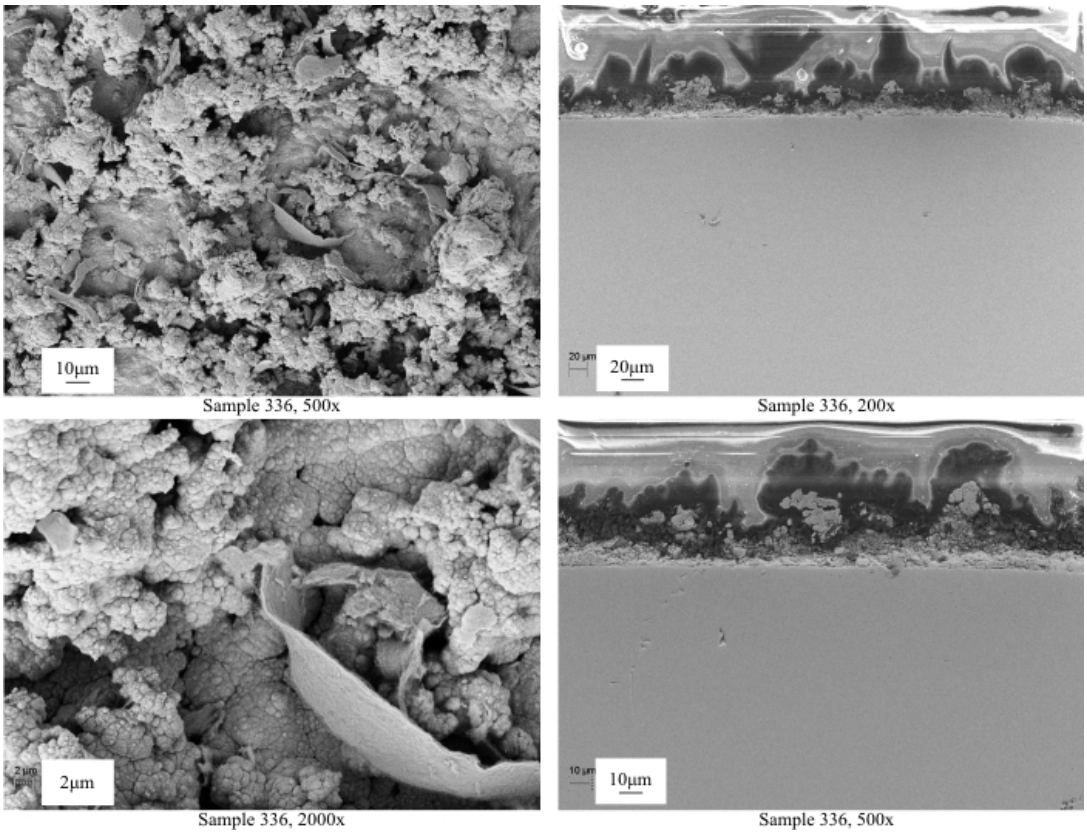

Sample 336, 500x Sample 336, 200x

Sample 336, 2000x Sample 336, 500x

Figure 97 Surface and cross sectional SEM images of sample 336 with Zn-12% Ni/ Dipsol.

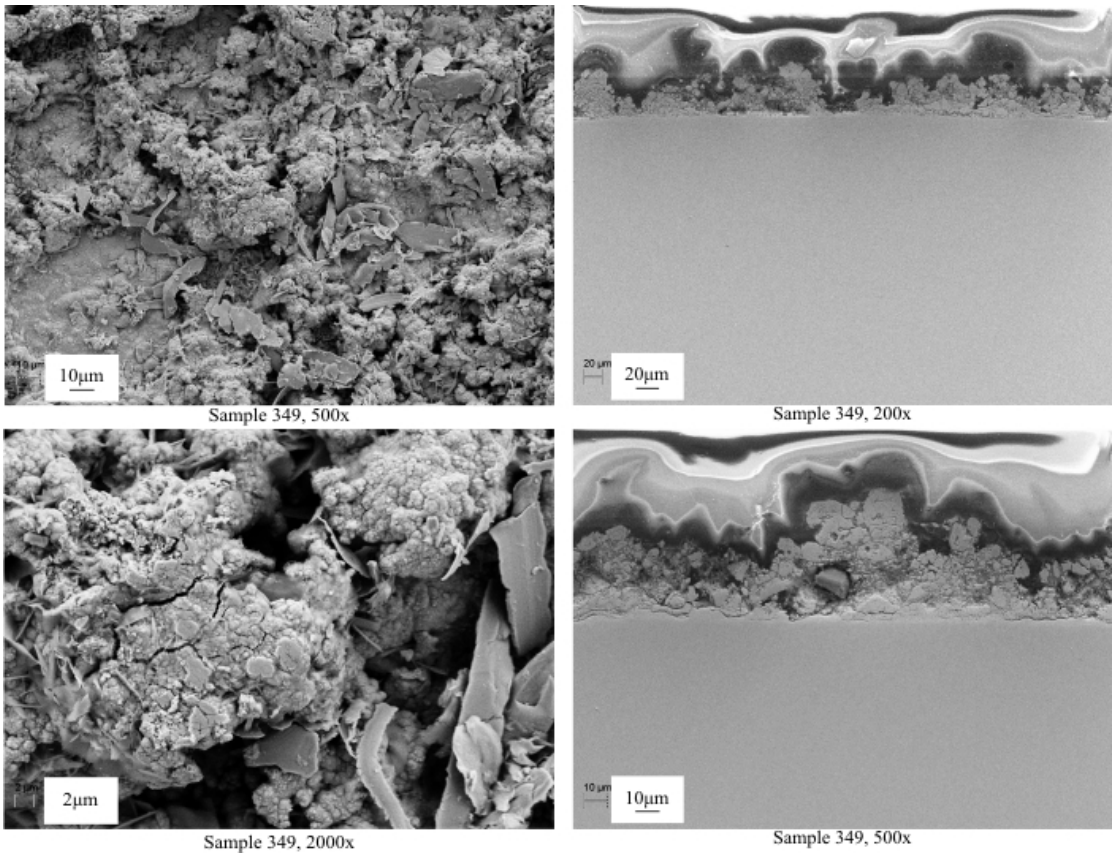

Sample 349, 500x | Sample 349, 200x

Sample 349, 2000x | Sample 349, 500x

Figure 98 Surface and cross sectional SEM images of sample 349 with Zn-12% Ni/ Metalast.

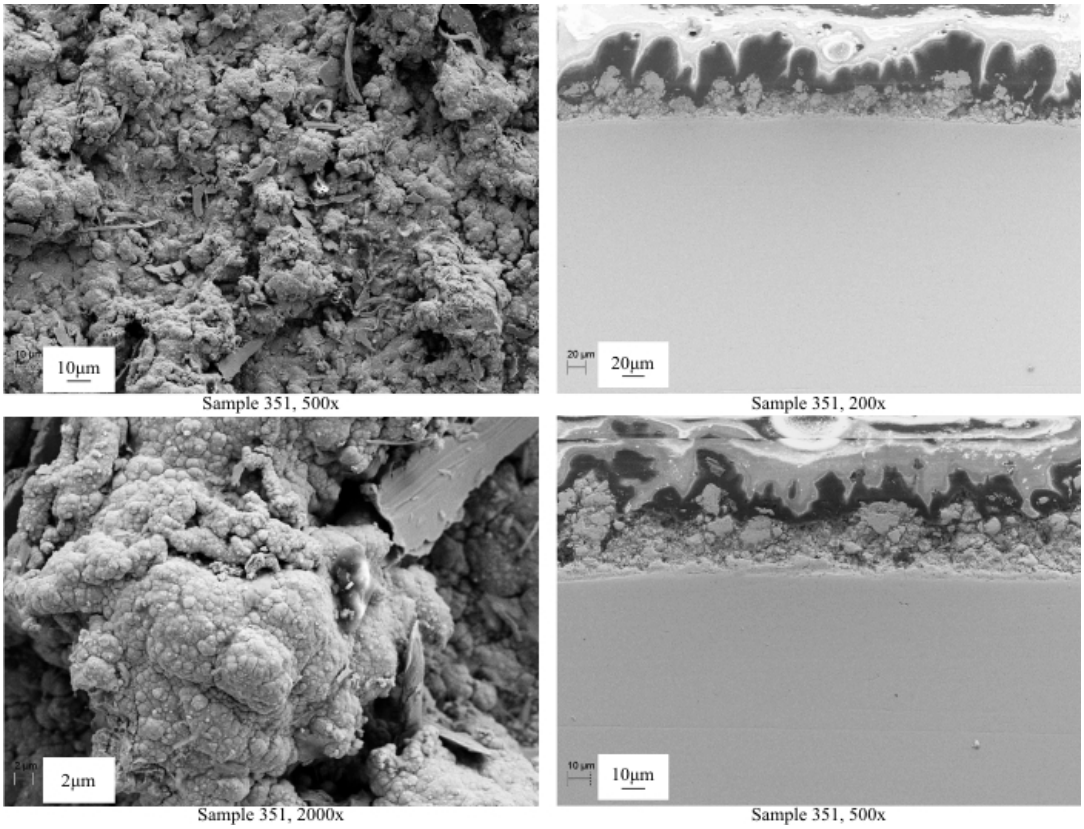

Sample 351, 500x | Sample 351, 200x

Sample 351, 2000x | Sample 351, 500x

Figure 99 Surface and cross sectional SEM images of sample351 with Zn-16% Ni/ no conversion coating.

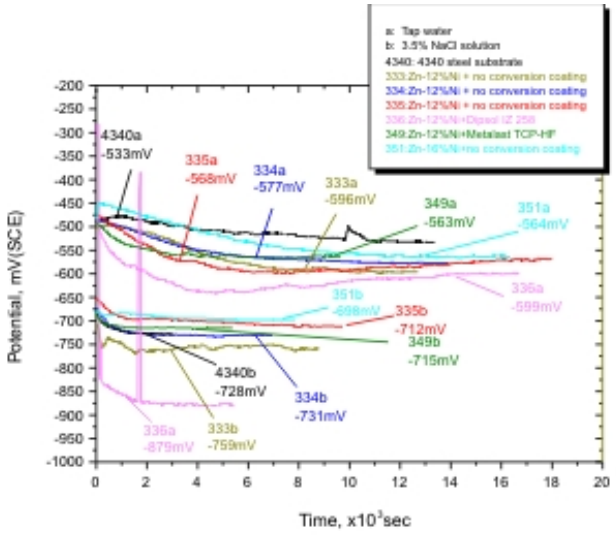

(a)

Figure 100 (a) Ecorr vs Time for the samples in tap water and 3.5% NaCl solution(Aerated): 4340a) Steel 4340 in tap water, 333a) sample 333 in tap water, 334a) sample 334 in tap water, 335a) sample 335 in tap water, 336a) sample 336 in tap water, 349a) sample 349 in tap water, 351a) sample 351 in tap water, 4340b) Steel 4340 in 3.5% NaCl solution, 333b) sample 333 in 3.5% NaCl solution, 334b) sample 334 in 3.5% NaCl solution 335b) sample 335 in 3.5% NaCl solution 336b) sample 336 in 3.5% NaCl solution 349b) sample 349 in 3.5% NaCl solution 351b) sample 351 in 3.5% NaCl solution.

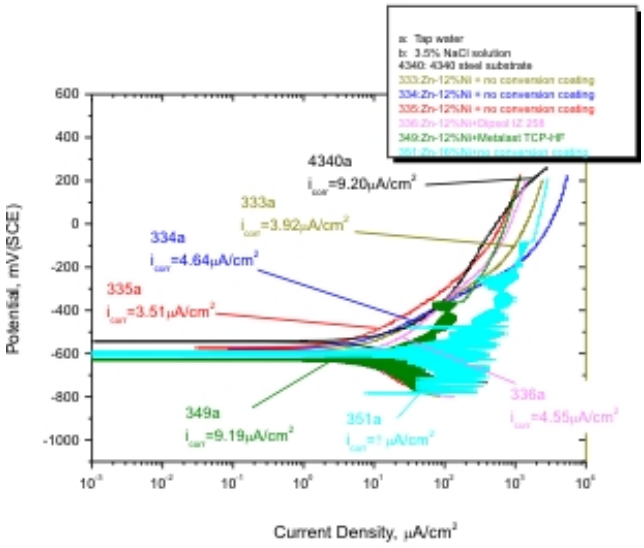

(b)

Figure 100. (b) Anodic polarization behavior of samples in tap water (Aerated): 4340a) Steel 4340 in tap water, 333a) sample 333 in tap water, 334a) sample 334 in tap water, 335a) sample 335 in tap water, 336a) sample 336 in tap water, 349a) sample 349 in tap water, 351a) sample 351 in tap water.

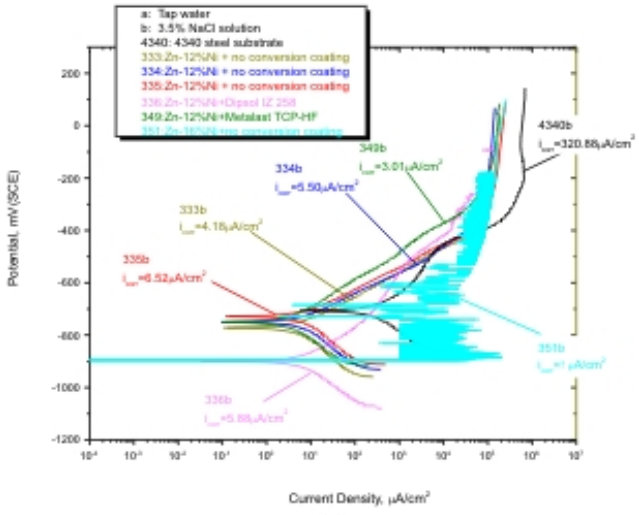

(c)

Figure 100. (c) Anodic polarization behavior of samples in 3.5% NaCl solution (Aerated): 4340b) Steel 4340 in 3.5% NaCl solution, 333b) sample 333 in 3.5% NaCl solution, 334b) sample 334 in 3.5% NaCl solution 335b) sample 335 in 3.5% NaCl solution 336b) sample 336 in 3.5% NaCl solution 349b) sample 349 in 3.5% NaCl solution 351b) sample 351 in 3.5% NaCl solution.

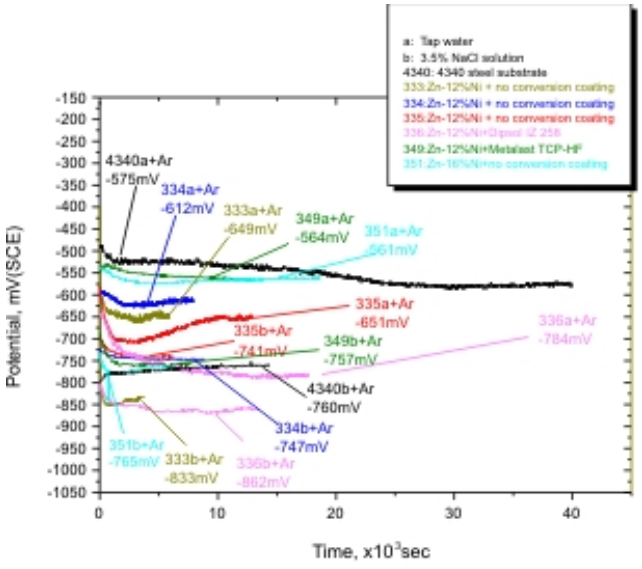

(a)

Figure 101 (a) Ecorr vs Time for the samples in tap water and 3.5% NaCl solution(Deaerated): 4340a+Ar) Steel 4340 in tap water with Ar, 333a+Ar) sample 333 in tap water with Ar, 334a+Ar) sample 334 in tap water v, 335a+Ar) sample 335 in tap water with Ar, 336a+Ar) sample 336 in tap water with Ar, 349a+Ar) sample 349 in tap water with Ar, 351a+Ar) sample 351 in tap water with Ar.

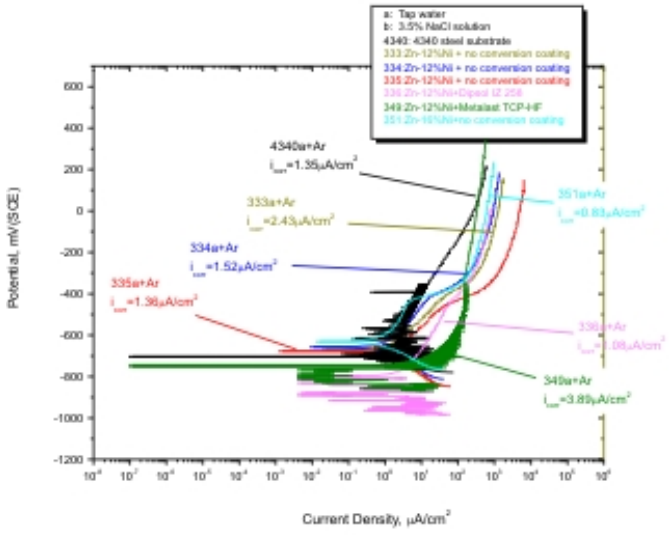

(b)

Figure 101. (b) Anodic polarization behavior of samples in tap water (Deaerated): 4340a+Ar) Steel 4340 in tap water with Ar, 333a+Ar) sample 333 in tap water with Ar, 334a+Ar) sample 334 in tap water v, 335a+Ar) sample 335 in tap water with Ar, 336a+Ar) sample 336 in tap water with Ar, 349a+Ar) sample 349 in tap water with Ar, 351a+Ar) sample 351 in tap water with Ar.

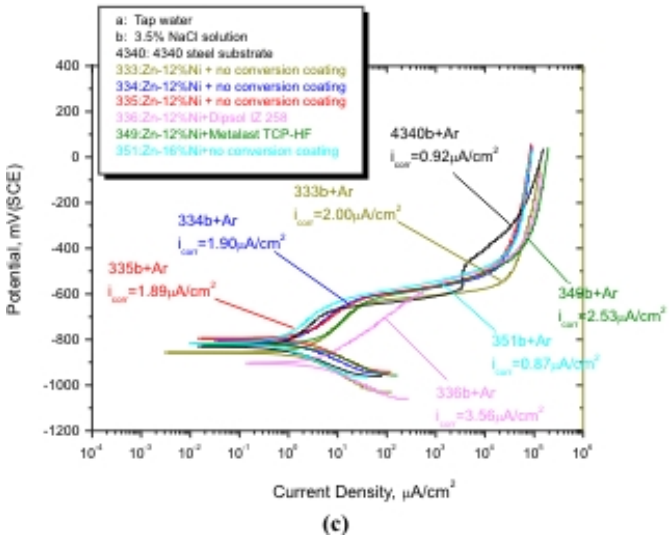

(c)

Figure 101. (c) Anodic polarization behavior of samples in 3.5% NaCl solution (Deaerated): 4340b+Ar) Steel 4340 in 3.5% NaCl solution with Ar, 333b+Ar) sample 333 in 3.5% NaCl solution with Ar, 334b+Ar) sample 334 in 3.5% NaCl solution with Ar, 335b+Ar) sample 335 in 3.5% NaCl solution with Ar, 336b+Ar) sample 336 in 3.5% NaCl solution with Ar, 349b+Ar) sample 349 in 3.5% NaCl solution with Ar, 351b+Ar) sample 351 in 3.5% NaCl solution with Ar.

5.3.5 Salt Fog Corrosion Testing and Evaluation

Based on the results of the previous section, several 4340 steel flat panels were EPT-cleaned and Zn-Ni coated at CAP Technologies. The coating thickness was around 12 μm. Twelve of these panels were selected for salt fog testing at the NAVAIR Inorganic Coatings Lab, Patuxent, MD (Andy Schwartz). Six of the panels, # 337, 338, 339, 340, 341 and 342, were treated with Dipsol I-Z 258 and the other six panels, #343, 344, 345, 346, 347, 348, were treated with Metalast TCP-HF. The detail deposition conditions are listed in the Table 27.

The surface appearance of these samples after 29 days of salt fog testing is shown in Figures 102 and 103. All samples with Zn-12Ni%/Dipsol (sample #337-342) exhibited significant corrosion. On the contrary, all the Metalast treated samples (sample #343~348) were intact exhibiting excellent corrosion resistance. In view of that behavior, salt fog testing continued for 2700 hours. It should be noted that thirty panels were tested in the chamber at the same time (12 from CAP and 18 from other sources) and the EPT Metalast treated specimens were the only specimens that survived the salt fog environment for more than one month while all the rest of the specimens had been corroded and removed from the testing chamber. The Metalast treated specimens continued to do great in terms of corrosion resistance even at 10 weeks (1700 hours). Fig. 104 presents the corrosion performance of the twelve CAP coated specimens in salt fog testing upto 2700 hours. The corrosion resistance showed by the Meatalst treated specimens is significant since Dipsol is an agent containing hexavalent chrome while Metalast contains trivalent chrome and thus, it is not poisonous. Thus, treatment of the EPT Zn-Ni coating with Metalast provides excellent corrosion resistance while is safe.

Table 27 Deposition procedures for the panels for salt fog testing.

Sample	Typeofcoating	pH	Conductivity(mS@°C)	Electrolyte temp(°C)	Voltage(V)	Current(Amps)	Dwelltime(sec)
337 (marked 39)	Zn-12%Ni/Dipsol	3.8	40@85	85	195	20	60
338 (marked 41)	Zn-12%Ni/Dipsol	3.7	40@85	85	195	20	60
339 (marked 42)	Zn-12%Ni/Dipsol	3.6	41@85	85	195	20	60
340 (marked 34)	Zn-12%Ni/Dipsol	3.6	41@85	85	195	20	60
341 (marked 40)	Zn-12%Ni/Dipsol	3.6	41@86	86	195	20	60
342 (marked 43)	Zn-12%Ni/Dipsol	3.5	42@85	85	195	20	60
343 (marked 44)	Zn-12%Ni/Metalast	4.1	38@85	85	195	20	60
344 (marked 45)	Zn-12%Ni/Metalast	4.0	38@85	85	195	20	60
345 (marked 46)	Zn-12%Ni/Metalast	3.9	38@85	85	195	20	60
346 (marked 47)	Zn-12%Ni/Metalast	3.9	39@85	85	195	20	60
347 (marked 48)	Zn-12%Ni/Metalast	3.8	39@85	85	195	20	60
348 (marked 48)	Zn-12%Ni/Metalast	3.8	39@85	85	195	20	60

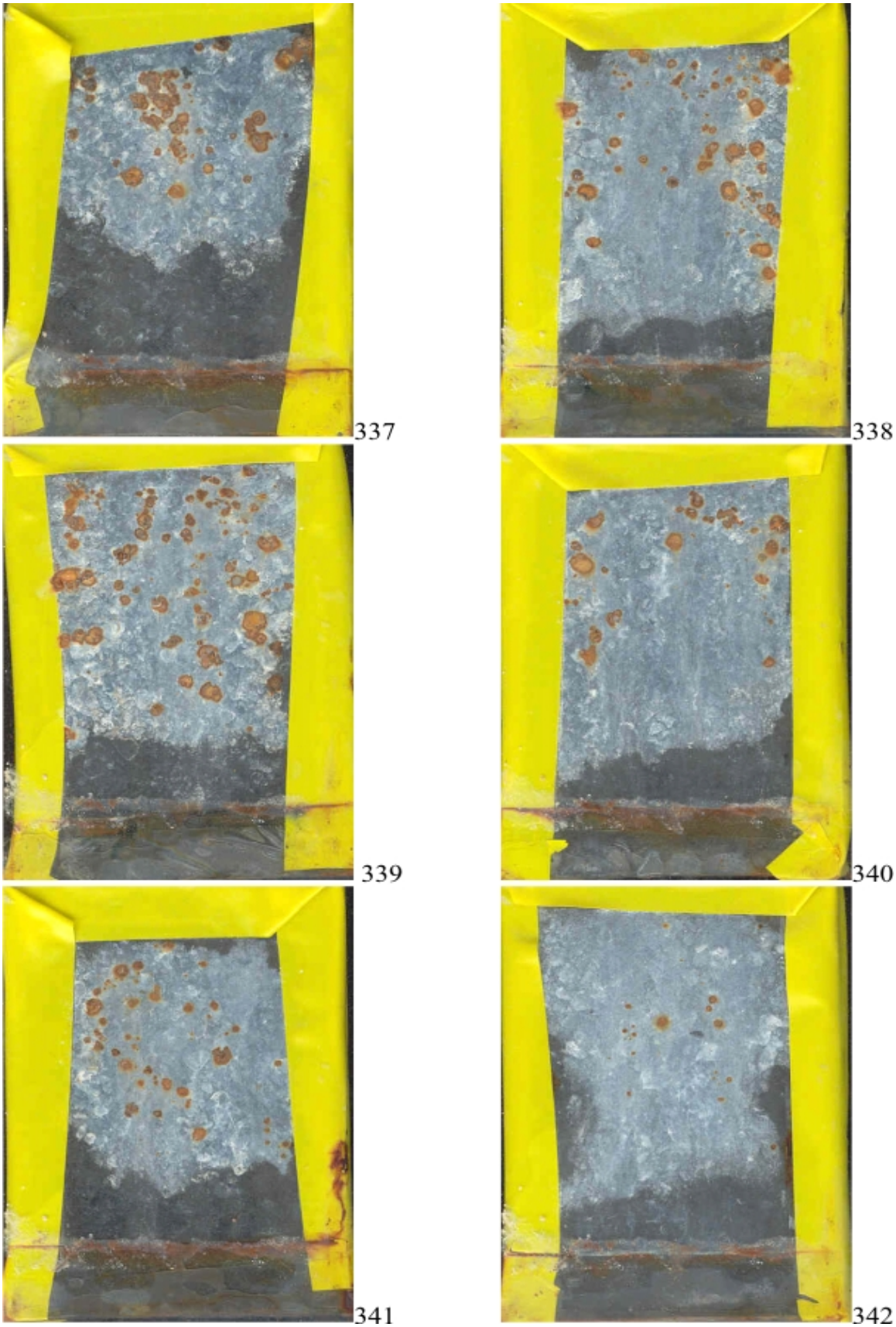

Figure 102 Surface appearance of Zn-12Ni%/Dipsol panels after 29 days of salt fog testing.

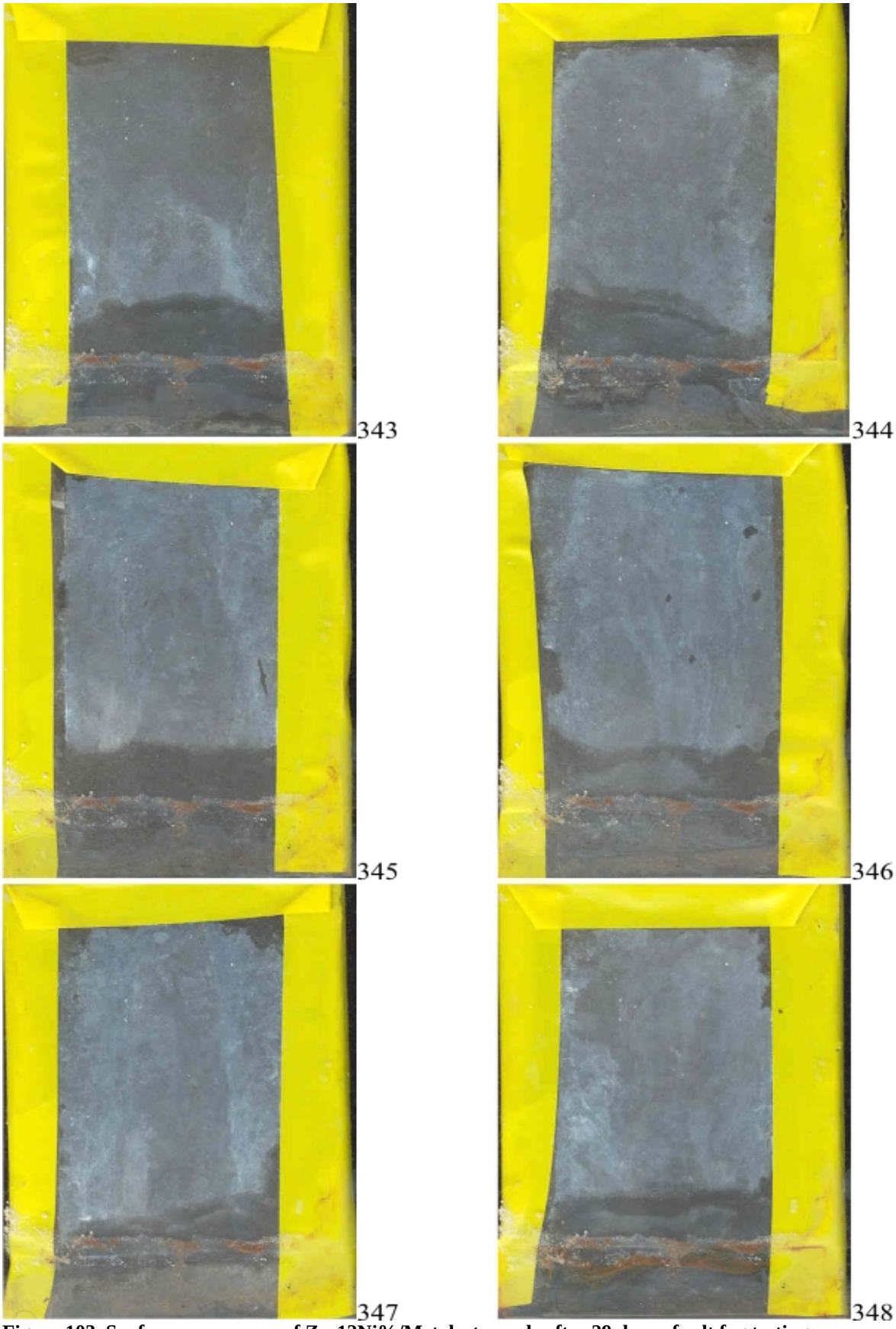

Figure 103 Surface appearance of Zn-12Ni%/Metalast panels after 29 days of salt fog testing.

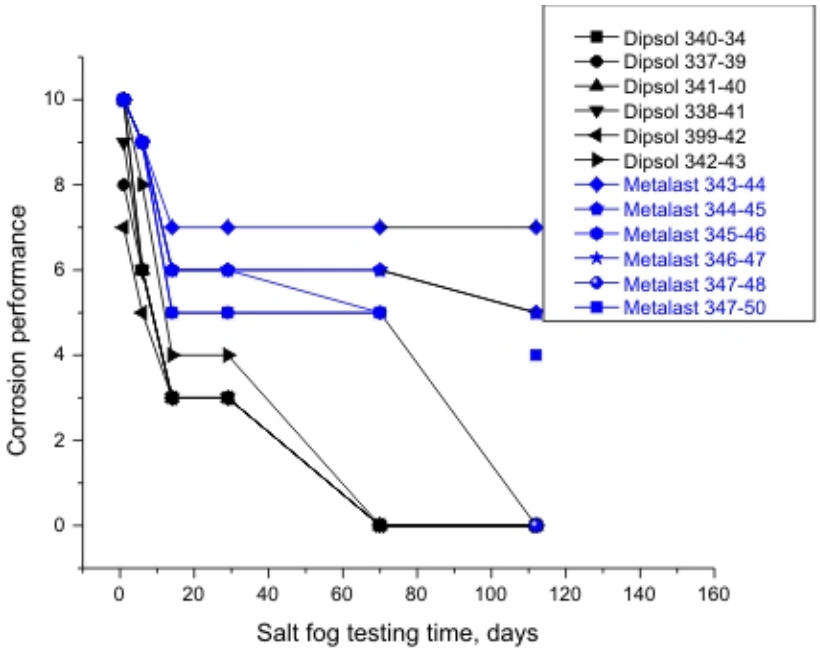

Note: The ranking is a measure of how much corrosion product accumulates on the surface. A ranking of 10 is no product, 0 is 50% of surface is covered, at which point the standard procedure is to remove the specimen from the chamber. The scale is non-linear.

Defect area (%)	Rank #
0	10
>0 – 0.1	9
>0.1 – 0.25	8
>0.25 – 0.5	7
>0.5 - 1	6
>1 – 2.5	5
>2.5 – 5	4
>5 – 10	3
>10 – 25	2
>25 – 50	1
>50	0

Figure 104 Corrosion performance of CAP Zn-Ni coatings in salt fog testing.

6. Summary of Findings

EPT Cleaning:

It was shown that EPT treatment of 4340 steel can produce an effectively clean surface with very low oxygen content and a desirable surface profile with roughness in the micron scale. The cleaning treatment was found to produce a fine and gradient microstructure in the near surface region composed of an amorphous top surface layer followed by a nanocrystalline layer.

It was found that a compressive internal stress develops at the surface during cleaning. After cleaning the material maintains its hardness. Hydrogen analysis showed either no hydrogen or presence of an insignificant amount of hydrogen in a shallow depth from the cleaned surface. No signs of Hydrogen Embrittlement (HE) were detected in the cleaned EPT HE specimens. Fatigue testing did not show any major fatigue debit in shot peened, EPT-cleaned specimens. Thus, EPT proved to be an effective cleaning process.

EPT Coating:

Three types of coatings were successfully deposited; Zn-Al coatings, Al-rich coatings, and Zn-Ni coatings. Even though deposition of Al-containing coatings was achieved, the produced coatings were very thin (<~4 μm). In the Al-containing coatings, Al was found to be present as Al hydroxide rather than Al oxide. So, for applications that require thin Al-containing coatings, EPT can present certain advantages.

Uniform and thick (20-30 μm) Zn-Ni coatings were deposited by EPT mainly composed of a single Zn-Ni phase. Variation in the Ni content was achieved by varying the percentage of the Ni salt in the electrolyte. Coatings with Ni content in the range of 10 – 30 at% could be deposited. Laboratory corrosion testing showed that only coatings with low Ni content (<15 at% Ni) can act as a sacrificial anode and provide protection to underlying 4340 steel.

HE ASTM-F-519 testing at ARL showed that the EPT processes passed the requirements for coatings and processes and “the EPT coatings and process is far better than most prospective cadmium replacement coatings at reducing hydrogen embrittlement risk on high strength steel”. Fatigue testing of Zn-Ni coated specimens at Metcut Research, Inc. showed a small fatigue debit compared to untreated 4340 steel.

Salt fog corrosion testing at NAVAIR showed that the Metalast post treated Zn-Ni coated specimens survived long duration testing and exhibited an excellent corrosion resistance. This is significant since Metalast contains trivalent chrome and is a safe treatment and thus, may present an additional advantage over existing hexavalent chrome containing treatments.

Thus, EPT can produce Zn-Ni sacrificial coatings providing corrosion protection to 4340 steel. An advantage of EPT in comparison to other deposition methods, is its ability to combine desirable cleaning and coating in a single treatment and can constitute an alternative to Cd replacement.

Publications

The following papers were produced from this project:

1. **Compressive stresses induced during electrolytic plasma cleaning of 4340 steel,**
   Y.H. Cheng, P. Gupta, and E.I. Meletis
2. **Metastable microstructure formed in electrolytic plasma processing treated 4340 steel**
   Y.H. Cheng and E.I. Meletis
3. **Influence of treatment time on the surface morphology, microstructure and internal stress in 4340 steel cleaned by electrolytic plasma processing**
   Y.H. Cheng, P. Gupta and E.I. Meletis
4. **Nanocrystalline Zn coatings deposited by electrolytic plasma processing**
   Y.H. Cheng, C. Cionea, P. Gupta and E.I. Meletis
5. **Structure of Zinc-Nickel coatings deposited by electrolytic plasma processing**
   Shaoxin You, Pratheesh George and Efstathios I. Meletis

Also, a poster paper was presented at the SERDP Meeting, Dec. 2007, Washington, DC.

1. **Electrolytic Plasma Technology: A Novel Cleaning and Coating Technology**
   Cristian Cionea, Shaoxin You, Edward Daigle, Prathesh George and Efstathios I. Meletis

References

1) A.L. Yerokhin, X. Nie, A. Leyland, A. Matthews, S.J. Dowey, Surf. Coat. Technol. 122(1999)73.

2) E.I. Meletis, X. Nie, F.L. Wang, J.C. Jiang, Surf. Coat. Technol 150(2002)246.

3) W. McNiell, L.L. Gruss, US patent 3 293 158, 1966.

4) L.A. Snezhko, L.A. Beskrovnyj, Yu.M. Nevkrytyj, V.I. Tchernenko, Zashch. Met. 16(3)(1980)365.

5) L.A. Snezhko, S.G. Pavlus, V.I. Tchernenko, Zashch. Met. 20(4)(1984)292.

6) G.A. Markov, M.K. Mironova, O.G. Potapova, Izv. AN SSSR. Ser. Neorgan. Mater. 19(7)(1983)1110.

7) V.A. Fyedorov, V.V. Belozerov, N.D. Velikosel'skaya, S.I. Bulychev, Fiz. Khim. Obrab. Materialov 4(1988)92.

8) P.S. Gordienko, P.M. Nedozorov, L.M. Volkova, T.P. Yarovaya, O.A. Khrisanfova, Zashch. Met. 25(1)(1989)125.

9) P. Kurze, W. Krysmann, G. Marx, Z. Wiss, Tech. Hochsch. Karl-Marx-Stadt 24(1982)139

10) P. Kurze, J. Schreckenbach, T. Schwarz, W. Krysmann, Metalloberflaeche 40(12)(1986)539

11) R.J. Gradkovsky, S.N. Bayles, US Patent 3 956 080, May 11, 1974.

12) S.D. Brown, K.J. Kuna, T.B. Van, J. Am. Ceram. Soc. 54(8)(1971)384.

13) W. Xue, Z. Deng, Y. Lai, R. Chen, J. Am. Ceram. Soc. 81(1998)1365.

14) A.A. Voevodin, AlL. Yerokhin, V.V. Lyubimov, M.S. Donley, J.S. Zabinski, Surf. Coat. Technol. 86-87(1996)516

15) A.L. Yerokhin, A.A. Voevodin, V.V. Lyubimov, J.S. Zabinski, M.S. Donley, Surf. Coat. Technol. 110(3)(1998)140.

16) R.H.U. Khan, A.L. Yerokhin, T. Pilkington, A. Leyland, A. Matthews, Surf. Coat. Technol. 200(2005)1580.

17) A.L. Yerokhin, L.O. Snizhko, N.L. Gurevina, A. Leyland, A. Pilkington, and A. Matthews, J. Phys. D: Appl. Phys. 36(2003)2110

18) 18.J. Baszkiewicz, D. Krupa, J. Mizera, J.W. Sobczak, A. Bilinski, Vacuum 78(2005)143.

19) P. Gupta, G. Tenhundfeld, E.O. Daigle, P.J. Schilling, Surf. Coat. Technol., in Press.

The University Of Sheffield.

Department Of Engineering Materials

Research Centre in Surface Engineering

Electrolytic Plasma Processing for Sequential Cleaning and Coating Deposition for Cd Plating Replacement

2004 – 2008

Final Project Report

Submitted by: Dr Aleksey Yerokhin
Tel.: +44 1142 225510
FAX: +44 1142 225943
E-mail: A.Yerokhin@sheffield.ac.uk

Principle Investigator (PI): Prof Allan Matthews
Tel: +44 1142 225466
FAX: +44 1142 225943
E-mail: A.Matthews@sheffield.ac.uk

Submitted to: Science Applications International Corporation
FAO: Mr Richard Breault
Senior Buyer
7 Wells Avenue
Newton, MA 02459
USA
Tel.: 617-618-4663
FAX: 617-964-1337

February 15, 2008

DoD EPA DOE SERDP
Strategic Environmental Research and Development Program
Improving Mission Readiness Through Environmental Research

RCSE

ACKNOWLEDGEMENT

The research was supported wholly by the U.S. Department of Defense through Strategic Environmental Research and Development Program (SERDP)

Summary

Results of the research activities at the University of Sheffield are discussed, aiming for the development of Electrolytic Plasma Processing (EPP) treatments for cleaning and coating of 4340 high-strength steel (HSS) substrates. The work included (i) development of experimental EPP facility; (ii) research and development in pulsed current EPP cleaning technology; (iii) research and development in novel pulsed current EPP technology for coating deposition of single component Zn- and Al-based electrolyte solutions and binary Zn-Al-containing electrolytes; (iv) deposition and evaluation of EPP coatings produced from ternary Al-Zn-Me (Me=V,Mn,Mg) electrolyte systems; (v) research and development in sequential surface treatments, involving EPP coating followed by passivation post-treatments; (vi) provision of EPP treated samples for further mechanical and corrosion evaluations. The coatings and treated surfaces were characterised using surface profilometry, SEM, EDX and microhardness tests. Tribological performance was evaluated from reciprocating sliding wear tests according to ASTM G133-95. Anti-corrosion performance was evaluated using electrochemical Potentiodynamic corrosion scans according to ASTM G5-94.

Keywords: Electrolytic plasma; Pulsed current; Surface cleaning; Zn based coating; High-strength steel; Corrosion; Hydrogen embitterment; Fatigue; Surface morphology; Surface composition.

Report contains: Pages: 58; Figures: 38; Tables: 6.

List of staff involved into project

Professor Allan Matthews	PI	General project management and supervision
Dr Aleksey L Yerokhin	Post-Doctoral Research Associate	Current project management; planning and performing experiments; data analysis, report submission
Mr Tony Pilkington	Research Associate	Preparation and performing experiments; data analysis
Mr Chris Miles	MSc student	Characterisation and testing
Mr Ravindu Wagage	Undergraduate student	Characterisation and testing

Contents

Contents 5
List of Figures 6
List of Tables 8
1. Introduction and Objectives 9
2. Surface Characterisation and Testing Techniques Employed 11
3. Development of Experimental Facility for Electrolytic Plasma Processing 12
3.1. Equipment design 12
3.2. Validation of the design solutions 14
3.2.1. Configurations with rotating samples 14
3.2.2. Configuration with linear reciprocating sample movement 21
4. Development of Pulsed Current EPP Cleaning Process 23
5. Development of Pulsed Current EPP Coating Processes 31
5.1. Research context 31
5.2. Provision and evaluation of benchmark coatings 31
5.3. Process development and characterisation of pulsed unipolar EPP Zn coatings 35
5.4. Process development and characterisation of EPP coatings produced from single-component Al-, and binary Al-Zn-containing electrolyte systems 41
5.4.1. Alkaline electrolyte systems 41
5.4.2. Acidic electrolyte systems 42
5.4.3. Discussion of the results 48
5.5. EPP coatings produced from ternary Zn-Al-Me electrolyte systems (Me= V, Mn, Mg) 48
6. Sequential Surface Treatments Involving EPP Coatings Obtained From Binary Zn-Mg Containing Electrolyte 50
7. Provision of EPP treated samples for further testing 56
7.1. Provision of cleaned samples for Hydrogen Embrittlement and Fatigue tests 56
7.2. Provision of EPP cleaned samples for additional Fatigue tests 56
7.3. Provision of EPP coated samples for Fatigue and Corrosion tests 58
8. Conclusions and future work 60

List of Figures

Figure 1 Schematic diagram of experimental EPP facility at Sheffield University accommodated for the treatment of different components: (a) bars and rods; (b) discs; (c) flat coupons 13

Figure 2 Experimental EPP facility at Sheffield University. 15

Figure 3 Plasma reactor with rotating sample and (a) vertical and (b) horizontal position of the counter-electrode (c). 16

Figure 4 Plasma reactor with reciprocating movement of the sample and vertical position of the counter-electrode, showing details of: (a) the sample holder (b) the graphite counter electrode in operation 17

Figure 5 (a) – current-voltage diagram of EPP cleaning system, showing characteristic regions of conventional electrolysis (0-Ua), transient (Ua-Ub) and plasma discharge (Ub-Uc). (b) and (c) – discharge appearance at the points Ub and Uc, accordingly 18

Figure 6 Typical current and voltage waveforms at different stages of EPP cleaning in DC (a, b, c and d) and pulsed unipolar current mode (e and f). 19

Figure 7 Cross-sectional micrographs of mild steel disc samples, illustrating a degree of structural changes in the substrate material introduced by EPP treatments under condition #2 (Table 1). (a) -200 V, (b) 20

Figure 8 Cross-sectional SEM images of EPP Zn coatings produced under conditions of experiments (a) - #4 and (b) - #5 (Table 2). 22

Figure 9 SEM micrographs of initial and EPP cleaned surfaces using DC and different parameters of pulsed current 24

Figure 10 Typical XRD patterns of initial and EPP cleaned surfaces 25

Figure 11 Effects of pulsed current parameters on surface roughness of EPP cleaned 4340 HSS. 26

Figure 12 GDOES patterns revealing characteristic Fe and O distributions in the surface region of untreated and EPP cleaned steel samples 27

Figure 13 Effects of EPP cleaning on surface hardness of 4340 HSS tested at different loads. For pulsed current conditions, f=10 kHz and corresponds to the sample series. .. 28

Figure 14 Residual stress map for pulsed current EPP cleaning 29

Figure 15 Potentiodynamic corrosion curves of EPP cleaned surfaces in deaerated 3.5% NaCl solution 30

Figure 16 XRD patterns of (a) 4340 steel substrate (black) and commercially available Cd (red) and (b) Zn plating coatings without passivation treatments. In chart (b), blue and red PDF patterns correspond to Fe and Zn respectively. 32

Figure 17 Dynamic friction coefficients of Cromate passivated Cd (a) and Zn (b) plating

coatings vs AISI 52100 steel ball during reciprocating sliding wear tests at 10 N load (ASTM G133-95)..... 32

Figure 18 Potentiodynamic polarisation curves for (a) substrate; (b) Cd and (c) Zn coatings. Data on the left and right represent results of Tafel and polarisation resistance fits, respectively. 34

Figure 19 SEM micrographs (a,c and d) and typical EDX pattern (b) of EPP Zn coatings produced at various frequencies at =0.8. (a) f=0.1 kHz; (c) f=1 kHz and (d) f=10 kHz. . 37

Figure 20 Typical example of the effects of applied load on microhardness of Zn coatings deposited under different parameters of pulsed current..... 38

Figure 21 Effect of parameters of pulsed current EPP deposition on friction coefficient of Zn coatings during reciprocating sliding wear tests vs AISI 52100 steel ball at 10 N load (ASTM G133-95)..... 38

Figure 22 Potentiodynamic polarisation curves for EPP Zn coatings deposited under DC (a) and various parameters of pulsed current at =0.8: (b) f=0.1 kHz; (c) f=1 kHz; (d) f=10 kHz. 39

Figure 23 GDOES profile of Al-Zn-O EPP coating deposited from alkaline electrolyte under pulsed bipolar current conditions: pos= neg=20ms; Upos=250 V; Uneg=450 V. 42

Figure 24 Typical XRD pattern of Al-O EPP coating deposited from acidic electrolyte under pulsed unipolar current conditions, showing presence of - and -Al2O3 in the surface layer. 43

Figure 25 Surface plane SEM micrographs (a-c) and EDX patterns (d and e) taken from characteristic features of Al-O EPP coatings deposited from acidic electrolyte by pulsed unipolar current with different frequencies at 0.8 duty cycle: (a) f=0.1 kHz; (b) f=1 k..... 44

Figure 26 Typical example of the effect of applied load on microhardness of Al-O coatings deposited from acidic electrolyte under different parameters of pulsed unipolar current. 45

Figure 27 Effect of parameters of pulsed unipolar EPP deposition in acidic bath on friction coefficient of Al-based coatings during reciprocating sliding wear tests vs AISI 52100 steel ball at 10 N load (ASTM G133-95)..... 45

Figure 28 Potentiodynamic polarisation curves of Al-based EPP coatings deposited from acidic solution under DC (a) and various parameters of pulsed unipolar current at =0.8: (b) f=0.1 kHz; (c) f=1 kHz; (d) f=10 kHz. 46

Figure 29 Comparative representation of corrosion behaviour for selected coatings studied in this project..... 47

Figure 30 Typical example of potentiodynamic polarisation curves of Al-based EPP coatings deposited from the acidic solution under various parameters of pulsed bipolar current at cat=0.8. 47

Figure 31 SEM images of surface (left) and cross-sectional view of EPP coatings produced from ternary electrolyte systems: (a) Zn-Al-V; (b) Zn-Al-Mn and (c) Zn-Al-Mg sulphates..... 49

Figure 32 SEM images of surface (left) and cross-sectional view of EPP coatings produced from binary Zn-Mg sulphate electrolyte systems with various concentrations of Mg sulphate: (a) 0.1 M; (b) 0.2 M; (c) 0.3 M, followed by the phosphate-silicate passivation tr 52

Figure 33 Typical GDOES depth profile patterns for (a) as received and (b) phosphate-silicate passivated EPP coatings 53

Figure 34 Typical XRD patterns of as deposited (black) and phosphate-silicate passivation treated EPP coatings. PDF patterns correspond to the following substances: Black – Zn, Red – Zn phosphate; Blue – Silica and Green – Zn silicate 54

Figure 35 Time dependencies of open circuit potential for as deposited and passivated EPP coatings in 3.5% NaCl solution. 54

Figure 36 Potentiodynamic polarisation curves of EPP coatings produced from binary Zn-Mg containing electrolytes illustrating effects of (a) the passivation post-treatment and (b) Mg salt content in the bath. 55

Figure 37 Samples for Hydrogen Embrittlement (top) and Fatigue tests (bottom) after different steps of EPP treatment procedure. 1 – prior to cleaning treatment; 2 – after the cleaning; 3 – after deionised water rinsing. 57

Figure 38 Samples for Fatigue tests (a) and 2 by 3 inch Salt Fog Corrosion Plates (b) after different steps of EPP treatment procedure: 1 – prior to EPP coating; 2 – after the coating; 3 – after the passivation treatment. 59

List of Tables

Table 1 Treatment parameters* and cleaning process characteristics for the modified EPP facility 20

Table 2 Treatment parameters* and Zn coating process characteristics for the modified EPP facility 21

Table 3 Matrix of experimental design and parameters of pulsed current EPP cleaning process 23

Table 4 Process parameters for pulsed current EPP deposition of Zn coatings 36

Table 5 Process parameters for pulsed current EPP deposition of Al coatings 42

Table 6 Thickness and roughness of EPP coatings 51

1. Introduction and Objectives

The University of Sheffield was involved in the above collaborative project, the overall objectives of which included research and development in electrolytic plasma processing (EPP) technology to provide surface cleaning and deposit multicomponent (e.g. Zn-Al based) coatings as possible alternative to Cd-plating. There are known difficulties in cathodic deposition of metallic Al from aqueous solutions. These difficulties arise from: (i) the low Standard Electrode Potential of Al (which is lower than that of hydrogen) preventing formation of a dense and continuous Al layer and (ii) high chemical activity causing instant hydration and/or oxidation of cathodically reduced Al. The main intention within this project was in utilizing a cathodic plasma discharge at the metal-electrolyte interface to minimize these adverse effects and thereby increase the Al content in the surface layer. Although coatings containing metallic Al were of primarily interest, it was deemed that Al-O/OH compounds could also be of some benefit for Zn-based coatings when improving their in-service performance by providing higher hardness and better tribological properties. Another important problem addressed within this project consisted in matching electrochemical behavior of EPP coatings to that of commercially available benchmark coatings (e.g. Cd and Zn). This was mainly associated with tailoring the chemical composition of the surface layer, in particular by doping coating material with the elements (e.g. V, Mn, Mg) extending Zn passivation towards the range of anodic activity of the steel substrate. Unlike other project partners, our approach was based on the application of pulsed current technology (in both unipolar and bipolar modes) which provides much more powerful means than conventional DC techniques to control coating composition, structure and properties. The objectives specific to our part of the project were identified as follows:

(i) Develop experimental EPP facility to allow uniform and reproducible treatment of different shapes of samples, including cylindrical and flat surfaces under pulsed current conditions;

(ii) Study effects of process parameters for pulsed current EPP cleaning on microstructure, phase composition and mechanical properties of 4340 HSS;

(iii) Study effects of process parameters for pulsed current EPP deposition on composition, structure and electrochemical properties of Zn-based coatings deposited on 4340 HSS substrates from single- and multi-component electrolyte systems;

(iv) Develop and investigate sequential methods for surface treatment, combining EPP coatings with passivating post-treatments;

(v) Provide samples for further evaluation and testing of the following properties of EPP cleaned and coated surfaces:

- *Process-induced hydrogen embrittlement (HE)*
- *Fatigue strength*
- *Corrosion resistance*

These objectives were pursued during the course of the project, with the outcomes achieved as discussed in sections 3 to 7.

2. Surface Characterisation and Testing Techniques Employed

Unless otherwise is stated in the text, the following characterisation and test procedures and equipment were utilised:

- The EPP treated samples were characterised in terms of surface roughness and hardness (measured under different loads ranging from 25 to 200 g) using a Dektak^{3}ST surface profilometer and a Mitutoyo MVK G1 microhardness tester. During the tests, 5 parallel measurements were made followed by statistical analysis to derive mean average values and to evaluate data variations.

- Phase composition and structural characteristics of the surface layer was evaluated by XRD techniques. XRD studies were carried out using a Siemens D5000 X-ray diffractometer operated in both locked and unlocked coupled modes to evaluate the phase structure and the stress state in the surface layer respectively. θ-2θ XRD scans ware carried out in the 2θ range of 110-120˚. The standard $d_{hkl}(\psi)$ versus $\sin^2\psi$ method was used to residual stressesin the surface layer.

- SEM analysis was employed to evaluate surface morphology both in top plane and cross-sectional views at a high (typically x1000) and a low (x250) magnification, using a Camscan electron microscope.

- Chemical analysis of the surface layer was performed by EDX and GDOES methods. For the qualitative EDX analysis a Link Analytical attachment to the SEM was used. Semi quantitative depth profiling of chemical elements was performed using a GD-Profiler™ HR 2 GDOES instrument (Horiba/Joblin-Yvon).

- Finally potentiodynamic electrochemical scans were carried out in a 3.5% NaCl solution, in deaerated conditions, using a Solartron 1286 potentiostat-galvanostat to evaluate anodic behaviour of the treated surfaces. The scans were performed at a rate of 1.667 mVs^{-1} in the potential range from -0.5 V (vs OCP) to the final potential of 1.0 V (vs SCE). A platinum plate served as a counter electrode and a Saturate Calomel Electrode (SCE) served as a reference electrode. The tests were performed in both aerated and deaerated conditions. For the deaerated tests, nitrogen gas was purged through the NaCl solution.

3. Development of Experimental Facility for Electrolytic Plasma Processing

3.1. Equipment design

The existing experimental EPP installation at Sheffield was based on a conventional non-agitated bath design, which possessed generic drawbacks (e.g. treatment non-uniformities caused by uncontrolled electrolyte temperature and hydrodynamic conditions as well as high transient currents). These features made it unsuitable for use in the present project. Modification of the existing rig was therefore essential to provide effective solutions to major technological problems, thereby achieving the following key advantages:

(i) Consistent control of electrolyte temperature

- Control over electrolyte thermolysis;
- Improved reproducibility of experiments;

(ii) Adjustable electrolyte flow onto the surface

- Uniform gas evolution rate;
- Control of pressure in gas envelope;

(iii)Movement of the surface in respect to treatment region

- Uniform conditions on large surfaces;
- Elimination of 'immersion depth' effect;

(iv) Pulsed current technology

- Exceptional flexibility in control over surface temperature and chemistry;
- Elimination of overheating;
- Reduction of hydrogen embrittlement;
- Reduction of transient current peak.

Figure 1 shows a schematic diagram of the laboratory-scale EPP rig which allows for controlled sample rotation and reciprocating movement, an adjustable inter-electrode gap as well as controlled electrolyte flow and temperature. The installation comprises the following modules:

- **kinematic module** based on a bench-top lathe with a variable speed drive. The module is equipped with an electrolytic cell with adjustable position for the counter-electrode nozzle. The module can operate in 3 different configurations that allow treatments to be given to different types of components, e.g. rods, discs and flat coupons (Figure 1 a,b and c respectively), thus ensuring high versatility of the installation;

- **power module**, including two DC power supplies (Advanced Energy Inc., MDX II), a pulsing unit, an insulated brush connector and the counter-electrode;

- **hydraulic module**, comprising of an electrolyte storage tank, a centrifugal pump, a plate heat exchanger and a recirculation temperature control unit (Grant GD120/12).

- **control and data acquisition module**, comprising of high current and high voltage probes (Tektronix A6303 and P5200, respectively), a current probe amplifier (Tektronix AM5030) , a digital oscilloscope (Tektronix TDS-340) and a temperature gauge, all connected to a PC via the GPIB bus. Peripheral devices are provided to control the rates of sample rotation and electrolyte flow.

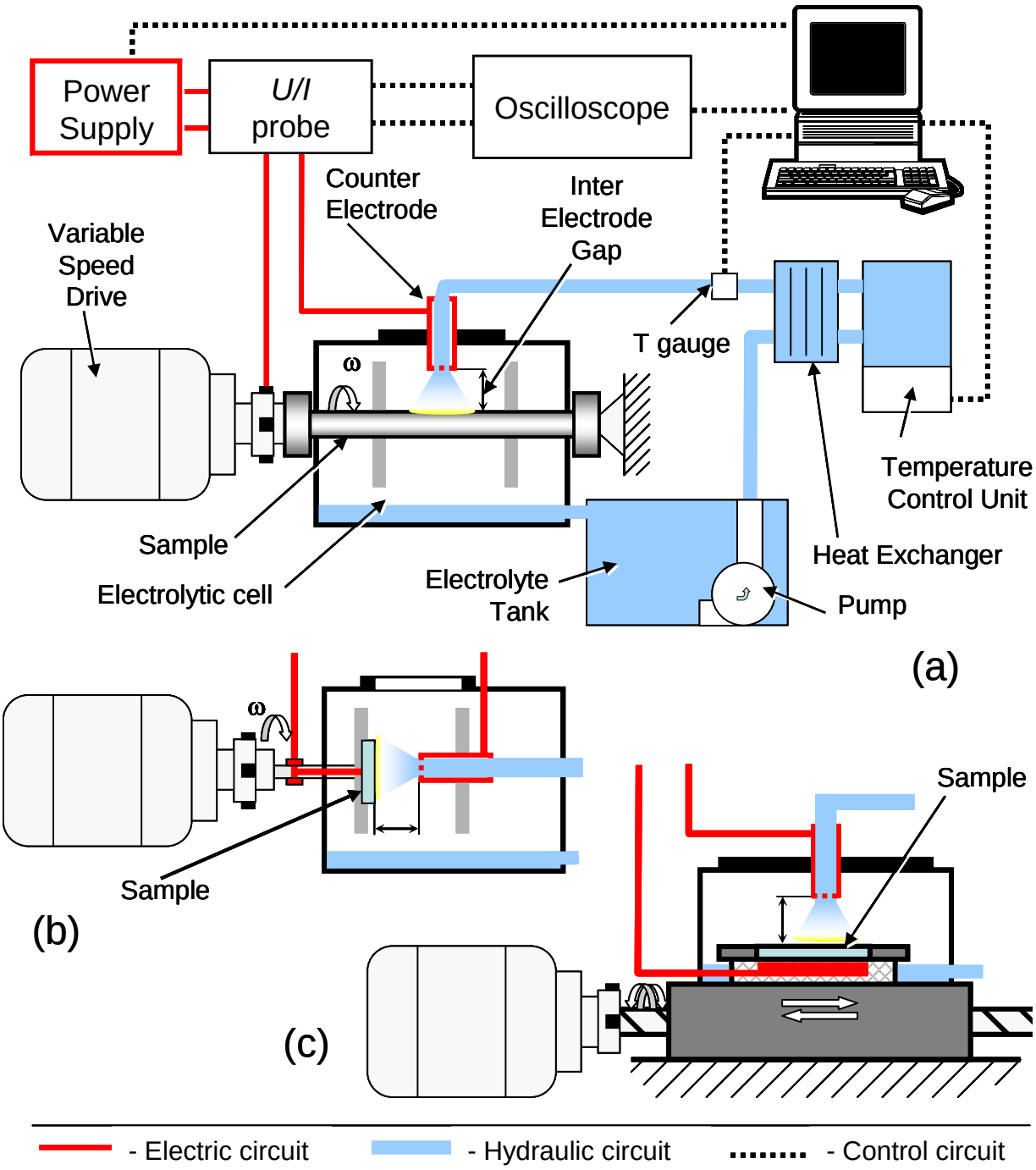

Figure 1 Schematic diagram of experimental EPP facility at Sheffield University accommodated for the treatment of different components: (a) bars and rods; (b) discs; (c) flat coupons

Main characteristics of the modified experimental EPP facility are given below:

Total power capacity		22 kW
Voltage range		1 to 1000 V
Mean current range		0.1 to 50 A
Peak current		200 A
Pulse:	ON time	2 to 2000 μs
	OFF time	2 to 2000 μs
Electrolyte:	temperature	-10 to +100^{o}C; ±0.1^{o}C
	flow rate	0.1 to 10 l s^{-1}
Sample rotation rate		0 to 2500 rpm
Sample linear speed		0 to 500 mm min^{-1}
Inter-electrode gap		5 to 100 mm.

Figure 2 shows a photograph of the prototype experimental facility for EPP processing, outlining general arrangement of the rig and structural links between the different components and modules. Figure 3 provides a detailed image, demonstrating the design solutions adopted for the electrolytic plasma reactor, operating with vertical (Figure 3a and Figure 4) and horizontal (Figure 3b) configurations of the counter-electrode. Typical design of the counter-electrode is shown in Figure 3c. Depending on the treatment requirements, the counter-electrode can be made of a stainless steel (Figure 3c) or graphite (Figure 4b).

3.2. Validation of the design solutions

A series of initial experiments were performed to validate the adopted experimental set-up, obtain basic information regarding characteristics of the modified EPP rig and determine the ranges of process parameters to ensure stable operation in EPP cleaning and coating applications.

3.2.1. Configurations with rotating samples

At the first stage of these initial trials, the effects of electrolyte flow, sample rotation rate and inter-electrode gap were addressed in relation to the DC EPP cleaning process. The electrolyte used for cleaning operations was a 10% solution of sodium bicarbonate, operating at 60^{o}C. Plain disc (25mm diameter by 3mm) and notched bar samples (8mm diameter by 200mm) made of a mild steel were used in rotating configurations with horizontal and vertical counter-electrode arrangements accordingly.

Figure 5 represents a typical example of voltage-current characteristics in the systems

under investigation. It can be seen that the electrolytic process progresses through several stages, including conventional electrolysis (0-Ua), followed by transient (Kellog) region (Ua-Ub) and plasma discharge stage which commences at the potentials U_b around 180…200 V. This is consistent with the results of our earlier studies as well as with the results reported by other project partner groups. Further voltage increase beyond Uc (typically 240-250 V) resulted in the discharge appearance changing from dull orange to bright yellow glow (Figure 4 b,c), which is characteristic for thermal electron emission from the metal electrode and accompanied with acoustic emission.

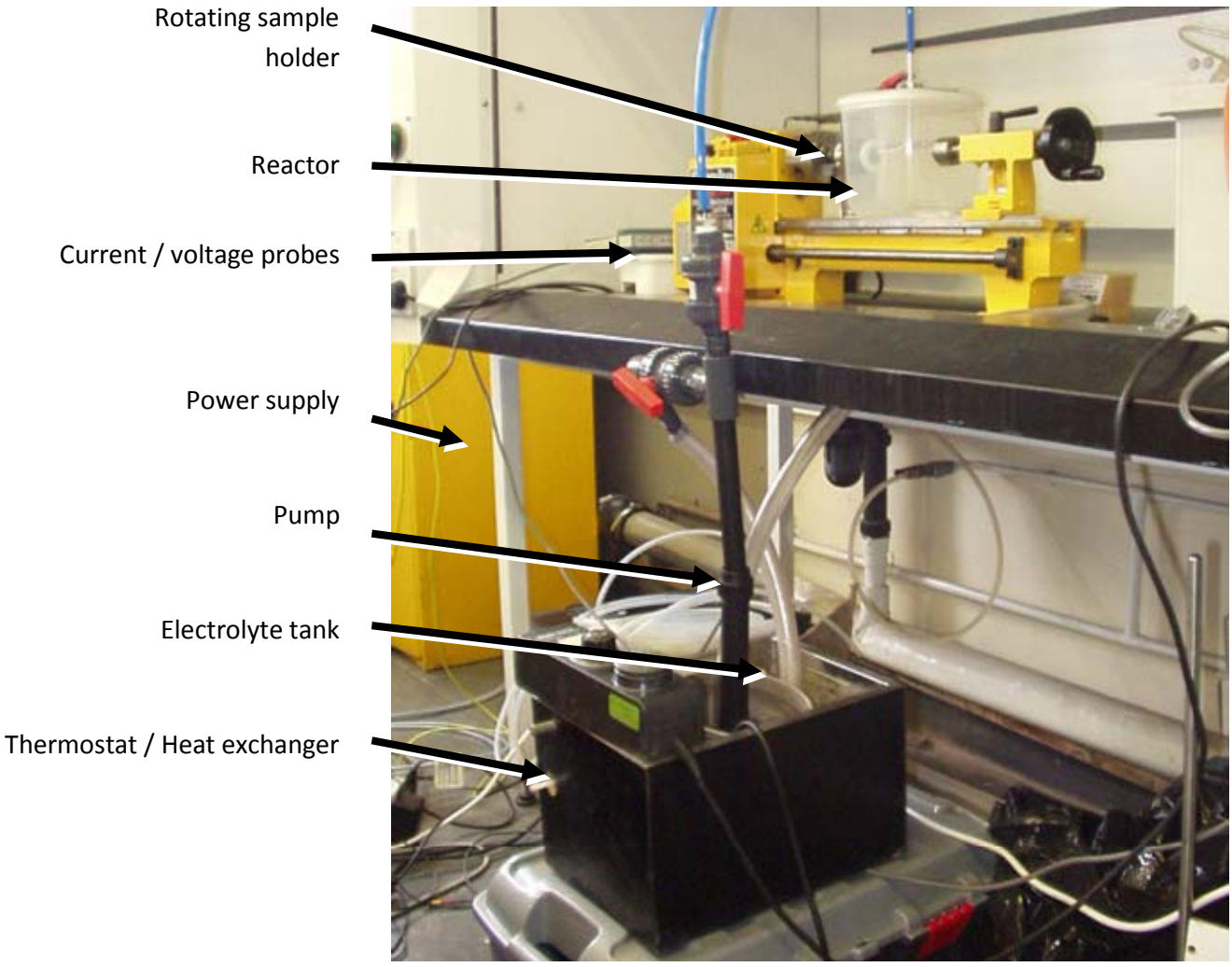

Figure 2 Experimental EPP facility at Sheffield University.

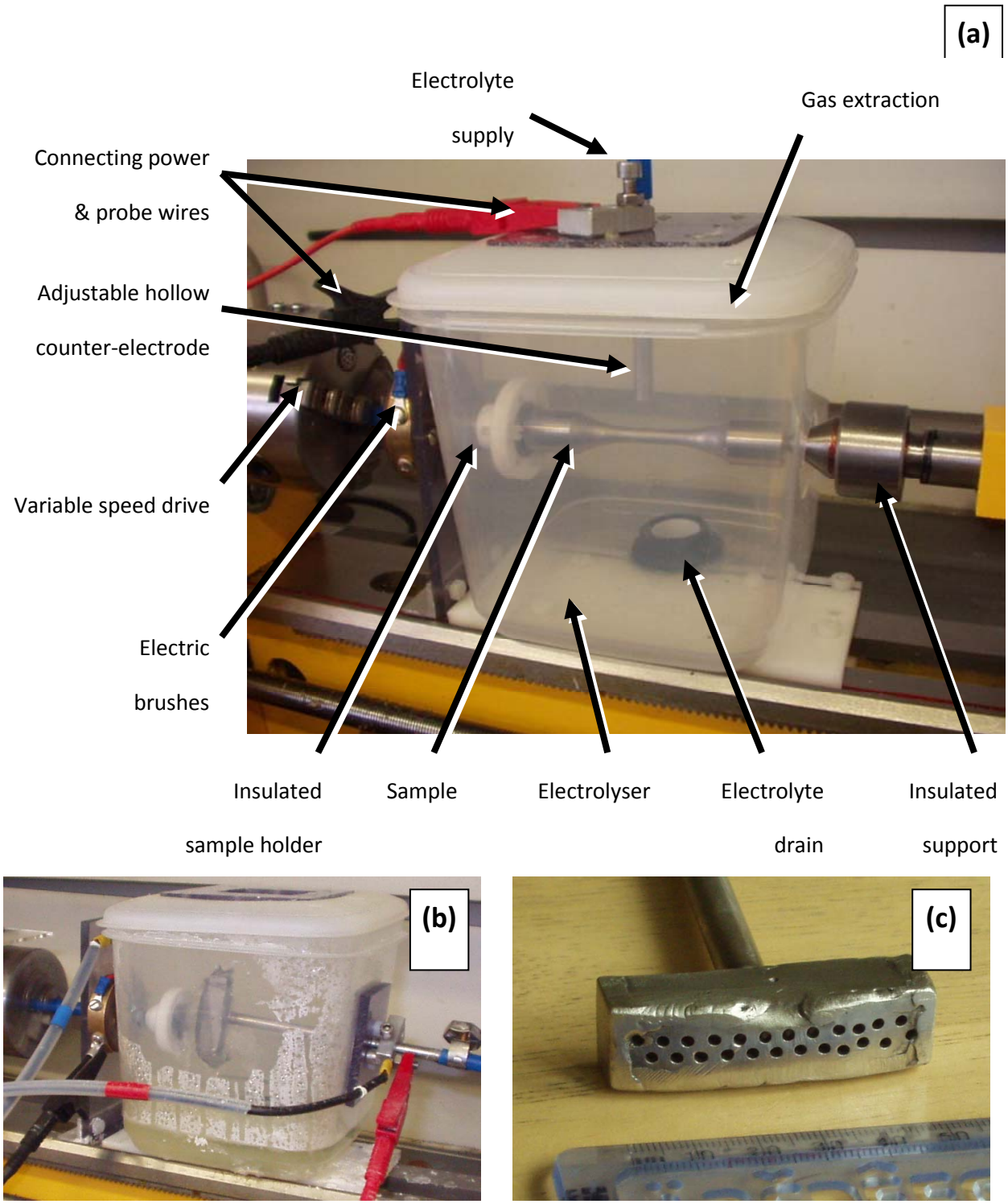

Figure 3 Plasma reactor with rotating sample and (a) vertical and (b) horizontal position of the counter-electrode (c).

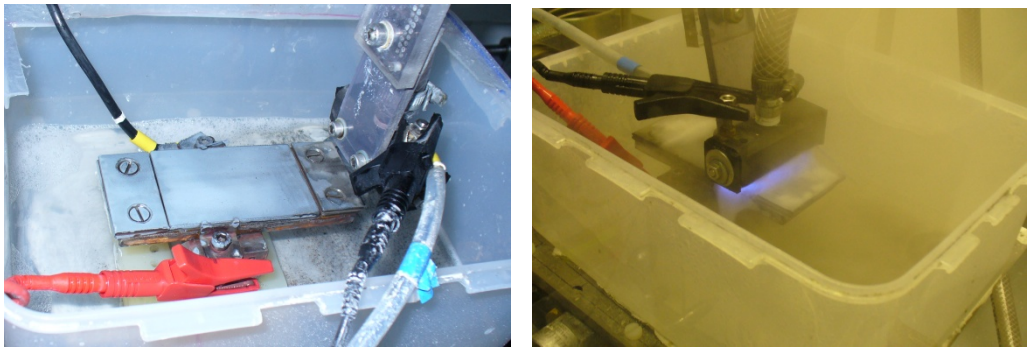

(a) (b)

Figure 4 Plasma reactor with reciprocating movement of the sample and vertical position of the counter-electrode, showing details of: (a) the sample holder (b) the graphite counter electrode in operation

Examples of current and voltage waveforms, corresponding to the above stages of the EPP cleaning process, are given in Figure 5. It is clear that both stages of conventional electrolysis and plasma discharge are featured by relatively stable voltage/current characteristics, although some fluctuation of the above parameters is observed at the latter stage due to the flexible nature of discharge-electrolyte interface. At the same time, major fluctuations of electrical characteristics can be observed during the transient stage of the process associated with hydrodynamic instabilities in transition from bubble to film boiling mode at the sample surface. Such adverse phenomena should be avoided when applying pulsed current modes, as the above fluctuations could affect the operation of control circuits in the pulsing unit, causing damage to electronics.

This major problem encountered during the course of the project was addressed by introducing a specially designed RC filter between power supply and plasma reactor. This is proved to be a reliable solution (Figure 6e and f) that enabled us to advance further with a series of experiments employing pulsed current, as discussed in the following section of the report.

Experimental data, illustrating effects of the process parameters for EPP cleaning on characteristic points Ub and Uc are collated in Table 1. Microstructural analysis of the samples treated at different voltages (Figure 7) showed that plasma treatments in the voltage region between Ub and Uc does not lead to structural alteration in the surface layer, whereas further increase in voltage beyond Uc results in noticeable surface melting and sub-surface recrystallisation. Thus these experimental results allowed us to validate design solutions utilised in a modified EPP rig as well as identifying the following ranges of process parameters, ensuring conditions of stable and reliable EPP cleaning treatments:

Inter-electrode gap:	6…12 mm;
Electrolyte flow rate:	3…7 lpm;
Sample rotation rate:	60…120 rpm;
Sample linear speed:	5…15 mm min^{-1}.

These parameters of DC cleaning treatment were adopted for further experiments, where effects of pulsed current modes were addressed.

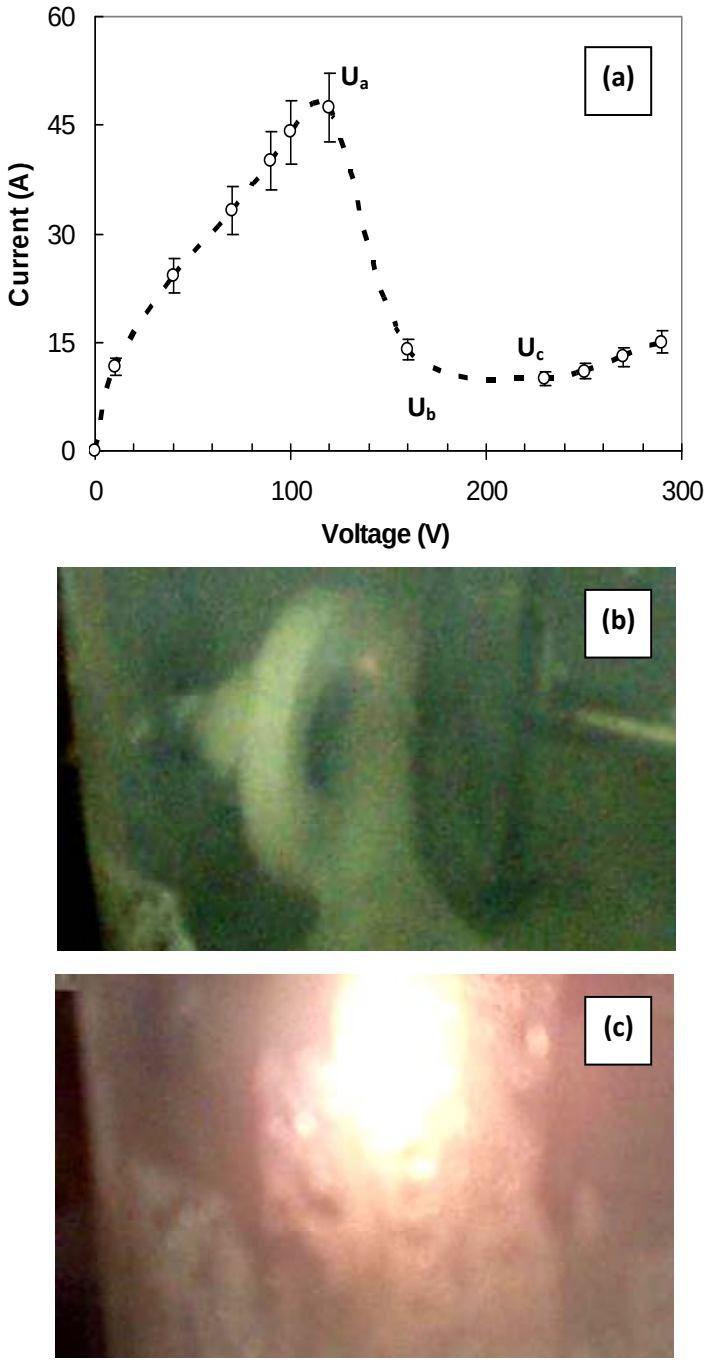

Figure 5 (a) – current-voltage diagram of EPP cleaning system, showing characteristic regions of conventional electrolysis (0-Ua), transient (Ua-Ub) and plasma discharge (Ub-Uc). (b) and (c) – discharge appearance at the points Ub and Uc, accordingly.

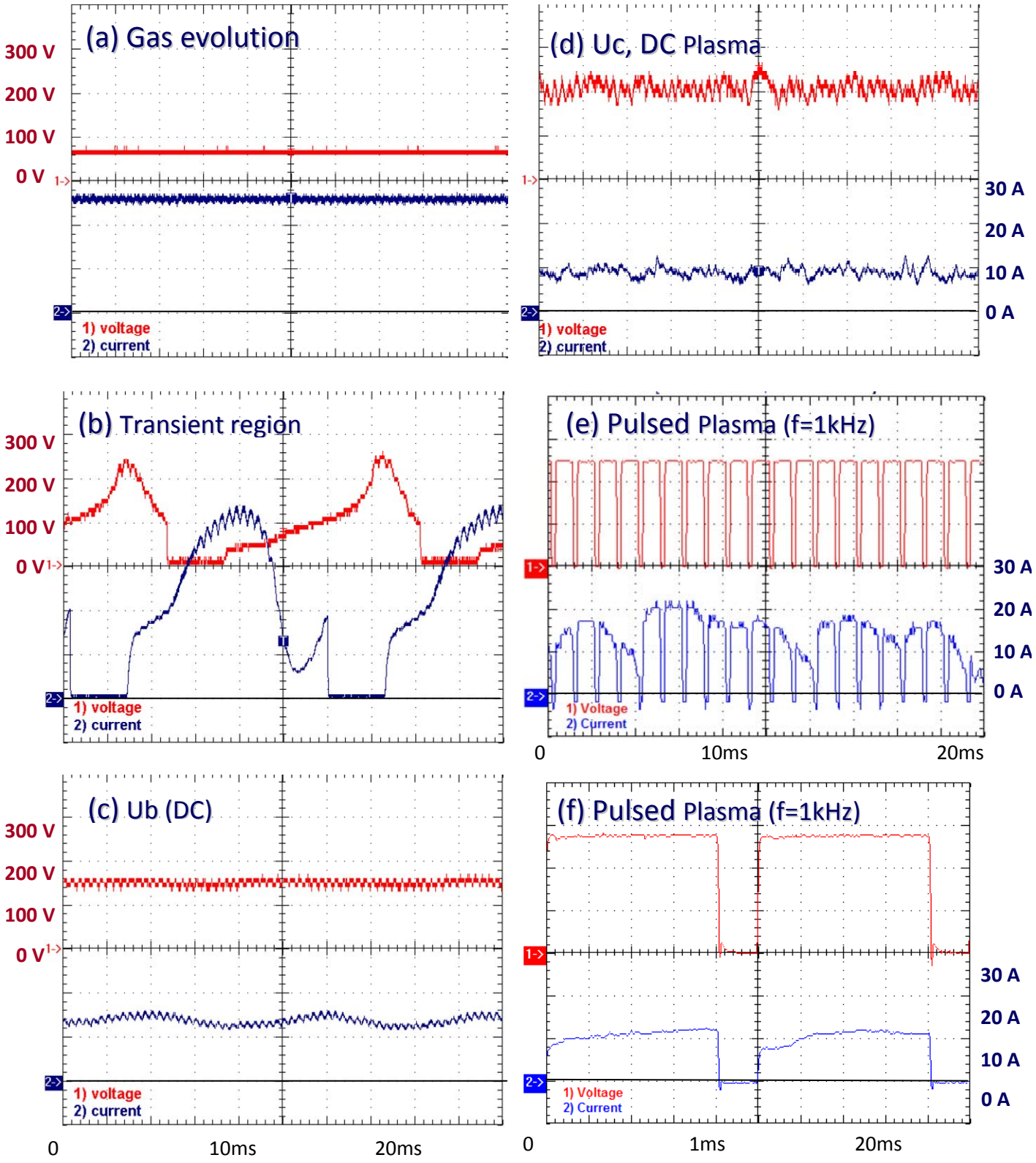

Figure 6 Typical current and voltage waveforms at different stages of EPP cleaning in DC (a, b, c and d) and pulsed unipolar current mode (e and f).

Table 1 Treatment parameters* and cleaning process characteristics for the modified EPP facility

#	Inter-electrode gap (mm)	Electrolyte flow rate (lpm)	Sample rotation rate (rpm)	Ub (V)	Uc (V)	Ib (A)	Comment
1	5	1	60	-170	-190	9	
2	10			-180	-230	7	
3	15			-220	-260	6	Insufficient electrolyte flow in horizontal configuration
4	10	3		-220	-250	7	
5		6		-240	-260	7	Unstable discharge
6		1	120	-185	-240	7	
7			180	-200	-250	8	Unstable discharge

* - Other parameters kept constant at the following levels: Electrolyte temperature =60^{o}C; Disc sample; Voltage sweep rate =25 V s^{-1}; Current mode =DC; Total treatment time =3

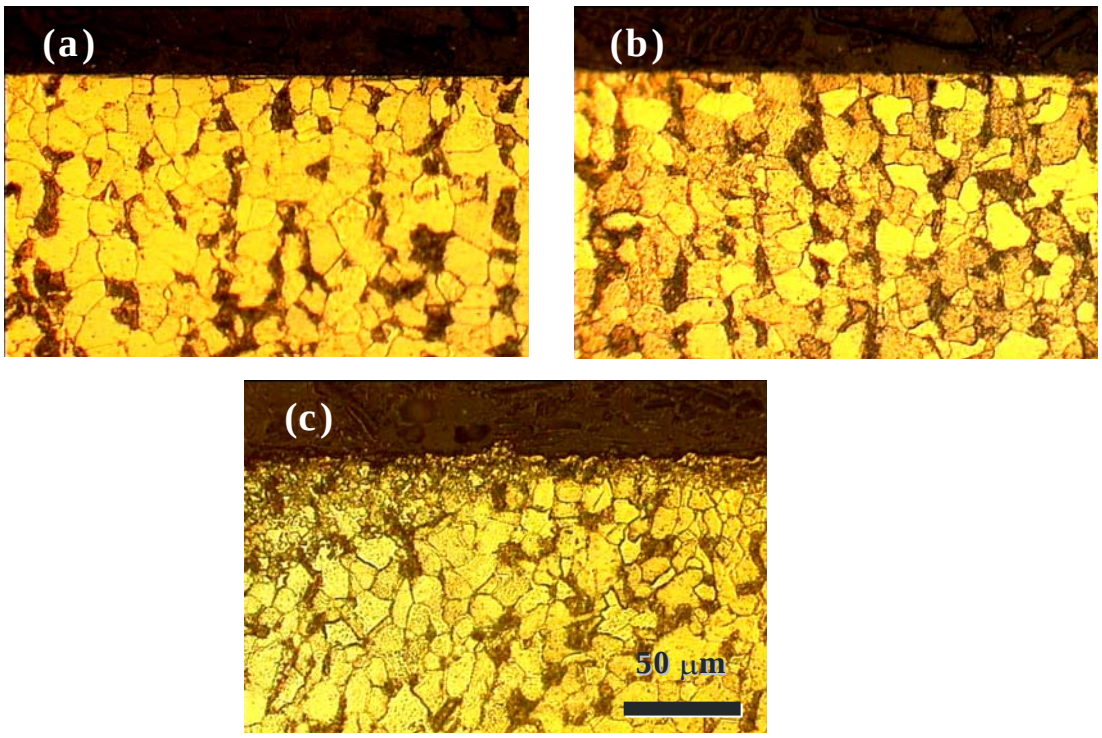

Figure 7 Cross-sectional micrographs of mild steel disc samples, illustrating a degree of structural changes in the substrate material introduced by EPP treatments under condition #2 (Table 1). (a) -200 V, (b)

3.2.2. Configuration with linear reciprocating sample movement

At the second stage, the experiments with coating deposition on flat coupons were carried out, with the effects of sample linear speed, electrolyte concentration and temperature studied (Table 2). For deposition of EPP Zn coatings, solutions of 0.1 and 0.2 M $ZnSO_4 \cdot 7H_2O$ (pH=5.5, conductivity σ=14.5 mS cm) were employed, operating within the temperature range between 60 to 90 ^oC. Mild steel flat coupons (50 mm by 75 mm by 4 mm) were treated in the experiments with reciprocating sample movement and vertical counter-electrode arrangement.

Table 2 Treatment parameters* and Zn coating process characteristics for the modified EPP facility

#	Electrolyte		Sample linear speed (mm min^{-1})	U_c (V)	I_{ave} (A)	Comment
	T (^oC)	C_{ZnSO4} (M)				
1	60	0.1	10	-450	10-16	Unstable arc discharge
2	80			-200	10	Current fluctuations
3	90			-190	14	Uneven coating
4	90	0.2	10	-200	12	Loose deposit on the surface
5			25	-250	14	
6			50	-250	14	Unstable discharge conditions
7			75	-250	16	

* - Other parameters kept constant at the following levels: Electrolyte flow rate = 1 l min^{-1}; Inter-electrode gap = 8 mm; Sample = Flat coupon; Anode = Graphite; Current mode = DC.

Experiments ##1-3 allowed optimisation of the electrolyte temperature to promote the discharge onset at the sample surface. It was noticed that unlike EPP cleaning treatment, U_b-U_c transition in Zn deposition was hindered at lower temperatures whereas it was facilitated by preliminary heating of the sample surface by the electrolyte flow and by increasing electrolyte temperature above 80 ^oC. A further experimentation (runs ##4-7) allowed establishing optimal electrolyte concentration (0.2 M) and sample speed (< 30 mm min^{-1}). Both more diluted electrolytes and faster sample feeds resulted in either discharge instabilities (at a constant voltage) or non-uniform coating appearances. The latter characteristic was examined by visual observations followed by a cross-sectional SEM analysis for the selected samples of interest.

Figure 8 shows cross-sectional SEM morphology of EPP Zn coatings produced under conditions of experiments #4 and #5 (Table 2) respectively. It can be seen that a longer

exposure to electrolytic plasma at a lower voltage (run #4) results in a thicker coating which however is featured by a columnar structure with highly deconvoluted surface and significant porosity. In some cases, a formation of loose $Zn(OH)_2$ deposit was noticed on the sample surface after the treatment; this seems to be a generic feature of the process operating in the transient U_b to U_c mode for this electrolyte system. Although this deposit can be easily washed out during subsequent rinsing in water, its formation is undesirable (from electrolyte in-service life prospective) and should be avoided, e.g. by adjusting electrolyte properties and process parameters.

Higher voltages (e.g. as in run #5) generally led to a reduced porosity but at the same time increased the probability of appearance of powerful arc discharges that caused 'burn' type defects on the surface. This was also influenced by reduced (<5 mm) and/or non-uniform inter-electrode gap across the sample and by uniform electrolyte flow through the hollow anode. This issue was addressed in the improved design of the array-type counter electrode, ensuring appropriate hydrodynamics and careful positioning.

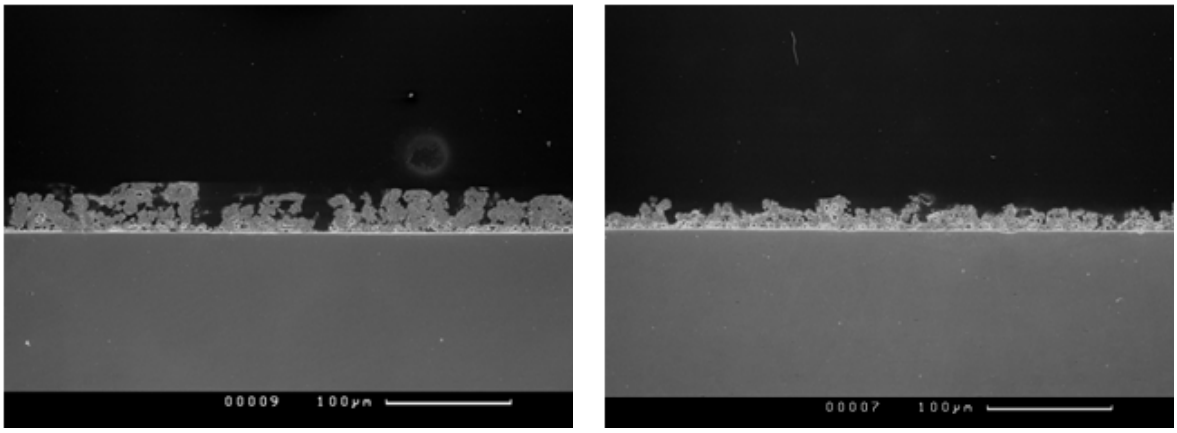

(a) (b)

Figure 8 Cross-sectional SEM images of EPP Zn coatings produced under conditions of experiments (a) - #4 and (b) - #5 (Table 2).

Thus experimental results allowed validating design solutions for treatment of large surface areas, with the following ranges of process parameters identified to ensure effective EPP deposition of Zn-based coatings:

Inter-electrode gap:	8…10 mm;
Electrolyte flow rate:	1…3 lpm;
Sample linear speed:	15…25 mm min^{-1}.

The above parameters of DC EPP Zn coating were adopted as benchmark for further experiments, where effects of pulsed current modes were addressed.

4. Development of Pulsed Current EPP Cleaning Process

At this stage of the project a further series of experiments was carried out, employing pulsed unipolar current mode. In these experiments the effects of frequency and duty cycle were studied for the EPP cleaning treatments of 4340 HSS disc substrates provided by the sponsor. Full factor 2^3 experimental design was implemented, with pulse frequency (f) set at 10^2, 10^3 and 10^4 Hz and duty cycle (δ) set at 0.8, 0.5 and 0.3 (Table 3). In addition, a reference sample was treated in DC mode under conditions #2 (Table 1). Treatment time for the reference DC sample was 30 s and for the samples treated using pulsed current it was adjusted according to the duty cycle to achieve the same charge passed through the surface, thereby ensuring similar electrochemical conditions.

Table 3 Matrix of experimental design and parameters of pulsed current EPP cleaning process

#	f (Hz)	δ	U (V)	t (s)	Comment
1	DC	1	180	30	
2	100	0.8	180	45	
3	1000		180		
4	10000		205		
5	100	0.5	180	60	
6	1000		240		
7	10000		340		
8	100	0.2	220	150	Unstable discharge conditions
9	1000		350		
10	10000		450		

Figure 9 illustrates surface morphologies of 4340 HSS disc samples exposed to electrolytic plasmas under conditions corresponding to Table 2. Initial untreated surface shown in Figure 9a is featured by grinding grooves and darker oxidised areas. Both visual and microscopic examinations of cleaned surfaces on samples #1 to #5 and #8 (e.g. DC, f=100 Hz to 10 kHz at δ=0.8 and f=100 Hz to 1 kHz at δ=0.5 and f=100 Hz at δ=0.2) revealed typical EPP-treated morphologies featured by traces of discharge events (Figure 9b). A trend for reduction in mean average dimensions of the characteristic features in the surface morphology with increase in current pulse frequency and decrease in duty cycle was noticed. Ultimately, the sample #4 (f=10 kHz, δ=0.8) exhibited a cleaned surface, with no direct evidence of fusion and solidification processes having occurred (Figure 9). Major surface carbide inclusions remained intact, indicating that thermal impact from electrolytic plasma was very low, yet the hydrodynamic effect was sufficient to provide adequate

surface cleaning.

In contrast to the previous group, the surface of sample #10 (for which no stable plasma discharge condition was achieved) was covered with a thin black film, associated with thermally induced surface oxidation processes. These treatment conditions were found to be unsuitable for EPP cleaning and this sample was excluded from further investigations. Samples #6, #7 and #9 (e.g. f=1 kHz at δ= 0.5 and 0.2 and f=10 kHz at δ=0.5) revealed transient surface morphologies with variable ratios of EPP-treated to oxidised regions (Figure 9d).

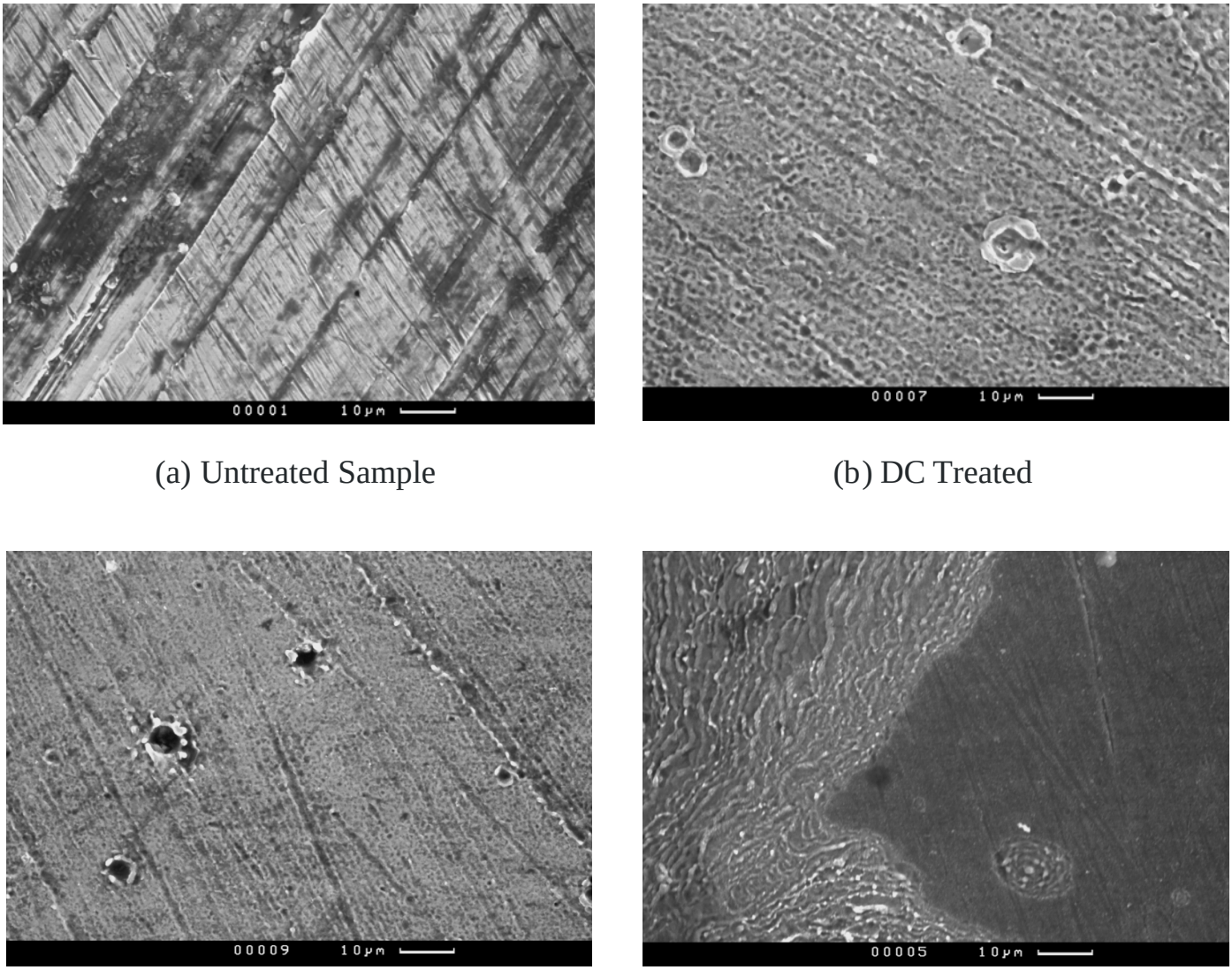

(a) Untreated Sample

(b) DC Treated

(c) f = 10 kHz; δ = 0.8

(d) f = 0.1 kHz; δ = 0.2

Figure 9 SEM micrographs of initial and EPP cleaned surfaces using DC and different parameters of pulsed current

Figure 10 represents XRD patterns characteristic for untreated and EPP treated 4340 HSS surfaces. Similar to untreated substrate material, all EPP cleaned samples exhibited only Fe peaks, with no significant effects of EPP treatment parameters identified. The cleaned samples' peaks were however noticeably lower and wider than those of untreated material, which could be associated with formation of specific surface topology as well as with amorphisation and crystallite refinement in the surface layer. Surface grain size measurements were carried out to evaluate characteristics of the thin surface layer affected by the plasma treatment. The crystallite size was evaluated using Scherer's equation for (110) Fe peak ($2\theta = 44.5^{o}$) in the XRD patterns. It was found that EPP treatment indeed causes a reduction of the size of crystallites within the first 100 nm from the surface from about 30 nm (characteristic to a martensitic structure of the substrate) to 5…20 nm (which is more typical for nanocrystalline or amorphous materials). However no significant effect of the treatment parameters, e.g. frequency and duty cycle, was observed.

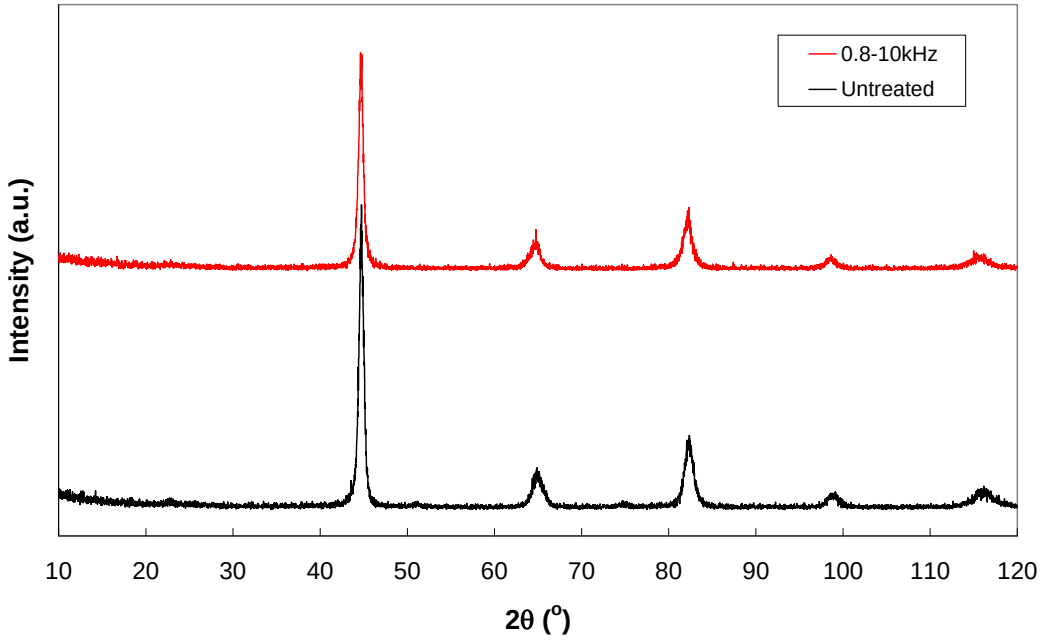

Figure 10 Typical XRD patterns of initial and EPP cleaned surfaces

Figure 11 shows the effects of current pulse parameters on the surface roughness of the disc samples. Initial substrate roughness was evaluated to be Ra 0.2 μm. DC treatment caused a reduction of Ra values to 0.15 μm. The samples treated using pulsed current mode EPP process showed further roughness reduction down to Ra 0.1…0.04 μm. The trends are clearly observed to decrease surface roughness with both increased frequency and decreased duty cycle. These trends can be associated with alterations in discharge characteristics when pulsed current is applied, except for the range of f=1 to10 kHz and d=0.5 to 0.2 where oxide scale formation seems to provide significant contribution to the smoothing effect.

Figure 12 shows GDOES patterns illustrating effects of EPP treatments on chemical composition of the surface layer. Apparently, EPP cleaning causes substantial reduction in oxygen content in the surface. Moreover, no significant differences in the quality of cleaning were found between DC and pulsed current treatment conditions, particularly those corresponding to the experiment #4 in Table 3.

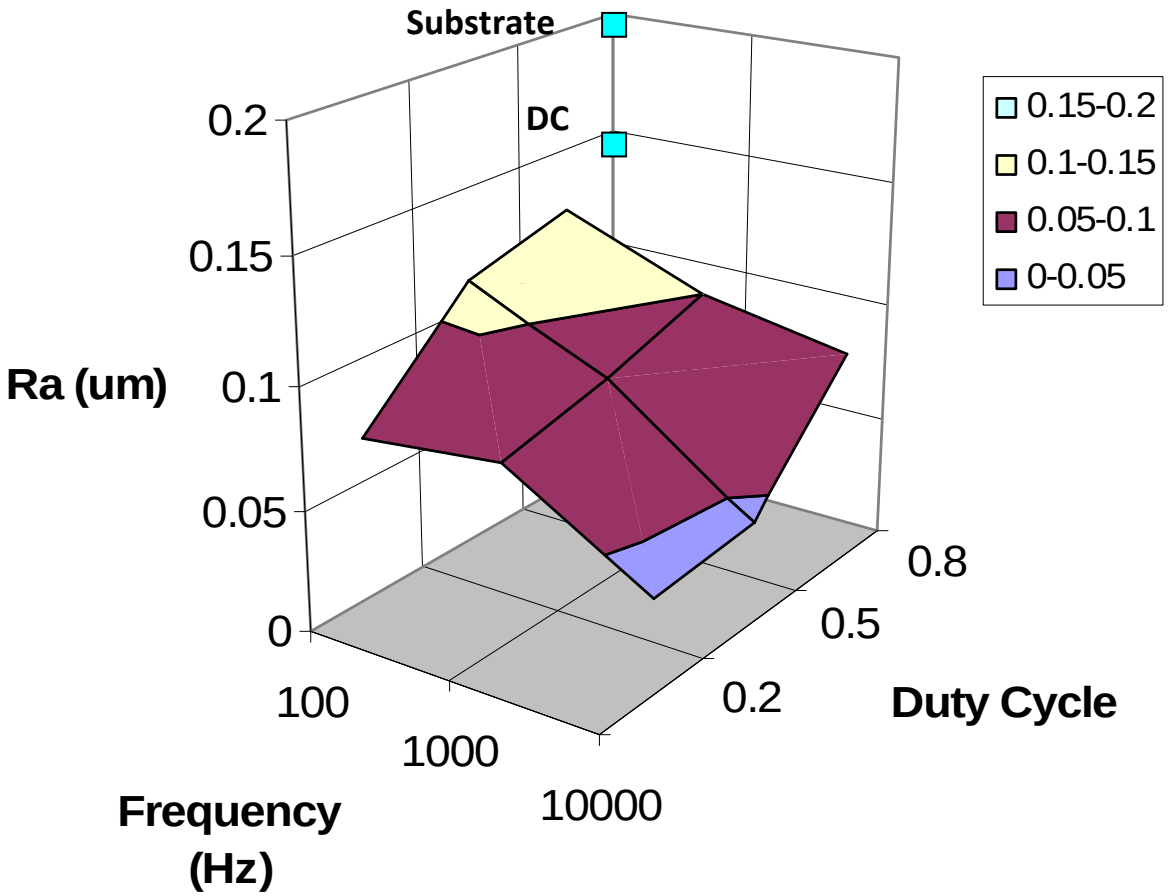

Figure 11 Effects of pulsed current parameters on surface roughness of EPP cleaned 4340 HSS.

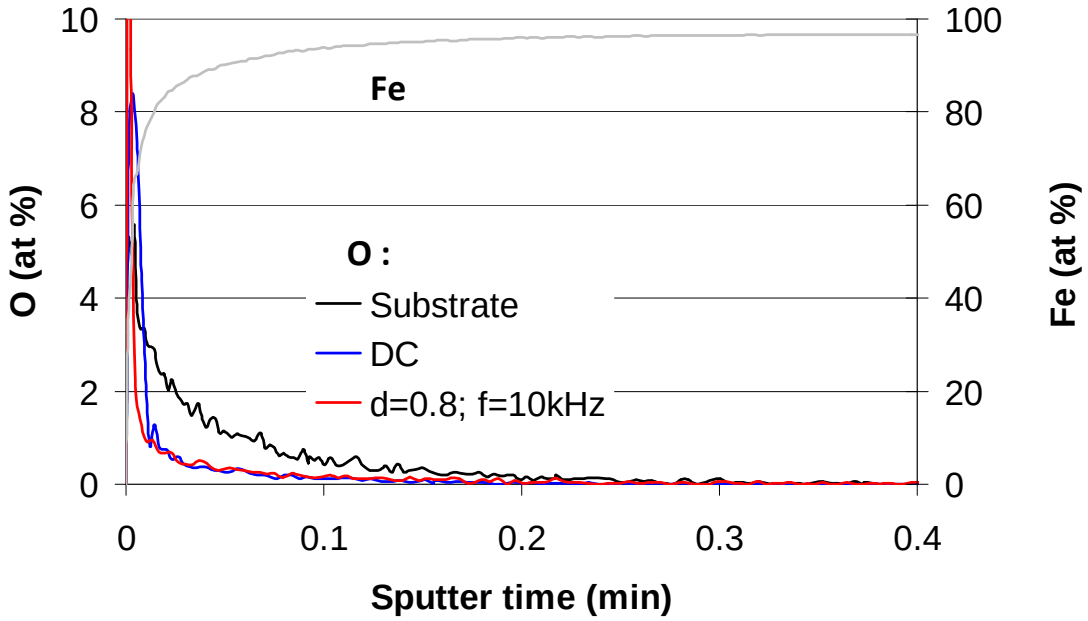

Figure 12 GDOES patterns revealing characteristic Fe and O distributions in the surface region of untreated and EPP cleaned steel samples

The Vickers microhardness of the EPP-treated surfaces measured under different loads ranged from 25 to 200 g is shown in Figure 13. The load variation allowed the hardness to be probed at different depths from the surface, which in our case varied in the range from 1 to 3.5 μm. Hardness of the untreated substrate sample increased gradually from 740 HV to 800HV with decrease in the applied load from 200 to 25 g. This behaviour is typical for hard materials and can be explained by increased contribution of elastic deformation at low loads. The reference DC-treated sample showed reduced hardness values at 50g load, compared to the untreated substrate. This indicates that some degradation of the mechanical properties occurs in a thin 1 to 1.5 μm surface layer, which is consistent with the results of the previous studies. The samples treated under pulsed current conditions showed similar trends, with slight variation in absolute hardness values, which are probably due to corresponding hardness variations of the substrate material. The most pronounced frequency effect can be observed for δ=0.8, showing that the degree of mechanical degradation in the surface layer is reduced with increased frequency of the current pulses.

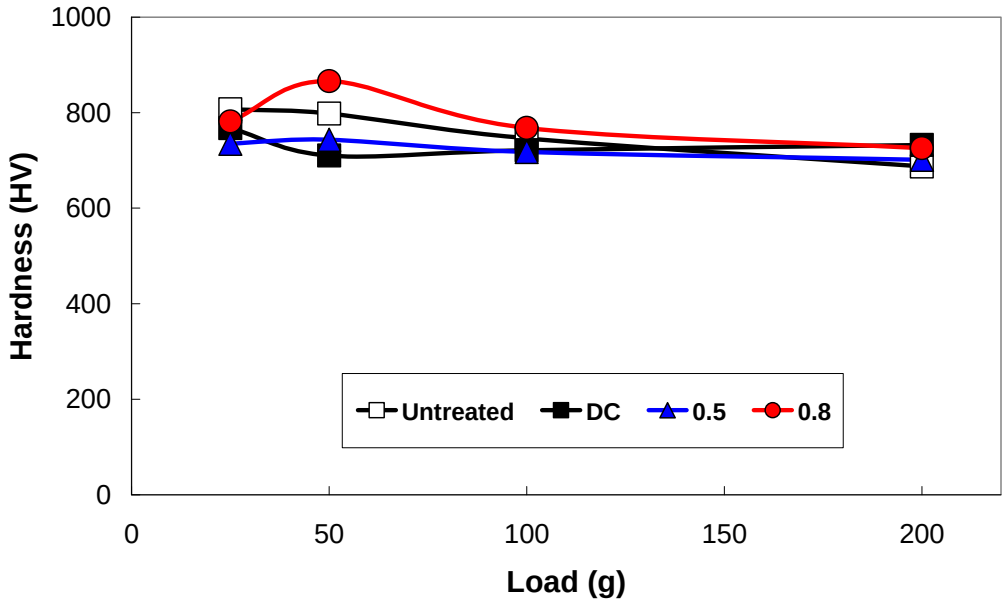

Figure 13 Effects of EPP cleaning on surface hardness of 4340 HSS tested at different loads. For pulsed current conditions, f=10 kHz and corresponds to the sample series.

It is significant that for the combination of the highest studied frequency and duty cycle (e.g. f=10 kHz and δ=0.8) the hardness profile approaches that of the untreated substrate. This observation is in agreement with optical microscopy data, showing minimal morphological transformations occurred on the surface during EPP treatment under the above conditions. These treatment parameters can therefore be considered as providing the optimal combination of surface cleaning with minimised detrimental effect to the mechanical properties of 4340 HSS.

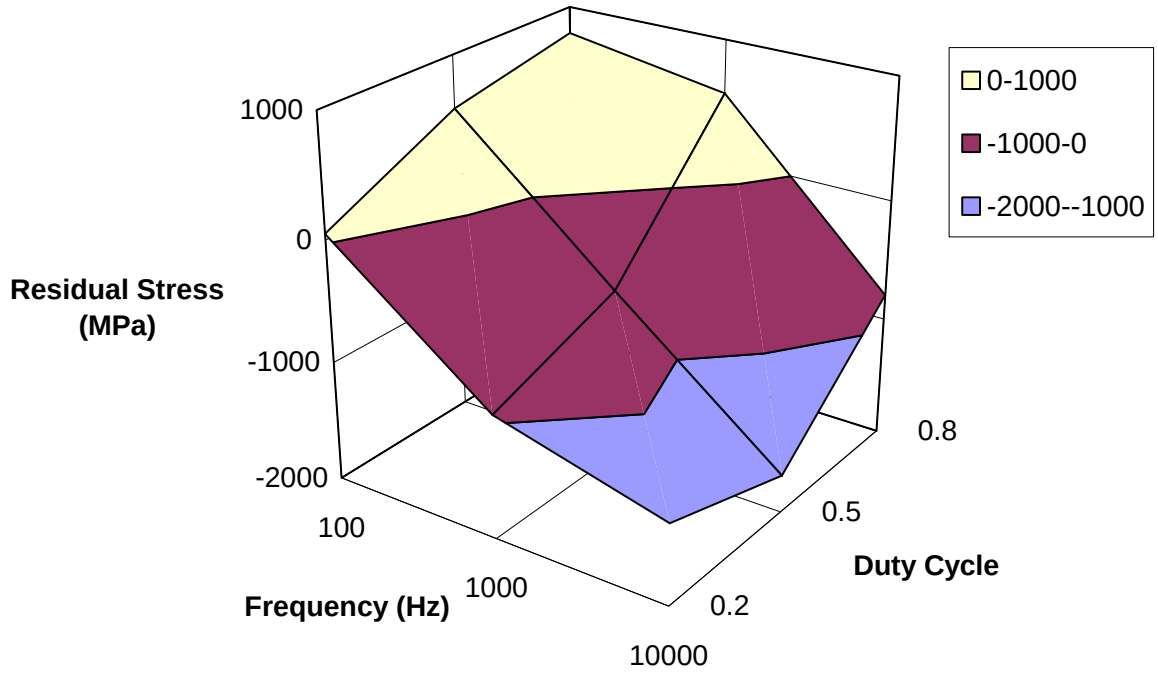

Figure 14 Residual stress map for pulsed current EPP cleaning

Internal stresses in the surface region were evaluated by XRD $\sin^2\psi$ method using a Siemens D 5000 X-ray diffractometer with a 2D goniometer. The scans were performed in an unlocked coupled mode, which allows a displacement from normal θ-2θ position to simulate the effect of ψ angle. Internal stresses in the as-received sample were found to be compressive -1440 MPa, whereas a DC treatment caused stresses to become tensile 670 MPa. Although in disagreement with the results by the collaborating group from CAP Technologies, this can have a simple explanation, e.g. the compressive stresses generated at the sample preparation stage are turned into tensile due to the rapid heating during DC EPP treatment. The stresses generated due to the pulse current EPP treatments are shown in Figure 2, indicating the following trends. At low frequencies and high duty cycles (0.1-1.0 kHz and 0.8-0.5, accordingly) internal stresses, similar to DC treatment, were tensile but slightly reduced in amplitude, whereas at the highest studied frequency (10 kHz) the stresses were compressive (e.g. -776 MPa at 0.8 duty cycle). This is consistent with the results of fatigue tests, showing progressive increase in fatigue strength with increased frequency of the pulse current EPP treatment.

Figure 15 shows effects of EPP cleaning on electrochemical corrosion behaviour of 4340 steel in deaerated 3.5% NaCl solution. The potentiodynamic corrosion scan technique was chosen as an express method for evaluation of anticorrosion performance of EPP cleaned and coated surfaces at the process development stage. This is complimented by salt fog corrosion tests carried out by our project partners. The results of express evaluation indicate that EPP cleaned surfaces exhibit shifts in corrosion potential towards more positive values which makes the cleaned surfaces less susceptible to corrosion attack. From

the Figure, it is clear that the shift is mainly caused by facilitation of cathodic processes at the metal surfaces; this is probably due to enhanced cation adsorption to the cleaned surface. The maximum potential shift was observed for DC treated samples that also showed most homogeneous surfaces (Figure 9). This also highlights an important role that is played by surface impurities and heterogeneities in the corrosion process.

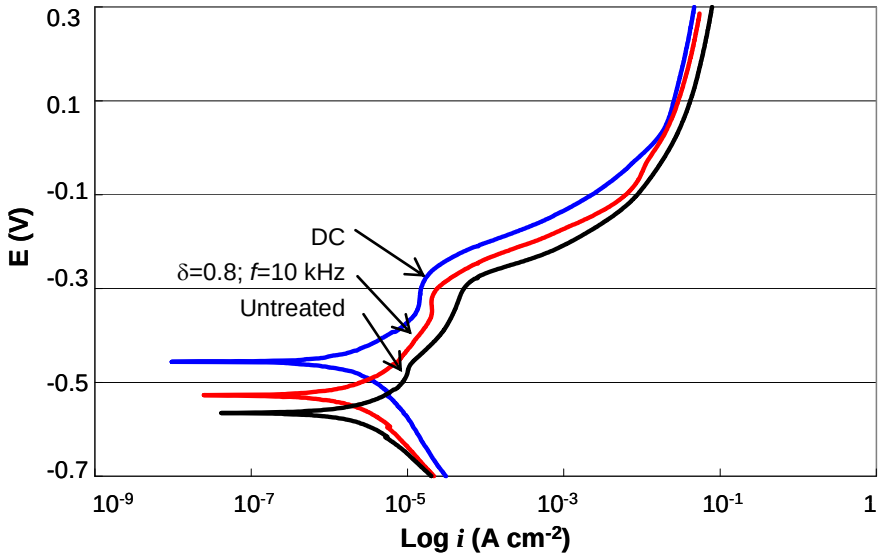

Figure 15 Potentiodynamic corrosion curves of EPP cleaned surfaces in deaerated 3.5% NaCl solution

Thus, the experiments performed have resulted in the development of a novel pulsed current EPP cleaning technology. Enhanced capabilities of this technique were illustrated compared to simple DC treatments. Following the characterisation studies carried out on the EPP cleaned 4340 steel samples it was evident that:

- Pulsed current EPP is an effective and environmentally friendly cleaning treatment for high strength steel, as illustrated by the SEM analyses, with the surface providing a suitable profile for further coating deposition processes. It was deduced that higher duty cycles (preferably $\delta = 0.8$) provide better cleaning throughout the studied frequency range of pulsed current.
- The hardness values are slightly lower or comparable to that of the untreated sample showing minimal mechanical degradation caused by the pulsed current cleaning treatment.
- At high frequencies, EPP cleaning leads to an introduction of compressive residual stresses in the treated surface, which provides a favourable condition for subsequent coating deposition process. This also minimises impact of the plasma treatment on fatigue strength of high strength steel substrates.
- EPP cleaning leads to the enhancement in anticorrosion performance of steel surfaces due to facilitation of cathodic reaction.
- Suitable ranges of pulse current parameters for EPP cleaning were identified as f = 100 – 10000 Hz at $\delta = 0.8$.

5. Development of Pulsed Current EPP Coating Processes

5.1. Research context

The main activities within this crucial phase of the project were directed towards development of electrolyte systems suitable for deposition of modified EPP Zn-based coatings with adequate anticorrosion performance. Following the original approach adopted for the entire project, the electrolyte modification with Al salts was considered, which at the later stages was complimented by other metals, such as V, Mn and Mg. Taking into account that particular tasks defined for this part of the project rely upon the application of pulsed current technology, additional activities associated with investigations of pulsed current effects on coating deposition from single-component electrolyte solutions, containing Zn and Al ions were carried out. Another specific to this project partner objective dictated investigation of the mechanical properties of the coatings obtained. The characterisation work discussed in the following sections contains therefore essential elements of the mechanical evaluation.

Similar to previous stages, anticorrosion performance of the coating systems under development was evaluated using potentiodynamic corrosion tests. Absence of appropriate reference data and apparent criteria for evaluation of anticorrosion performance of sacrificial coatings when using this technique made it necessary to obtain, characterise and test several benchmark coatings, as discussed in the following subsection of the report.

5.2. Provision and evaluation of benchmark coatings

As an important part of the project, a provision of commercial Cd and Zn plating coatings was considered to ensure adequate benchmark data for evaluation of the surface treatments being developed. The coatings were obtained from a UK based electroplater, Stainless Plating, Ltd (Sheffield), operating within the US DOD sector. Three specifications of Cd coatings were provided, designated as ‘No passivate’, ‘Clear passivate’ and ‘Chromate passivate’. XRD patterns of all three types were similar (Figure 16), revealing strong <0010> texture in hexagonal Cd structure. With such texture, closely packed basal planes of Cd elementary cells are arranged parallel to the surface, which is believed to be responsible for its low intrinsic coefficient of friction ($\mu \approx 0.27$). To evaluate actual friction coefficient of Cd coatings, reciprocating sliding wear tests were carried out according to ASTM G133-95. Results of the tests shown in Figure 4 indicate that the friction coefficient of Cd against AISI 52100 steel is higher, varying within the 0.3 to 0.5 range. Taking into account the fact that all the coatings have been perforated well before the end of the test, it would be reasonable to assume that most of the time the friction was affected by underlying hardened substrate. Severe coating plastic deformation at peripheral regions of the wear path led to occasional redistribution of Cd within the contact area, resulting in fluctuations of the observed friction coefficient.

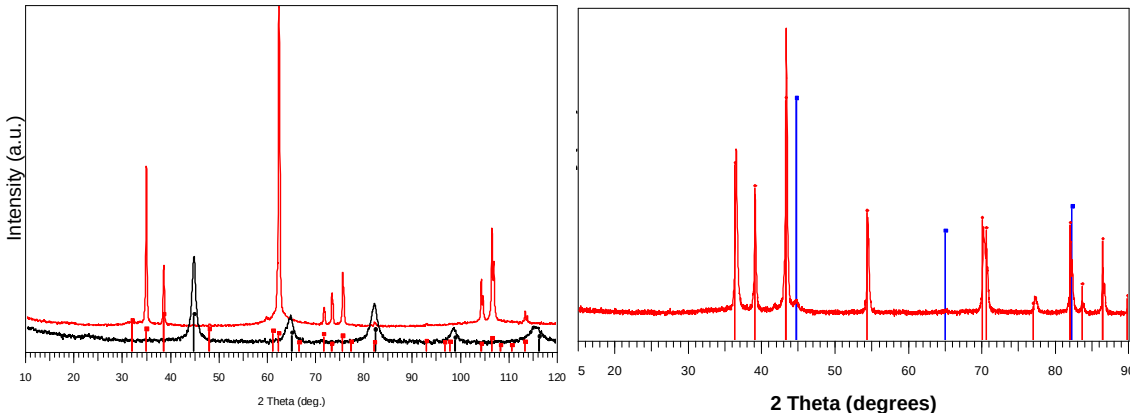

(a) (b)

Figure 16 XRD patterns of (a) 4340 steel substrate (black) and commercially available Cd (red) and (b) Zn plating coatings without passivation treatments. In chart (b), blue and red PDF patterns correspond to Fe and Zn respectively.

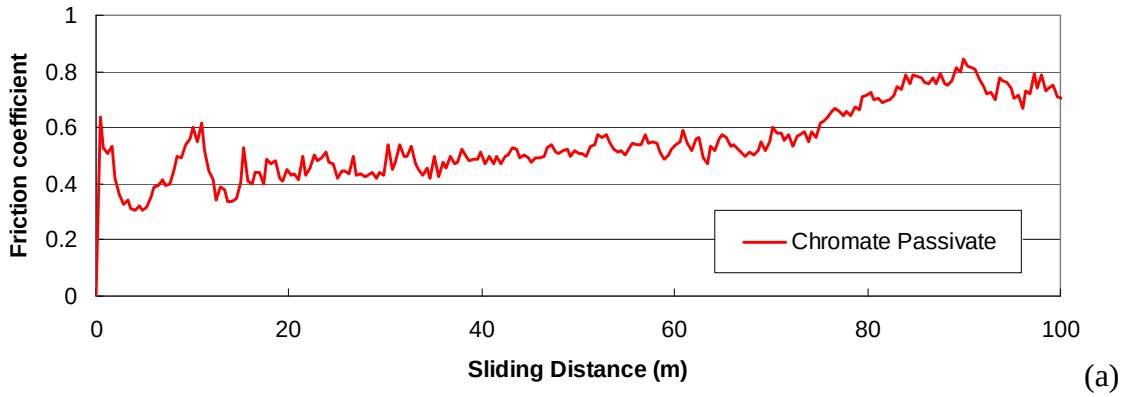

(a)

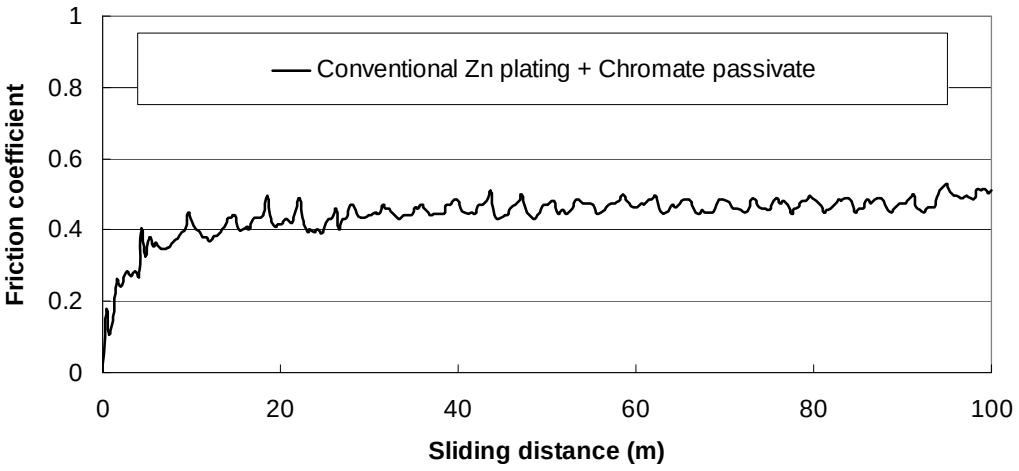

(b)

Figure 17 Dynamic friction coefficients of Cromate passivated Cd (a) and Zn (b) plating coatings vs AISI 52100 steel ball during reciprocating sliding wear tests at 10 N load (ASTM G133-95).

Similar tests were performed for commercial Zn plated coatings supplied in the 'Chromate passivate' condition (Figure 5). The test revealed more regular and stable behaviour of Zn coatings compared to Cd, with friction coefficient μ=0.4…0.5 recorded.

Corrosion behaviour of the coated surfaces was qualitatively judged by corrosion potential and current density measurements within the anodic part of polarisation curve. Additionally, some attempts were made for quantitative evaluation of corrosion rates. These were evaluated (in moles per year) via two independent fitting procedures, i.e. Tafel fit and Polarisation Resistance fit, incorporated into the CorView® software developed by Solarton Analytical (U.K.), under assumption of bivalent iron dissolution. Although quite crude, such analyses allow accelerated evaluation of the film electrochemical performance, which could be extremely useful, in particular at the initial process R&D stages.

Results of Potentiodynamic corrosion tests for both the substrate material and the benchmark coatings are given in Figure 18. Corrosion potential of the substrate was found to be Ec=-0.5 V, whereas Cd and Zn plating caused Ec drop down to -0.8 V and -1.03 V, respectively. Thus the potential difference between steel and sacrificial Cd and Zn coatings is 0.3 V and 0.53 V, respectively. It also should be noticed that both benchmark coatings showed significantly (about 3 orders of magnitude) higher corrosion currents compared to the bare substrate, although a tendency for surface passivation was observed at around -0.5 V. The fact that this trend was more pronounced in the case of Zn coating could indicate a possible effect of the chromate passivation post-treatment; however this speculation was not confirmed by further studies. The above data were used at the later stage of the project as reference points for accelerated evaluation of sacrificial ability of the coatings developed.

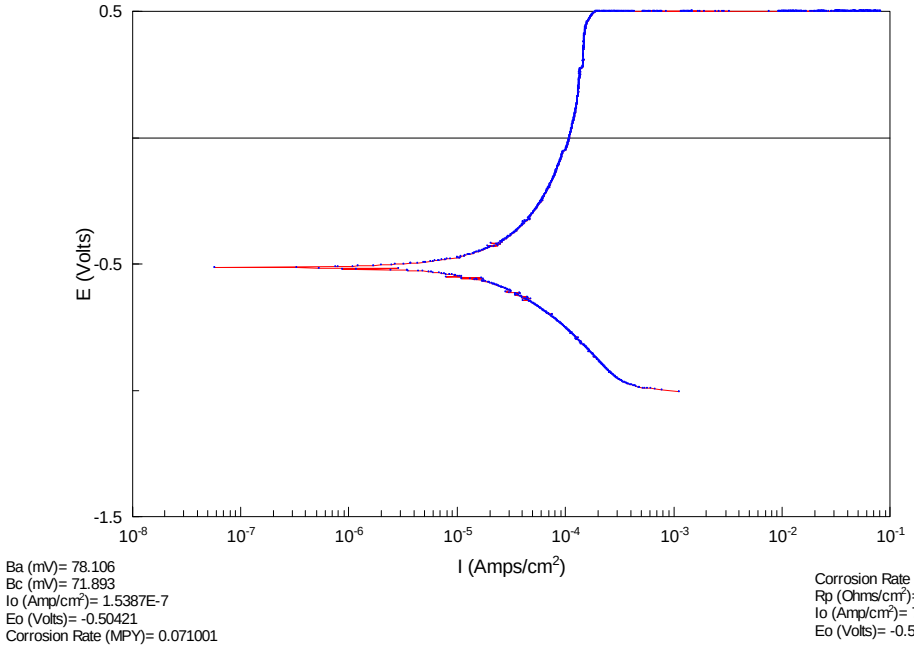

(a) Substrate

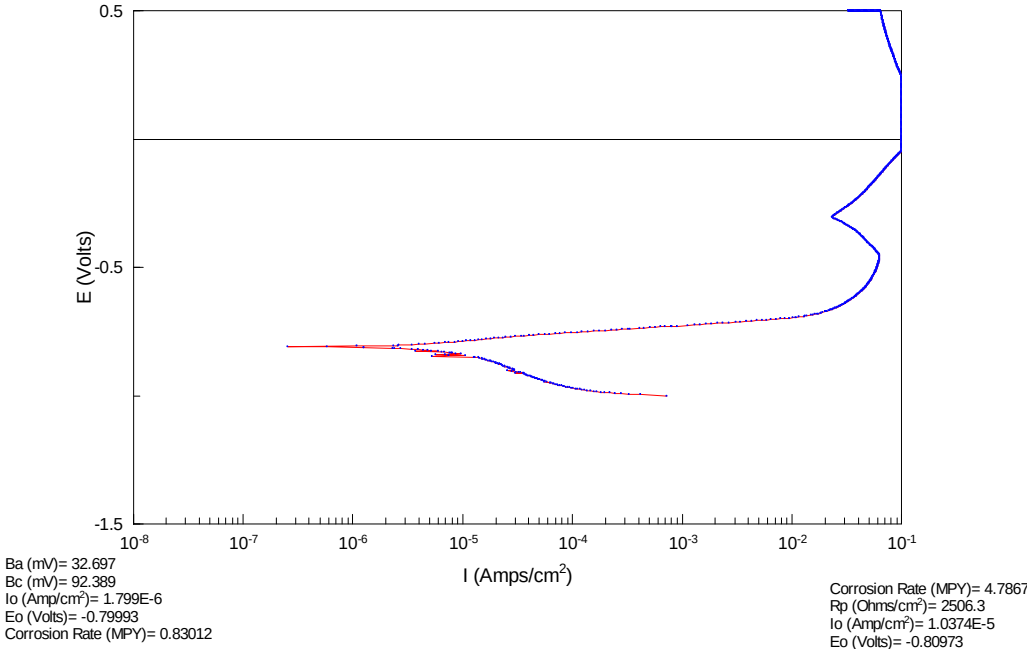

(b) Cd no passivate

Figure 18 Potentiodynamic polarisation curves for (a) substrate; (b) Cd and (c) Zn coatings. Data on the left and right represent results of Tafel and polarisation resistance fits, respectively.

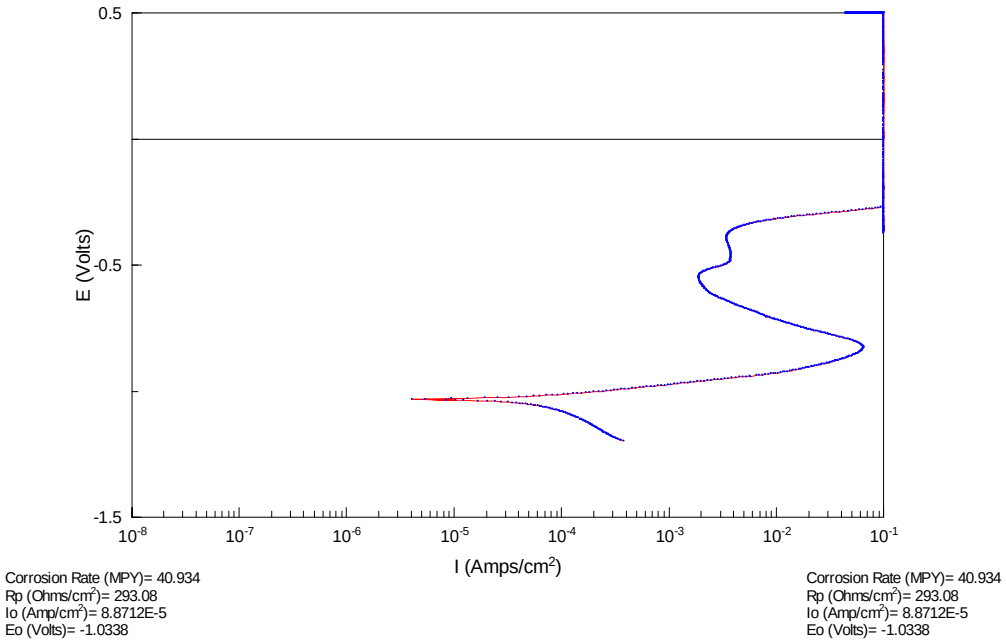

(c) Zn-Chromate passivate

Fig. 18. (completed)

5.3. Process development and characterisation of pulsed unipolar EPP Zn coatings

A series of experiments was carried out on deposition of single component Zn coatings, employing a pulsed unipolar current mode. The electrolyte was 0.2M solution of $ZnSO_4$ (pH 5.5, conductivity 14.5 mS cm^{-1}) operated at 60°C. Effects of frequency and duty cycle were studied using the experimental design approach similar to that applied for studies of EPP cleaning. Full factor 2^3 experimental design was realised, with pulse frequency (*f*) set at 10^2, 10^3 and 10^4 Hz and duty cycle (δ) set at 0.8, 0.5 and 0.2 (Table 4). A reference sample was treated in DC mode for 24 s and the treatment time for the pulsed current conditions was adjusted according to the duty cycle to achieve the same charge passed through the surface. For some coatings a loose outer layer was observed after the deposition, which was easily washed out during subsequent rinsing. Thickness of the remaining surface layer was evaluated form the step formed at the part of the surface masked during the treatment using a Dektak^{3}ST surface profilometer. The coating morphology and elemental composition were studied using a Camscan SEM equipped with a Links Analytical EDX attachment. Surface hardness was measured using a Mitutoyo MVK G1 microhardness tester equipped with a Vickers pyramid. Five parallel measurements were made followed by statistical analysis to derive mean average values and evaluate data variation. Tribological and corrosion tests were performed according to the procedure adopted for the benchmark coatings, as discussed in Section 5.2.

Table 4 Process parameters for pulsed current EPP deposition of Zn coatings

#	*f* (Hz)	δ	t (s)	U (V)	I (A)	Thickness (μm)	Comment
1	DC	1	24	250	12…14	3.2	Loose outer layer removed
2	100	0.8	30		12.5	2.6	
3	1000				8.6	2.6	
4	10000				3	4.2	
5	100	0.5	48		12.5	2.8	
6	1000				6.5	3.0	
7	10000				2.4	5.5	
8	100	0.2	120	290	11.8	7.4	
9	1000			320	7.5	8.5	
10	10000			340	2.8	2.7	Unstable discharge conditions

Typical surface morphologies of EPP Zn coatings deposited under different parameters of pulsed current are shown in Figure 19. The coatings appear to be uniform, with nodular crystallites observed on the surface, following the paths of grinding grooves in the substrate. Characteristic size of the nodular features increases from 0.5 to 1 μm to about 3 to 5 μm with the frequency increased from 0.1 to 10 kHz. EDX analysis confirmed a presence of substantial amount of Zn in the surface layer.

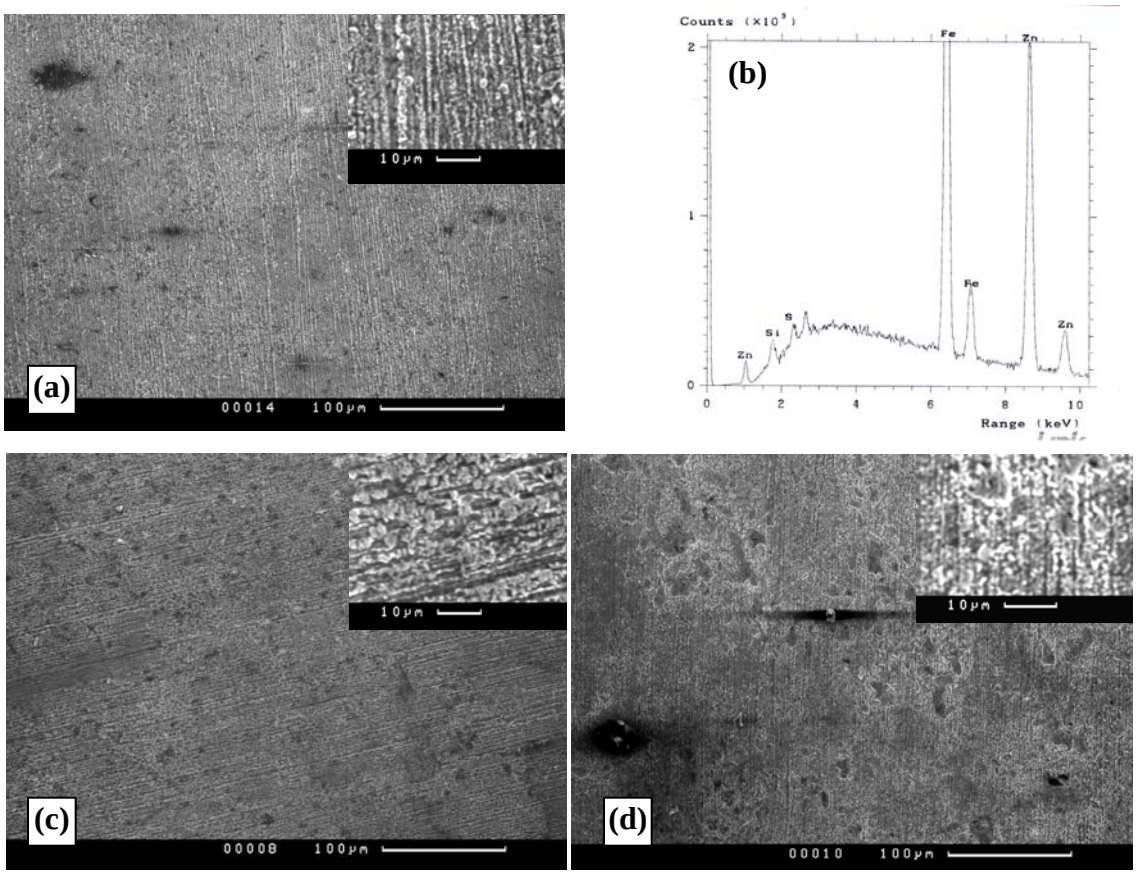

Figure 19 SEM micrographs (a,c and d) and typical EDX pattern (b) of EPP Zn coatings produced at various frequencies at =0.8. (a) f=0.1 kHz; (c) f=1 kHz and (d) f=10 kHz.

Microhardness tests revealed no significant effects of applied loads on the hardness of surface layer for the DC sample (Figure 20), with typical hardness values measured to be around HV150-170. Very minor deviations in the coating hardness were generally observed with varying parameters of the pulsed current, except for 10 kHz sample series, where lower hardness values (around HV120) wider scatter were recorded for δ=0.2 and δ=0.8 and 0.5, accordingly. Similar to hardness data, results of wear tests appear to be independent of the treatment parameters (Figure 21). After a short running-in stage, friction coefficient stabilised around μ=0.45, similar to the tribological behaviour of reference Zn coating. However after 30 m of sliding, the friction increased to μ=0.6, indicating possible failure of the relatively soft coatings.

Key results of Potentiodynamic corrosion tests for EPP Zn coatings are presented in Figure 22. It can be seen that overall corrosion behaviour of EPP Zn coatings is similar to that of electroplated Zn (Figure 6c), with corrosion potential being around Ec=-1.08V. The only exception was for f=10 kHz sample series (Ec=-0.85V). The exact reasons for such anomalous behaviour are unclear and this issue would require additional investigations.

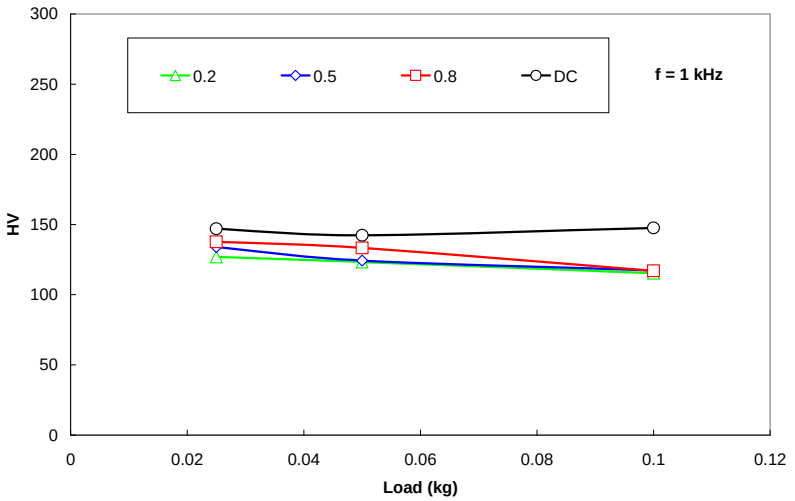

Figure 20 Typical example of the effects of applied load on microhardness of Zn coatings deposited under different parameters of pulsed current.

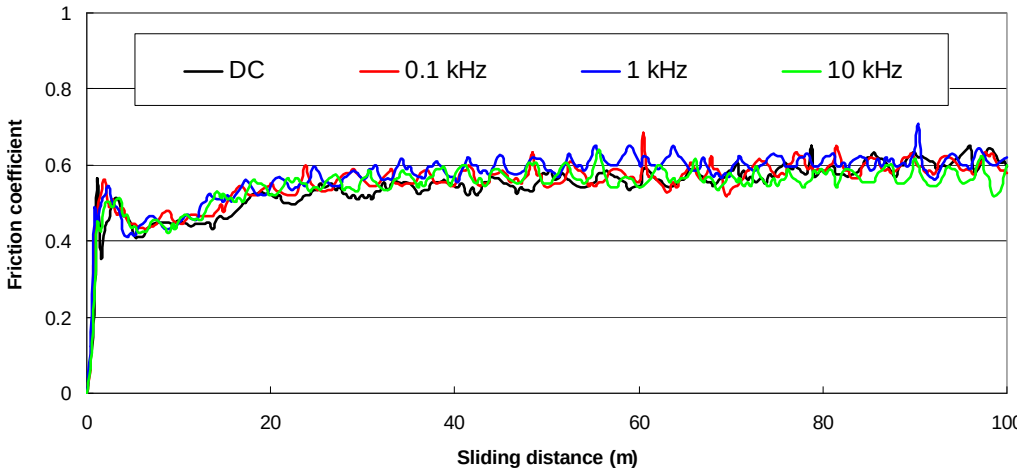

Figure 21 Effect of parameters of pulsed current EPP deposition on friction coefficient of Zn coatings during reciprocating sliding wear tests vs AISI 52100 steel ball at 10 N load (ASTM G133-95).

The following conclusions can be derived regarding this part of the work. Zn coatings have been successfully deposited using a pulsed current EPP process. The effect of pulsed current was mainly manifested in hindering the formation of the coating loose outer layer whereas tribological and corrosion behaviours were barely affected. The former was compromised by insufficient coating hardness and the latter is likely to be similar to corrosion behaviour of conventional Zn plated coatings.

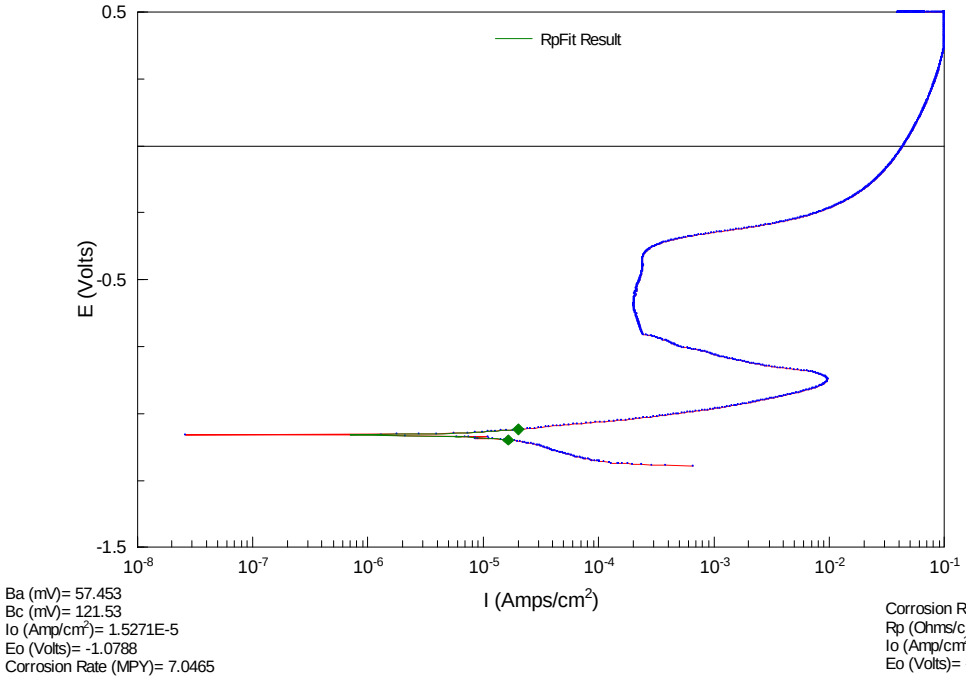

(a)

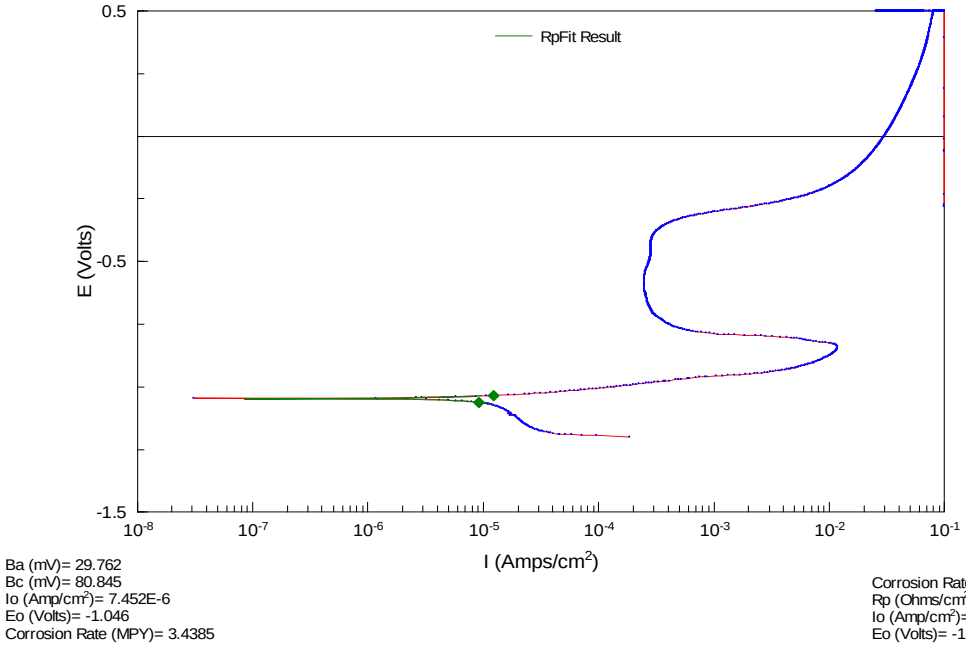

(b)

Figure 22 Potentiodynamic polarisation curves for EPP Zn coatings deposited under DC (a) and various parameters of pulsed current at =0.8: (b) f=0.1 kHz; (c) f=1 kHz; (d) f=10 kHz.

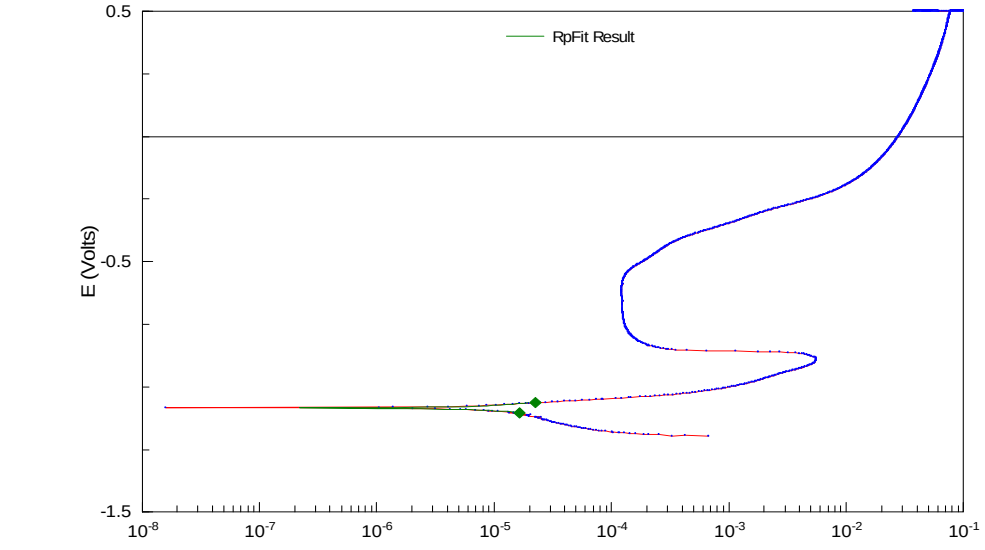

Ba (mV)= 31.598
Bc (mV)= 54.462
Io (Amp/cm^2)= 7.1494E-6
Eo (Volts)= -1.0825
Corrosion Rate (MPY)= 3.2989

Corrosion Rate (MPY)= 11.455
Rp (Ohms/cm^2)= 1047.4
Io (Amp/cm^2)= 2.4825E-5
Eo (Volts)= -1.084

(c)

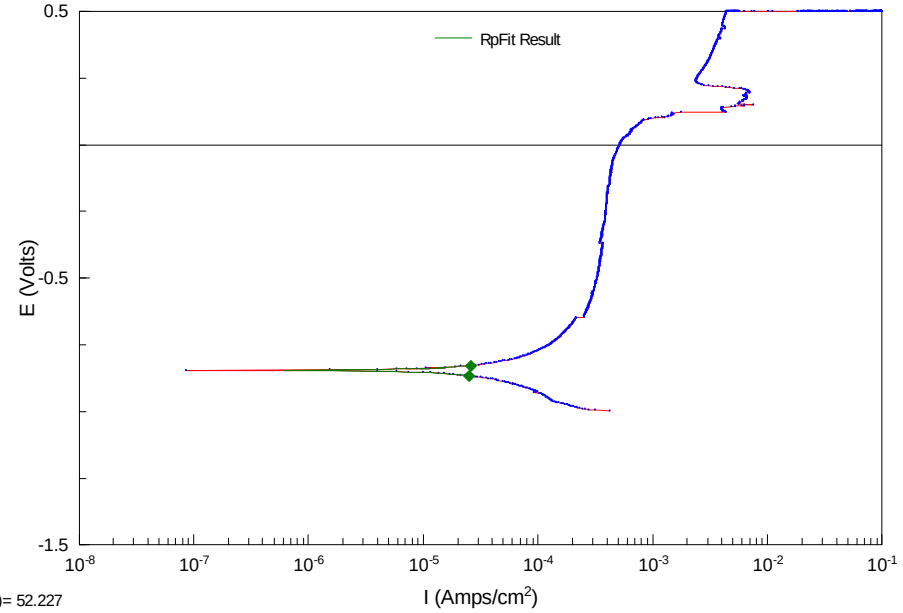

Ba (mV)= 52.227
Bc (mV)= 62.572
Io (Amp/cm^2)= 1.5357E-5
Eo (Volts)= -0.84529
Corrosion Rate (MPY)= 7.086

Corrosion Rate (MPY)= 15.835
Rp (Ohms/cm^2)= 757.62
Io (Amp/cm^2)= 3.4318E-5
Eo (Volts)= -0.84575

(d)

Fig. 22. (completed)

5.4. Process development and characterisation of EPP coatings produced from single-component Al-, and binary Al-Zn-containing electrolyte systems

5.4.1. Alkaline electrolyte systems

Our activities within this part of the project included three steps of experimentation. Initial set of experiments were carried out in a pulsed bipolar current mode using 0.2M $NaAlO_2$ electrolyte solution and a hollow Zn counter electrode. For further trials, a 0.1M $Al_2(SO_4)_3$ electrolyte was employed, in combination with pulsed unipolar current which at the final step was substituted by pulsed bipolar current. In all experiments, electrolyte temperature and flow rate were maintained at 60 ^oC and 3 l min^{-1}, respectively. Substrates used were 4340 HSS disks (1 inch in diameter) provided by Metcut, Inc and mild steel disks (1.5 inch in diameter) obtained elsewhere.

The experiments with aluminate electrolyte were designed based on the assumption that Zn^{2+} and AlO_2^- ions attain opposite charges in alkaline media. Polarisation by alternating current pulses was therefore considered to facilitate independent control over the deposition of Zn and AlO/OH compounds. For this purpose, an existing power supply module at the EPP facility was modified to allow application of pulsed bipolar current, the main parameters of which were chosen as follows. Voltage amplitudes during positive and negative biasing were varied within the ranges of 50 to 600 V and 50 to 450 V, accordingly; whereas durations of both positive and negative biasing were set equal, varied within 10^{-4} to 10^{-2} s range.

GDOES studies (Figure 23) carried out to determine depth profiles of main constituents, i.e. Al, Zn, O and Fe, of the coatings produced have shown that maximal contents of Zn and Al in the surface layer were about the same, although the distribution of the above elements was dissimilar. The maximum of Zn was observed at the surface, whereas Al concentrated in the subsurface region, coinciding with the maximum of oxygen.

The major problems encountered during these experiments were associated with a non-uniform coating distribution across the sample surface. Also, the electrolyte solution proved to be unstable under the conditions of EPP treatment employed, so it was difficult to ensure reproducible results. A decision was therefore taken to change to a more stable aluminium sulphate solution.

5.4.2. Acidic electrolyte systems

The second set of experiments was designed to investigate effects of pulsed current on EPP deposition of Al-based coatings from acidic media. The matrix of the experimental design is collated in Table 5 along with main electrical parameters of the process and coating thickness obtained by surface profilometry.

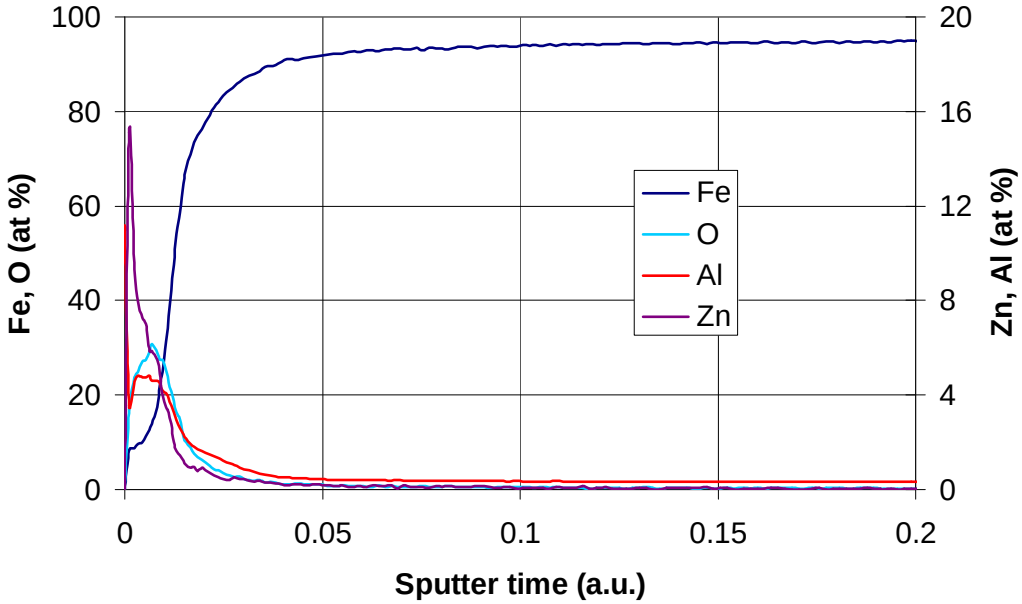

Figure 23 GDOES profile of Al-Zn-O EPP coating deposited from alkaline electrolyte under pulsed bipolar current conditions: pos= neg=20ms; Upos=250 V; Uneg=450 V.

Table 5 Process parameters for pulsed current EPP deposition of Al coatings

#	*f* (Hz)	δ	t (s)	U (V)	I (A)	Thickness (μm)
1	DC	1	24	250	14	3.2
2	100	0.8	30		13	2.9
3	1000				14	0.9
4	10000				14	2.2
5	100	0.5	48		11.4	2
6	1000			270	12.1	1.3
7	10000				7	1.8
8	100	0.2	120	300	7	1
9	1000			330	9	0.7
10	10000			390	7	0.9

The overall coating appearance was more uniform compared to that in the previous batch of samples treated in alkaline bath. The presence of Al in the surface layer was confirmed by both XRD and EDX analyses (Figure 24 and Figure 25 accordingly). The former showed minor peaks belonging to various alumina modifications and the latter (carried out as a part of SEM investigations) allowed identification of the regions with increased Al concentration in the surface. They are associated with the brighter areas in SEM micrographs (see inset to Figure 25b) featured by increased surface roughness, which have probably been more affected by plasma discharge during the EPP treatment. In these micrographs, the effect of pulsed current on the surface morphology can also be easily traced, i.e. increased current frequency results in more uniform surface appearance with

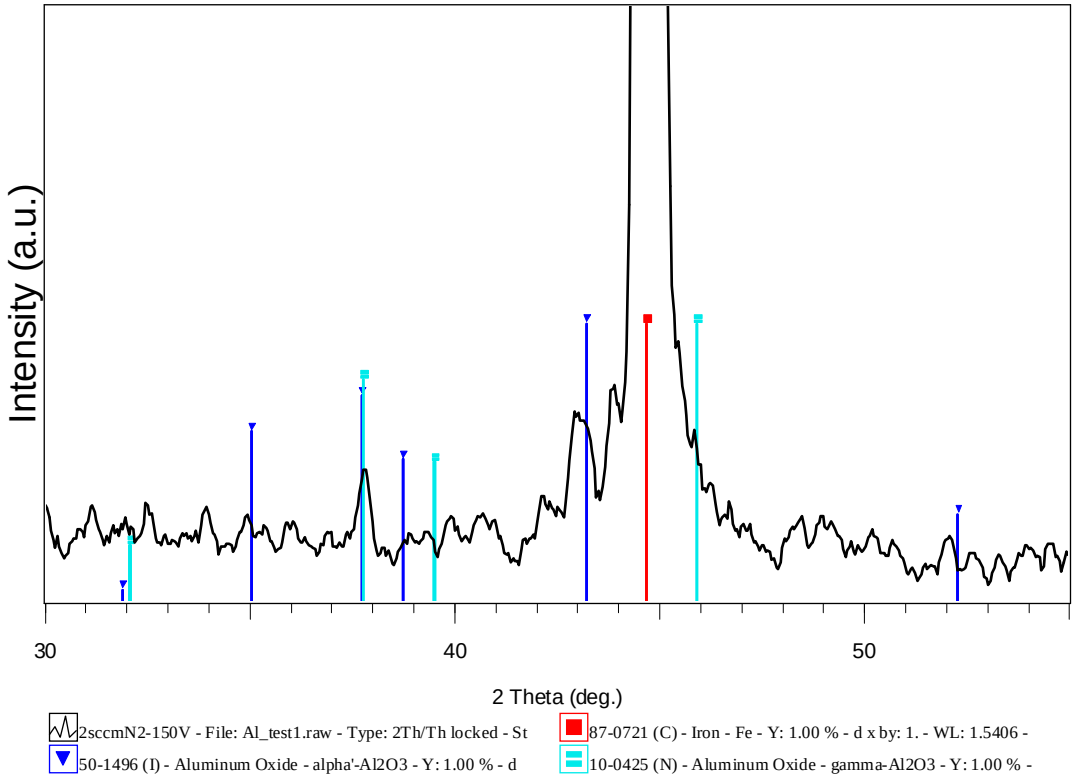

Figure 24 Typical XRD pattern of Al-O EPP coating deposited from acidic electrolyte under pulsed unipolar current conditions, showing presence of - and -Al2O3 in the surface layer.

lower roughness.

Unlike Zn EPP coatings, Al-based layers caused noticeable increase in surface hardness (Figure 26), particularly at lower applied loads, indicating enhanced stiffness of the deposits formed. Typical coating hardness was measured to be within the range 200 to 250 HV, however the effects of current pulse parameters could not be unambiguously identified. This affected tribological behaviour of the coatings during reciprocating sliding wear tests (Figure 27), where similar dependencies of friction coefficient on sliding distance were observed for all Al-O coatings. The friction coefficient increased gradually at the beginning of the test to reach a steady state with $\mu \approx 0.4$ after about 10 m of sliding. The steady state was then maintained throughout the test, with slight increase in friction

associated probably with the increase in contact area due to the pin wear. Thus Al-O EPP coatings have demonstrated better tribological behaviour compared to corresponding Zn coatings.

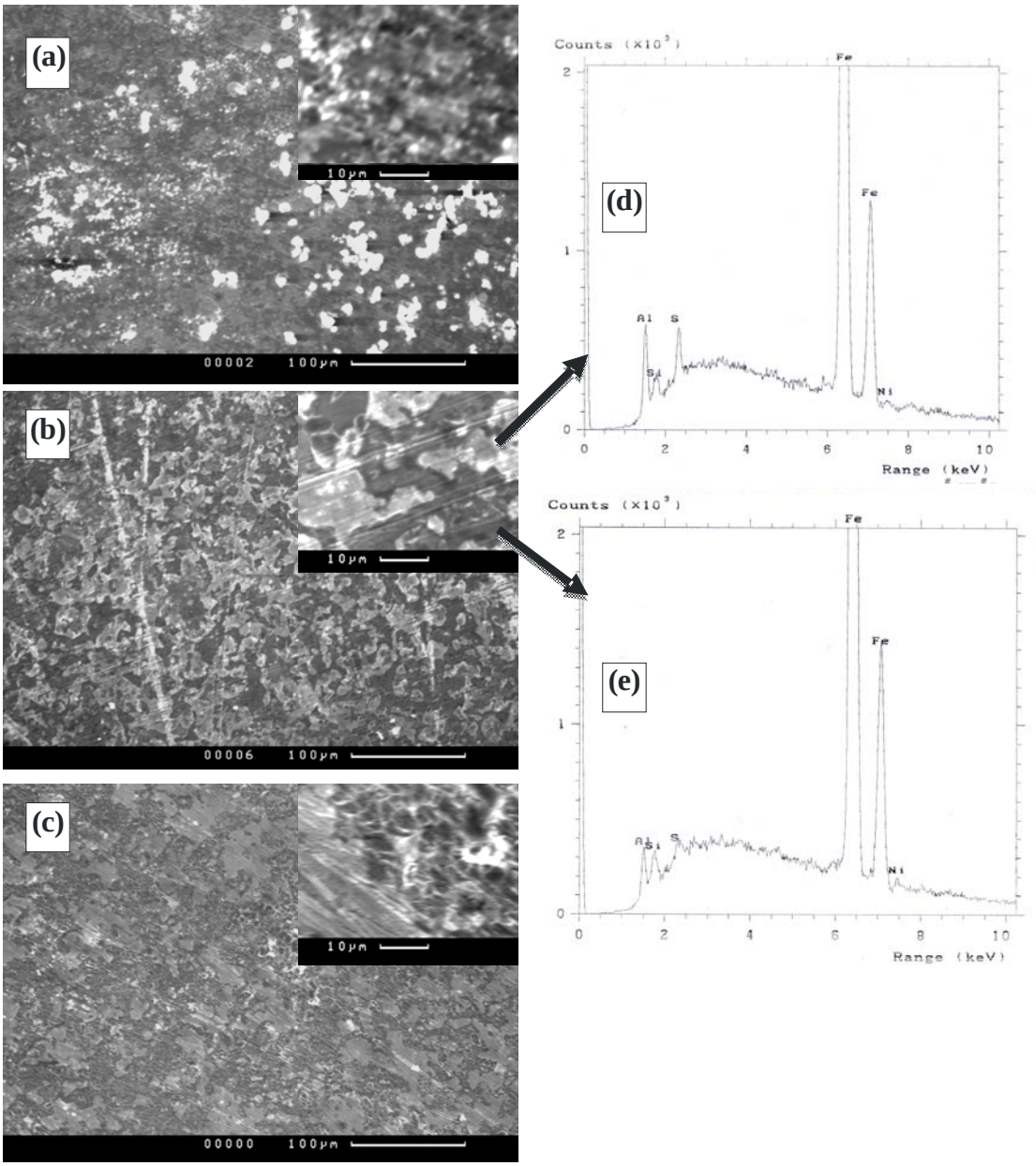

Figure 25 Surface plane SEM micrographs (a-c) and EDX patterns (d and e) taken from characteristic features of Al-O EPP coatings deposited from acidic electrolyte by pulsed unipolar current with different frequencies at 0.8 duty cycle: (a) f=0.1 kHz; (b) f=1 k

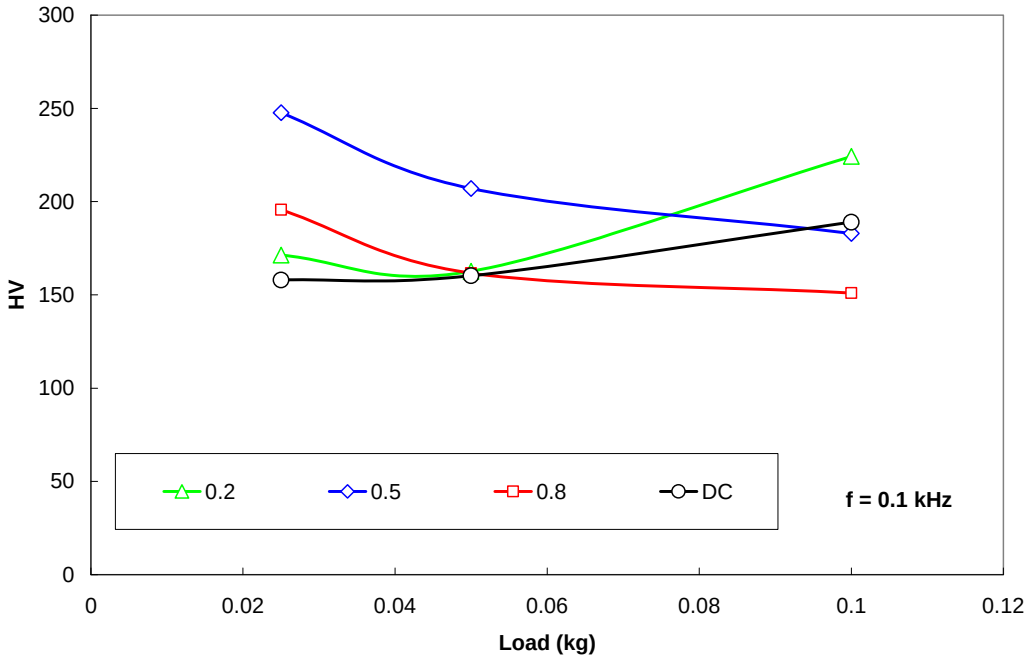

Figure 26 Typical example of the effect of applied load on microhardness of Al-O coatings deposited from acidic electrolyte under different parameters

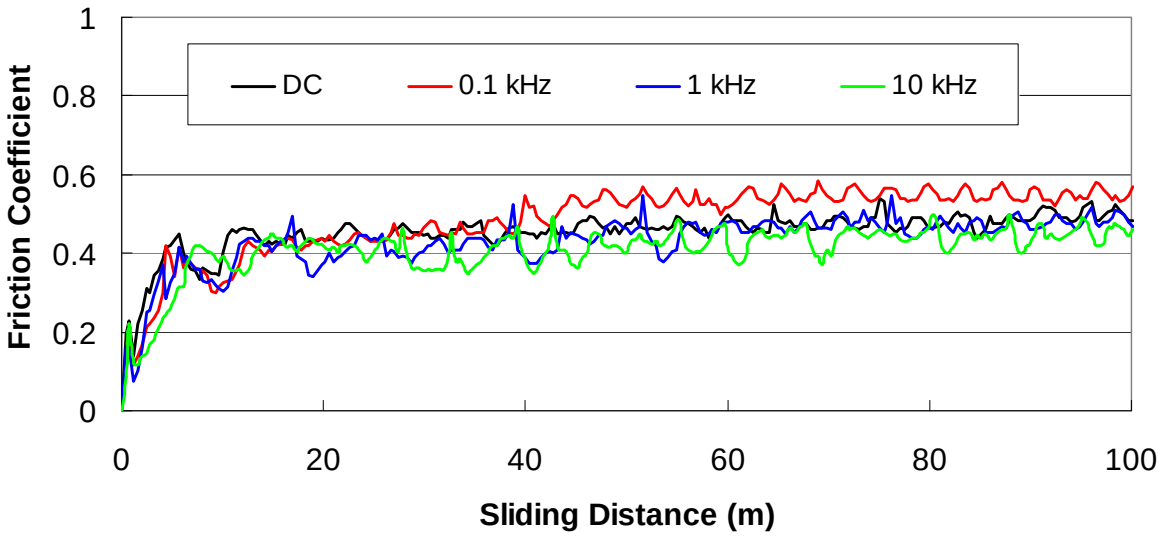

Figure 27 Effect of parameters of pulsed unipolar EPP deposition in acidic bath on friction coefficient of Al-based coatings during reciprocating sliding wear tests vs AISI 52100 steel ball at 10 N load (ASTM G133-95).

Figure 28 shows results of potentiodynamic corrosion scans for the Al-O EPP coatings produced under different conditions of the experimental matrix discussed in Table 5. The effect of pulse frequency can be clearly observed whereby corrosion potentials for DC and 0.1 kHz samples were similar Ec=-0.89V and further increases in current frequency to 1 and 10 kHz resulted in increased Ec values - 0.5V and -0.62V, accordingly. It is interesting to notice that for DC and 0.1 kHz treatments, both corrosion potential and current behaviour within anodic part of the polarisation curve were quite similar to those characteristics of reference Cd coating (Figure 6). This implies that overall corrosion

performance for these coatings could be similar to Cd plating. However, the absence of a passivation region at around corrosion potential of 4340 steel substrate that is characteristic of e.g. benchmark Zn and Cd coatings, could seriously undermine a long-term protection ability of these coating systems.

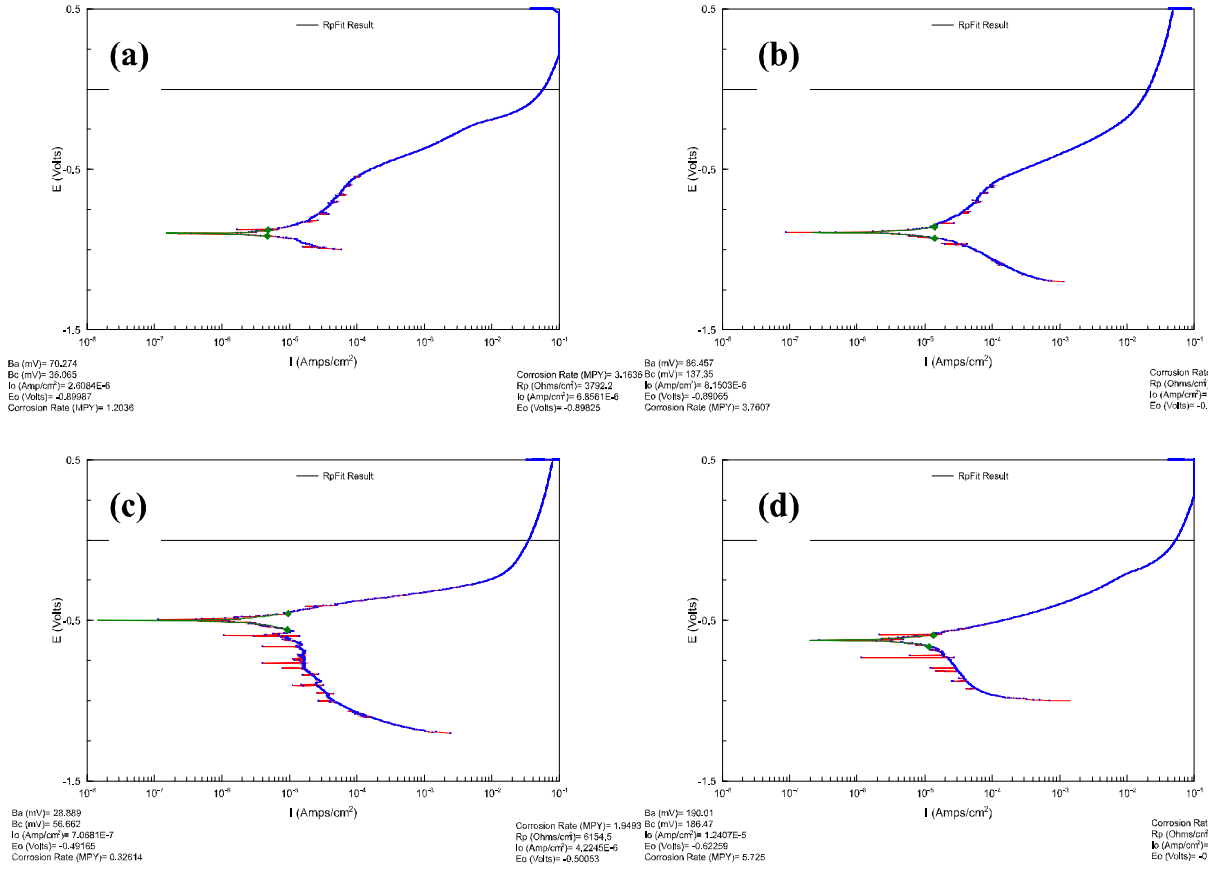

Figure 28 Potentiodynamic polarisation curves of Al-based EPP coatings deposited from acidic solution under DC (a) and various parameters of pulsed unipolar current at =0.8: (b) f=0.1 kHz; (c) f=1 kHz; (d) f=10 kHz.

Finally, we have considered possible ways for further increase of Al content in the surface layer and improvement of coating uniformity. Our approach was based on the data of $Al(OH)_3$ stability depending on the solution pH. It was proposed that more uniform deposition of Al compounds should be achieved when instantaneous pH at the sample surface reaches the range of $Al(OH)_3$ precipitation pH≈5 to 8. Bulk pH of 0.1M aluminium sulphate solution is about 3.5, and it is further reduced due to collateral hydrogen evolution at the cathode surface. However, desirable surface pH could be achieved by a temporal current reversal to increase a concentration of OH- anions at the metal surface. Following this approach, a set of experiments was designed utilising bipolar current pulses. In contrast with the experiments set up in Table 5, the current was reversed for only 20% of total time and positive voltage was set rather low, i.e. within the 50 to 250 V range. Although these experiments have resulted in a uniform surface appearance, they did not give a desirable electrochemical response from potentiodynamic corrosion scans (Figure 29).

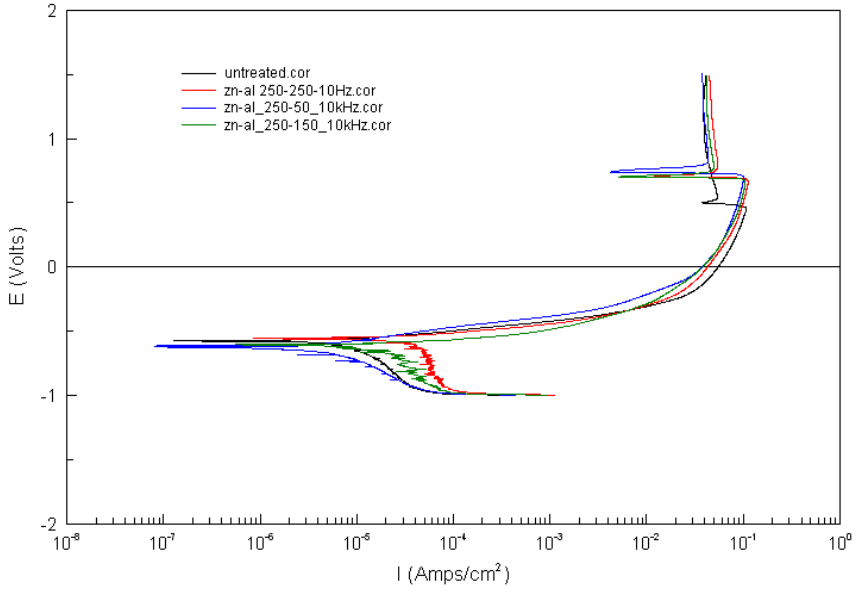

Figure 30 Typical example of potentiodynamic polarisation curves of Al-based EPP coatings deposited from the acidic solution under various parameters of pulsed bipolar current at cat=0.8.

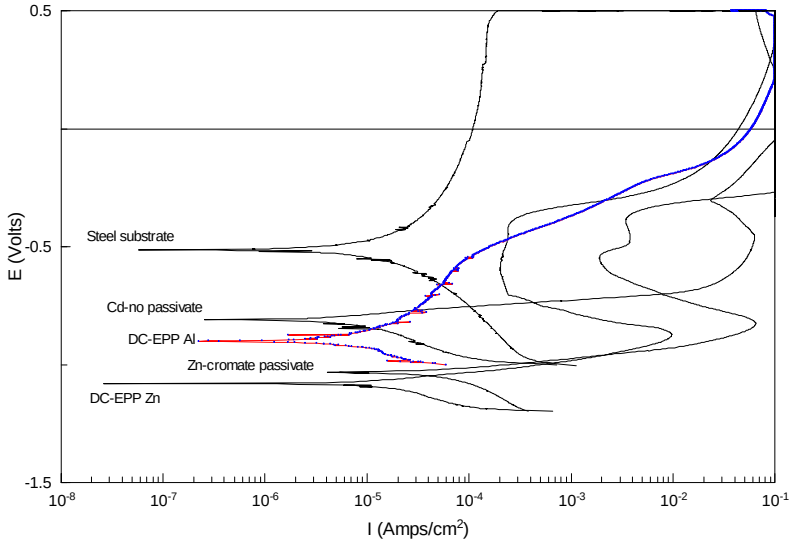

Figure 29 Comparative representation of corrosion behaviour for selected coatings studied in this project.

5.4.3. Discussion of the results

A better understanding of electrochemical properties of the coatings developed within this part of the project can be obtained from Figure 30, where straight comparison between selected new and benchmark coatings is made. It can be seen that none of the EPP coatings developed at this stage is capable of satisfying at the same time the following two criteria for successful replacement of Cd plated coatings on 4340 HSS:

(i) possess a corrosion potential around -0.8V vs SCE

and

(ii) have a region of passivity above -0.5V vs SCE.

A further work was therefore scheduled to tailor electrochemical properties of the EPP coatings, with the following two approaches explored. Firstly, a possibility of incorporation of V, Mn and Mg into EPP Zn-Al coatings should be addressed by developing ternary Zn-Al-Me electrolyte systems. The interest in these particular elements was driven by the following considerations: V is known to promote iron passivation and could also serve as oxygen sink in the coating; Mn acts anodically with respect to Fe but cathodically with respect to Al, so it should remain in a reduced form, providing the required corrosion potential to the coating; and finally Mg acts anodically with respect to Al, so it should promote reduction of Al oxides/hydroxides in the coating. An alternative approach would comprise development and application of passivating post-treatments to the EPP coatings produced from simple, hence more reliable, electrolyte systems. Corresponding trials and associated results of are discussed in the following two sections of the report.

5.5. EPP coatings produced from ternary Zn-Al-Me electrolyte systems (Me= V, Mn, Mg)

Relevant experiments were performed in a configuration with linear reciprocating movement of the flat coupon specimens. Base electrolyte was composed of 0.2 M each of Zn and Al sulphate salts, to which 0.1 M of corresponding Me sulphate was added. Operation temperature was maintained at 85-90 ^{o}C and linear sample speed was set at 15 mm min^{-1}. Other processing parameters corresponded to the conditions of Table 2. Pulsed unipolar current was used, with frequency and duty cycle selected within 10-15 kHz and 0.6-0.8 ranges, respectively. The amplitude of voltage pulses at -230…-270 V resulted in the mean average current to be within the range of 12-14 A. To investigate electrolyte in-service life, up to 5 runs was repeatedly carried using the same electrolyte batch, with coating appearance and thickness examined after each run.

Figure 31 shows typical results of SEM analysis of EPP coatings deposited from the ternary electrolyte systems. It can be seen that the coating thickness varies from about 10 μm for V-containing coating to about 15-25 μm for Mn- and Mg-containing coatings;

however the latter two exhibited much greater porosity. Both V- and Mn-containing coatings changed their appearance from the beginning to the end of the first sample, whereas the appearance of the first two samples treated in Mg-containing electrolyte was uniform. By the third run, dark hydroxide precipitate has formed in the tank, preventing electrolyte from further use. Based on these observations it was concluded that electrolytes containing aluminium, vanadium and manganese sulphates possess insufficient stability for long term usage under EPP conditions. These electrolyte systems were subsequently ruled out from further trials and it was decided to focus on binary Zn-Mg system.

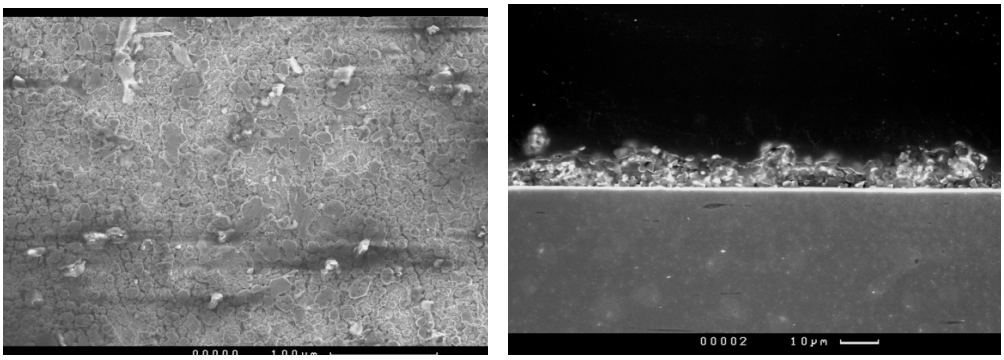

(a) Zn-Al-V

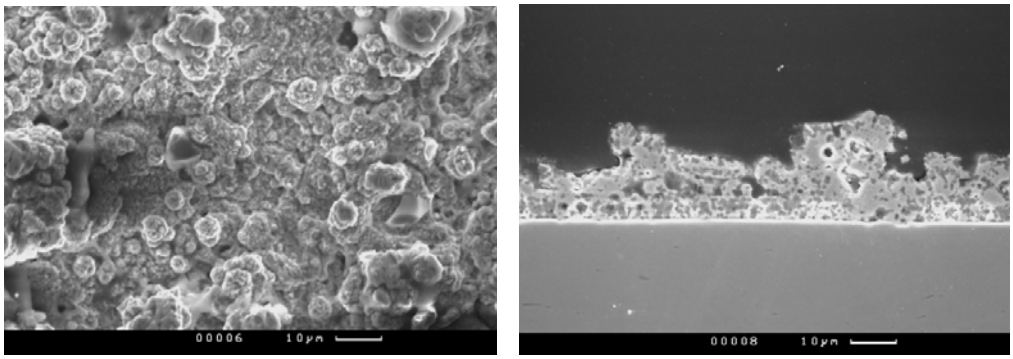

(b) Zn-Al-Mn

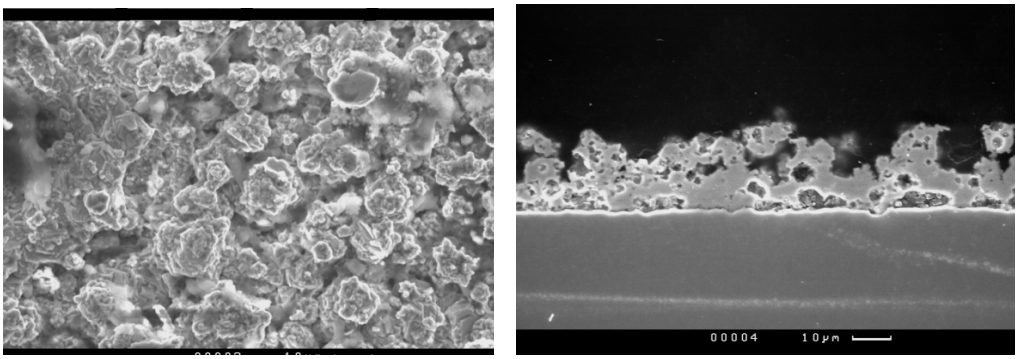

(c) Zn-Al-Mg

Figure 31 SEM images of surface (left) and cross-sectional view of EPP coatings produced from ternary electrolyte systems: (a) Zn-Al-V; (b) Zn-Al-Mn and (c) Zn-Al-Mg sulphates.

6. Sequential Surface Treatments Involving EPP Coatings Obtained From Binary Zn-Mg Containing Electrolyte

As discussed in section 5.4.3, an alternative approach to application of complex electrolyte systems for hybrid EPP deposition of multicomponent coatings consists in development of sequential treatment procedures wherein EPP coating is followed by a passivation treatment. It should be noted that a number of diverse passivation methods is readily available for both bare steel substrate, Cd and Zn coatings and some of them have been provided together with the benchmark coatings discussed in section 5.2. Within the context of this research it was reasonable to address environmentally benign passivation treatments, for example conversion zinc phosphate coatings. A further synergetic enhancement in anticorrosion performance can be achieved sequential phosphating and silicate post-sealing as discussed in recent scientific literature (see for example B Lin et al, SCT **202** (2008) 1831). This simple post-treatment technique was utilised in the experiments discussed within the present section.

The sequential treatments implemented for the treatment of flat coupons made from 4340 HSS consisted of the following three steps:

(i) Deposition of EPP coating using Zn-Mg sulphate bath. The concentration of Zn salt was maintained at 0.2 M and the concentration of Mg salt was varied in the range from 0.1 to 0.2 M. A pulsed unipolar current was applied with voltage amplitude set at -250…-270 V, f= 10…15 kHz and δ=0.6…0.8. Other processing parameters corresponded to the experimental conditions given in Table 2.

(ii) Zinc phosphating for 5 min in the solution containing 1.2 g l^{-1} ZnO, 15 g l^{-1} $NaNO_3$and 11 ml l^{-1} H_3PO_4 at 45 ^oC.

(ii) Post-sealing for 5 min in a solution of 5 g l-1 Na_2SiO_3 at 85 ^oC.

After each step, the samples were rinsed in cold water and dried by hot air.

Table 6 illustrates the effect of Mg concentration in the electrolyte on the resulting coating thickness and surface roughness. The coatings produced in electrolytes with low Mg content (Batch 1) are rough and thick. Increases in Mg content in the electrolyte from 0.1 to 0.2 M result in decreased coating thickness and roughness in terms of Rz value, however now significant difference is observed for Ra values.

Table 6 Thickness and roughness of EPP coatings

Batch #	$MgSO_4$ concentration (M)	Coating thickness (μm)	Ra (μm)	Rz (μm)
1	0.1	18.1±1.01	3.9±0.70	20.30±3.00
2	0.15	16.7±0.87	3.4±0.26	17.3±1.7
3	0.2	13.9±0.75	3.8±1.13	16.9±3.34

Figure 32 shows SEM images in both surface plane and cross-sectional views of the passivated EPP coatings. The surface topology is constituted by needle like deposits characteristic for phosphate conversion coatings. The needles tend to fill in voids formed by open porosity within the coatings. With increased concentration of Mg salt, the coating becomes slightly thinner and porosity is reduced substantially. This indicates that introduction of Mg salt into the electrolyte is beneficial for the coating morphology. The electrolyte was observed to become more stable, so it was possible to treat up to 10 flat coupons using the same electrolyte batch (approximately 3 litres).

Figure 33 shows the results of GDOES analysis illustrating effects of phosphate-silicate post treatment on the distribution of main chemical elements across the EPP coating. It can be seen that phosphate deposition occurs not only in the outer region but penetrates into inner coating regions, probably through surface related porosity. At the same time, the deposition of silicate occurs mainly in the outer regions to enhance sealing the coating porosity. This is also accompanied with chemical interactions between zinc phosphate and sodium silicate in the surface layer, as reflected in crystallographic structure of the coating revealed by XRD analysis (Figure 34). Peaks associated with zinc silicate phase were identified in RXD patterns, together with those attributed to zinc phosphate and silica.

Electrochemical corrosion behaviour of the treated surfaces was studied using both potentiostatic and potentiodynamic techniques. Typical evolution patterns of the open circuit potential of coated surfaces with exposure time in 3.5% NaCl solution is shown in Figure 35. It can be seen that open circuit potential values are similar for both as received and passivated coatings, corresponding to -1.05V vs SCE, which is characteristic for Zn coatings. The potential remains steady with time, with no apparent perturbations observed, which is indicative of stable equilibrium between anodic and cathodic processes at the surface. Figure 36 represents results of potentiodynamic corrosion studies carried out for the EPP coated and passivated surfaces. It is clear that as, a result of passivation, the region of passivity shifts from (-0.8…-0.55) V to (-0.6…-0.25) V (Figure 36 a). This means that, compared with the as received EPP coating, the phosphate-silicate post-treatment promotes coating passivation at higher anodic potentials, superposing the corrosion potential of steel. Thus, should any galvanic coupling be formed between the coating and the substrate, the coating corrosion would be inhibited most of the times due to surface passivation; this should enhance the coating anticorrosion performance and durability. Another positive aspect to be noticed is that the region of passivity for the passivated EPP coatings is not affected by the coating open circuit potential (Figure 36 b).The latter appears to be controlled by the cathodic reaction; the effect is similar to that observed for EPP cleaned

surfaces. This seems to represent a generic feature of EPP technology and further investigations are needed to provide a better insight into the mechanisms underlying this phenomenon.

Thus, it was shown that at the current evolution stage of EPP technology, sequential treatments combining pulsed current EPP cleaning and coating with subsequent passivating post-treatments appear to offer the most ecologically benign, technically feasible and reliable solutions to the corrosion problem of 4340 HSS that could in some cases be considered as an alternative to Cd electroplating. However a further work is desirable to address the issues associated with coating morphology, electrolyte stability and understanding of corrosion mechanisms for EPP treated surfaces.

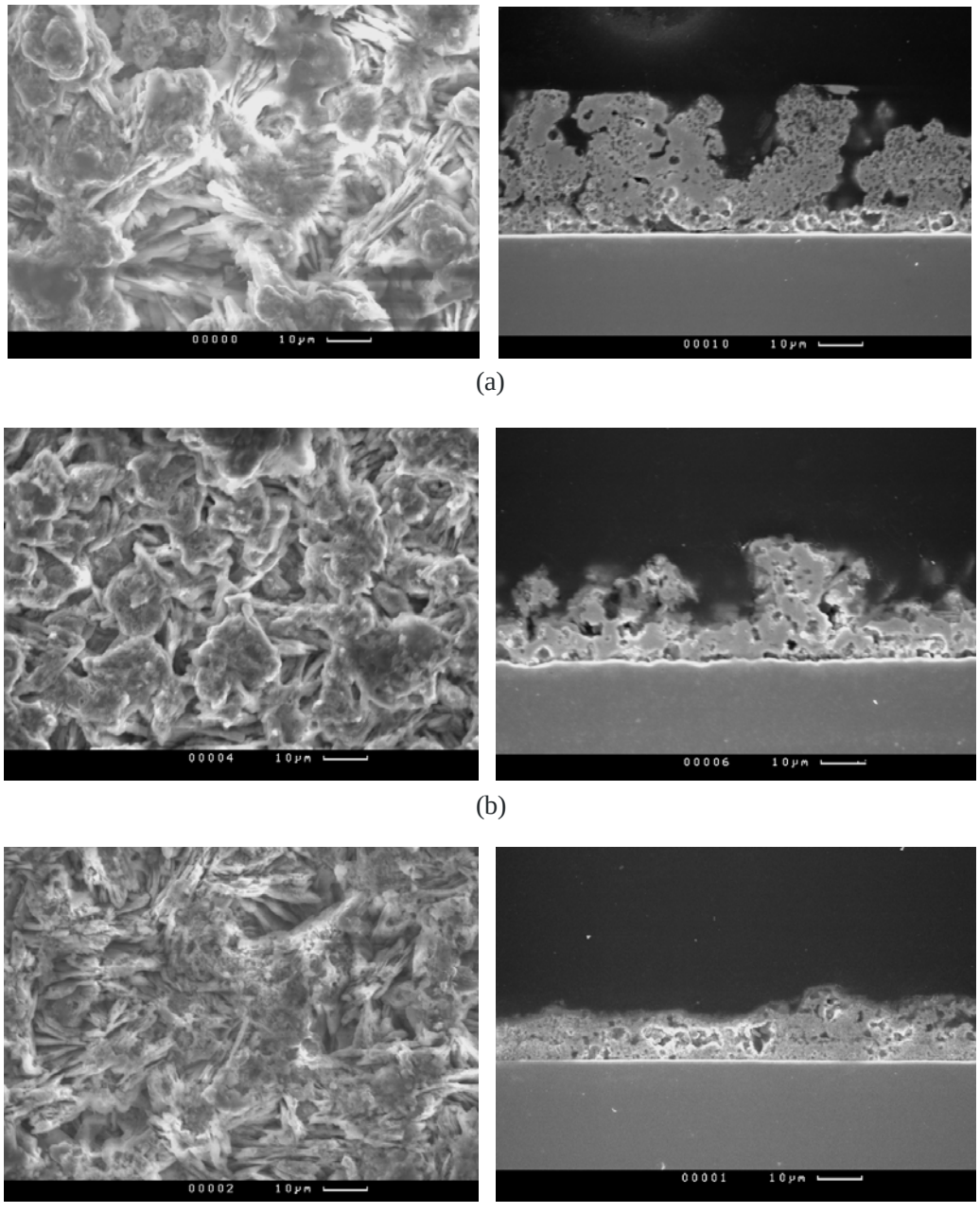

Figure 32 SEM images of surface (left) and cross-sectional view of EPP coatings produced from binary Zn-Mg sulphate electrolyte systems with various concentrations of Mg sulphate: (a) 0.1 M; (b) 0.2 M; (c) 0.3 M, followed by the phosphate-silicate passivation tr

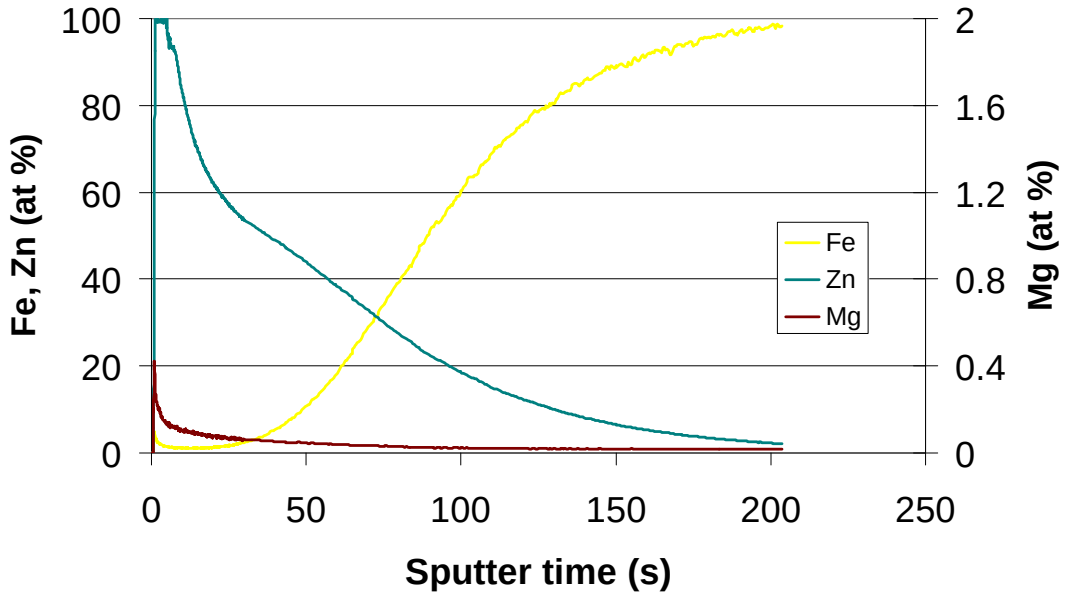

(a)

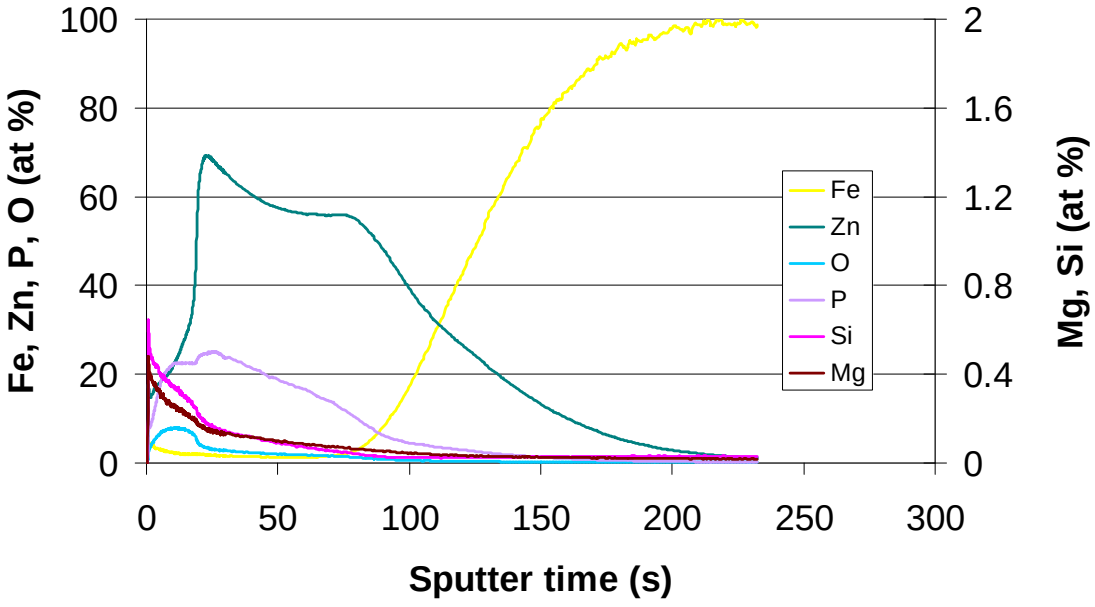

(b)

Figure 33 Typical GDOES depth profile patterns for (a) as received and (b) phosphate-silicate passivated EPP coatings

.

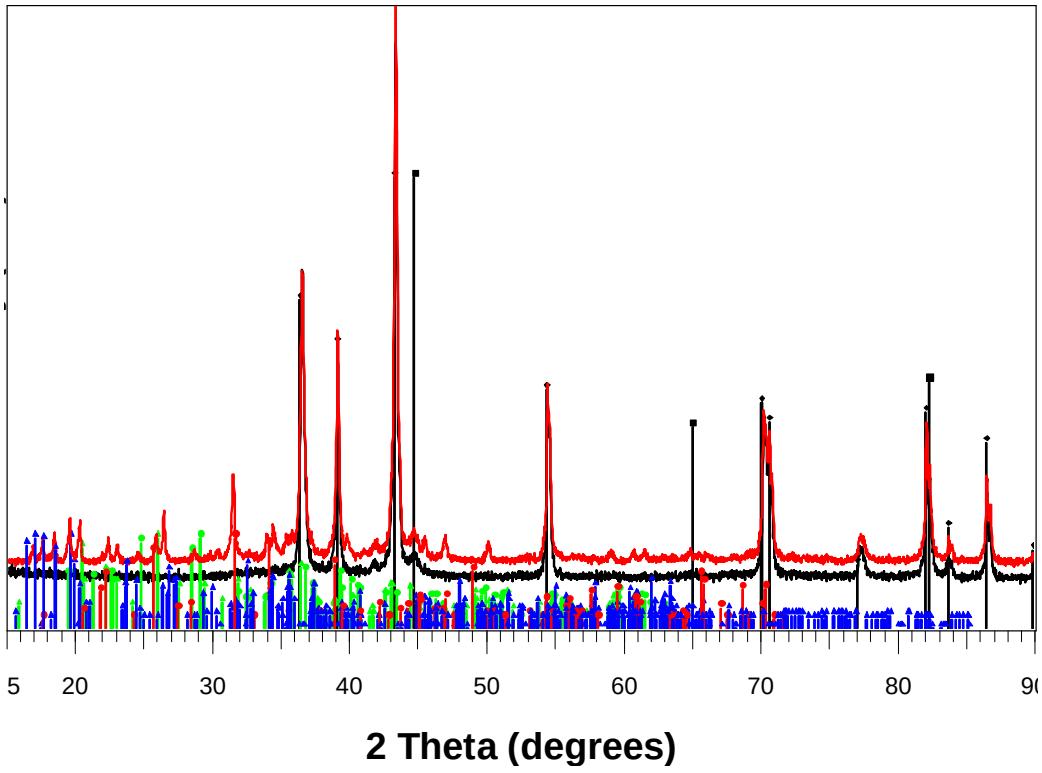

Figure 34 Typical XRD patterns of as deposited (black) and phosphate-silicate passivation treated EPP coatings. PDF patterns correspond to the following substances: Black – Zn, Red – Zn phosphate; Blue – Silica and Green – Zn silicate

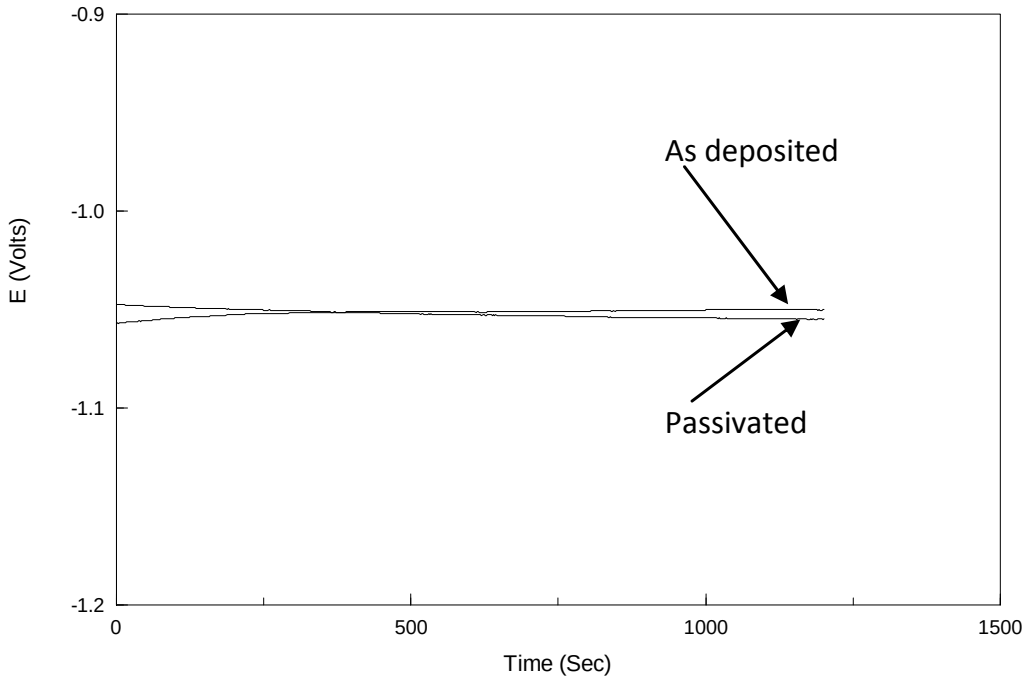

Figure 35 Time dependencies of open circuit potential for as deposited and passivated EPP coatings in 3.5% NaCl solution.

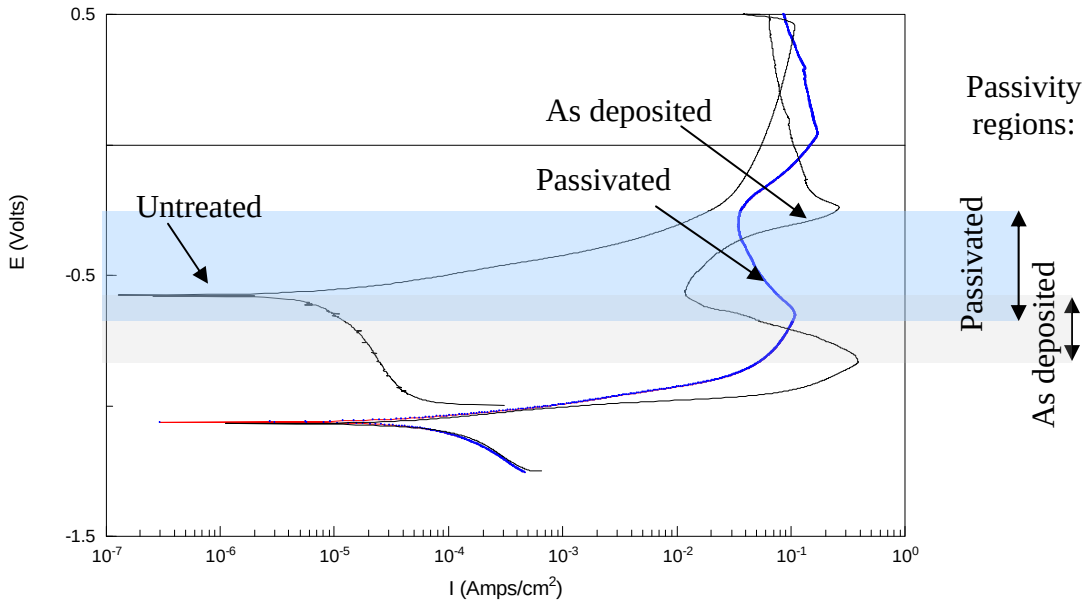

(a)

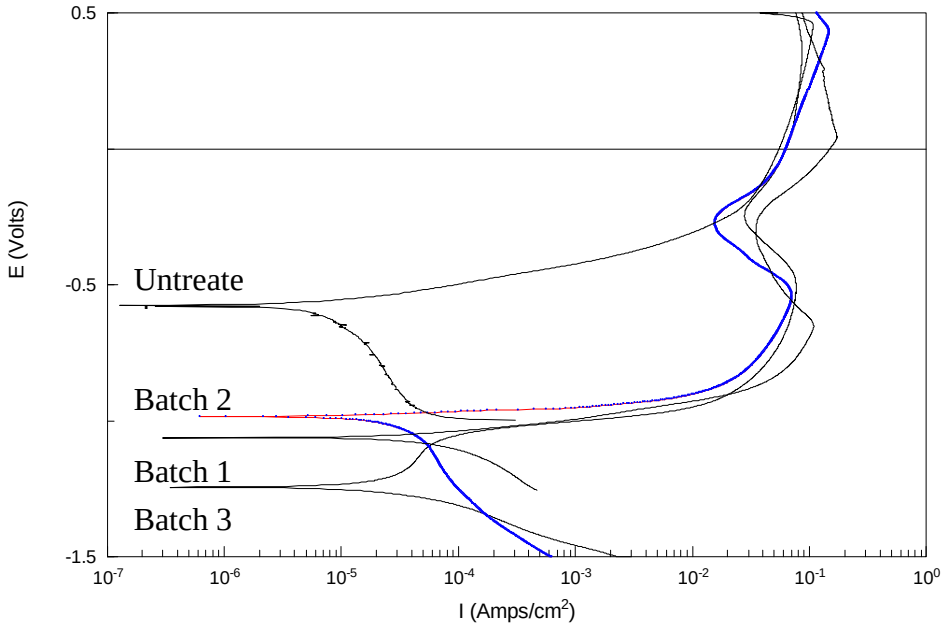

(b)

Figure 36 Potentiodynamic polarisation curves of EPP coatings produced from binary Zn-Mg containing electrolytes illustrating effects of (a) the passivation post-treatment and (b) Mg salt content in the bath.

7. Provision of EPP treated samples for further testing

7.1. Provision of cleaned samples for Hydrogen Embrittlement and Fatigue tests

Based on the results of the investigations discussed in section 4, the following conditions were selected for the cleaning treatment of Hydrogen Embrittlement and Fatigue test samples, provided by the project partners:

	Batch 1	Batch 2	Batch 3
Frequency (Hz)	100	1000	10000
Duty cycle	0.8	0.8	0.8
Voltage amplitude (V)	180	180	205
Current amplitude (A)	6-8	6-9	5-10
Time (s)	45	45	45
No of HE samples	6	6	6
No of Fatigue samples	8	8	8

Figure 37 illustrates the typical appearance of HE and Fatigue test samples at different steps of the cleaning process. The EPP cleaning treatments of all the samples were successfully carried out in the rotating sample configuration with the vertical counter-electrode arrangement. The cleaned samples were subjected to a conservation procedure (i.e. spraying with oil) to prevent corrosion and dispatched for further evaluations.

7.2. Provision of EPP cleaned samples for additional Fatigue tests

Following the results of mechanical evaluations carried out using the samples provided as discussed in section 7.1, it was suggested to introduce a grit-blasting type of pre-treatment operation prior to EPP cleaning. This was deemed to induce deeper compressive internal stresses which would remain in the sub-surface region after the pulsed current EPP treatment. An additional batch of 10 fatigue samples with appropriate pre-treatment was therefore supplied by the project partner (Metcut, Inc) and treated at the following parameters of EPP cleaning:

Electrolyte: 10% sodium bicarbonate; Temperature: 60^{o}C;

Flow rate: 3 l min^{-1}; Interelectrode gap:6 mm;

Duty cycle: 0.8; Frequency: 10 kHz;

Treatment time: 45 s.

The samples have been provided to the project partner for additional fatigue tests. The test results showed no reduction in fatigue strength, compared to the untreated substrate. Thus the hypothesis on a significant role of internal stresses in fatigue behaviour of EPP treated 4340 HSSs was verified.

Figure 37 Samples for Hydrogen Embrittlement (top) and Fatigue tests (bottom) after different steps of EPP treatment procedure. 1 – prior to cleaning treatment; 2 – after the cleaning; 3 – after deionised water rinsing.

7.3. Provision of EPP coated samples for Fatigue and Corrosion tests

Based on the results of the investigations discussed in sections 5 and 6, the following conditions were selected for the coating treatment of Fatigue test samples and Corrosion plates, provided by the project partners:

I Coating deposition:

	Batch 1	Batch 2	Batch 3
Electrolyte:			
(0.2 M $ZnSO_4$) +			
+ x M MgSO4; x =	0.1	0.15	0.2
Temperature (^oC)	90	90	90
Flow rate (l min^{-1})	1	1	1
Current mode:			
Frequency (kHz)	10	10	15
Duty cycle	0.6	0.6	0.7
Voltage amplitude (V)	250	250	270
Average Current (A)	6-8	6-9	5-10
Reactor:			
Interelectrode gap (mm)	8	8	8
Linear speed (mm min^{-1})	15	15	15
Rotation rate (rpm)	120	120	120
No of Fatigue samples	**10**	**10**	**10**

II Post-treatment:

Step 1:			
Electrolyte:	1.2g l^{-1} ZnO + 15 g l^{-1} $NaNO_3$ + 11 ml l^{-1} 85%H_3PO_4		
Temperature (^oC)	45	45	45
Time (min)	5	5	5

Step 2:

Electrolyte:	5 g l-1 Na_2SiO_3		
Temperature (^oC)	85	85	85
Time (min)	5	5	5
No of Corrosion plates	**6**	**6**	**6**

Figure 38 illustrates the typical appearance of Fatigue test samples and Corrosion test plates at different steps of the coating deposition process. The coating of the Fatigue samples was carried out in a rotating sample configuration with the vertical counter-electrode arrangement. The coating of the Corrosion test plates was carried out in the linear reciprocating configuration with the vertical counter-electrode arrangement. Before being dispatched for further evaluations, Fatigue samples were subjected to a conservation procedure (i.e. spraying with oil) to prevent corrosion of uncoated areas.

1

2

(a)

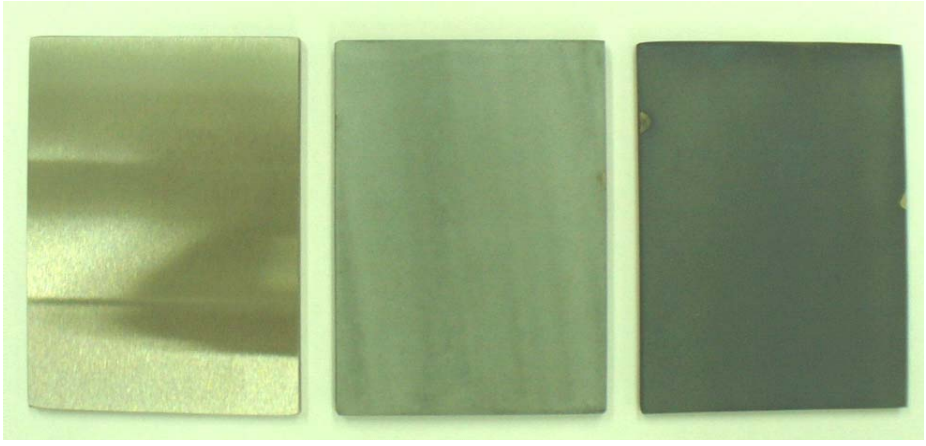

1 2 3

(b)

Figure 38 Samples for Fatigue tests (a) and 2 by 3 inch Salt Fog Corrosion Plates (b) after different steps of EPP treatment procedure: 1 – prior to EPP coating; 2 – after the coating; 3 – after the passivation treatment.

8. Conclusions and future work

As a result of the extensive work programme during the course of the project all major objectives are met and the main conclusions can be formulated as follows:

- A modification has been carried out to the existing experimental EPP facility to allow uniform and reproducible EPP treatments of different components, with particular attention paid to the treatment of the surfaces that are difficult to access by electrolytic plasma, e.g. notches, grooves and cavities. A possibility of uniform EPP treatment was also provided to the relatively large flat surfaces that require high power capacity. The adopted design solutions were validated by a series of experiments, which allowed identification of the ranges of process parameters to ensure stable and reliable operation of the equipment.

- The work programme on EPP cleaning has led to the development of a novel EPP cleaning technology based on pulsed unipolar current modes. Enhanced capabilities of this technology compared to simple DC treatments were demonstrated, showing substantial reduction of surface roughness and minimisation of detrimental effects of electrolytic plasmas on surface hardness of 4340 HSS substrates. Optimal ranges of pulsed current parameters for EPP cleaning were identified as f=100 to 10000 Hz at δ=0.8 and δ=0.2 to 0.8 at f=100 Hz.

- Detailed characterisation of EPP cleaned surfaces, including SEM studies of surface morphology, evaluation of crystallite size in the surface layer and XRD analysis of internal stress achieved an in-depth insight into the mechanisms underlying the effects of EPP treatments on fatigue performance of 4340 HSS substrates. The crucial role of internal stresses in fatigue life was demonstrated and possible ways to control the stress state are suggested, using the induction of a compressive stress profile by appropriate surface pre-treatment procedures (e.g. by grit blasting) combined with application of pulsed current EPP treatments. The samples treated in such a way did not show any measurable reduction in fatigue strength.

- Capabilities of pulsed current EPP technology were explored in process development for coating deposition from Al-based single component and binary Al-Zn-containing electrolyte systems. A relatively high content of Al was achieved in the coatings produced using pulsed bipolar current modes, in particular from alkaline electrolytes, although Al was likely to be present in an oxidised form. The oxidation of aluminium and associated precipitation of $Al(OH)_3$ compounds, both at the sample surface and in the bulk of the electrolyte, appear to represent a fundamental problem affecting both coating morphology and electrolyte life. It was therefore concluded that, at the current stage of technology development, electrolyte systems containing inorganic compounds of Al cannot be recommended for a large-scale EPP treatment without additional anti-oxidative treatments.

- Accelerated corrosion tests carried out using potentiodynamic techniques allowed evaluation of the feasibility of various EPP coatings as Cd alternatives. It was shown that the addition of passivating agents, e.g. salts of V and Mn, to the binary Zn-Al-containing

electrolyte allowed tailoring of the electrochemical properties of EPP coatings to match those of benchmark Cd plating. However these additions dramatically affected the electrolyte life, undermining the process scalability.

- Alternative solutions were offered in the form of sequential treatments, combining EPP coatings with passivating post-treatments. It was demonstrated that binary Zn-Mg based electrolyte systems offer enhanced reliability and reproducibility of EPP coatings together with adequate electrolyte durability. The EPP process developed based on the Zn-Mg electrolyte system was implemented for coating relatively large surface areas (e.g. flat corrosion test coupons) as the first step of the sequential treatment procedure. Subsequent two-step zinc phosphate-silicate passivating treatment applied to the coatings allowed expansion of their passivity region, thereby enhancing electrochemical performance of the surface layer.

- Developed pulsed current EPP cleaning and sequential coating processes were successfully implemented for the treatment of series of test samples that have been made available to other project partners for mechanical and corrosion evaluations, including Hydrogen Embrittlement, Fatigue and Salt Fog Corrosion tests.

In regard to the future work, it would certainly be of benefit to explore further the potential of sequential surface treatments incorporating EPP technology for both cleaning and coating applications. Significant prospectives offered by pulsed current technology to control both plasma discharge characteristics and surface layer properties should not be overlooked. One of the major challenges in this direction is represented by the number of electrical parameters that can be varied, making the process optimisation procedure extremely laborious. This could be addressed by applying intelligent methods of experimental design and analysis, e.g. based on neural networks.

In terms of multicomponent Zn-based EPP coating systems, apparent interest for tailoring electrochemical performances of Zn and Zn-Al coatings represents incorporation of passivating additions, e.g. V and Mn. Similar to Al-containing electrolyte systems, the major obstacle here lies in ensuring adequate performance of electrolyte systems. A more fundamental investigation into the chemistry of these electrolyte systems together with detailed studies of electrochemical aspects of EPP technology would therefore be necessary.

Finally, a better understanding has to be achieved in the fundamental mechanisms underlying corrosion behaviour of EPP treated surfaces. This could for example include application of electrochemical scanning probe techniques for potential mapping of both cleaned and coated surfaces. Although rather fundamental in nature, the work in this direction is potentially very useful and could trigger new breakthrough developments in the field of electrolytic plasma technology.